KARAGANDA BUKETOV UNIVERSITY

ISSN 2959-0663 (Print)
ISSN 2959-0671 (Online)
ISSN-L 2959-0663

EURASIAN JOURNAL OF CHEMISTRY

2024. Vol. 29 No. 2(114)

ISSN 2959-0663 (Print)
ISSN 2959-0671 (Online)
ISSN-L 2959-0663

EURASIAN JOURNAL OF CHEMISTRY

2024

Volume 29, No. 2 (114)

Founded in 1996

Published 4 times a year

Karaganda
2024

Publisher: **Karagandy University of the name of academician E.A. Buketov**
Postal address: 28, University Str., Karaganda, 100024, Kazakhstan
E-mail: chemistry.vestnik@ksu.kz; irina.pustolaikina@ksu.kz; ipustolaikina@gmail.com
Tel./fax: +7(7212) 34-19-40.
Web-site: https://ejc.buketov.edu.kz

Editor-in-Chief

Ye.M. Tazhbayev, Doctor of Chemical sciences

Executive Editor

I.A. Pustolaikina, Candidate of Chemical sciences

Editorial board

Z.M. Muldakhmetov,	Academician of NAS RK, Doctor of chem. sciences, Institute of Organic Synthesis and Coal Chemistry of the Republic of Kazakhstan, Karaganda (Kazakhstan);
S.M. Adekenov,	Academician of NAS RK, Doctor of chem. sciences, International Research and Production Holding “Phytochemistry”, Karaganda (Kazakhstan);
S.E. Kudaibergenov,	Doctor of chem. sciences, Institute of Polymer Materials and Technologies, Almaty (Kazakhstan);
V. Khutoryanskiy,	Professor, University of Reading, Reading (United Kingdom);
Fengyun Ma,	Professor, Xinjiang University, Urumqi (PRC);
Xintai Su,	Professor, South China University of Technology, Guangzhou (PRC);
R.R. Rakhimov,	Doctor of chem. sciences, Norfolk State University, Norfolk (USA);
N. Nuraje,	Associate Professor, Nazarbayev University, Astana (Kazakhstan);
S.A. Beznosyuk,	Doctor of phys.-math. sciences, Altai State University, Barnaul (Russia);
B.F. Minaev,	Doctor of chem. sciences, Bohdan Khmelnytsky National University of Cherkasy, Cherkasy (Ukraine);
I.V. Kulakov,	Doctor of chem. sciences, University of Tyumen (Russia);
R.P. Bhole,	PhD, Associate Professor, Dr. D.Y. Patil Institute of Pharmaceutical Sciences and Research, Sant Tukaram Nagar, Pimpri, Pune (India);
A.M. Makasheva,	Doctor of techn. sciences, Zh. Abishev Chemical-Metallurgical Institute, Karaganda (Kazakhstan);
M.I. Baikenov,	Doctor of chem. sciences, Karagandy University of the name of acad. E.A. Buketov (Kazakhstan);
L.K. Salkeeva,	Doctor of chem. sciences, Karagandy University of the name of acad. E.A. Buketov (Kazakhstan);
G.I. Dzhardimalieva,	Doctor of chem. sciences, Federal Research Center of Problems of Chemical Physics and Medicinal Chemistry, Russian Academy of Sciences, Chernogolovka, Moscow Region (Russia);
S.K. Filippov,	PhD, Project Leader, DWI-Leibniz Institute for Interactive Materials, Aachen, North Rhine-Westphalia, (Germany);
S.A. Ivasenko,	Doctor of pharm. sciences, Karaganda Medical University (Kazakhstan).

Editor I.N. Murtazina

Computer layout V.V. Butyaikin

Eurasian Journal of Chemistry. — 2024. — Vol. 29, No. 2(114). — 105 p.

ISSN 2959-0663 (Print). ISSN 2959-0671 (Online). ISSN-L 2959-0663

Proprietary: NLC “Karagandy University of the name of academician E.A. Buketov”.

Registered by the Ministry of Information and Social Development of the Republic of Kazakhstan. Re-registration certificate No. KZ95VPY00063697 dated 30.01.2023.

Signed in print 27.06.2024. Format 60×84 1/8. Offset paper. Volume 13,12 p.sh. Circulation 200 copies. Price upon request. Order № 53.

Printed in the Publishing house of NLC “Karagandy University of the name of academician E.A. Buketov”.
28, University Str., Karaganda, 100024, Kazakhstan. Tel.: +7(7212) 35-63-16. E-mail: izd_kargu@mail.ru

© Karagandy University of the name of academician E.A. Buketov, 2024

CONTENTS

ORGANIC CHEMISTRY

PHYSICAL AND ANALYTICAL CHEMISTRY

CHEMICAL TECHNOLOGY

How to Cite: Tazhbayev, Y.M., Kazhmuratova, A.T., Zhaparova, L.Zh., Tuleuov, U.B., Nassikhatuly, Y., Mitricheva, E.S., Kwiatkowski, A.L., & Shibaev A.V. (2024) Synthesis of Water-Soluble Polyethylene Glycol Fumarates for Biomedical Applications. *Eurasian Journal of Chemistry, 29, 2(114), 4-12.* https://doi.org/10.31489/2959-0663/2-24-7

ORGANIC CHEMISTRY

Article

Received: 15 March 2024 | Revised: 24 May 2024 |
Accepted: 31 May 2024 | Published online: 11 June 2024

UDC 544.42+519.242.7

https://doi.org/10.31489/2959-0663/2-24-7

Yerkeblan M. Tazhbayev[1], Akerke T. Kazhmuratova[1], Lyazzat Zh. Zhaparova[1]*, Ulugbek B. Tuleuov[1], Yermauyt Nassikhatuly[1], Elizaveta S. Mitricheva[2], Alexander L. Kwiatkowski[2], Andrey V. Shibaev[2]

[1]*Karaganda Buketov University, Karaganda, Kazakhstan;*
[2]*Physics Department, Lomonosov Moscow State University, Moscow, Russia*
*(*Corresponding author′s e-mail: lyazzh@mail.ru)*

Synthesis of Water-Soluble Polyethylene Glycol Fumarates for Biomedical Applications

Polyethylene glycol fumarate (PEGF) with controlled structural composition has been obtained for further synthesis of double network cross-linked hydrogels for biomedical applications. The copolymer has been synthesized by polycondensation reaction of fumaric acid and polyethylene glycol (PEG-600). Molecular weight of PEGF has been determined by gel permeation chromatography to be approximately 6000 Da with gel permeation chromatography. The polycondensation of fumaric acid and PEG-600 was studied throughout the reaction process. The structure of the reaction product has been evidenced using FTIR- and 1H NMR-spectroscopy. The quantitative ratios of the amount of –C=C– bonds and –COO groups to –C=O groups in the obtained PEGF have been estimated from IR-spectra for different synthesis time. The time-dependence of molar ratio of double bonds to methyl groups in PEGF has been obtained from corresponding 1H NMR-spectra. FTIR and 1H NMR-spectroscopy, both, demonstrate that after the end of reaction the unsaturated –C=C– double bonds remain in the structure of the macromonomer, that is essential for further preparation of cross-linked hydrogels. The addition of the tightly cross-linked network of polyvinyl alcohol leads to formation of highly tough biocompatible material for preparation of the artificial meniscus which can further be used as a solution in the treatment of diseases such as osteoarthritis.

Keywords: polyethylene glycol, polyethylene glycol fumarate, fumaric acid, polyester resin, macromonomer, hydrogels, FTIR- spectroscopy, 1H NMR-spectroscopy.

Introduction

The creation of novel materials with sufficient mechanical properties for use in various areas of science and industry is of great importance. Due to their unique properties such materials have a wide range of applications starting from additives for building materials to use in medicine [1–16]. Varieties of copolymers have been studied to obtain the systems used in medicine for different purposes [17–29], e.g. in tissue engineering [18, 22, 27], metallic nanocomposites [25, 26], double network stimuli-responsive hydrogels [23, 30] and so on. Among other polymers the oligo-/polyethylene glycol fumarates are recommended and investigated as medical hydrogel systems for tissue regeneration and drug delivery purposes due to their best mechanical properties [13, 14, 24]. Besides, the cryogels based on oligo-/polyethylene glycol fumarates were effectively synthesized for the biomedical applications [27]. High elasticity and simplicity of the synthesis of polyethylene glycol fumarates make them an interesting and promising object for the development of hydrogels for the biomedical application. Biocompatible soft materials made of hydrogels with high toughness based on double polymer networks can be used for the replacement of the soft tissue with endoprosthesis which could be a solution for the treatment of such severe disease as osteoarthritis [5–9]. Such gels consist of two compartments: the first should have rigid and highly cross-linked structure, while the other must be weakly-crosslinked and possess elasticity [6] to be able to restore after huge deformations applied to a knee joint. In this regard, polyesters can serve as building blocks for the second elastic network. For instance, oligo/polyethylene glycol fumarates were suggested in the literature as promising polymers for hydrogels in medicine [10–12]. Thus, it could be used for the preparation of biocompatible hydrogels based on a of double cross-linked network. In this case, polyvinyl alcohol could be a material for the first rigid network [13–16].

The present article focuses on the synthesis of water-soluble polyethylene glycol fumarate (PEGF) of controlled structural composition and the investigation of the changes of the process parameters on the structure, composition and properties of the final product.

Experimental

Materials

Polyethylene glycol with molecular weight of 600 Da (PEG-600) and fumaric acid were purchased from Sigma Aldrich. Milli-Q water was used in all the experiments.

Synthesis of PEGF

Polyester resin was synthesized by direct polycondensation reaction of PEG-600 with fumaric acid at a molar ratio of the monomers of 1:1 in three-necked round bottom flask equipped with magnetic stirrer, condenser with Dean-Stark nozzle, thermometer and vacuum outlet. The system was submerged into glycerin or silicone bath to provide uniform heating and was blown with nitrogen. The reaction flask was heated to 160–170 °C for 4–8 hours and then under high vacuum (147.1 millimeters of mercury) for 10 minutes at the same temperature. The reaction was stopped when the calculated amount of water was collected.

Obtained polymer was purified from low molecular substances by dialysis by submerging the dialysis membrane (MWCO 3500 Da (Sigma Aldrich)) into deionized water at room temperature and constant mixing at 250 rpm for 3 days. The deionized water was changed every 6 hours.

The samples were then dried in a vacuum oven at 80 °C for several days until the copolymer with constant weight was obtained.

Molar weight estimation

Molar weights (number-average (Mn) and weight-average (Mw) molecular weights) of the oligo-/polyesters obtained during the reaction after 4, 5, 6 and 8 hours of polycondensation have been determined by gel permeation chromatography (GPC) on a Malvern chromatograph equipped with a Viscotek 270 max dual detector (polystyrene was used as a standard; the standard deviation of the molecular weight was ±100-120). The samples of PEGF were dissolved in water, filtered and analyzed by GPC.

Bromatometry

Bromatometry is an analytical method based on the determination of the amount of bromine released into the medium as a result of the reaction with unsaturated double bonds [31]. For the analysis 1 g of the sample (PEGF) was dissolved in 10 ml of water or the organic solvent and left for 24 hours. Then the mixture of KBr and $KBrO_3$ solution was then poured into the sample solution which had been preacidified with 0.1 N solution of HCl. In acidic medium the bromine molecules react with the unsaturated double bonds in the system. So, the bromide-bromate mixture is then left for 4 hours in a dark place. The access of bromine is titrated with the 0.1 N solution of $Na_2S_2O_3$ in the presence of indicator phenolphthalein using microburette. The sample containing PEGF was analyzed in parallel with the control sample. The bromine index corresponds to the amount of bromine which can be added to 100 g of the substance analyzed.

FTIR- and 1H NMR-spectroscopy

The structure of obtained copolymers has been confirmed by FTIR-spectroscopy on a device FSM 2201, using standard procedure by preparation of KBr tablets in the wavenumber range 4000–400 cm^{-1} with a resolution of 1 cm^{-1}.

^1H NMR-spectroscopy has been performed on a device Bruker AMX-400 spectrometer at 22 °C. For the analysis 0.01 g of dried sample was dissolved in deuterium oxide within 24 hours followed by exposure to US-homogenization at 200 W for 10 min. The peak of chemical shift of D_2O (4.79 ppm) was used as a reference. The frequency range was 950-4100 Hz. This signal was taken as indicated in the references [32, 33].

Results and Discussion

The synthesis of PEGF has been carried out by polycondensation reaction of PEG-600 and fumaric acid at the molar ratio of PEG 600 and fumaric acid of 1:1 according to the scheme:

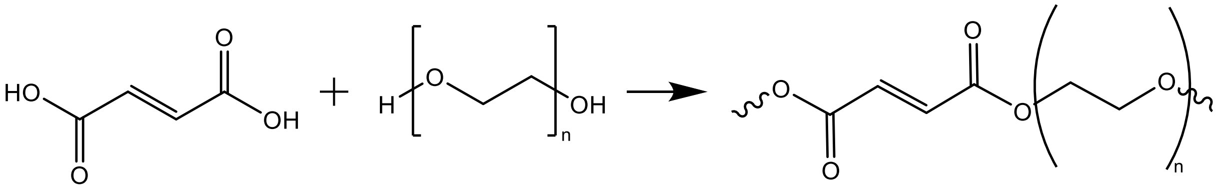

As was measured by GPC, after 8 h of reaction the macromonomer with molecular weight around 6000 Da was formed (Fig. 1).

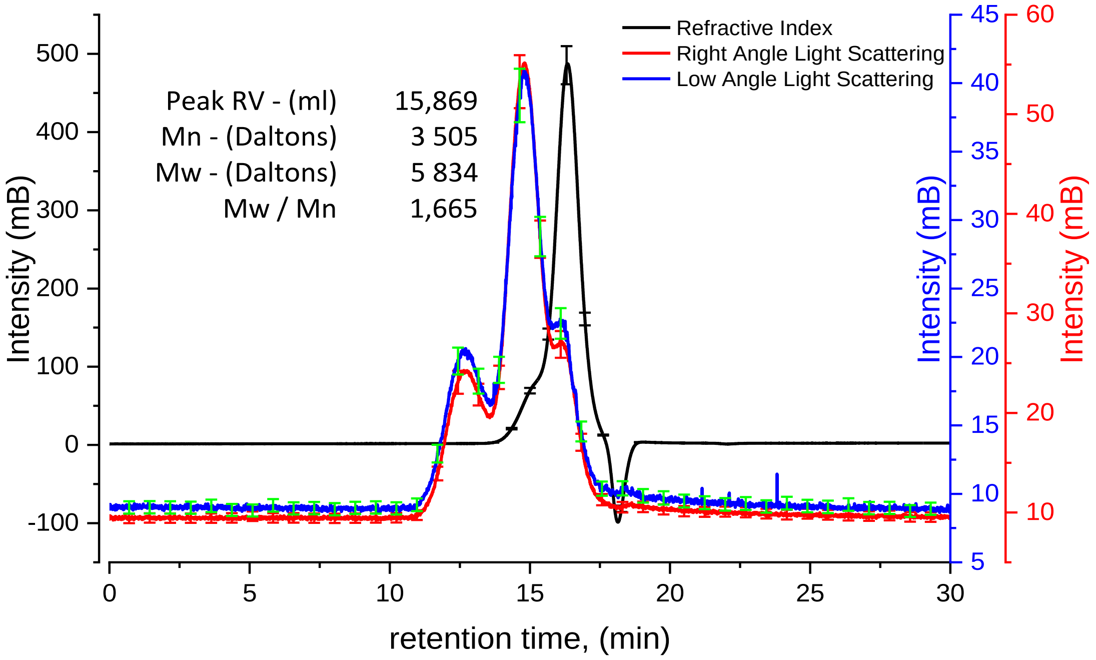

Figure 1. Molecular mass of the final product of PEGF obtained after 8 hours of polycondensation

In order to study the influence of the duration of reaction on the chemical structure of PEGF, the samples were removed from the reaction mixture after a certain time. The obtained purified products were analyzed by FTIR-spectroscopy for the presence of active double bonds necessary for the formation of double network hydrogels. Figure 2 shows the FTIR-spectra of PEGF formed after 1–8 h of polycondensation.

The FTIR spcterum of PEFG has typical –C–O– signal of the ether bond in PEG at 1100 cm^{-1}, in addition, it contains the peaks at 1730 and 1640 cm^{-1} which respectively correspond to the –C=O and –C=C– groups of the fumaryl moiety [12] (Fig. 2). From the FTIR-spectrum of the macromonomer it is obvious that with the time the intensity of –C=C– bond decreases, whereas the signal of ester bond –O–C=O– increases gradually with deepening the conversion. Note, after 8 h of polycondensation process in PEGF there are still active double bonds that are required for further polymerization and the preparation of hydrogels containing cross-linked network [12].

From Figure 2, the ratios of number of carboxylic groups –O-C=O– and unsaturated double bonds –C=C– to the –C=O bonds for different duration of polycondensation reaction were calculated (Fig. 3). The dependence shows decreasing number of double bonds and, simultaneously, increasing number of ester bonds during the reaction. This effect was previously observed in literature [9].

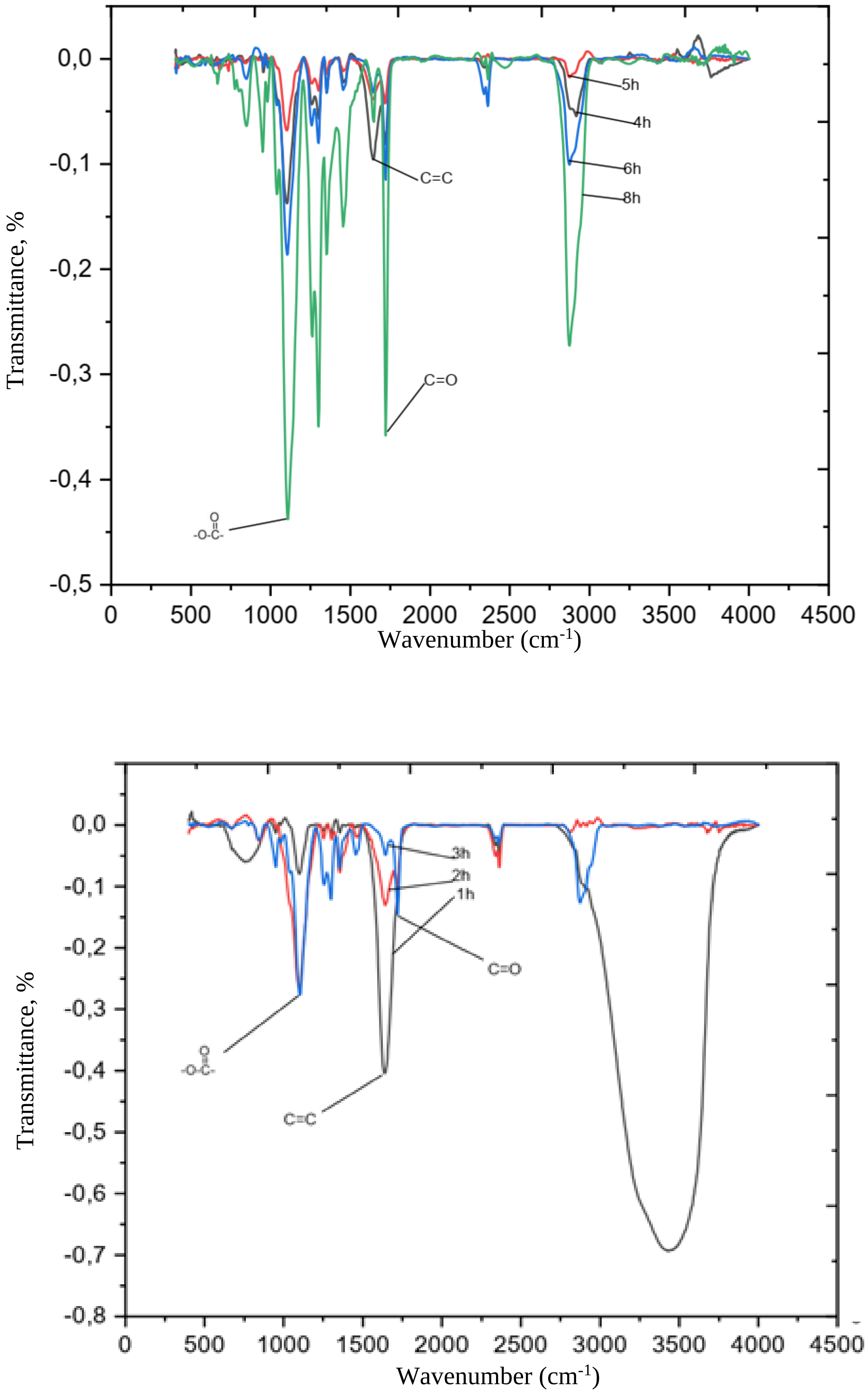

Figure 2. FTIR-spectra of PEGF obtained after different time of polycondensation of PEG-600 and fumaric acid

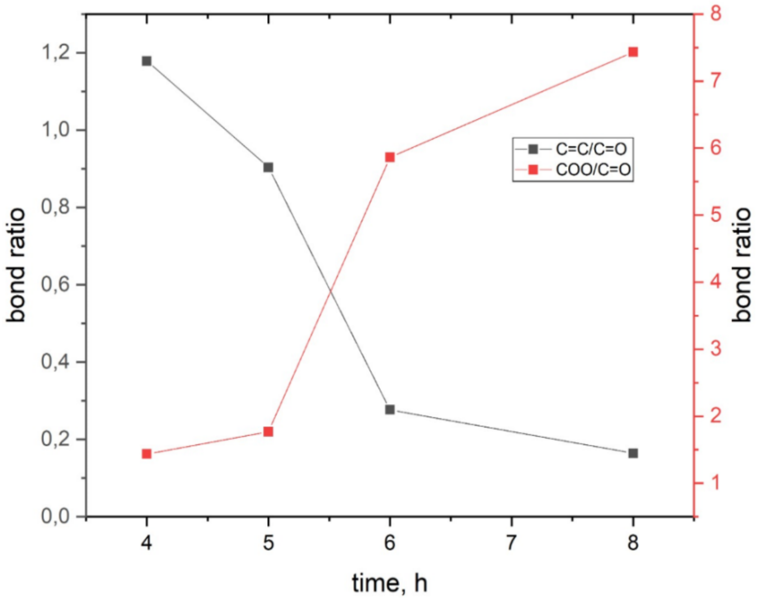

Figure 3. The dependence of the ratio of number of double bonds –C=C– and carboxylic groups –COO– to the –C=O bonds in chemical structure of PEGF, obtained at different time of polycondensation of PEG-600 and fumaric acid

The average degree of unsaturation of the samples obtained at different time of the reaction determined by bromatometry decreases from 7.5 to 5.1 % as the the reaction time increases (Fig. 4). The results of bromatometric analysis are in good correlation with the FTIR-spectroscopy data also indicating on the decrease of the number of double bonds during the reaction (Fig. 4). Thus, after 8 h of polycondensation, only 5 % of double bonds which are essential for further preparation of the double network remain unchanged.

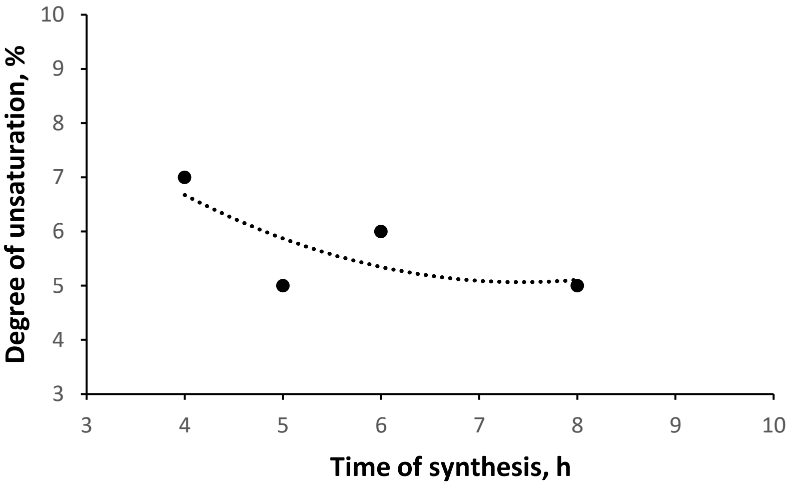

Figure 4. Degree of unsaturation for the samples of PEGF obtained at a different time of polycondensation of PEG-600 and fumaric acid

The following chemical shifts are observed on the spectra of the macromonomer [13]: 1) 3.7–3.9 ppm — the peak of methylene protons (related to $–CH_2–$ groups conjugated with the ether groups); the peak is characteristic for molecules of polyethylene glycol, built-in the structure of PEGF; 2) 4.3–4.5 ppm — the groups of peaks of methylene protons (related to $–CH_2–$ groups conjugated with the ester groups); 3) 6.7–6.8 ppm — signal related to the protons of double bond of fumaric acid built-in the structure of PEGF (polyester). These peak positions are consistent with the ^{1}H NMR data presented in the works [9, 12] for PEGF. Thus, NMR data confirm the chemical structure of the synthesized macromonomer (Fig. 5).

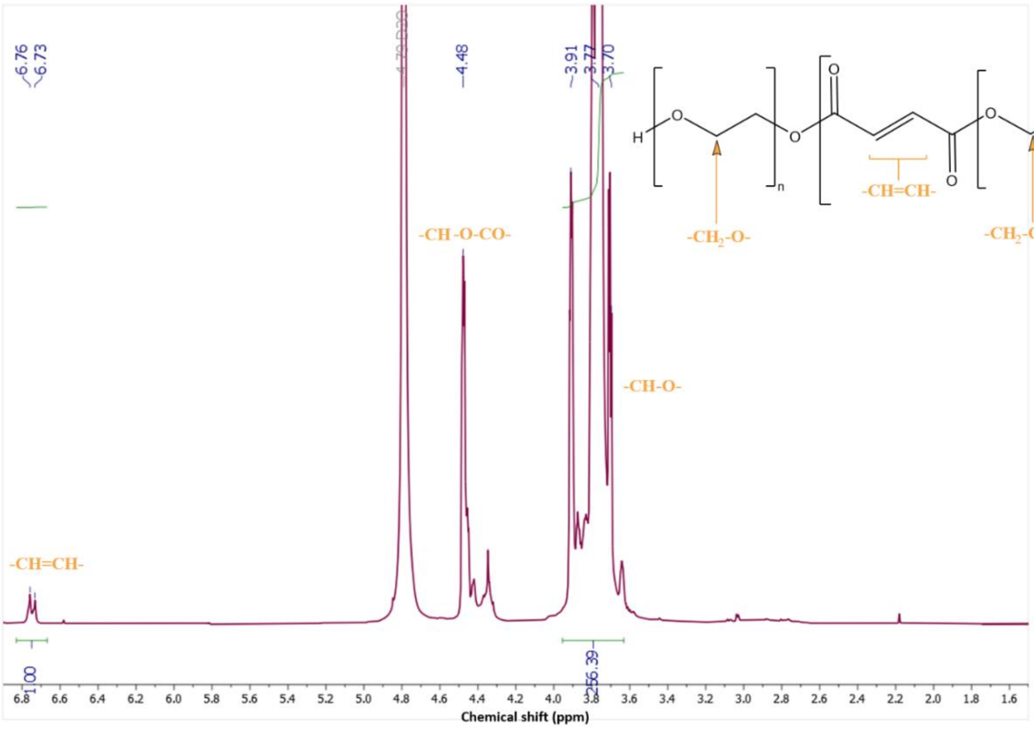

Figure 5. ^{1}H NMR-spectra of PEGF obtained after 8 h of polycondensation

From the NMR spectrum, the ratio of integrals of the peaks of double bonds and of methylene groups of PEG600 was calculated, which is equal to 0.004. The obtained amount of the double bonds in PEGF is 11 % of that theoretically estimated for the “ideal” structure of PEGF to be obtained in polycondensation. Therefore, NMR data are in semi-qualitative agreement with the FTIR and bromatometry results presented above, and they show that a certain fraction of double bonds remains in the PEGF structure after synthesis.

Thus, ^{1}H NMR- and FTIR-spectroscopies confirmed the formation of PEGF by polycondensation of PEG and fumaric acid. At high conversions (after more than 4 hours of polycondensation) the degree of unsaturation of PEGF decreases, so that after 8 h of reaction the amount of unsaturated double bonds in its structure is sufficiently reduced.

Conclusions

Macromonomers of PEGF with the molecular weight of about 6 kDa has been synthesized by polycondensation of PEG-600 with fumaric acid for 8 h. The time-dependence of the structure of PEGF was analyzed using bromatometry and FTIR- and ^{1}H NMR-spectroscopies. According to bromatometric analysis and IR-spectroscopy, the amount of unsaturated –CH=CH– groups of fumaric acid in PEGF decreases from 4 to 8 h of synthesis. After 8 h of polycondensation the bromatometry and ^{1}H NMR-spectroscopy both indicate the sufficiently smaller amount of unsaturated double bonds that are required for further polymerization of PEGF for the formation of hydrogels for biomedical purposes.

Funding

This research is funded by the Science Committee of the Ministry of Science and Higher Education of the Republic of Kazakhstan (Grant No. AP19677568).

*Author Information**

**The authors' names are presented in the following order: First Name, Middle Name and Last Name*

Yerkeblan Muratovich Tazhbayev — Doctor of Chemical Sciences, Professor, Vice Rector for Research, Karaganda Buketov University, Universitetskaya street, 28, 100024, Karaganda, Kazakhstan; e-mail: tazhbaev@mail.ru; https://orcid.org/0000-0003-4828-2521

Akerke Temirgalievna Kazhmuratova — Candidate of Chemical Sciences, Associate Professor, Department of Organic Chemistry and Polymers, Faculty of Chemistry, Karaganda Buketov University, Universitetskaya street, 28, 100024, Karaganda, Kazakhstan; e-mail: kazhmuratova@mail.ru; https://orcid.org/0000-0003-4044-8419

Lyazzat Zhanybekovna Zhaparova (*corresponding author*) — PhD, Associate Professor, Department of Organic Chemistry and Polymers, Faculty of Chemistry, Karaganda Buketov University, Universitetskaya street, 28, 100024, Karaganda, Kazakhstan; e-mail: lyazzh@mail.ru; https://orcid.org/0000-0003-1894-0255

Ulugbek Borashevich Tuleuov — MSc., Researcher, Research Institute on Chemical Problems, Karaganda Buketov University, Universitetskaya street, 28, 100024, Karaganda, Kazakhstan; e-mail: bekalols1@gmail.com; https://orcid.org/0000-0002-2664-6884

Yermauyt Nassikhatuly — MSc., Lecturer, Department of Organic Chemistry and Polymers, Faculty of Chemistry, Karaganda Buketov University, Universitetskaya street, 28, 100024, Karaganda, Kazakhstan; e-mail: ermauit@gmail.com; https://orcid.org/0000-0003-4574-0902

Elizaveta Sergeevna Mitricheva — Student, Physics Department, Lomonosov Moscow State University, GSP-1, Lenenskiye Gory, 1, 2, 119991, Moscow, Russia; e-mail: elizaveta.mitricheva@gmail.com

Alexander Lvovich Kwiatkowski — PhD, Senior Research Associate, Physics Department, Lomonosov Moscow State University, GSP-1, Lenenskiye Gory, 1, 2, 119991, Moscow, Russia; e-mail: kvyatkovskij@physics.msu.ru; https://orcid.org/0000-0002-0514-384X

Andrey Vladimirovich Shibaev — PhD, Senior Research Associate, Physics Department, Lomonosov Moscow State University, GSP-1, Lenenskiye Gory, 1, 2, 119991, Moscow, Russia; e-mail: shibaev@polly.phys.msu.ru; https://orcid.org/0000-0002-3019-5764

Author Contributions

All authors contributed to the preparation of the manuscript. All authors approved the final version of the manuscript. CRediT: **Yerkeblan Muratovich Tazhbayev** conceptualization of the research, discussion of the results, review and editing the draft; **Akerke Temirgalievna Kazhmuratova** writing an original draft preparation, review and editing; **Lyazzat Zhanybekovna Zhaparova** writing an original draft, preparation, review and editing; **Ulugbek Borashevich Tuleuov** carrying out the experiments; **Yermauyt Nassikhatuly** analysis of the samples on FTIR-spectrometer and GPC; **Elizaveta Sergeevna Mitricheva** analysis of the samples on ^{1}H NMR-spectrometer; **Alexander Lvovich Kwiatkowski** discussion of the results, review and editing the draft; **Andrey Vladimirovich Shibaev** discussion of the results, review and editing the draft.

Conflicts of Interest

The authors declare no conflict of interest.

References

1 Hunter, D.J., & Bierma-Zeinstra, S. (2019). Osteoarthritis. *The Lancet*, *393*(10182), 1745–1759. https://doi.org/10.1016/S0140-6736(19)30417-9

2 Ferket, B.S., Feldman, Z., Zhou, J., Oei, E.H., Bierma-Zeinstra, S.M.A., & Mazumdar, M. (2017). Impact of total knee replacement practice: Cost effectiveness analysis of data from the Osteoarthritis Initiative. *BMJ (Online)*, *356*, 1–12. https://doi.org/10.1136/bmj.j1131

3 Bortoluzzi, A., Furini, F., & Scirè, C.A. (2018). Osteoarthritis and its management — Epidemiology, nutritional aspects and environmental factors. *Autoimmunity Reviews*, *17*(11), 1097–1104. https://doi.org/10.1016/j.autrev.2018.06.002

4 Mihalko, W.M., Haider, H., Kurtz, S., Marcolongo, M., & Urish, K. (2020). New materials for hip and knee joint replacement: What's hip and what's in kneed? *Journal of Orthopaedic Research*, *38*(7), 1436–1444. https://doi.org/10.1002/jor.24750

5 Shibaev, A.V., & Philippova, O.E. (2022). New Approaches to the Design of Double Polymer Networks: a Review. *Polymer Science, Series C*, *64*(1), 26–39. https://doi.org/10.1134/S1811238222200012

6 Chen, Q., Chen, H., Zhu, L., & Zheng, J. (2015). Fundamentals of double network hydrogels. *Journal of Materials Chemistry B*, *3*(18), 3654–3676. https://doi.org/10.1039/c5tb00123d

7 Chen, W., Li, N., Ma, Y., Minus, M. L., Benson, K., Lu, X., Wang, X., Ling, X., & Zhu, H. (2019). Superstrong and Tough Hydrogel through Physical Cross-Linking and Molecular Alignment. *Biomacromolecules*, *20*(12), 4476–4484. https://doi.org/10.1021/acs.biomac.9b01223

8 Lee, D., Hwang, H., Kim, J.S., Park, J., Youn, D., Kim, D., Hahn, J., Seo, M., & Lee, H. (2020). VATA: A Poly(vinyl alcohol)- And Tannic Acid-Based Nontoxic Underwater Adhesive. *ACS Applied Materials and Interfaces*, *12*(18), 20933–20941. https://doi.org/10.1021/acsami.0c02037

9 Burkeev, M.Z., Zhunissova, M. S., Tazhbayev, Y. M., Fomin, V. N., Sarsenbekova, A. Z., Burkeyeva, G.K., Kazhmuratova, A.T., Zhumagalieva, T.S., Zhakupbekova, E.Z., & Khamitova, T.O. (2022). Influence of RAFT Agent on the Mechanism of Copolymerization of Polypropylene Glycol Maleinate with Acrylic Acid. *Polymers*, *14*(9), 1–10. https://doi.org/10.3390/polym14091884

10 Selvam, S., Pithapuram, M.V., Victor, S.P., & Muthu, J. (2015). Injectable in situ forming xylitol-PEG-based hydrogels for cell encapsulation and delivery. *Colloids and Surfaces B: Biointerfaces*, *126*, 35–43. https://doi.org/10.1016/j.colsurfb.2014.11.043

11 Cai, Z., Wan, Y., Becker, M.L., Long, Y.Z., & Dean, D. (2019). Poly(propylene fumarate)-based materials: Synthesis, functionalization, properties, device fabrication and biomedical applications. *Biomaterials*, *208* (August 2018), 45–71. https://doi.org/10.1016/j.biomaterials.2019.03.038

12 Navarro, L., Minari, R.J., & Vaillard, S.E. (2019). Photo-curable poly-(ethylene glycol)-fumarate elastomers with controlled structural composition and their evaluation as eluting systems. *RSC Advances*, *9*(1), 482–490. https://doi.org/10.1039/C8RA09336A

13 Dadsetan, M., Pumberger, M., & Yaszemski, M.J. (2009). Incorporation of electrical charge into oligo (polyethylene glycol) fumarate hydrogel for cartilage regeneration. *Abstracts of Papers of the American Chemical Society*, *238*.

14 Dadsetan, M., Runge, M. B., & Yaszemski, M.J. (2009). Doxorubicin release from microspheres encapsulated within oligo (polyethylene glycol) fumarate hydrogel. *Abstracts of Papers of the American Chemical Society*, *238*.

15 Dadsetan, M., Giuliani, M., Wanivenhaus, F., Runge, M.B., Charlesworth, J.E., & Yaszemski, M.J. (2012). Incorporation of phosphate group modulates bone cell attachment and differentiation on oligo(polyethylene glycol) fumarate hydrogel. *Acta Biomaterialia*, *8*(4), 1430–1439. https://doi.org/10.1016/j.actbio.2011.12.031

16 Koosehgol, S., Ebrahimian-Hosseinabadi, M., Alizadeh, M., & Zamanian, A. (2017). Preparation and characterization of in situ chitosan/polyethylene glycol fumarate/thymol hydrogel as an effective wound dressing. *Materials Science and Engineering C-Materials for Biological Applications*, *79*, 66–75. https://doi.org/10.1016/j.msec.2017.05.001

17 Judas, D., Fradet, A., & Maréchal, E. (1984). ^{13}C NMR characterization of branched structures in polyesters resulting from the reaction of maleic and phthalic anhydride with 1,2-propanediol. *Die Makromolekulare Chemie*, *185*(12), 2583–2597. https://doi.org/10.1002/macp.1984.021851210.

18 Díez-Pascual, A.M., & Díez-Vicente, A.L. (2016). Poly(propylene fumarate)/Polyethylene Glycol-Modified Graphene Oxide Nanocomposites for Tissue Engineering. *Acs Applied Materials & Interfaces*, *8*(28), 17902–17914. https://doi.org/10.1021/acsami.6b05635

19 Burkeev, M.Z., Kudaibergen, G.K., Tazhbayev, Y.M., Hranicek, J., Burkeyeva, G.K., & Sarsenbekova, A.Z. (2019). Synthesis and investigation of copolymer properties on the basis of poly(ethylene glycol) fumarate and methacrylic acid. *Bulletin of the University of Karaganda – Chemistry* (93), 32–38. https://doi.org/10.31489/2019Ch1/32-38

20 Burkeyeva, G.K., Kovaleva, A.K., Tazhbayev, Y.M., Ibrayeva, Z.M., Zhaparova, L.Z., Meiramova, D.R., & Plocek, J. (2023). Investigation of the Influence of UV-Irradiation on Thermal Stability of Binary Systems on the Basis of Polyethylene Glycol Fumarate with Some Vinyl Monomers. *Eurasian Journal of Chemistry*, *110*(2), 86–93. https://doi.org/10.31489/2959-0663/2-23-11

21 de Girolamo, L., Niada, S., Arrigoni, E., Di Giancamillo, A., Domeneghini, C., Dadsetan, M., ... Brini, A.T. (2015). Repair of osteochondral defects in the minipig model by OPF hydrogel loaded with adipose-derived mesenchymal stem cells. *Regenerative Medicine*, *10*(2), 135–151. https://doi.org/10.2217/rme.14.77

22 Diez-Pascual, A.M. (2017). Tissue Engineering Bionanocomposites Based on Poly(propylene fumarate). *Polymers*, *9*(7), Article 260. https://doi.org/10.3390/polym9070260

23 Gaihre, B., Liu, X.F., Miller, A.L., Yaszemski, M., & Lu, L.C. (2021). Poly(Caprolactone Fumarate) and Oligo Poly(Ethylene Glycol) Fumarate : Two Decades of Exploration in Biomedical Applications. *Polymer Reviews*, *61*(2), 319–356. https://doi.org/10.1080/15583724.2020.1758718

24 George, M.N., Liu, X.F., Miller, A.L., Xu, H.C., & Lu, L.C. (2020). Phosphate functionalization and enzymatic calcium mineralization synergistically enhance oligo poly(ethylene glycol) fumarate hydrogel osteoconductivity for bone tissue engineering. *Journal of Biomedical Materials Research Part A*, *108*(3), 515–527. https://doi.org/10.1002/jbm.a.36832

25 Salehi-Abari, M., Koupaei, N., & Hassanzadeh-Tabrizi, S.A. (2020). Synthesis and Characterisation of semi-interpenetrating network of Polycaprolactone/polyethylene glycol diacrylate/zeolite-CuO as wound dressing. *Materials Technology*, *35*(5), 290–299. https://doi.org/10.1080/10667857.2019.1678088

26 Wang, Y.T., Wang, X.X., Chen, W.X., Zhu, L.G., & Zhang, B.J. (2024). Environmental stimulant-responsive hydrogels based on polyethylene glycol-derived polymer for underwater bonding and extraction of fragile wooden relics: Synthesis, characterization, and preliminary application. *International Journal of Adhesion and Adhesives*, *131*, Article 103651. https://doi.org/10.1016/j.ijadhadh.2024.103651

27 Zoughaib, M., Dayob, K., Avdokushina, S., Kamalov, M.I., Salakhieva, D.V., Savina, I.N., ... Abdullin, T.I. (2023). Oligo (Poly(Ethylene Glycol)Fumarate)-Based Multicomponent Cryogels for Neural Tissue Replacement. *Gels*, *9*(2), Article 105. https://doi.org/10.3390/gels9020105

28 Burkeev, M.Zh., Kudaibergen, G.K., Burkeeva, G.K., Seilkhanov, T.M., Tazhbayev, Y.M., Hranicek, J., Omasheva, A.V., Davrenbekov, S.Zh. (2018). New Polyampholyte Polymers Based on Polypropylene Glycol Fumarate with Acrylic Acid and Dimethylaminoethyl Methacrylate. *Russian Journal of Applied Chemistry*, *91*(7). 1145–1152. http://doi.org/10.1134/S1070427218070121

29 Sarsenbekova, A.Z., Kudaibergen, G.K., Burkeev, M.Z., & Burkeeva, G.K. (2019). Comparative Analysis of the Thermal Decomposition Kinetics of Polyethylene Glycol Fumarate-Acrylic Acid Copolymers. *Russian Journal of Physical Chemistry A*, *93*(7), 1252–1257. https://doi.org/10.1134/s0036024419060281

30 Burkeev, M.Zh., Shibayeva, S.R., Khamitova, T.O., Plocek, J., Tazhbayev, Y.M., et al. (2021). Synthesis and Catalytic Properties of New Polymeric Monometallic Composites Based on Copolymers of Polypropylene Glycol Maleate Phthalate with Acrylic Acid. *Polymers 13*(24): 4369–4380. http://doi.org:10.3390/polym13244369

31 Toroptseva, A.M., Belogorodskaya, K.V., & Bondarenko, V.M. (1972). Laboratory Manual on chemistry and technology of high molecular compounds. — 416 p.

32 Gottlieb, H.E., Kotlyar, V., & Nudelman, A. (1997). NMR Chemical Shifts of Common Laboratory Solvents as Trace Impurities. *J. Org. Chem.*, *62*, 7512–7515.

33 Kwiatkowski, A.L., Molchanov, V.S., Sharma, H., Kuklin, A.I., Dormidontova, E.E. & Philippova, O.E. (2018) Growth of wormlike micelles of surfactant induced by embedded polymer: role of polymer chain length. *Soft Matter*. *09*, 35–49. http://doi.org:10.1039/c8sm00776d.

How to Cite: Kulakov, I.I., Chikunov, S.Y., Elyshev, A.V., Kulakov, I.V. (2024) Multicomponent Synthesis of Novel Unsymmetric 6-Aryl Substituted 5-Nitropyridines. *Eurasian Journal of Chemistry, 29, 2(114), 13-20.* https://doi.org/10.31489/2959-0663/2-24-3

Article

Received: 28 February 2024 ǀ Revised: 29 March 2024 ǀ
Accepted: 5 April 2024 ǀ Published online: 23 April 2024

UDC 547.822 + 547-304.1

https://doi.org/10.31489/2959-0663/2-24-3

Ilya I. Kulakov[1, 3], Semyon Y. Chikunov[1, 3],
Andrey V. Elyshev[1, 2, 3], Ivan V. Kulakov[2, 3*]

[1]*Laboratory of Theory and Optimization of Chemical and Technological Processes, University of Tyumen, Tyumen, Russia;*
[2]*Center for Nature-Inspired Engineering, University of Tyumen, Tyumen, Russia;*
[3]*Higher School of Natural Science, University of Tyumen, Tyumen, Russia*
*(*Corresponding author′s e-mail:* i.v.kulakov@utmn.ru*)*

Multicomponent Synthesis of Novel Unsymmetric 6-Aryl Substituted 5-Nitropyridines

We have previously studied a multicomponent reaction for the synthesis of unsymmetrical 5-nitro-1,4-dihydropyridines using unsubstituted 2-nitroacetophenone, 1,3-dicarbonyl compounds, and various aldehydes such as formaldehyde, acetaldehyde, and furfural. This paper reports the use of unsymmetrical 3-acetyl-5-nitro-1,4-dihydropyridines containing aryl substituents at the 6-position in a multicomponent synthesis reaction. The starting aryl-substituted nitroacetophenones were prepared by two methods. The first method involved the two-step Katritzky method, which is described in the literature. This method consists of preparing N-acylbenzotriazoles from the corresponding substituted derivatives of benzoic acid and 1,2,3-benzotriazole in the presence of thionyl chloride. This is followed by C-acylation of nitromethane in supernatron medium (t-BuOK – DMSO). A number of 2-nitroacetophenone derivatives were prepared from more commercially available aromatic aldehydes by the Henry reaction with nitromethane followed by oxidation of the resulting secondary nitroalcohols. The multicomponent reaction of 6-aryl-substituted 5-nitro-1,4-dihydropyridines and their subsequent aromatization into 5-nitropyridines allowed us to reduce the overall reaction time by more than 40 times and to increase the total yield of 5-nitro-6-arylpyridines by an average of twofold compared to the method described in the literature. Furthermore, the 3-acetyl-5-nitropyridines we have obtained are significant intermediates in the synthesis of novel, more complex heterocyclic systems with potential biological activity. These systems include δ-carbolines and epoxybenzooxocyno[4,3-b]pyridines, which are currently of great interest for the study of their properties.

Keywords: green chemistry, multicomponent reaction, substituted 2-nitroacetophenones, pyridine derivatives, 5(3)-nitro-1,4-dihydropyridines, 5(3)-nitropyridines, 3-acetyl-5-nitropyridines, heterocyclic compounds.

Introduction

During the 1980s and 1990s, pharmaceuticals containing 1,4-dihydropyridine were developed and proved to be effective. These pharmaceuticals are now known as “Dihydropyridine calcium channel blockers” and are used as L-type calcium channel blockers [1]. They are commonly used to treat cardiovascular diseases such as hypertension, angina pectoris, arrhythmias, and for the prevention of heart disease. The drugs work by blocking the entry of calcium into the cells of the heart and blood vessels, causing them to relax and dilate [2].

Dihydropyridine calcium channel blockers primarily lower blood pressure by causing relaxation of the smooth muscle in the walls of blood vessels. In contrast, certain L-type calcium channel blockers, such as those from the phenylalkylamine class like verapamil, exert a notable impact on the heart [3-4].

An example of the use of compounds from the 1,4-dihydropyridine class in pharmacology is nifedipine. It was patented in 1967 and is listed in the World Health Organization’s Essential Medicines List. As of 2021, this medication was the 128th most frequently prescribed drug in the United States, with over 4 million prescriptions [5–7].

Ongoing research continues to explore novel methods for synthesizing and discovering effective medications based on 1,4-dihydropyridine (1,4-DHP) and its derivatives (Fig.).

For instance, over 20 years ago, the neuroprotective drug cerebrocrast 4 was discovered in the search for more effective drugs for high blood pressure.

Cerebrocrast exhibits a high affinity for DHP-receptors and is recognized for enhancing cognitive abilities. It functions as a nootropic agent, improving cognitive functions and memory, while also providing neuroprotective benefits by tackling age-related, hypoxic, and alcohol-induced neuronal disorders [8].

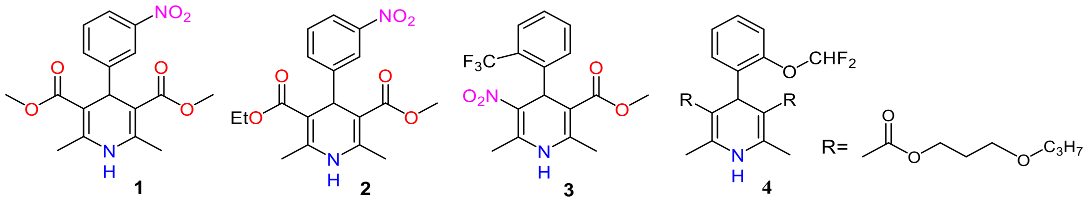

Figure. The structural formulas of bioactive 1,4-DHPs

The synthesis of symmetrical derivatives of 1,4-dihydropyridine of types **1** and **2** using the Hantzsch method with a double equivalent of the dicarbonyl compound is straightforward and yields are consistently high. However, the one-step synthesis of unsymmetrical derivatives of 1,4-dihydropyridine of type **3** using the Hantzsch method is challenging. This is mainly due to the different reactivity of the carbonyl compounds used, which leads to a mixture of different products, including symmetrical 1,4-dihydropyridines.

The synthesis of unsymmetrical 5-nitropyridines of type **10a-c** involves the reaction of enamines β-dicarbonyl compound and nitrochalcone, followed by oxidation of the obtained 1,4-dihydropyridines **9a-c** (Scheme 1) [9]. This method of preparation requires the synthesis of starting enamines [11] and nitrochalcone [10], high time and energy costs, and 1,4-dihydropyridines **9a-c** are formed with relatively low overall yields.

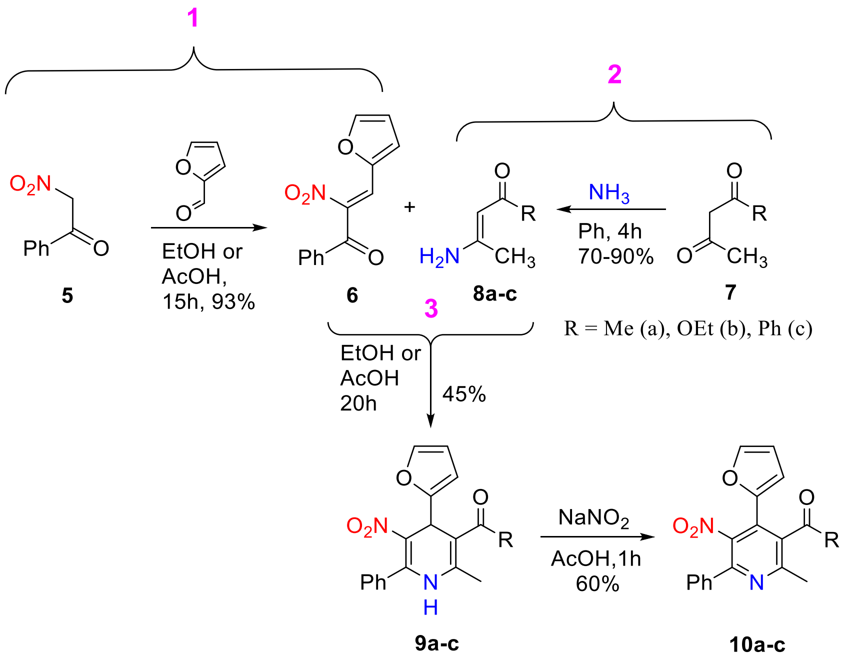

Scheme 1. Three step synthesis of 4-substituted 5-nitro-6-phenylpyridines

A one-step, three-component method for the preparation of 4-substituted 5-nitro-6-phenylpyridines **11a-c**, which are prepared from nitroacetophenone **5**, enamine β-dicarbonyl compounds **8a-c** and triethylorthoformate [12-13], is also reported in the literature (Scheme 2).

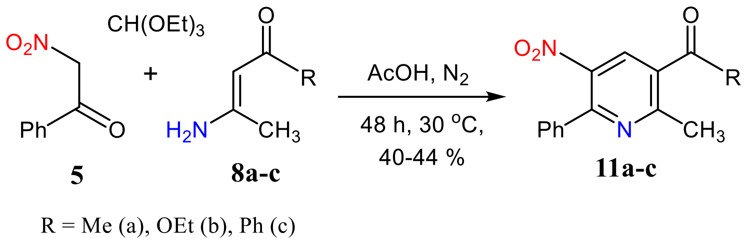

Scheme 2. A one-step method for the preparation of 4-substituted 5-nitro-6-phenylpyridines

This method, in comparison with the classical method, proceeds in one stage and does not require oxidative aromatization. However, in our opinion, this method has a number of disadvantages, namely high duration of all reactions (from 50 to 122 hours), long heating time, use of inert gas, use of more expensive triethylorthoformate, relatively low overall reaction yield, as well as an additional stage of preliminary preparation of β-dicarbonyl compounds **8a-c** with enamine.

In [14–16], we successfully applied and extensively tested the methodology for the four-component synthesis of **12-c** type 1,4-DHP. Nitroacetophenone (or nitroacetone) **5**, the corresponding β-dicarbonyl compound **7** in equivalent molar amounts, an excess of ammonium acetate and an aldehyde (formaldehyde, furfural, acetaldehyde) or its sources (urotropine, acetal) were used for the reaction (Scheme 3).

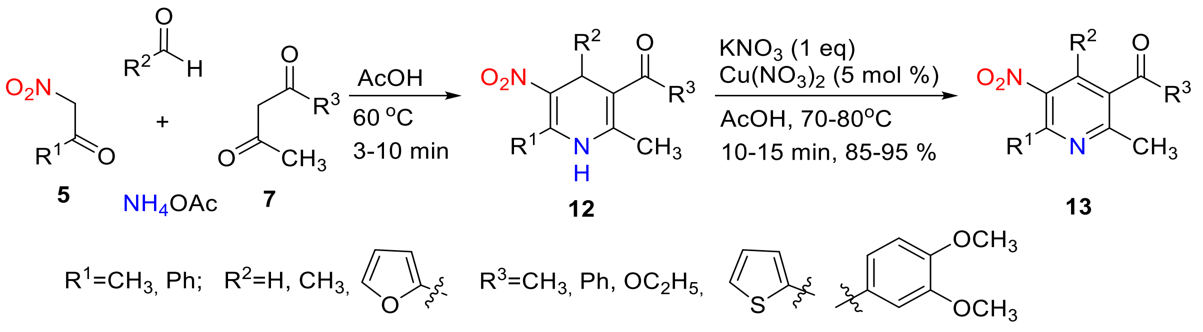

Scheme 3. Synthesis of 4-unsubstituted and 4-substituted 5-nitro-6-phenylpyridines

Therefore, our proposed method for the synthesis of 4-unsubstituted and 4-substituted 5-nitro-6-phenyl-1,4-dihydropyridines and their subsequent conversion into pyridines enabled us to reduce the overall reaction time and increase the overall combined yield of 5-nitro-6-phenylpyridines by almost twofold compared to established methods in the literature.

Experimental

Materials

^{1}H and ^{13}C NMR spectra were recorded on a Magritek spin solve 80 carbon ultra (81 and 20 MHz, respectively) instruments using DMSO-d_6 and $CDCl_3$ the internal standard, with residual solvent signals (2.49 and 39.9 ppm for ^{1}H and ^{13}C nuclei in DMSO-d_6; 7.25 and 77.0 ppm for ^{1}H and ^{13}C nuclei in $CDCl_3$).

The physicochemical and spectral characteristics of compounds **19a-c** were in agreement with the literature data [13].

6-aryl-5-nitro-1,4-dihydropyridines 18a-f (general method). To previously dissolved substituted nitroacetophenone (5 mmol) in glacial acetic acid (4-5 mL), 0.18 g (1.3 mmol) of urotropine, 1.16 g (15 mmol) of ammonium acetate and 0.50 g (5 mmol) of acetylacetone were added. The reaction mixture was stirred at 60 °C for 3–10 min. The reaction mixture with crystalline precipitate was cooled to 0–5 °C, filtered, washed first with 50 % aqueous 2-propanol solution, then with water. The product was recrystallized from 2-propanol.

1-(2-methyl-5-nitro-6-(p-tolyl)-1,4-dihydropyridin-3-yl)ethan-1-one (18a). Yield 0.530 g (39 %), orange crystals, mp 157–159 °C.

^{1}H NMR (81 MHz, DMSO-d6) δ ppm: 2.16 (s, 3 H, CH_3); 2.24 (s, 3 H, CH_3); 2.37 (s, 3 H, CH_3); 3.69 (s, 2 H, CH_2); 7.26 (br. s, 4 H, H-2,3,5,6 Ar); 9.15 (s, 1 H, NH). ^{13}C NMR (20 MHz, DMSO-d6) δ ppm: 18.0; 20.9; 27.2; 30.2; 111.0; 122.4; 127.6; 128.8; 131.0; 138.9; 143.4; 147.7; 197.0.

1-(6-(4-bromophenyl)-2-methyl-5-nitro-1,4-dihydropyridin-3-yl)ethan-1-one (18b). Yield 0.826 g (60 %), red crystals, mp 166–167 °C.

^{1}H NMR (81 MHz, DMSO-d6) δ ppm: 2.15 (s, 3H, CH_3); 2.25 (s, 3H, CH_3); 3.70 (s, 2 H, CH_2); 7.33 (d, J= 8.30 Hz, 2 H, H-2,6 Ar); 7.68 (d, J=8.30 Hz, 2 H, H-3,5 Ar); 9.23 (br. s., 1 H, NH). ^{13}C NMR (20 MHz, DMSO-d6) δ ppm: 18.0; 27.0; 30.2; 111.1; 122.6; 122.8; 129.9 (2 C); 131.3 (2 C); 133.3; 143.2; 146.5; 197.0.

1-(6-(4-methoxyphenyl)-2-methyl-5-nitro-1,4-dihydropyridin-3-yl)ethan-1-one (18c). Yield 0.547 g (38 %), orange crystals, mp 264–266 °C.

^{1}H NMR (81 MHz, DMSO-d6) δ ppm: 2.23 (s, 3 H, CH_3); 2.29 (s, 3 H, CH_3); 3.77 (s, 2 H, CH_2); 3.88 (s, 3 H, OCH_3); 7.00 (d, J=8.60 Hz, 2 H, H-3,5 Ar); 7.32 (d, J=8.60 Hz, 2 H, H-2,6 Ar), 9.03 (br. s., 1 H, NH). ^{13}C NMR (20 MHz, DMSO-d6) δ ppm: 18.0; 27.1; 30.2; 55.7; 110.8; 111.3; 120.4; 123.2; 123.8; 128.5; 130.6; 143.6; 144.4; 156.2; 197.0.

1-(6-(4-fluorophenyl)-2-methyl-5-nitro-1,4-dihydropyridin-3-yl)ethan-1-one (18d). Yield 0.856 g (62 %), orange crystals, mp 178–179ºC.

^{1}H NMR (81 MHz, DMSO-d6) δ ppm: 2.16 (s, 3 H, CH_3); 2.25 (s, 3 H, CH_3); 3.70 (s, 2 H, CH_2); 7.18–7.54 (m, 4 H, H-2,3,5,6 Ar); 9.22 (br. s., 1 H, NH). ^{13}C NMR (20 MHz, DMSO-d6) δ ppm: 18.5; 27.7; 30.7; 111.6; 115.3; 116.4; 123.3; 130.5; 130.9 (2 C); 143.8; 147.2; 169.2; 197.6.

1-(6-(2-methoxyphenyl)-2-methyl-5-nitro-1,4-dihydropyridin-3-yl)ethan-1-one (18e). Yield 0.706 g (49 %), orange crystals, mp 156–157 °C.

^{1}H NMR (81 MHz, DMSO-d6) δ ppm: 2.14 (s, 3 H, CH_3); 2.24 (s, 3 H, CH_3); 3.69 (br. s., 2 H, CH_2); 3.76 (s, 3 H, OCH_3); 7.02–7.44 (m, 4 H, H-3,4,5,6 Ar); 9.15 (s, 1 H, NH). ^{13}C NMR (20 MHz, DMSO-d6) δ ppm: 18.0; 27.1; 30.2; 55.7; 110.8; 111.3; 120.4; 123.2; 123.8; 128.5; 130.6; 143.6; 144.4; 156.2; 197.0.

1-(6-(3,4-dimethoxyphenyl)-2-methyl-5-nitro-1,4-dihydropyridin-3-yl)ethan-1-one (18f). Yield 0.429 g (27 %), orange crystals, mp 217–219 °C.

^{1}H NMR (81 MHz, DMSO-d6) δ ppm: 2.16 (s, 3 H, CH_3); 2.24 (s, 3 H, CH_3); 3.68 (s, 2 H, CH_2); 3.75 (s, 3 H, OCH_3); 3.80 (s, 3 H, OCH_3); 6.78 — 7.09 (m, 3 H, H-2,5,6 Ar); 9.13 (s, 1 H, NH). ^{13}C NMR (20 MHz, DMSO-d6) δ ppm: 18.0; 27.2; 30.2; 55.6; 55.7; 110.9; 111.5; 111.7; 120.5; 122.1; 125.1; 143.5; 147.5; 148.5; 149.8; 196.9.

6-aryl-5-nitropyridines 19a-f (general method). To a mixture of 1,4-dihydropyridine (0.2 mmol) in glacial acetic acid (1 mL) cooled to 0 °C, a solution of 0.03 g CrO_3 (0.3 mmol) in H_2O (0.5 mL) was added dropwise at such a rate that the temperature of the reaction mixture did not exceed 10 °C. After addition of the CrO_3 solution, stirring was continued for 2 hours, and then the mixture was poured into an ice-water mixture (20 mL) and neutralized with aqueous ammonia. The crystals were filtered and recrystallized from ethanol.

1-(2-methyl-5-nitro-6-(p-tolyl)pyridin-3-yl)ethan-1-one (19a). Yield 0.481 g (89 %), white crystals, mp 97–98 °C. (lit. mp — 98–99 °C) [18].

^{1}H NMR (81 MHz, $CDCl_3$) δ ppm: 2.42 (s, 3H, CH_3); 2.67 (s, 3H, CH_3); 2.88 (s, 3H, CH_3); 7.28 (d, J=7.10 Hz, 2H, H-3,5 Ar); 7.52 (d, J=7.10 Hz, 2H, H-2,6 Ar); 8.42 (s, 1H Py). ^{13}C NMR (20 MHz, $CDCl_3$) δ ppm: 21.2; 25.2; 29.3; 128.1; 129.1; 130.9; 133.3; 135.2; 137.6; 143.3; 152.7; 161.9; 197.5.

1-(6-(4-bromophenyl)-2-methyl-5-nitropyridin-3-yl)ethan-1-one (19b). Yield 0.516 g (77 %), light yellow crystals, mp 146–147 °C. (lit. mp — 148–149 °C) [18].

^{1}H NMR (81 MHz, $CDCl_3$) δ ppm: 2.69 (s, 3H, CH_3); 2.88 (s, 3H, CH_3); 7.46 (d, J= 8.40 Hz, 2 H, H-3,5 Ar); 7.63 (d, J=8.30 Hz, 2 H, H-2,6 Ar); 8.47 (s, 1H, H-4 Py). ^{13}C NMR (20 MHz, $CDCl_3$) δ ppm: 25.2; 29.3; 125.1; 129.9; 130.9; 132.0; 133.3; 134.6; 143.2; 152.7; 162.0; 197.4.

1-(6-(4-methoxyphenyl)-2-methyl-5-nitropyridin-3-yl)ethan-1-one (19c). Yield 0.378 g (66 %), white crystals, mp 103–104 °C. (lit. mp — 101–102 °C) [18].

^{1}H NMR (81 MHz, $CDCl_3$) δ ppm: 2.64 (s, 3H, CH_3); 2.86 (s, 3H, CH_3); 3.85 (s, 3H, OCH_3); 7.00 (d, J=8.60 Hz, 2 H, H-3,5 Ar); 7.32 (d, J=8.60 Hz, 2 H, H-2,6 Ar); 8.39 (s, 1H, H-4 Py). ^{13}C NMR (20 MHz, $CDCl_3$) δ ppm: 25.3; 29.1; 55.4; 114.3; 121.6; 127.8; 129.8; 130.2; 133.4; 143.0; 153.1; 161.6; 197.5.

1-(6-(4-fluorophenyl)-2-methyl-5-nitropyridin-3-yl)ethan-1-one (19d). Yield 0.499 g (91 %), light yellow crystals, mp 119–120 °C.

^{1}H NMR (81 MHz, $CDCl_3$) δ ppm: 2.76 (s, 3 H, CH_3); 2.96 (s, 3 H, CH_3); 7.13–7.34 (m, 2 H, H-3,5 Ar); 7.60–7.77 (m, 2 H, H-2,6 Ar); 8.54 (s, 1 H, H-4 Py). ^{13}C NMR (20 MHz, $CDCl_3$) δ ppm: 25.2; 29.2; 115.4; 116.5; 130.3; 130.8; 131.8; 133.4; 135.0; 143.3; 152.6; 157.9; 161.9; 170.3; 197.5.

1-(6-(2-methoxyphenyl)-2-methyl-5-nitropyridin-3-yl)ethan-1-one (19e). Yield 0.418 g (73 %), white crystals, mp 144–145 °C.

^{1}H NMR (81 MHz, $CDCl_3$) δ ppm: 2.76 (s, 3 H, CH_3); 2.96 (s, 3 H, CH_3); 3.79 (s, 3 H, OCH_3); 6.98 (d, J=8.01 Hz, 1 H, H-3 Ar); 7.13-7.64 (m, 2 H, H-4,5 Ar); 7.80 (d, J=7.17 Hz, 1 H, H-6 Ar); 8.58 (s, 1 H, H-4 Py). ^{13}C NMR (20 MHz, $CDCl_3$) δ ppm: 25.2; 29.2; 55.0; 110.6; 121.5; 125.6; 130.3; 130.8; 131.8; 132.7; 144.3; 151.4; 156.4; 162.0; 219.8.

1-(6-(3,4-dimethoxyphenyl)-2-methyl-5-nitropyridin-3-yl)ethan-1-one (19f). Yield 0.600 g (95 %), white crystals, mp 127–128 °C.

^{1}H NMR (81 MHz, $CDCl_3$) δ ppm: 2.79 (s, 3 H, CH_3); 3.01 (s, 3 H, CH_3); 4.06 (s, 6 H, OCH_3); 7.05 (d, J=8.80, 1 H, H-5 Ar); 7.33 (d, J=8.80, 1 H, H-6 Ar); 7.35 (s, 1 H, H-2 Ar); 8.51 (s, 1 H, H-4 Py). ^{13}C NMR

(20 MHz, $CDCl_3$) δ ppm: 25.3; 29.1; 56.0 (2 C); 111.1; 111.4; 121.7; 127.8; 129.9; 133.3; 143.2; 149.2; 151.2; 153.0; 161.6; 197.4.

Results and Discussion

The previously described syntheses were based on the use of only unsubstituted 2-nitroacetophenone or nitroacetone in multicomponent reactions. In order to extend the possibilities of using this multicomponent reaction to synthesize new unsymmetrical derivatives of 5-nitropyridines containing an aryl substituent at the sixth position, it was necessary to synthesize aryl-substituted nitroacetophenones. For the preparation of aryl-substituted nitroketones, the Katritzky method [17-18], which is carried out in two stages, is widely used (Scheme 4).

In the first stage, the corresponding N-acylbenzotriazoles **15a-d** are prepared by interaction of commercially available substituted benzoic acid derivatives **14a-d** with 1,2,3-benzotriazole in the presence of thionyl chloride. Further, the required nitroacetophenones **16a-d** were prepared by C-acylation of nitromethane with the obtained N-acylbenzotriazoles **15a-d**. The reaction was carried out in superbase (t-BuOK – DMSO), with the benzotriazole acting as a good leaving group.

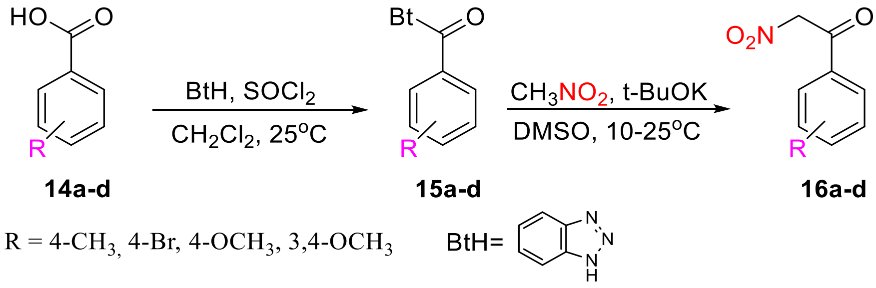

Scheme 4. Synthesis of aryl-substituted nitroketones by the Katritzky method

Nitroacetophenones **16e, f** were prepared from more readily available aromatic aldehydes by the Henry reaction with nitromethane, followed by oxidation of the resulting secondary nitroalcohols **17a, b** [19] (Scheme 5). During the reaction, in addition to hydroxynitro compounds, nitroalkenes were formed in small amounts (up to 20 % according to GC-MS data), i.e. products of elimination of a water molecule from the nitro alcohols formed in the first stage. The purification of the obtained target nitro alcohols was carried out by column chromatography on silica gel (hexane/ethyl acetate) according to the provided method [19].

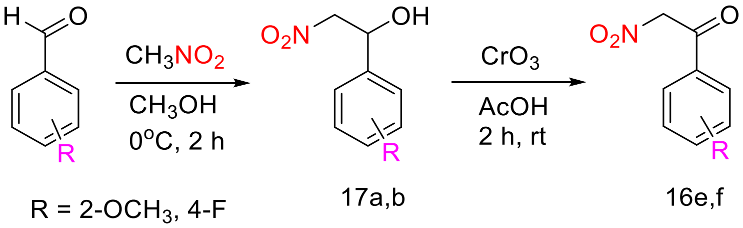

Scheme 5. Synthesis of aryl-substituted nitroketones by the Henry reaction

The prepared aryl-substituted nitroketones were then incorporated into a multicomponent reaction for the synthesis of unsymmetrical 4-substituted 3-acetyl-5-nitro-1,4-dihydropyridines **18a-f** according to the method described in [14] (Scheme 6). However, experimental syntheses showed that the aryl-substituted nitroketones used are rather poorly soluble in acetic acid, the solvent we use, which ultimately leads to their insufficient involvement in the reaction and, as a consequence, the formation of a significant amount of symmetrical side 3,5-diacetyl-1,4-dihydropyridine. To avoid unwanted side processes, we first predissolved the nitroacetophenones in acetic acid, and then added excess ammonium acetate and urotropine, and finally acetylacetone.

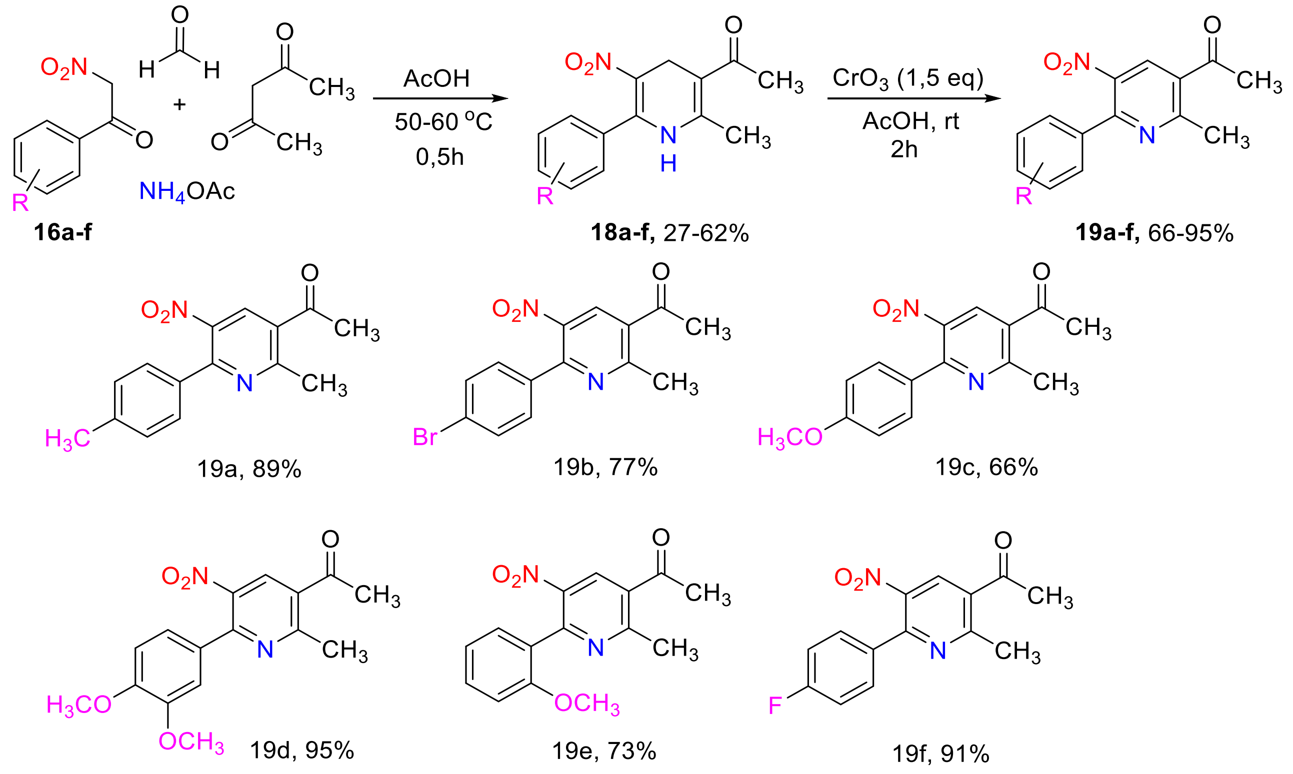

Scheme 6. Synthesis of 4-unsubstituted 3-acetyl-5-nitro-6-arylpyridines

It was found that the yields of the corresponding 3-acetyl-5-nitro-6-aryl-1,4-dihydropyridines **18a-f** are also related to the presence of electronic effects of the substituent in the aromatic ring. Thus, the donor substituents slightly reduce the yield of the target product due to a decrease in the partial positive charge on the carbon atom of the carbonyl group and, accordingly, lead to a decrease in the CH-acidity of the methylene group of nitroketones, which is the main reaction center in the Knoevenagel reaction.

The oxidation of 5-nitro-6-aryl-1,4-dihydropyridines to the corresponding 5-nitro-6-arylpyridines **19a-f** was carried out according to the standard method with chromium oxide (VI) in acetic acid solution at room temperature. The oxidation proceeded quite smoothly and in high yields (from 66 to 95 %) (Scheme 6).

Conclusions

Thus, we have extended the possible scope of application of the multicomponent reaction in the synthesis of six new 6-aryl-substituted 3-acetyl-5-nitro-1,4-dihydropyridines, not previously described in the literature, whose oxidation afforded the corresponding 5-nitropyridines.

The multicomponent reaction of 6-aryl-substituted 5-nitro-1,4-dihydropyridines and their subsequent aromatization to pyridines allowed the overall reaction time to be reduced by more than 40-fold and the overall yield of the target 5-nitro-6-arylpyridines to be almost doubled on average compared to the method reported in the literature [12-13].

In conclusion, the new 3-acetyl-5-nitro-6-arylpyridines **19a-f** synthesized by us can be of great interest as intermediate synthons in the synthesis of more complex heterocyclic systems. For example, 3-(5)-nitropyridines have proved to be good precursors in the synthesis of synthetic analogs of the alkaloid chindoline and other structural analogs of substituted δ-carbolines obtained by the Cadogan reaction [20-21]. The presence of 3-acetyl and 2-methyl groups in the structure of 5-nitro-6-arylpyridines **19a-f** simultaneously suggests their potential use as important synthons and in the synthesis of epoxybenzooxocino[4,3-b]pyridine derivatives [22–24], which are structural analogs of natural integrastatins.

Funding

This research was conducted with the support of the Ministry of Science and Higher Education of the Russian Federation: “Priority 2030” in the Center of Nature-Inspired Engineering.

Author Information*

**The authors' names are presented in the following order: First Name, Middle Name and Last Name*

Ilya Ivanovich Kulakov — Master Student, Laboratory of Theory and Optimization of Chemical and Technological Processes, University of Tyumen, 625003 Tyumen, Russia; e-mail: kulakov.ii.chem@gmail.com; https://orcid.org/0009-0000-2141-1923

Semyon Yuryevich Chikunov — Postgraduate Student, Higher School of Natural Science, Laboratory of Theory and Optimization of Chemical and Technological Processes, University of Tyumen, Tyumen, Russia; e-mail: s.y.chikunov@utmn.ru; https://orcid.org/0000-0003-1918-6936

Andrey Vladimirovich Elyshev — Candidate of chemical sciences, Laboratory of Theory and Optimization of Chemical and Technological Processes, Center for Nature-Inspired Engineering, Higher School of Natural Science, University of Tyumen, Tyumen, Russia; e-mail: a.v.elyshev@utmn.ru; https://orcid.org/0000-0001-8277-2626

Ivan Vyacheslavovich Kulakov — Doctor of chemical sciences, Associated Professor, Center for Nature-Inspired Engineering, Higher School of Natural Science University of Tyumen, 625003 Tyumen, Russia; e-mail: i.v.kulakov@utmn.ru; https://orcid.org/0000-0001-5772-2096

Author Contributions

The manuscript was written through contributions of all authors. All authors have given approval to the final version of the manuscript. CRediT: **Ilya Ivanovich Kulakov** investigation, formal analysis, data curation and writing–original draft preparation; **Semyon Yuryevich Chikunov** investigation, formal analysis; **Andrey Vladimirovich Elyshev** supervision, project administration, funding acquisition; **Ivan Vyacheslavovich Kulakov** conceptualization, methodology, validation, writing–review and editing and supervision.

Acknowledgements

Spectrophotometric studies were carried out using the equipment of the Center for Collective Use "Rational Nature Management and Physico-chemical Research" and the Laboratory of Theory and Optimization of Chemical and Technological Processes of University of Tyumen.

Conflicts of Interest

The authors declare no conflict of interest.

References

1 Brown, A. M., Kunze, D. L., & Yatani, A. (1984). The agonist effect of dihydropyridines on Ca channels. *Nature*, 311, 570–572. https://doi.org/10.1038/311570a0.

2 Bladen, C., Gündüz, M. G., Şimşek, R. et al (2014). Synthesis and Evaluation of 1,4-Dihydropyridine Derivatives with Calcium Channel Blocking Activity. *Pflugers Arch — Eur J Physiol*, 466, 1355–1363. https://doi.org/10.1007/s00424-013-1376-z

3 Xu, L., Li, D., Li, T., Yang, Y., Li, Y., & Hou, T. (2016). Binding mechanisms of 1,4-dihydropyridine derivatives to L-type calcium channel Cav1.2: a molecular modeling study. *Molecular BioSystems*, *12*(2), 379–390. https://doi.org/10.1039/c5mb00781j

4 Frishman, W. H. (2007). Calcium Channel blockers: Differences between subclasses. *American Journal of Cardiovascular Drugs*, 7(Suppl 1), 17–23. https://doi.org/10.2165/00129784-200707001-00003

5 World Health Organization (2019). World Health Organization model list of essential medicines: 21st list 2019. https://iris.who.int/handle/10665/325771

6 Kane SP. The Top 300 of 2021, ClinCalc DrugStats Database, Version 2024.01. ClinCalc: https://clincalc.com/DrugStats/Top300Drugs.aspx. Updated January 1, 2024. Accessed January 15, 2024.

7 Kane SP. Nifedipine, ClinCalc DrugStats Database, Version 2024.01. ClinCalc: https://clincalc.com/DrugStats/Drugs/Nifedipine. Updated January 1, 2024. Accessed January 15, 2024.

8 Soldatenkov, A. T., Kolyadina, N. M., & Shendrik, I. V. (2001). *Osnovy organicheskoi khimii lekarstvennykh veshchestv [Foundations of Organic Chemistry of Drugs]. Moscow: Khimiia*, 191 [in Russian].

9 Sagitullina, G. P., Glizdinskaya, L. V. & Sagitullin, R. S. (2007). Nitropyridines: IV. Synthesis of 3-(2-furyl)biphenyls by recyclization of nitropyridinium salts. *Russ J Org Chem*, *43*(4), 602–606. https://doi.org/10.1134/S1070428007040197

10 Berestovitskaya, V. M., Aboskalova, N. I., Ishmaeva, E. A., Bakhareva, S. V., Berkova, G. A., Vereshchagina, Y. A., ... & Fattakhova, G. R. (2001). Synthesis and Structural Features of 1-Acyl-1-nitro-2-furyl (thienyl) ethenes. *Russian journal of general chemistry*, *71*, 1942–1949.

11 Baraldi, P. G., Daniele, S., & Manfredini, S. (1983). An Improved Preparation of Enaminones from 1,3-Diketones and Ammonium Acetate or Amine Acetates. *Synthesis*, *1983*(11), 902–903. https://doi.org/10.1055/s-1983-30557

12 Sagitullina, G. P., Garkushenko, A. K. & Sagitullin, R. S. (2009). Synthesis of substituted 5-nitro- 6-phenylpyridines by the cyclo- condensation of nitroacetophenone, ethyl orthoformate, and enamines. *Chem. Heterocycl. Comp*., *45*, 1147. https://doi.org/10.1007/s10593-009-0395-3

13 Zobenko, Y. A, Pozhidaeva, S. A., Kuratova, A. K., Glyzdinskaya, L. V., Vorontsova, M. A., Sagitullina, G. P. (2017). New method for the synthesis of nitrobiaryls. *Chem Heterocycl Compd*., 53, 1014–1025. https://doi.org/10.1007/s10593-017-2164-z

14 Kulakov, I. V., Oleshchuk, A. L., Koveza, V. A., & Palamarchuk, I. V. (2020). Multicomponent synthesis of 4-unsubstituted 5-nitropyridine derivatives. *Synthetic Communications*, 50, 2432–2439. https://doi.org/10.1080/00397911.2020.1780261

15 Koveza, V. A., Kulakov, I. V., Shulgau, Z. T., *&* Seilkhanov T. M. (2018). Multicomponent synthesis of unsymmetrical 5-nitropyridines. *Chemistry of Heterocyclic Compounds*, *54*(12), 1127–1130. https://doi.org/10.1007/s10593-019-02403-x

16 Turgunalieva, D. M., Stalinskaya, A. L., Kulakov, I. I., Sagitullina, G. P., Atuchin, V. V., Elyshev, A. V., & Kulakov, I. V. (2023). Multicomponent synthesis of unsymmetrical derivatives of 4-Methyl-Substituted 5-Nitropyridines. *Processes*, *11*(2), 576. https://doi.org/10.3390/pr11020576

17 Katritzky, A. R., Zhang, Y., & Singh, S. K. (2003). Efficient conversion of carboxylic acids intoN-Acylbenzotriazoles. *Synthesis*, 18, 2795–2798. https://doi.org/10.1055/s-2003-42462

18 Katritzky, A. R., Abdel-Fattah, A. a. A., Gromova, A. V., Witek, R. M., & Steel, P. J. (2005). A-Nitro ketone synthesis using N-Acylbenzotriazoles. *The Journal of Organic Chemistry*, *70*(23), 9211–9214. https://doi.org/10.1021/jo051231x

19 Pan, Subhas Chandra; Maity, Rajendra (2018). Organocatalytic Asymmetric Michael/Hemiacetalization/Acyl Transfer Reaction of α-Nitroketones with o-Hydroxycinnamaldehydes: Synthesis of 2,4-Disubstituted Chromans. *Organic & Biomolecular Chemistry*. https://doi.org/10.1039/c8ob00078f

20 Shuvalov, V., Rupp, A., Kuratova, A., Fisyuk, A., Nefedov, A., & Sagitullina, G. (2019). Synthesis of δ-Carbolines and the Alkaloid Quindoline through a Molybdenum-Catalyzed Cadogan Cyclization and their Photoluminescent Properties. *Synlett*, 30. https://doi.org/10.1055/s-0037-1612416

21 Shuvalov, V., Rupp, A., Fisyuk, A., Kuratova, A., Nefedov, A., & Sagitullina, G. (2019). Synthesis and Optical Properties of Alkaloid Quindoline, Its Structural Analogues and Substituted δ-Carbolines. *ChemistrySelect*, 4, 1696–1699. https://doi.org/10.1002/slct.201803515

22 Stalinskaya, A. L., Martynenko, N. V., Shulgau, Z. T., Shustov, A. V., Keyer, V. V., & Kulakov, I. V. (2022). Synthesis and Antiviral Properties against SARS-CoV-2 of Epoxybenzooxocino[4,3-b]Pyridine Derivatives. *Molecules*, 27, 3701. https://doi.org/10.3390/molecules27123701

23 Stalinskaya, A. L., Martynenko, N. V., Alkhimova, L. E., Dilbaryan, D. S., Vasilchenko, A. S., Dengis, N. A., Vlasenko, V. S., & Kulakov, I. V. (2023). Synthesis and bacteriostatic properties of epoxybenzooxocino[4,3-b]pyridine derivatives. *Journal of Molecular Structure*, 1275, 134689. https://doi.org/10.1016/j.molstruc.2022.134689

24 Stalinskaya, A. L., Chikunov, S. Y., Pustolaikina, I. A., Gatilov, Yu. V., Kulakov I. V. (2024). Synthesis of New Structural analogues of Natural Integrastatins with a Basic Epoxybenzo[7,8]oxocine Skeleton: Combined Experimental and Computational Study. *Synthesis*, 56, 329–345. https://doi.org/10.1055/s-0042-1751521

How to Cite: Shakhabutdinov, S.Sh., Yugay, S.M., Ashurov, N.Sh., Ergashev, D.J., Atakhanov, A.A., & Rashidova, S.Sh. (2024) Characterization Electrospun Nanofibers Based on Cellulose Triacetate Synthesized from Licorice Root Cellulose. *Eurasian Journal of Chemistry, 29, 2(114), 21-31.* https://doi.org/10.31489/2959-0663/2-24-2

Article

Received: 15 January 2024 | Revised: 22 April 2024 |
Accepted: 24 April 2024 | Published online: 7 May 2024

UDC 677.464.1

https://doi.org/10.31489/2959-0663/2-24-2

Siroj Sh. Shakhabutdinov, Svetlana M. Yugay, Nurbek Sh. Ashurov,
Doniyor J. Ergashev, Abdumutolib A. Atakhanov*, Sayyora Sh. Rashidova

Institute of Polymer Chemistry and Physics, Tashkent, Uzbekistan
*(*Corresponding author's e-mail: a-atakhanov@yandex.com)*

Characterization Electrospun Nanofibers Based on Cellulose Triacetate Synthesized from Licorice Root Cellulose

Cellulose triacetate (CTA) nanofibers were formed by electrospinning using two binary solvent systems: methylene chloride/ethanol and chloroform/acetone. Previously, licorice root cellulose (LRC) with a degree of polymerization (DP) of 710 was extracted from licorice root waste by alkaline treatment and hydrogen peroxide bleaching at high temperatures. Then CTA with a degree of substitution (DS) of 2.9 and an average molecular weight of 175 kDa was synthesized from LRC using acetic acid and acetic anhydride, sulfuric acid was as a catalyst. The influence of the electrospinning process and various solvent systems on the morphology and structure of nanofibers was studied. The structure and morphology of the nanofibers were characterized by Fourier transform infrared (FTIR) spectroscopy, X-ray diffraction, scanning electron microscopy (SEM), thermal gravimetric analysis (TGA), and the sorption characteristics were also investigated. The results showed that the morphology and structure of nanofibers depended on the solvent mixture used. The average diameters of the CTA nanofibers with grooved morphology varied 200–700 nm (solvent methylene chloride/ethanol) and the dumbbell-shaped (flat ribbon) CTA nanofibers in a wide range from 200 nm to 4 mkm (solvent chloroform/acetone).

Keywords: electrospinning, cellulose triacetate, nanofibers, X-ray diffraction, FTIR, degree of crystallinity, sorption, thermal stability.

Introduction

As an eco-friendly and renewable biopolymer on the earth, cellulose gains an extensive interest in producing novel polymer materials. In this foreshortening, cellulose- and its derivatives-based fibres and nanofibres are very attractive because of their high strength and firmness, biodegradability and safety [1–5].

Cellulose can be extracted from different native sources, such as wood, cotton, flax, hemp, ramie, etc. [6–8]. In recent years, there has been an increasing trend towards extracting cellulose from agro-industrial wastes. The properties and structure of cellulose derived from these wastes vary considerably and can be used in different industrial sectors [9-10]. One of such agro-industrial waste is licorice root which consists of about 40–45 % cellulose. Products based on licorice root are used to treat ailments like heartburn, acid reflux, hot flashes, coughs, and bacterial and viral infections [11]. After separating the medicinally active component from the licorice root using selective solvents, a large mass of fibre waste remains, which can be used as raw material for the cellulose and paper [12]. Using cellulose extracted from licorice root waste offers several advantages compared to traditional sources like wood or cotton. Licorice root waste provides an alternative source of cellulose that utilizes a byproduct of the licorice industry, reducing waste and promoting sustainability. Unlike wood, which requires deforestation, or cotton, which requires extensive water and pesticide usage, licorice root waste repurposes a material that would otherwise be discarded.

The cellulose derivatives having different functional groups in the cellulose chain have great demand, and some of them, including cellulose acetate, are produced in large quantities. Cellulose acetate can be used for producing membranes, packaging films, optical devices, and polymer composites [13, 14]. Usually, conventional spinning methods such as melt spinning, wet spinning, dry spinning, and gel spinning are used for forming cellulose acetate fibres with a few microns in diameter. However, a breakthrough came with the advent of electrospinning, which allowed researchers to produce ultrathin fibre [15]. Electrospinning is an electrohydrodynamic method used for producing synthetic and natural polymer fibres by electrical force, gathering significant interest due its ability to produce fibres at the nanoscale [16]. Electrospinning of nanofibers is an attracting method to fabricate cellulose acetate membranes with large surface, high porosity and they have been extensively used in biomedicine, filtration and protection, energy storage and energy catalyst [17].

In this work, cellulose was extracted from licorice root waste, and then cellulose triacetate (CTA) was synthesized based on it. The CTA nanofibres were formed by the electrospunning method using new solvent systems as a mixed solvent of methylene chloride:ethanol and chloroform:acetone, and their structure and morphology were investigated.

Experimental

Chemicals and Materials

The following chemicals and materials were used: sodium hydroxide (NaOH, 99 %), hydrogen peroxide (H_2O_2, 60 %), sodium hypochlorite (17 %), sulfuric acid (H_2SO_4, 95–97 %), nitric acid (HNO_3, 65 %), hydrochloric acid (HCl, 37 %) were purchased from “Himreactiv invest” Company Ltd., Uzbekistan Acetic acid (CH_3COOH, 99 %), ethanol (C_2H_5OH), acetone ($(CH_3)_2CO$) were purchased from “Fortek” Company Ltd., Uzbekistan Acetic anhydride ($(CH_3CO)_2O$, 99.5 %), methylene chloride (CH_2Cl_2), chloroform ($CHC1_3$) were purchased from Sigma–Aldrich, USA.

Cellulose Extraction

The cellulose was isolated from wastes. It is a complex procedure that involves chemical or mechanical methods and sometimes a combination of both of them. The licorice root waste was treated in 4 % sodium hydroxide solution at 120 °C for 2 h to remove noncellulose substances (hemicellulose, lignin etc.), as reported previously [3]. Then the mass was washed with deionized water three times (the pH of the solution was neutral) and bleached in 4 % hydrogen peroxide solution at 120 °C for 2 h. The bleached product was separated by filtering, and washed three times with deionized water and dried in the drying oven at 100 °C for 4 h. The degree of polymerization (DP) of LRC was 710, and it was used for the synthesis of the CTA.

Cellulose Triacetate Preparation

The acetylation of LRC was carried out using an acetic acid and acetic anhydride in the presence of sulphuric acid as catalyst [18]. Briefly, 2.5 g of licorice root cellulose (LRC) was placed in a flask with a ground stopper and treated with a mixture pre-cooled to 15 °C with 15–20 ml of acetic acid, 0.5 ml of H_2SO_4, and 10–20 ml of acetic anhydride. The mixture was left to stand for 2 days at room temperature (or 4 hours at 40 °C). During this time, the formation of syrup (a viscous concentrated solution of cellulose acetate) occurs. The resulting thick syrup was diluted by half with glacial acetic acid and poured into a large vessel with ice water. This produces white flakes of cellulose triacetate, which were left in water for 24 hours to decompose completely the acetic anhydride. After this time, cellulose triacetate was filtered, washed, and dried at 95–100 °C. CTA had DS of 2.9, average molecular weight of 175 kDa.

Solution Preparation

CTA solutions were prepared from CTA samples that previously were condensed in a vacuum oven at 80 °C for about 8 h. CTA solutions were prepared by dissolving CTA in solvent mixtures at 25 °C with constant stirring for 2 h. As a solvent the mixtures methylene chloride:ethanol (9:1) (CTA-NF-1) and chloroform:acetone (9:1) (CTA-NF-2) were used.

Electrospinning of CTA Nanofibers

The fabrication of nanofibers was carried out by the electrospinning machine NanoNCeS-robots (South Korea). Elestrospinning conditions were the following: the applied voltage was 25 kV, the needle tip and collector distance was 14 cm; the needle diameter was 0.353 mm; the rate of the injecting solution was 45 mkl/min. During the spinning process the relative humidity was 60 % and temperature was 25 °C. The electrospun CTA fibers were vacuum-dried at 60 °C for 1 h.

Characterization Methods

FTIR

The FTIR spectrometer “Inventio-S” (Bruker) was used and FTIR spectra were recorded in 400–4000 cm^{-1} wavenumber range with a resolution of 2 cm^{-1} and 32 scans at a temperature of 25 °C. Software of OPUS was applied to determine the peaks at specific points.

Wide-Angle X-ray Diffraction

XRD studies were carried out using XRD Miniflex 600 (Rigaku, Japan) with monochromatic CuKα radiation isolated by a nickel filter with a wavelength of 1.5418 Å at 40 kV and the current strength of 15 mA. The spectrum was recorded in the interval of $2\theta = 5°–40°$. The data processing of experimental diffraction patterns, peak deconvolution, describing the peaks used by Miller indices, peak shape, and the basis for the amorphous contribution were conducted using the software “SmartLab Studio II” and data base PDF-2 (2020 Powder diffraction file, ICDD).

Thermogravimetric analysis (TGA)

TG-DSC/DTA synchronous thermal analyzer STA PT1600 (Linseis, Germany) was used for thermal analysis of the samples. The process was carried out by heating ~ 20 mg of the sample in an air atmosphere at a heating rate of 10 °C/min from 25 °C to 900 °C. The samples were previously dried to constant weight.

SEM

Scanning electron microscopy studies were performed using SEM equipment Veritas-3100 (Korea). Magnification of the device is x10-300000, voltage 200V–300V, maximum scanning area (x÷y÷z) is 120÷120÷65 μm.

Sorption Measurements

The McBain balance with quartz spirals of 1 mg/mm sensitivity was used for the sorption investigation. Measurements were carried out in the relative humidity (P/Ps) range 0.10–1.0 at 25 °C until sorption equilibrium was established. KM-8 cathetometer was used for observing the change in sample mass during the sorption process.

Statistical analysis

All experimental data were collected in triplicates and data expressed as average ± standard deviation. Data were compared using a one-way ANOVA with post-Bonferroni test using GraphPad Prism 5.04 (GraphPad Software Inc.)

Results and Discussion

Electrospinning has important tunable working parameters (solution, process and ambient parameters) that can affect the fiber diameter and morphology. With control and proper manipulation of these parameters, one can produce electrospunnanofibers with desirable physical properties for advanced applications [19].

The FTIR spectra of LRC (Fig. 1) have all peaks corresponding to cellulose structure [3]. Around 3400 cm^{-1}, valence vibrations of the hydroxyl groups engaged in intra- and intermolecular hydrogen bonding were visible. The C–H bond valence vibrations in the cellulose methylene groups were observed in the range of 2895 cm^{-1} and 1635 cm^{-1} vibrations of adsorbed water molecules. In the areas of 1420 cm^{-1}, 1335–1375 cm^{-1}, 1202 cm^{-1}, and 1075–1060 cm^{-1}, the absorption bands matched the valence vibrations of the C–O pyranose ring and the strain vibrations of –H, –CH$_2$, –OH, and –CO.

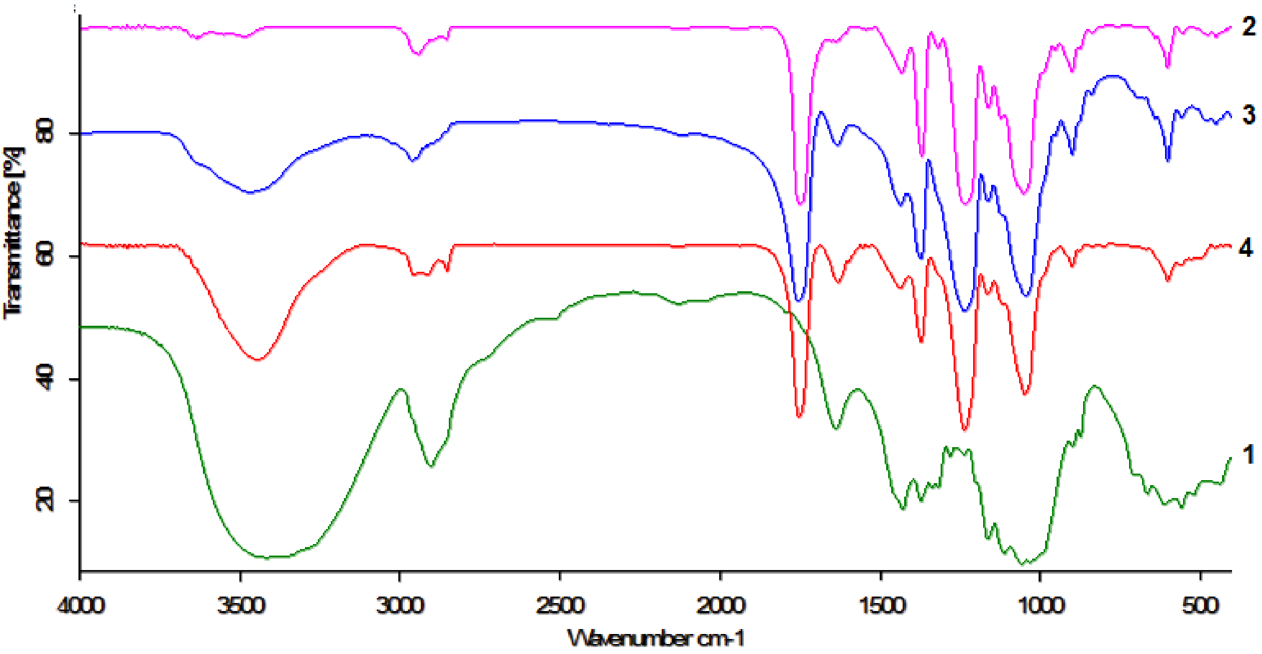

Figure 1. FTIR spectra of LRC (1), CTA (2), CTA-NF-1 (3) and CTA-NF-2 (4)

The FTIR spectrum of CTA typically shows characteristic peaks associated with the acetylated cellulose structure. There is a decrease in the intensity of the –OH absorption band that the hydroxyl group contents in LRC were reduced after esterification. The weakening of peaks related to hydroxyl groups (–OH) in the region (around 3300–3500 cm^{-1}) indicates successful acetylation of cellulose. The ester carbonyl absorption peaks at 1746.6 cm^{-1}, carbonyl hydrogen (C–H) peak at 1374.3 cm^{-1} in acetyl group and 1230 cm^{-1} absorption (C–O) in O–C=O group confirmed that the ester bond have been formed in the CTA and their relative intensity is enhanced. This is in agreement with the author's work in [20] where the characteristic peaks developed confirmed the acetylation of cellulose extracted from cotton stalk.

The FTIR spectra of CTA-NF-1 and CTA-NF-2 show all the peaks characteristic of the CTA, which confirms that the structure of nanofibers is similar as CTA. However, an increase in peak intensity at 3400 cm^{-1} and 1630 cm^{-1} is observed in the spectra of nanofibers, which can be related to the water molecules adsorbed on the active surface of the nanofibers.

The XRD analysis showed of LRC typically exhibits crystalline diffraction peaks corresponding to the native cellulose structure. The presence of well-defined peaks in the XRD pattern indicates the crystalline nature of cellulose in the licorice root material. There are four crystal reflections in the regions of 2θ = 14°, 16°, 22° and 34°, corresponding to the planes $1\bar{1}0$, 110, 200, and 004 in the X-ray diffraction patterns (Fig. 2*a*).

The acetylation process of cellulose disturbs the cellulose crystal structure and leads to the decrease in the degree of crystallinity of CTA (Fig. 2(1*b*)) [21]. CTA has a characteristic wide crystal reflection at 2θ = 15°–30°, associated with interplanar distances. There are crystalline reflections in the regions of 2θ = 9.56°, 17.01°, 18.69°, 29.30° and 39.06°, corresponding to the planes (020), (100), (001), (150) and (022). The functionalization process leads to the change in the supramolecular structure, which becomes orthorhombic with lattice parameters *a* = 5.64 Å, *b* = 20.36 Å, *c* = 4.58Å, α = β = γ = 90.00°.

X-ray diffraction analysis of CTA nanofibers showed (Fig. 2 (2*b* and 3*b*)) that there are regions of coherent scattering at the angles of 2θ = 10÷15° and 20÷25°. During the electrospinning process, CTA macromolecules organize well-ordered structures, so CTA-NF-1 and CTA-NF-2 nanofibers have a higher crystal index (in the range of 41–46 %) than CTA (Table 1).

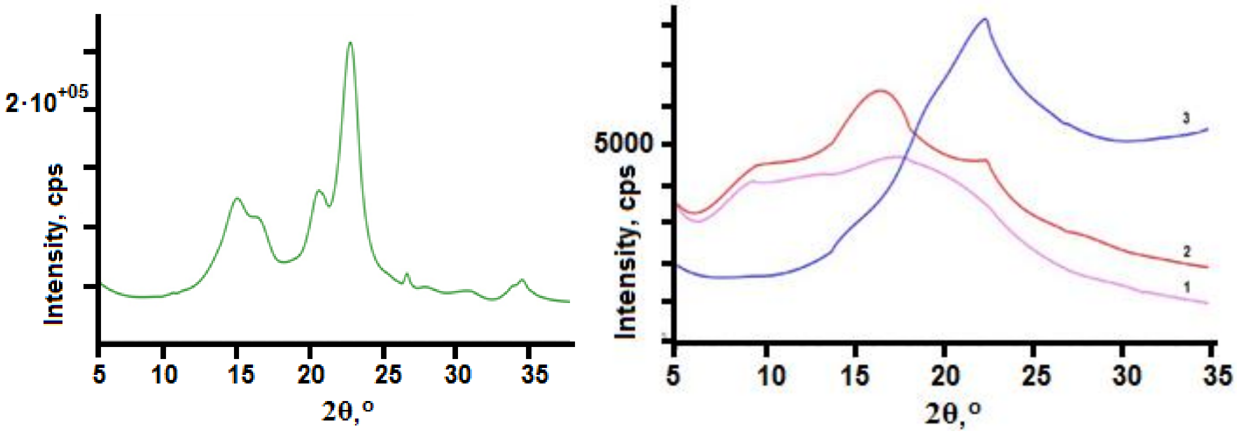

a *b*

Figure 2. X-ray diffraction patterns of LRC (*a*), CTA (*b*, line 1), CTA-NF-1 (*b*, line 3) and CTA-NF-2 (*b*, line 2)

Table 1

Structural parameters of LRC, CTA, CTA-NF-1 and CTA-NF-2

Sample	Miller indices *hkl*	2θ, deg.	d-spacing, Å	FWHM, °	Crystallite size τ, Å	CrI, %	Unit cell size, Å		
							a	*b*	*c*
1	2	3	4	5	6	7	8	9	10
LRC	1-10	14.92	5.93	1.92	43	63	7.81	8.17	10.35
	110	16.40	5.39	1.62	52				
	102	20.69	4.28	1.40	60				

Continuation of Table 1

1	2	3	4	5	6	7	8	9	10
LRC	200	22.76	3.90	1.44	58	63	7.81	8.17	10.35
	103	29.00	3.00	8.00	11				
	113	30.96	2.88	1.83	47				
	004	34.62	2.58	0.99	87				
CTA	020	9.56	9.25	5.20	16	36	5.64	20.36	4.58
	100	17.01	5.21	3.00	30				
	001	18.69	4.75	10.60	8				
	150	29.30	3.05	17.90	5				
	022	39.06	2.0	28.00	3				
CTA-NF-1	100	15.02	5.90	3.90	22	46	6.07	16.04	5.34
	021	20.12	4.41	4.40	19				
	130	22.16	4.01	2.16	39				
	140	26.63	3.35	7.90	11				
	022	35.92	2.49	11.10	8				
CTA-NF-2	020	10.01	8.83	4.75	17	41	3.19	18.09	5.50
	001	16.48	5.38	6.89	12				
	011	17.08	5.18	0.26	325				
	031	22.24	3.99	3.70	23				
	100	28.43	3.13	0.32	271				

The thermal properties of the LCR, CTA, CTA-NF-1 and CTA-NF-2 were studied with TGA (Fig. 3). The weight loss for all investigated samples proceeds in three stages. In the initial stage, occurring at lower temperatures (up to 120 °C), the weight loss (5–9 %) is primarily attributed to the release of adsorbed water (moisture) [5, 22].

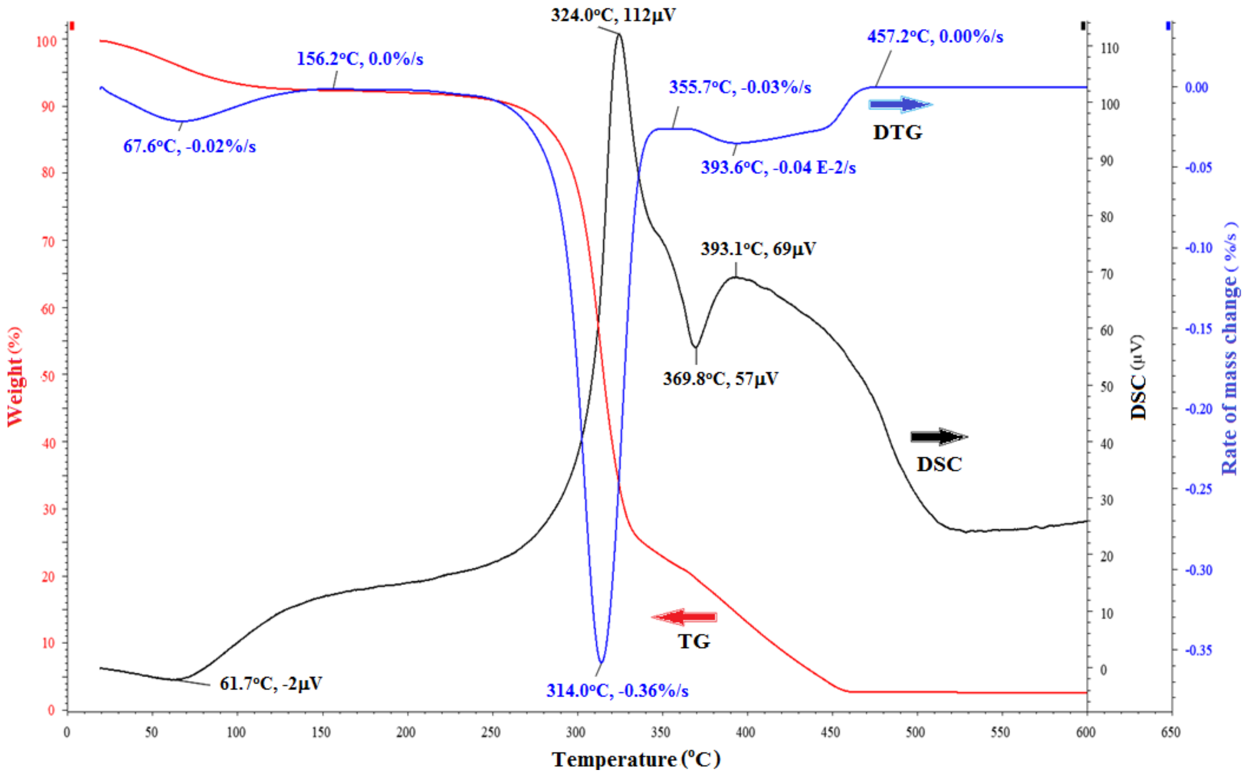

a

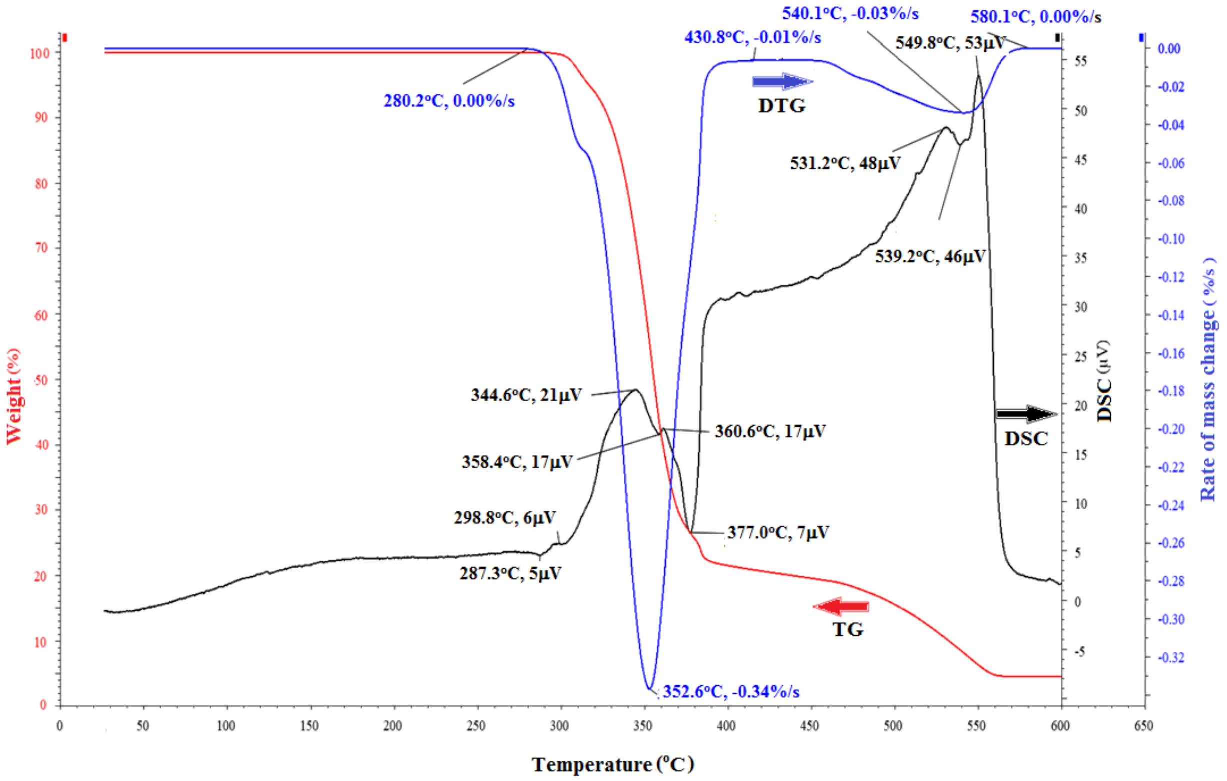
540.1°C, -0.03%/s
580.1°C, 0.00%/s
430.8°C, -0.01%/s
549.8°C, 53μV
280.2°C, 0.00%/s
DTG
531.2°C, 48μV
539.2°C, 46μV
344.6°C, 21μV
360.6°C, 17μV
358.4°C, 17μV
298.8°C, 6μV
377.0°C, 7μV
287.3°C, 5μV
TG
DSC
352.6°C, -0.34%/s
Weight (%)
DSC (μV)
Rate of mass change (%/s)
Temperature (°C)
100
90
80
70
60
50
40
30
20
10
0
55
50
45
40
35
30
25
20
15
10
5
0
-5
0.00
-0.02
-0.04
-0.06
-0.08
-0.10
-0.12
-0.14
-0.16
-0.18
-0.20
-0.22
-0.24
-0.26
-0.28
-0.30
-0.32
0
50
100
150
200
250
300
350
400
450
500
550
600
650

b

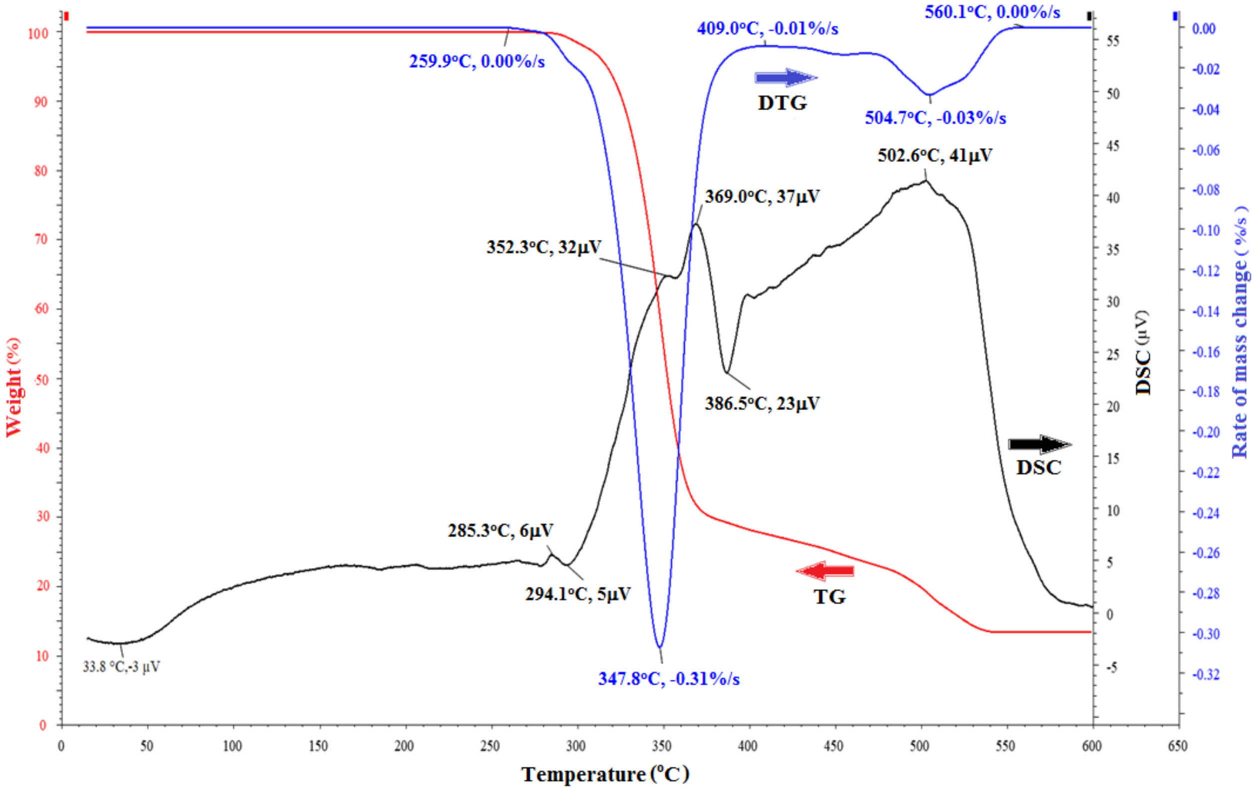
560.1°C, 0.00%/s
409.0°C, -0.01%/s
259.9°C, 0.00%/s
DTG
504.7°C, -0.03%/s
502.6°C, 41μV
369.0°C, 37μV
352.3°C, 32μV
386.5°C, 23μV
DSC
285.3°C, 6μV
294.1°C, 5μV
TG
33.8 °C,-3 μV
347.8°C, -0.31%/s
Weight (%)
DSC (μV)
Rate of mass change (%/s)
Temperature (°C)
100
90
80
70
60
50
40
30
20
10
0
55
50
45
40
35
30
25
20
15
10
5
0
-5
0.00
-0.02
-0.04
-0.06
-0.08
-0.10
-0.12
-0.14
-0.16
-0.18
-0.20
-0.22
-0.24
-0.26
-0.28
-0.30
-0.32
0
50
100
150
200
250
300
350
400
450
500
550
600
650

c

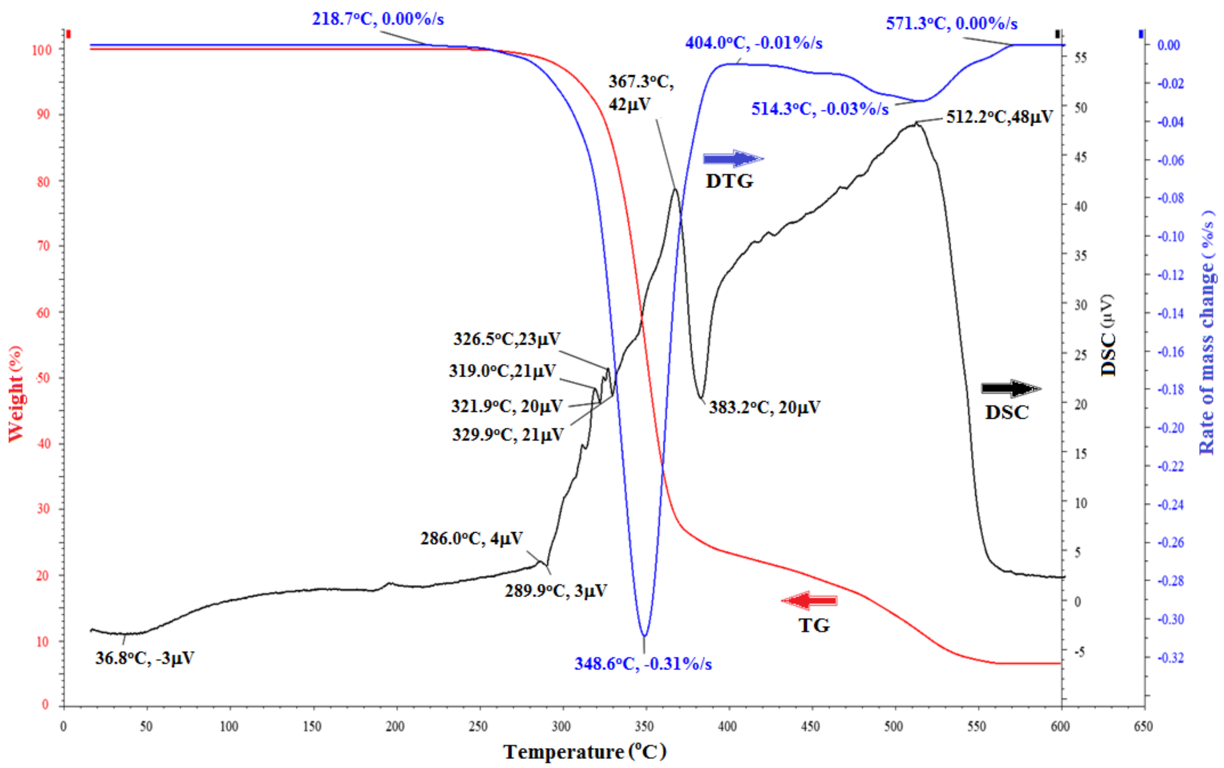

d

Figure 3. TG, DTG and DSC thermograms of LRC (*a*), CTA (*b*), CTA-NF-1 (*c*) and CTA-NF-2 (*d*)

The weight loss was not observed in the CTA, CTA-NF-1, and CTA-NF-2 over the temperature range from 40 °C to 120 °C, indicating that the CTA fibers are more hydrophobic than the LRC. On the weight-loss stage, which took place between 218 and 580 °C, the esterified chains of cellulose acetate are degraded first (in the range of 280–312 °C for CTA, 260–305 °C for CTA-NF-1, 219-280 °C for CTA-NF-2), and then the cellulose chain undergoes the depolymerization process, resulting in the formation of carbon residue [18, 23]. The onset and end thermal degradation temperature of LRC (157–476 °C) are lower than those of the CTA (280–580 °C), CTA-NF-1 (260–560 °C) and CTA-NF-2 (218–571 °C). Moreover, the maximum weight loss rate peak of LCR is also lower, than the CTA, CTA-NF-1 and CTA-NF-2 which were 314 °C, 353 °C, 347 °C and 348 °C, respectively. The CTA and nanofibers show higher thermal stability and a wider range of degradation than the cellulose material, which was also shown in the work [24].

In electrospinning, along with such important parameters as the solution viscosity, the distance between the needle tip and the ground electrode, acceleration voltage, etc., the nature of solvent also plays an important role in the formation of nanofibers. The electrospinning of cellulose acetate in acetone was found to produce a short fibres or a “beads on the string” morphology. The rapidevaporation of solvent and the gelation of cellulose acetate solution, which clog the needle, are the causes of beading [25]. In order to solve this problem a new solvent system was used where ultrafine cellulose acetate fibers were successfully prepared via electrospinning of cellulose acetate in a mixed solvent of acetone/water at water contents of 10–15 wt % [26].

In our investigation, we used two binary mixed solvent systems: methylene chloride:ethanol and chloroform:acetone. The solvent system influences the solution properties and directly impacts the morphology and diameter of the resulting nanofibers. Being highly volatile the solvents used evaporated quickly during electrospinning, leading to the formation of thinner nanofibers. On the other hand, solvents with lower volatility may result in thicker fiber formation. Additionally, the choice of solvent system affects the drying kinetics and the solidification process of the electrospun fibers, which further influences their morphology, such as bead formation, uniformity, and alignment. Figure 4 displays SEM images of CTA-NF-1 and CTA-NF-2 nanofibers. The CTA-NF-1 nanofibers have a long uniform with a parallel grooved morphology, smooth surfaces, and few defects, and their size varies in the range of 200–700 nm. The grooved structure of nanofibers can be attributed to using solvents with different boiling temperatures in the mixed solvent system. Nanofibres with a similar surface texture were also formed from cellulose acetate butyrate solutions using a solvent mixture of acetone and N,N′-dimethylacetamide, and the authors explained this effect that there must be sufficient differences in the evaporation rate between the two solvents to initiate groove formation. It was discovered that the rapid evaporation of a highly volatile solvent from the polymer solution was crucial in the creation of surface voids, whereas the high viscosity of the residual solution after the solvent evaporation ensured the line surface to be formed following solidification [27].

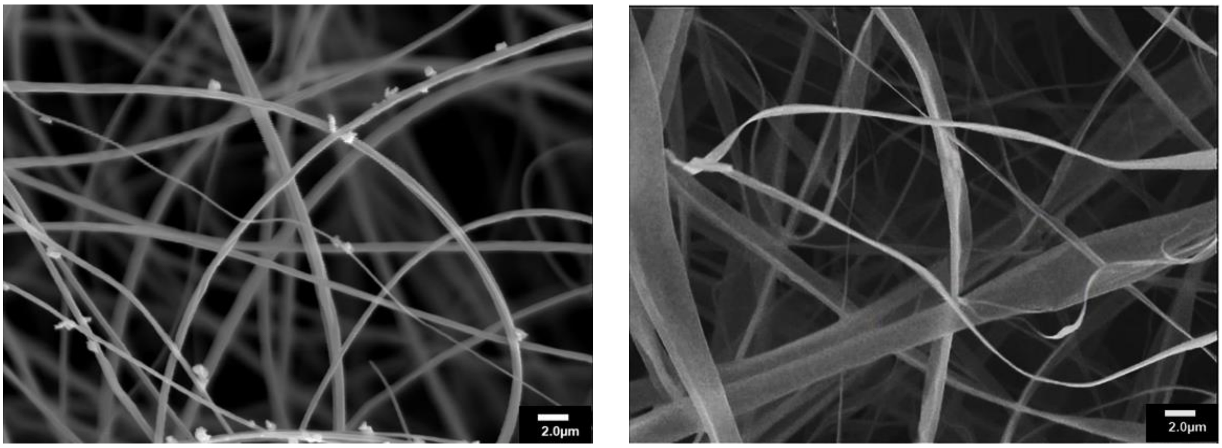

a *b*

Figure 4. SEM images of CTA-NF-1 (*a*) and CTA-NF-2 (*b*) nanofibers

The CTA-NF-2 nanofibers, ranging in size from 200 nm to 4 mkm, have a flat ribbon shape with two tubes (dumbbell shape) (Fig. 4, *b*), and it is related to the formation of the skin layer during electrospinning, which subsequently collapsed. Such ribbons have been formed by electrospinning various polymers [28]. The formation of this shape of nanofibers is associated with several parameters of the electrospinning process: the polymer molecular weight, the polymer solution concentration, the solution feed rate, the nature of the solvent, etc. [29–31]. Ribbon-like or flat nanofibres are produced while electrospinning with a more volatile solution [32-33]. The rapid vaporization of solvent results in the formation of a stable skin layer, as mentioned above, and the collapse of thin walls in the middle section of fibre, but this is insufficient to avoid material buildup at its sides [28].

Differences in capillary-porous structure parameters among LRC, CTA and CTA nanofibers can have significant implications for their respective applications in sorption studies. Sorption studies of the LCR, CTA, CTA-NF-1 and CTA-NF-2 using low molecular weight liquids (water) were carried out, and the capillary-porous structure parameters (monolayer capacity (X_m), specific surface area (S), total pore volume(W_o), average pore radius (r)) of the samples were calculated based on isotherms of water vapour sorption (Table 2).

Table 2

Sorption characteristics of samples

Sample	LRC	CTA	CTA-NF-1	CTA-NF-2
X_m, g/g	0.021	0.0036	0.0039	0.0081
S, m^2/g	86.0	12.83	13.89	28.94
W_o, cm^3/g	0.097	0.016	0.017	0.030
r, Å	45.5	16,76	18.56	24.12
Result presented as mean ±0.04 % standard deviation, n = 3				

The sorption process is a complex mechanism where several factors (capillary-porous, crystalline, supramolecular structure, content of non-cellulose substances) are simultaneously applied to the sorption kinetics. With its natural cellulose structure, LRC may exhibit high sorption capacity for water and other polar solvents due to its abundant hydroxyl (–OH) groups. The presence of hydroxyl groups in LRC provides opportunities for selective sorption of polar molecules or ions through hydrogen bonding and other interactions [8]. In case of CTA and nanofibers based on it, the parameters of the capillary-porous structure decrease in the series: CTA-NF-2 > CTA-NF-1 > CTA. The acetylation of cellulose in CTA reduces the number of hydroxyl groups available for sorption, resulting in lower sorption capacity compared to LRC. CTA nanofibers offer enhanced surface area and porosity compared to CTA, potentially leading to increased sorption capacity. Nanofibrous structures of CTA-NF-1 and CTA-NF-2 may exhibit faster sorption kinetics compared to CTA due to their high surface area and short diffusion pathways. The high surface-to-volume ratio of nanofibers can promote efficient sorption and adsorption of target molecules, making them suitable for applications such as filter material, adsorber, and sensing material.

Conclusions

The cellulose was extracted from licorice root waste and cellulose triacetate was successfully synthesized from licorice cellulose based on esterification method. In order to prepare cellulose nanofibers, the electrospinning has been studied using various solvent systems. In this study, a mixed solvent of methylene chloride/ethanol and chloroform/acetone were developed as a new solvent system for the electrospinning of CA nanofibers. The structural characteristics and morphology of LRC, CTA, CTA-NF-1 and CTA-NF-2 were investigated by the XRD, FT-IR, TGA, SEM, and compared. It was shown that the structure, properties, shape and size of nanofibers depend on using the solvent mixture. To the best of our knowledge, this is the first study reporting the formation nanofibers based on CTA, synthesized from licorice root cellulose. Such CTA nanofibers would be interesting for applications such as filtration materials due to their large surface area.

Funding

This research was funded by the Ministry of Higher Education, Science, and Innovation of the Republic of Uzbekistan (Grant No. FZ-4721055613).

*Author Information**

**The authors' names are presented in the following order: First Name, Middle Name and Last Name*

Siroj Shamsitdinovich Shakhabutdinov — Junior researcher, Institute of Polymer Chemistry and Physics, 100128, Tashkent, Uzbekistan; e-mail: sirojiddin_55@mail.ru; https://orcid.org/0000-0003-3804-9750

Svetlana MihaylovnaYugay — Candidate of chemical sciences, Senior researcher, Institute of Polymer Chemistry and Physics, 100128, Tashkent, Uzbekistan; e-mail: polymer@academy.uz; https://orcid.org/0000-0001-6829-4111

Nurbek Shodievich Ashurov — Candidate of physic-mathematic sciences, Senior researcher, Institute of Polymer Chemistry and Physics, 100128, Tashkent, Uzbekistan; e-mail: ansss72@mail.ru; https://orcid.org/0000-0001-5246-434X

Doniyor Jabborovich Ergashev — Junior researcher, Institute of Polymer Chemistry and Physics, 100128, Tashkent, Uzbekistan; e-mail: polymer@academy.uz; https://orcid.org/0000-0003-4547-9142

Abdumutolib Abdupatto o'g'li Atakhanov (*corresponding author*) — Doctor of technical sciences, Professor, Head of Laboratory "Physic and physic-chemical methods of investigation", Institute of Polymer Chemistry and Physics, 100128, Tashkent, Uzbekistan; e-mail: a-atakhanov@yandex.com; https://orcid.org/0000-0002-4975-3658

Sayyora Sharafovna Rashidova — Doctor of science, Professor, Academician, Director of Institute of Polymer Chemistry and Physics, 100128, Tashkent, Uzbekistan; e-mail: polymer@academy.uz; https://orcid.org/0000-0003-1667-4619

Author Contributions

The manuscript was written through contributions of all authors. All authors have given approval to the final version of the manuscript. CRediT: **Siroj Shamsitdinovich Shakhabutdinov** investigation, validation; **Svetlana Mihaylovna Yugay** investigation, methodology, visualization, writing-review; **Doniyor Jabborovich Ergashev** investigation, methodology, formal analysis; **Abdumutolib Abdupatto o'g'li Atakhanov** conceptualization, data curation, formal analysis, validation, writing-original draft, writing-review & editing; **Nurbek Shodievich Ashurov** conceptualization, data curation, investigation, methodology, visualization, writing-original draft, writing-review & editing; **Sayyora Sharafovna Rashidova** conceptualization, supervision, editing

Conflicts of Interest

The authors declare no conflict of interest.

References

1 Hernández-Becerra, E., Osorio, M., & Marín, D. (2023). Isolation of cellulose microfibers and nanofibers by mechanical fibrillation in a water-free solvent. *Cellulose*, 30: 4905–4923. https://doi.org/10.1007/s10570-023-05162-3

2 Wan, F., Wan, F., & Rizafizah O. (2019). Electrospun Cellulose Fibres and Applications. *Sains Malaysiana*, *48*(7): 1459–1472. http://dx.doi.org/10.17576/jsm-2019-4807-15

3 Saidmuhamedova, M. Q., Turdiqulov, I. H., Atakhanov, A. A., Ashurov, N. Sh., Abdurazakov, M., Rashidova, S. Sh., & Surov, O. V. (2023). Biodegradable Polyethylene-Based Composites Filled with Cellulose Micro- and Nanoparticles. *Eurasian Journal of Chemistry, 110* (2): 94–106. https://doi.org/10.31489/2959-0663/2-23-16

4 Inukai, S., Kurokawa, N., & Hotta, A. (2018). Annealing and saponification of electrospun cellulose-acetate nanofibers used as reinforcement materials for composites. *Composites*, Part A, 113: 158–165. https://doi.org/10.1016/j.compositesa.2018.07.028

5 Kuzieva, M., Atakhanov, A. A., Shahobutdinav, S., Ashurov, N. S., Yunusov, K. E., & Guohua, (2023). Preparation of oxidized nanocellulose by using potassium dichromate. *Cellulose*, 30: 5657–5668. https://doi.org/10.1007/s10570-023-05222-8

6 Suhas, V. K., Gupta, P. J. M., Carrott, R. S., Chaudhary, M., & Kushwah, S. (2016). Cellulose: A review as natural, modified and activated carbon adsorbent. *Bioresource Technology*, 216: 1066–1076. https://doi.org/10.1016/j.biortech.2016.05.106

7 Lavanya, D., Kulkarni, P. K., Dixit, M., Raavi, P. K., & Krishna L. N. V. (2011). Sources of cellulose and their applications. *IJDFR*, 2(6).

8 Atakhanov, A. A., Mamadiyorov, B., Kuzieva, M., Yugay, S. M., Shahobutdinav, S., Ashurov, N. S., & Abdurazakov, M. (2019). Comparative studies of physic-chemical properties and structure of cotton cellulose and its modified forms. *Khimiia Rastitelnogo Syria*, 3: 5–13. https://doi.org/10.14258/jcprm.2019034554

9 Sun, J. X., Sun, X. F, Zhao, H., & Sun, R. C. (2004) Isolation and characterization of cellulose from sugarcane bagasse. *Polym. Degrad. and Stab., 84*(2): 331–339 https://doi.org/10.1016/j.polymdegradstab.2004.02.008

10 Daud, Z., Hatta, M. Z. M., Kassim, A., Awang, H., & Aripin A. M. (2013). Analysis the chemical composition and fiber morphology structure of corn stalk. *Austr. J. Basic and Appl. Sci., 7*: 401–405.

11 Deutch., M. R., Grimm, D., Wehland., M., Infanger, M., & Krüger, M. (2019). Bioactive Candy: Effects of Licorice on the Cardiovascular System. *Foods, 14*(8, 10): 495. https://doi.org/10.3390/foods8100495

12 Alimova, D., Nabieva, I., & Atakhanov A. (2023). Paper production from the waste of medicinal plants. *E3S Web of Conferences*, 452: 05013. https://doi.org/10.1051/e3sconf/202345205013

13 Saeed, U., Dawood, U., & Ali, A. M. (2021). Cellulose triacetate fiber-reinforced polystyrene composite. *J. Thermoplast. Compos. Mater*, 34: 707–721. https://doi.org/10.1177/0892705719847249.

14 Goetz, L. A., Jalvo, B., Rosal, R., & Mathew, A. P. (2016). Superhydrophilic anti-fouling electrospun cellulose acetate membranes coated with chitin nanocrystals for water filtration. *Journal of Membrane Science*, 510, 238–248. https://doi.org/10.1016/j.memsci.2016.02.069

15 Greiner, A., & Wendorff, J. H., (2007). Electrospinning: a fascinating method for the preparation of ultrathin fibers. *Angewandte Chemie Inter. Edit*. 46: 5670–5703. https://doi.org/10.1002/anie.200604646.

16 Xue, J., Wu, T., Dai, Y., & Xia, Y. (2019). Electrospinning and Electrospun Nanofibers: Methods, Materials, and Applications. *Chem Rev, 119*(8): 5298–5415. https://doi.org/10.1021/acs.chemrev.8b00593

17 Jiang, L., Li, K., Yang, H., Liu, X., Li, W., Xu, W., & Deng, B. (2020). Improving mechanical properties of electrospun cellulose acetate nanofiber membranes by cellulose nanocrystals with and without polyvinylpyrrolidone. *Cellulose*, 27: 955–967. https://doi.org/10.1007/s10570-019-02830-1

18 Shaikh, H. M., Anis, A., & Poulose, A. M. (2022). Synthesis and Characterization of Cellulose Triacetate Obtained from Date Palm (Phoenix dactylifera L.) Trunk Mesh-Derived Cellulose. *Molecules, 27*(4): 1434. https://doi.org/10.3390/molecules27041434

19 Frey, M. W. (2008). Electrospinning cellulose and cellulose derivatives. *Polym Rev., 48*(2): 378–391. https://doi.org/10.1080/15583720802022281

20 Abdulhanan, B., Muhammed, T. I., Benjamin, O. A., & Bello, M. (2016). Acetylation of Cotton Stalk for Cellulose Acetate Production. *ASRJETS, 15*(1): 137–150.

21 Ifuku, S., Nogi, M., Abe, K., Handa, K., Nakatsubo, F., & Yano, H. (2007). Surface Modification of Bacterial Cellulose Nanofibers for Property Enhancement of Optically Transparent Composites: Dependence on Acetyl-Group DS. *Biomacromolecules, 8*(6), 1973–1978. https://doi.org/10.1021/bm070113b

22 Kargarzadeh, H., Ahmad, I., Abdullah, I., Dufresne, A., Zainudin, S. Y., & Sheltami R. M. (2012). Effects of hydrolysis conditions on the morphology, crystallinity, and thermal stability of cellulose nanocrystals extracted from kenaf bast fibers. *Cellulose*, 19: 855–866. https://doi.org/10.1007/s10570-012-9684-6

23 Barud, H. S., de Araújo Júnior, A. M., Santos, D. B., de Assunção, R. M. N., Meireles, C. S., Cerqueira, D. A., Rodrigues Filho, G., Ribeiro, C. A., Messaddeq, Y., & Ribeiro, S. J. L. Thermal behavior of cellulose acetate produced from homogeneous acetylation of bacterial cellulose. (2008). *Thermochim. Acta*., 471: 61–69. https://doi.org/10.1016/j.tca.2008.02.009.

24 Chen, J., Xu, J., Wang, K., Cao, X., & Sun, R. (2016). Cellulose acetate fibers prepared from different raw materials with rapid synthesis method. *Carbohydr. Polym*., 137: 685–692. https://doi.org/10.1016/j.carbpol.2015.11.034.

25 Liu, H., Hsieh, Y. L. (2002). Ultrafine fibrous cellulose membranes from electrospinning of cellulose acetate. J. Polym. Sci. Part B: Polym. Phys., 40: 2119–2129. https://doi.org/10.1002/polb.10261

26 Son, W. K., Youk, J. H., Lee, T. S., & Park, W. H. (2004). Electrospinning of ultrafine cellulose acetate fibers: Studies of a new solvent system and deacetylation of ultrafine cellulose acetate fibers. J. Polym. Sci. Part B: Polym. Phys., 42: 5–11. https://doi.org/10.1002/polb.10668

27 Huang, C., Tang, Y., Liu, X., Sutti, A., Ke, Q., Mo, X., Wang, X., Morsic, Y., & Lin, T. (2011). Electrospinning of nanofibres with parallel line surface texture for improvement of nerve cell growth. *Soft Matter*., 7: 10812–10817. https://doi.org/10.1039/C1SM06430D

28 Koombhongse, S., Liu, W., & Reneker, D. H. (2001). Flat polymer ribbons and other shapes by electrospinning. J. Polym. Sci. Part B, 39: 2598–2606. https://doi.org/10.1002/POLB.10015

29 Dhanalakshmi, M., & Jog, J. P. (2008). Preparation and characterization of electrospun fibers of Nylon 11. eXPRESS Polym. Lett., 2(8): 540–545. https://doi.org/10.3144/expresspolymlett.2008.65

30 Koski, A., Yim, K., & Shivkumar, S. (2004). Effect of molecular weight on fibrous PVA produced by electrospinning. *Mater. Lett., 58*(3-4): 493–497. https://doi.org/10.1016/S0167-577X(03)00532-9

31 Chen, S. H., Chang, Y., Lee, K. R., & Lai, J. Y. (2014). A three-dimensional dual-layer nano/microfibrous structure of electrospun chitosan/poly(D,L-lactide) membrane for the improvement of cytocompatibility. *J. Membr.Sci*., 450: 224–234. https://doi.org/10.1016/j.memsci.2013.08.007

32 Ghorani, B., Russell, S. J., & Goswami, P. (2013). Controlled morphology and mechanical characterisation of electrospun cellulose acetate fibre webs. *Int. J. Polym. Sci.* ID 256161. https://doi.org/10.1155/2013/256161

33 Choktaweesap, N., Arayanarakul, K., Aht-Ong, D., Meechaisue, C., & Supaphol, P. (2007). Electrospun gelatin fibers: effect of solvent system on morphology and fiber diameters. *Polym. J. 39*: 622–631. https://doi.org/10.1295/polymj.PJ2006190

How to Cite: Palamarchuk, I.V., & Kulakov, I.V. (2024) A New Method for Obtaining Carboxylic Derivatives of Oxazolo[5,4-b]pyridine Based on 3-Aminopyridine-2(1*H*)-ones. *Eurasian Journal of Chemistry, 29, 2(114), 32-44.* https://doi.org/10.31489/2959-0663/2-24-11

Article

Received: 3 March 2024 | Revised: 18 April 2024 |
Accepted: 26 April 2024 | Published online: 10 May 2024

UDC 547.853 + 547.88

https://doi.org/10.31489/2959-0663/2-24-11

Irina V. Palamarchuk*, Ivan V. Kulakov

School of Natural Sciences, University of Tyumen, Tyumen, Russia
*(*Corresponding author's e-mail: i.v.palamarchuk@utmn.ru)*

A New Method for Obtaining Carboxylic Derivatives of Oxazolo[5,4-b]pyridine Based on 3-Aminopyridine-2(1*H*)-ones

Current methods for synthesis of oxazolo[5,4-b]- and oxazolo[4,5-b]pyridines have several limitations, such as severe reaction conditions, lengthy reaction times, low yields and concurrent formation of side reaction products. This article presents the results of study focused on a one-step method for the synthesis of new derivatives of oxazolo[5,4-b]pyridine incorporating an aliphatic carboxylic group as a linker. During the investigation of acylation reactions of 3-aminopyridine-2(1H)-ones with cyclic anhydrides of dicarboxylic acids (succinic, maleic and glutaric), it was found that the monoamides formed at the initial stage undergo intramolecular cyclization yielding derivatives of oxazolo[5,4-b]pyridine. Subsequently, the reaction conditions were studied and optimized to achieve the target compounds with high yield and purity. The potential anti-inflammatory activity of the obtained derivatives of oxazolo[5,4-b]pyridine was evaluated by molecular docking method using AutoDock Vina software. Compounds 11-14b exhibited higher binding affinity with the selected target protein Prostaglandin synthase-2 (1CX2) compared to the reference anti-inflammatory drug diclofenac. Thus, taking into account the results of in silico analyses, the newly synthesized oxazolo[5,4-b]pyridine derivatives based on 3-aminopyridine-2(1*H*)-ones are promising candidates for further investigation of their potential anti-inflammatory activity through in vivo methods.

Keywords: 3-aminopyridin-2(1*H*)-ones, oxazolo[5,4-b]pyridines, oxazolo[4,5-b]pyridines, intramolecular heterocyclization, biological activity, anti-inflammatory activity, molecular docking.

Introduction

Over the past decade, the interest of scientists in oxazolo[5,4-b]- and oxazolo[4,5-b]pyridines has increased due to their application in various areas of chemistry and a wide range of biological activities, including antimicrobial, anticancer, anti-inflammatory, analgesic, herbicidal, antioxidant, anticoagulant, and antidiabetic activities (Fig. 1) [1–9]. Recently, modulators of calcium channel activity have been discovered within this class [10]. Some derivatives of oxazolopyridines exhibit activity comparable to phenylbutazone or indomethacin, but without causing gastrointestinal irritation, which is commonly associated with many acidic anti-inflammatory compounds [11]. Preclinical studies on human and animal cell lines have shown that oxazolopyridines are generally non-toxic [12]. Furthermore, these compounds meet the criteria for potential drug candidates due to their lack of asymmetric carbon atoms and low molecular weight, which adhere to Lipinski's rule of five [13].

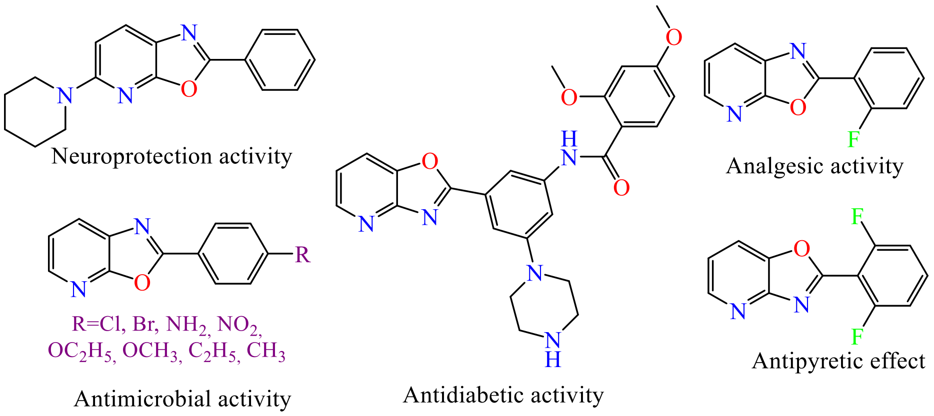

Figure 1. Examples of biologically active oxazolopyridines

However, only a limited number of synthetic strategies exist for the synthesis of 2-substituted oxazolo[5,4-b]- and oxazolo[4,5-b]pyridines [14–19]. One such approach involves the reaction of halogenated aminopyridine derivatives with trimethylsilyl polyphosphate ether or polyphosphoric acid [4]. Another commonly employed method entails the condensation of 2- or 3-aminohydroxypyridines with carboxylic acid derivatives under acidic conditions using such agents as boric acid, aromatic carboxylic acids and polyphosphoric acid at elevated temperatures [20] (Scheme 1).

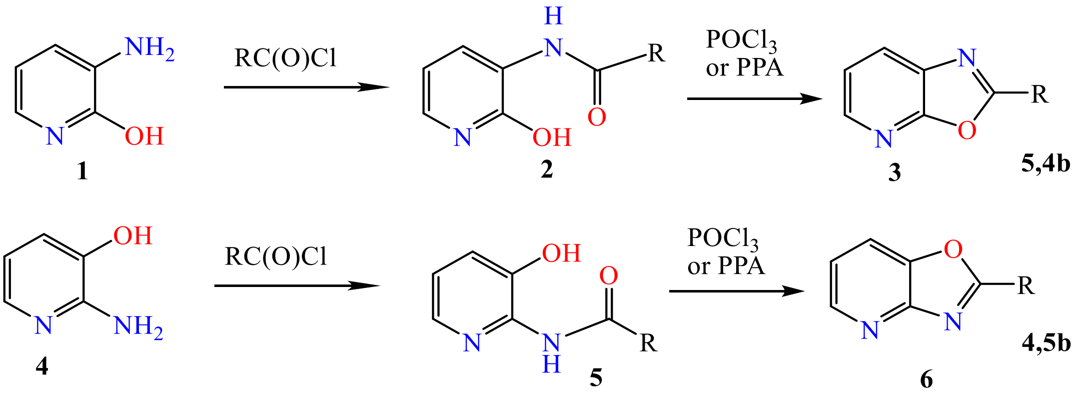

Scheme 1. Formation of oxazolo[5,4-b]- and oxazolo[4,5-b]pyridines derivatives **3,6**

Mainly, oxazolo[5,4-b]pyridine **3** obtained based on unsubstituted N-(2-hydroxypyridin-3-yl)benzamides **2** are described in the literature, particularly for amides of aromatic, rather than aliphatic acids [21]. Examples of 5,7-disubstituted and 2-alkyl-substituted oxazolo[5,4-b]pyridines syntheses are presented in the literature only in isolated cases [22–24].

Continuing our study on the modification of 3-amino-pyridin-2(1*H*)-ones, derivatives of which exhibit high antiradical, neurotropic, antidiabetic, hemorheological, and cytoprotective activity [25–30], we obtained corresponding oxazolo[5,4-b]pyridines using a general Scheme 2, by reacting phosphorus oxychloride with previously obtained chloroacetamide **8a** or benzamide **8b**.

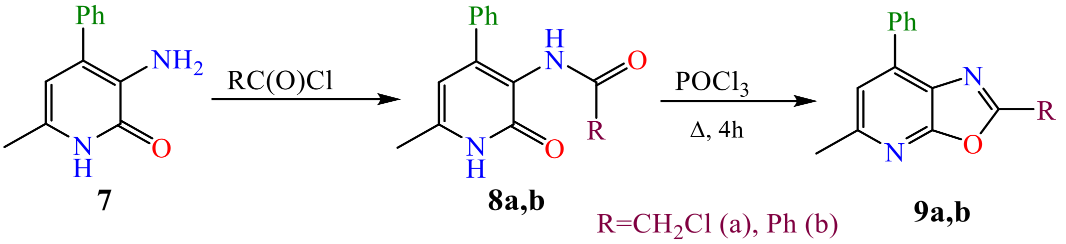

Scheme 2. Intramolecular cyclization of chloroacetamide **8a** or benzamide **8b** under the action of $POCl_3$ into the corresponding oxazolo[5,4-b]pyridines **9a, b**

Additionally, the obtained 2-(chloromethyl)oxazolo[5,4-b]pyridine **9a** served as a very effective synthon for obtaining various N-substituted derivatives through the reaction of nucleophilic substitution of the chlorine atom with various N-nucleophiles, including natural alkaloids [31].

However, existing synthetic methods for the production of oxazolo[5,4-b]- and oxazolo[4,5-b]pyridines have a number of limitations, including harsh reaction conditions, long reaction time, low yields of target products and simultaneous formation of by-products. Therefore, the development of new methods for obtaining oxazolo[5,4-b]pyridines and/or optimization of existing methods is an urgent task.

Experimental

Materials

The obtained compounds were analyzed on an Agilent 1260 Infinity II chromatograph connected to an Agilent 6545 LC/Q-TOF high-resolution mass spectrometer equipped with an AJS ESI dual ion source operating in positive ion mode. Mass spectra with LC/MS precision were obtained in the range of 100–1000 m/z, at a scan rate of 1.5 spectra per second.

The chromatographic separation was carried out using ZORBAX RRHD Eclipse Plus C18 columns (2.1×50 mm, particle size 1.8 μm). The column temperature was kept at 35 °C during the analysis. The mobile phase consisted of eluents A and B. For positive ionization mode, eluent A was a 0.1 % formic acid solution in deionized water, and eluent B was a 0.1 % formic acid solution in acetonitrile. The chromatographic separation was achieved with the following elution gradient: 0–10 min with 95 % A, 10–13 min with 100 % B, and 13–15 min with 95 % A. The mobile phase flow rate was maintained at 400 μL/min throughout the analysis. A sample injection volume of 1 μL was used in all experiments. The sample was prepared by dissolving the entire sample (in 1000 μL) in methanol for HPLC analysis. Sample dilution was performed immediately before analysis.

The recorded data were processed using Agilent MassHunter 10.0 software.

The ^{1}H and ^{13}C NMR spectra in DMSO-d6 solutions were recorded on Bruker AVANCE 500 (500 MHz, 125 MHz) and Magritek spinsolve 80 carbon ultra (81 MHz, 20 MHz) spectrometers.

Melting points of synthetic compounds were determined on a Stuart SMP10 hot bench. All reactions were monitored by thin-layer chromatography (TLC) and identified by UV or iodine vapor.

3-Aminopyridine-2(1*H*)-ones were prepared according to a similar literature procedure [30].

Synthesis and Spectral Analysis of Synthesized Compounds

The synthesis of **oxazolo[5,4-b]pyridine derivatives 11-14a-c** involved heating a mixture of 1 mmol of 3-amino-pyridin-2-(1*H*)-one and 5 mmol of the corresponding anhydrides (succinic, maleic, glutaric, phthalic anhydrides) in 5 mL of acetic acid at reflux temperature with vigorous stirring for 10 hours. The mixture was then cooled and poured into 25 mL of water. The resulting precipitates were filtered and recrystallized from a mixture of hexane, 2-propanol, and dichloromethane.

3-(5,7-Dimethyloxazolo[5,4-b]pyridin-2-yl)propanoic acid 11a. Yield: 0.116g (53 %), grey crystals, M.p.: 270–272°C.

^{1}H NMR spectrum (500 MHz, DMSO-d6), δ ppm: 1.89 (s., 3H, CH_3); 2.16 (s., 3H, CH_3); 2.81 (d., 4H, CH_2-CH_2); 5.98 (s., 1H, H-6); 11.85 (br.s., 1H, OH).

^{13}C NMR spectrum (125 MHz, DMSO-d6), δ ppm: 17.2 (CH_3); 18.3 (CH_3); 28.4 (2C CH_2-CH_2); 106.3 (C-6); 118.0; 145.2; 150.2; 158.8; 176.5 (2C).

HRMS m/z: calcd for $C_{11}H_{13}N_2O_3^+$ $[M + H]^+$: 221.0921; found: 221.0935.

3-(5-methyl-7-phenyloxazolo[5,4-b]pyridin-2-yl)propanoic acid 11b. Yield: 0.182 g (64 %), grey powder, M.p.: 280–281°C.

^{1}H NMR spectrum (500 MHz, DMSO-d6), δ ppm: 2.25 (s., 3H, CH_3); 2.57 (d.d., 2H, CH_2CO); 2.76 (d.d., 2H, CH_2); 6.13 (s., 1H, H-6); 7.21 (m., 2H, H-2,6 Ph); 7.40 (m., 3H, H-3,4,5 Ph); 12.20 (br.s., 1H, OH).

^{13}C NMR spectrum (125 MHz, DMSO-d6), δ ppm: 18.6 (CH_3); 28.2 (2C CH_2-CH_2); 105.6 (C-6); 116.6; 126.8 (2C Ph); 128.6 (2C Ph); 130.0 (C Ph); 136.1; 146.6; 152.3; 159.2; 176.8 (2C).

HRMS m/z: calcd for $C_{16}H_{15}N_2O_3^+$ $[M + H]^+$: 283.1077; found: 283.1075.

3-(5-methyl-7-(thiophen-2-yl)oxazolo[5,4-b]pyridin-2-yl)propanoic acid 11c. Yield: 0.165 g (57 %), grey powder, M.p.: 327–329°C.

^{1}H NMR spectrum (500 MHz, DMSO-d6), δ ppm: 2.25 (s., 3H, CH_3); 2.84-2.92 (m., 4H, CH_2-CH_2); 6.57 (s., 1H, H-6); 7.17 (d.d., ^{3}J=5.1 Hz, ^{4}J=3.9 Hz, 1H, H-4 thiophen); 7.63 (d.d., ^{3}J=3.9 Hz, ^{4}J=1.0 Hz, 1H, H-3 thiophen); 7.74 (d.d., ^{3}J=5.1 Hz, ^{4}J=1.0 Hz, 1H, H-5 thiophen); 12.05 (br.s., 1H, OH).

^{13}C NMR spectrum (20 MHz, DMSO-d6), δ ppm: 18.6 (CH_3); 28.7 (2C CH_2-CH_2); 103.0 (C-6); 114.2; 127.8 (C thiophen); 129.7 (C thiophen); 130.4 (C thiophen); 135.6; 143.3; 145.9; 159.3; 176.9 (2C).

HRMS m/z: calcd for $C_{14}H_{13}N_2O_3S^+$ $[M + H]^+$: 289.0641; found: 289.0648.

(E)-3-(5,7-dimethyloxazolo[5,4-b]pyridin-2-yl)acrylic acid 12a. Yield: 0.111g (51 %), white crystals, M.p.: 215-218°C.

^{1}H NMR spectrum (80 MHz, DMSO-d6), δ ppm: 1.93 (s., 3H, CH_3); 2.17 (s., 3H, CH_3); 6.00 (s, 1H, H-6); 7.18 (s., 2H, 2-CH=CH); 11.86 (s., 1H, OH).

^{13}C NMR spectrum (125 MHz, DMSO-d6), δ ppm: 17.3 (CH_3); 18.3 (CH_3); 106.4 (C-6); 135.1 (4C); 145.4; 151.4; 159.3; 170.0.

HRMS m/z: calcd for $C_{11}H_{11}N_2O_3^+$ $[M + H]^+$: 219.0764; found: 219.0768.

(E)-3-(5-methyl-7-phenyloxazolo[5,4-b]pyridin-2-yl)acrylic acid 12b. Yield: 0.216g (77 %), white crystals, M.p.: 282–284°C.

^{1}H NMR spectrum (500 MHz, DMSO-d6), δ ppm: 2.26 (s., 3H, CH_3); 6.16 (s., 1H, H-6); 7.07 (s., 2H, H-2,6 Ph); 7.21 (d.d., *J*=7.5, 2.0, 2H, CH=CH); 7.36-7.39 (m., 3H, H-3,4,5 Ph); 12.23 (br.s., 1H, OH).

^{13}C NMR spectrum (125 MHz, DMSO-d6), δ ppm: 18.6 (CH_3); 105.8 (C-6); 115.4; 126.9 (2C Ph); 128.6 (2C Ph); 129.0; 135.3 (CH=CH); 136.2; 164.8; 153.7; 159.9; 170.4 (2C).

HRMS m/z: calcd for $C_{16}H_{13}N_2O_3^+$ $[M + H]^+$: 281.0921; found: 281.0919.

(E)-3-(5-methyl-7-(thiophen-2-yl)oxazolo[5,4-b]pyridin-2-yl)acrylic acid 12c. Yield: 0.152g (53 %), beige crystals, M.p.: 315-316°C.

^{1}H NMR spectrum (80 MHz, DMSO-d6), δ ppm: 2.26 (s., 3H, CH_3); 6.62 (s., 1H, H-6); 7.18 (t., 1H, *J*=5.1 Hz, H-4 thiophen); 7.30 (s., 2H, 2-CH=CH); 7.67-7.76 (m., 2H, H-3,5 thiophen); 12.05 (s., 1H, OH).

^{13}C NMR spectrum (21 MHz, DMSO-d6), δ ppm: 18.6 (CH_3); 102.8 (C-6); 127.8 (1C thiophen); 129.9 (1C thiophen); 130.8 (1C thiophen); 135.4; 135.9 (4C); 144.5; 146.2; 159.9; 170.5.

HRMS m/z: calcd for $C_{14}H_{11}N_2O_3S^+$ $[M + H]^+$: 287.0485; found: 287.0490.

4-(5,7-Dimethyloxazolo[5,4-b]pyridin-2-yl)butanoic acid 13a. Yield: 0.110g (47 %), white crystals, M.p.: 236–239°C.

^{1}H NMR spectrum (80 MHz, DMSO-d6), δ ppm: 1.82 (s., 3H, CH_3); 1.90-1.98 (m., 2H, 3-CH_2); 2.13 (s., 3H, CH_3); 2.70 (t., *J*=5.7 Hz, 4H, 4,2-CH_2); 5.91 (s., 1H, H-6); 11.67 (s., 1H, OH).

^{13}C NMR spectrum (21 MHz, DMSO-d6), δ ppm: 17.1 (CH_3); 18.2 (CH_3); 32.2 (3C 2,3,4-CH_2); 106.2 (C-6); 121.4; 143.9; 148.7; 159.1; 171.9 (2C).

HRMS m/z: calcd for $C_{12}H_{15}N_2O_3^+$ $[M + H]^+$: 235.1077; found: 235.1081.

4-(5-Methyl-7-phenyloxazolo[5,4-b]pyridin-2-yl)butanoic acid 13b. Yield: 0.166 g (56 %), white crystals, M.p.: 312–314°C.

^{1}H NMR spectrum (80 MHz, DMSO-d6), δ ppm: 1.43-1.87 (m., 2H, 3-CH_2); 2.23 (s., 3H, CH_3); 2.49-2.64 (m., 4H, 4,2-CH_2); 6.05 (s., 1H, H-6); 7.17 (d., *J*=3.1 Hz, 2H, H-2,6 Ph); 7.35 (br.s., 3H, H-3,4,5 Ph); 12.00 (br.s., 1H, OH).

^{13}C NMR spectrum (21 MHz, DMSO-d6), δ ppm: 18.4 (CH_3); 32.2 (3C 2,3,4-CH_2); 105.4 (C-6); 120.2; 126.7 (2C Ph); 128.4 (2C Ph); 128.6; 136.5; 145.1; 150.8; 159.3; 172.2 (2C).

HRMS m/z: calcd for $C_{17}H_{17}N_2O_3^+$ $[M + H]^+$: 297.1234; found: 297.1230.

4-(5-Methyl-7-(thiophen-2-yl)oxazolo[5,4-b]pyridin-2-yl)butanoic acid 13c. Yield: 0.157 g (52 %), white crystals, M.p.: 299–302°C.

^{1}H NMR spectrum (80 MHz, DMSO-d6), δ ppm: 1.90-2.06 (m., 2H, 3-CH_2); 2.22 (s., 3H, CH_3); 2.73 (t., *J*=6.0 Hz, 4H, 4,2-CH_2); 6.49 (s., 1H, H-6); 7.14 (d.d., ^3J=5.0 Hz, ^4J=3.8 Hz, 1H, H-4 thiophen); 7.55-7.60 (m., 1H, H-3 thiophen); 7.67-7.73 (m., 1H, H-5 thiophen); 12.85 (br.s., 1H, OH).

^{13}C NMR spectrum (21 MHz, DMSO-d6), δ ppm: 17.1 (CH_3); 32.9 (3C 2,3,4-CH_2); 106.2 (C-6); 118.9; 127.9 (C thiophen); 129.6 (C thiophen); 130.3 (C thiophen); 136.6; 142.4; 144.9; 159.9; 172.7 (2C).

HRMS m/z: calcd for $C_{15}H_{15}N_2O_3S^+$ $[M + H]^+$: 303.0798; found: 303.0801.

2-(5,7-Dimethyloxazolo[5,4-b]pyridin-2-yl)benzoic acid 14a. Yield: 0.161 g (60 %), light brown crystals, M.p.: 302–305°C.

^{1}H NMR spectrum (80 MHz, DMSO-d6), δ ppm: 2.00 (s., 3H, CH_3); 2.20 (s., 3H, CH_3); 6.05 (s., 1H, H-6); 7.92 (br.s., 4H, H-3,4,5,6 Ar); 11.96 (br.s., 1H, OH).

^{13}C NMR spectrum (21 MHz, DMSO-d6), δ ppm: 17.5 (CH_3); 18.4 (CH_3); 106.5 (C-6); 117.2; 123.5 (3C); 131.6; 134.8 (3C); 145.6; 151.4; 159.3; 166.9.

HRMS m/z: calcd for $C_{15}H_{13}N_2O_3^+$ $[M + H]^+$: 269.0921; found: 269.0930.

2-(5-Methyl-7-phenyloxazolo[5,4-b]pyridin-2-yl)benzoic acid 14b. Yield: 0.225 g (68 %), light brown powder, M.p.: 312–314°C.

^{1}H NMR spectrum (80 MHz, DMSO-d6), δ ppm: 2.29 (s., 3H, CH_3); 6.21 (s., 1H, H-7); 7.30 (br.s., 5H, H-2,3,4,5,6 Ph); 7.88 (br.s., 4H, H-3',4',5',6' Ar); 12.31 (br.s., 1H, OH).

^{13}C NMR spectrum (21 MHz, DMSO-d6), δ ppm: 18.6 (CH_3); 105.8 (C-6); 115.8; 123.6 (3C); 126.8 (3C); 128.6 (3C); 128.9; 131.2; 135.0; 136.2; 146.9; 153.5; 159.6; 167.4.

HRMS m/z: calcd for $C_{20}H_{15}N_2O_3^+$ $[M + H]^+$: 331.1077; found: 331.1085.

2-(5-Methyl-7-(thiophen-2-yl)oxazolo[5,4-b]pyridin-2-yl)benzoic acid 14c. Yield: 0.209g (62 %), gray crystals, M.p.: 341–343°C.

^{1}H NMR spectrum (80 MHz, DMSO-d6), δ ppm: 2.29 (s., 3H, CH_3); 6.67 (s., 1H, H-6); 7.14 (d.d., ^3J=5.0 Hz, ^4J=3.8 Hz, 1H, H-4 thiophen); 7.60-7.69 (m., 2H, H-3,5 tiophene); 7.97 (br.s., 4H, H-3,4,5,6 Ar); 12.45 (br.s., 1H, OH).

^{13}C NMR spectrum (21 MHz, DMSO-d6), δ ppm: 18.7 (CH_3); 102.9 (C-6); 113.5; 123.8; 127.8; 128.4; 130.01; 130.8; 130.9; 131.7; 132.8; 135.3; 135.5; 144.5; 146.4; 159.9; 167.5; 168.7.

HRMS m/z: calcd for $C_{18}H_{13}N_2O_3S^+$ $[M + H]^+$: 337.0641; found: 337.0638.

Molecular Docking

Molecular docking is a method used to predict the optimal position of a ligand relative to a protein receptor to form a stable complex [32]. This method takes into account scoring functions and allows the estimation of binding strength or affinity between a ligand and a protein. Molecular docking is commonly used to predict how potential drug compounds may bind to target proteins, allowing their effectiveness and binding strength to be assessed. This technique is essential for the design and development of pharmaceuticals [33].

The main goal of molecular docking is computer modeling of the molecular identification process and achieving optimal conformation with minimal free energy of the entire system. The discovery of a new drug is a complex task, and modern approaches are mainly based on the *in silico* approach. The use of computer technologies in the discovery and development of drug compounds is becoming increasingly popular and recognized. Therefore, molecular docking plays a key role in the search for new pharmacologically active compounds in medical science, and its utility is leveraged in the field of structure-based drug design and biochemical investigations.

The docking procedure was performed using AutoDock Vina software [34]. Ligand molecules were designed using ChemBio3D Ultra 14.0 software, and 3D protein structures were obtained from the Protein Data Bank (RCSB) [35]. Before docking, the protein structures underwent preparation steps, including removing native ligands and water molecules, addition of polar hydrogen atoms, and conversion of the structures to.pdbqt format using AutoDock MGL software package [36]. For the enzyme COX-1 (PDB: 1EQG), the active site grid coordinates (X=29.29, Y=34.10, Z=199.90; 19.61 × 15.10 × 18.40 Å^3) were specified, and for the enzyme COX-2 (PDB: 1CX2), the active site grid coordinates (X=24.25, Y=20.06, Z=16.66; 17.26×14.75×15.26 Å^3) were provided. The ligands interactions within the binding sites were examined using Discovery Studio Visualizer software [37].

Results and Discussion

Chemistry

Cyclic anhydrides of dicarboxylic acids were chosen to study new cases of the cyclization reaction of amide derivatives of 3-aminopyridin-2(1H)-ones into the corresponding oxazolo[5,4-b]pyridines. It was assumed that monoamides containing a carboxylic linker fragment could be synthesized through the acylation of 3-aminopyridine-2(1H)-ones 7a-c with cyclic anhydrides of dicarboxylic acids (Scheme 4). Activation of the carboxyl group followed by aminolysis of 3-aminopyridine-2(1H)-one may lead to the formation of diamides from the respective acids, which can efficiently cyclize to produce the corresponding bisderivatives of oxazolo[5,4-b]pyridine.

For this purpose, we carried out the reaction of 3-aminopyridones **7a-c** with succinic anhydride according to Scheme 3. The reaction was carried out by refluxing in acetic acid using a slight excess (1.5 equiv.) of succinic anhydride. Analysis of the reaction mixture by thin-layer chromatography showed the presence of unreacted starting 3-aminopyridine-2(1*H*)-one. To increase the conversion of the starting 3-aminopyridine-2(1*H*)-one into the desired product, we gradually added an additional excess of succinic anhydride to the reaction mixture. The optimal amount of succinic anhydride added to the reaction until the complete disappearance of the starting 3-aminopyridine-2(1*H*)-one was 5 equiv.

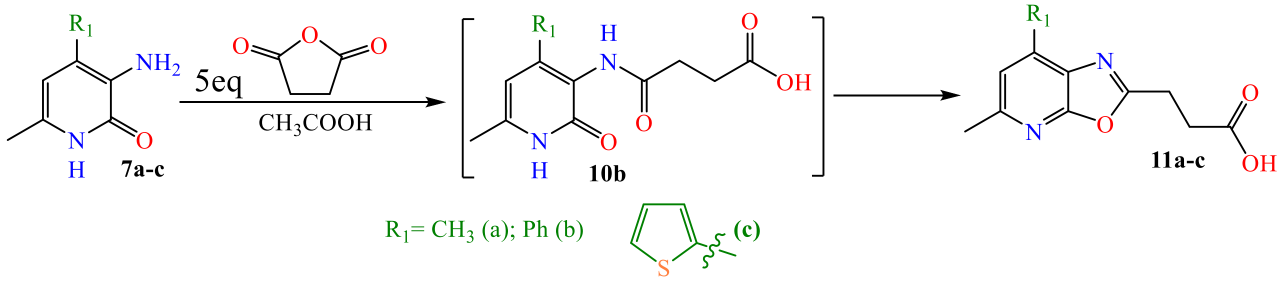

Scheme 3. Cyclization reaction of 3-aminopyridones **7a-c** with 5 equiv of succinic anhydride into oxazolo[5,4-b]pyridine **11a-c**

Analysis of the isolated product of the reaction of aminopyridone **11b** with succinic anhydride by high-resolution mass spectrometry showed that the target product had a molecular ion peak not at [M+] = 300.3140, as expected for the monoamide **10b**, but at [M+] = 282.3573, i.e., 18 a.m.u. lower, indicating the loss of one water molecule. Based on this, we hypothesized that under the excess anhydride conditions, the monoamide part underwent cyclization to form the corresponding oxazolopyridine **11b**.

The formation of oxazolopyridine **11b** was unambiguously confirmed by ^1H and ^{13}C NMR spectral analysis, which showed the absence of the amide NH proton singlet in the spectrum. A slight shift was observed for the H-5 proton, registering from 5.98 ppm in the starting 3-aminopyridone **11a** to 6.13 ppm, indirectly confirming the aromatization of the condensed pyridine ring. The spectrum also showed characteristic multiplets as two doublets of doublets of two aliphatic methylene groups at 2.57 ppm and 2.76 ppm. The acidic proton of the carboxyl OH group appeared as a singlet at 12.20 ppm. Similar reactions took place between 3-aminopyridones **11a-c** and maleic and glutaric anhydrides.

In order to expand the arsenal of new derivatives of oxazolo[5,4-b]pyridine and verify their synthesis using cyclic anhydrides of dicarboxylic acids, we carried out a similar intramolecular heterocyclization of 3-aminopyridine-2(1*H*)-ones with a five-fold excess of maleic and glutaric anhydrides (Scheme 4).

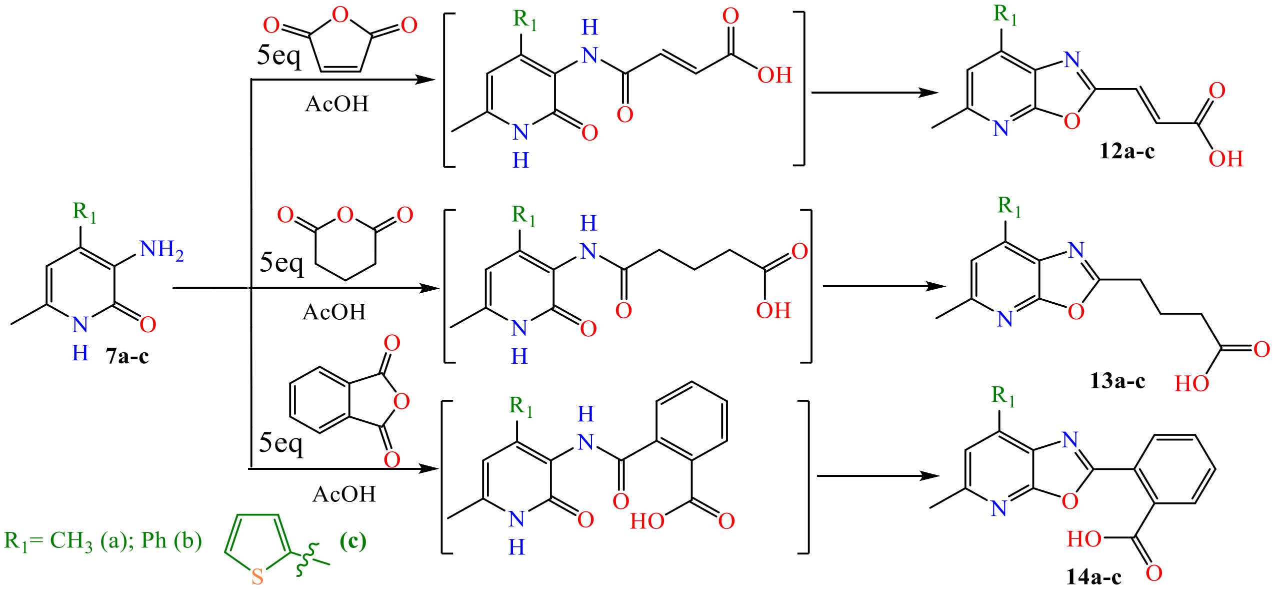

Scheme 4. Cyclization reaction of 3-aminopyridones **7a-c** with 5 equiv. of maleic or glutaric anhydride into the corresponding oxazolo[5,4-b]pyridine **12-14a-c**

The structure of all obtained compounds **11-14a-c** was confirmed by ^1H and ^{13}C NMR spectroscopy and high-resolution mass spectrometry.

Apparently, the monoamide formed at the first stage under the excess anhydride, which acts as an effective dehydrating agent in this case, undergoes intramolecular cyclization as follows (Scheme 5). In this case, intramolecular nucleophilic addition of the hydroxyl group of the lactim form of pyridone to the amide carbonyl with subsequent elimination of water occurs.

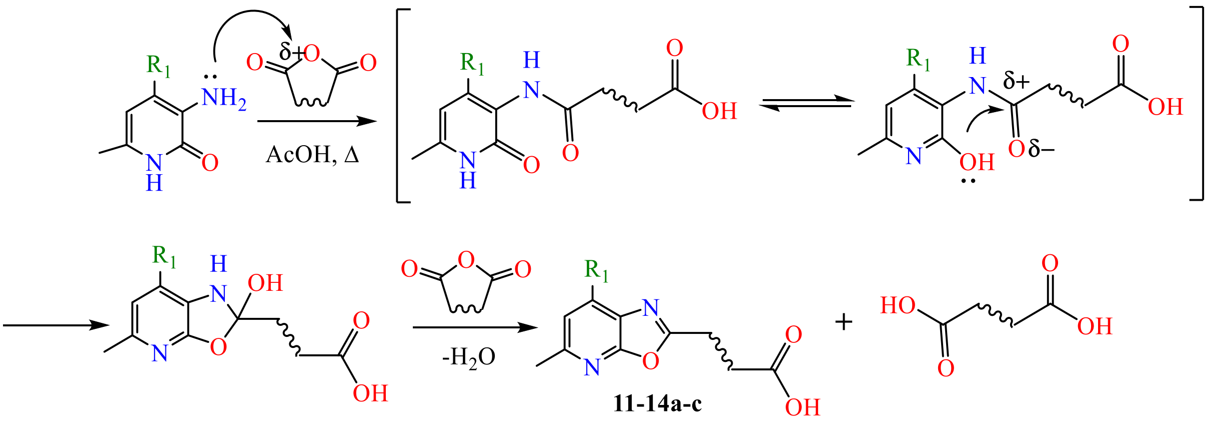

Scheme 5. The proposed reaction mechanism

It is worth noting that only one example of a similar method for obtaining unsubstituted oxazolo[4,5-b]pyridine **15** is given in the literature, based on the cyclization reaction of 2-amino-3-hydroxypyridine with benzoic anhydride (Scheme 6) [38, 32].

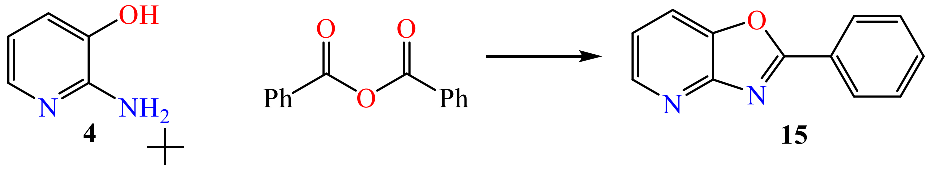

Scheme 6. Cyclization reaction of 2-amino-3-hydroxypyridine with benzoic anhydride into oxazolo[4,5-b]pyridine **15**

Thus, the reaction we discovered between 3-aminopyridones and dicarboxylic acid anhydrides leads to a one-step cyclization into oxazolo[5,4-b]pyridines **11-13a-c** with an acidic carboxylic linker. This transformation not only improves the water solubility of the compounds for bioassays but also facilitates additional structural modifications.

Molecular Docking

The literature contains data confirming the anti-inflammatory activity of oxazolopyridines [11]. Therefore, molecular docking was used to evaluate presumed anti-inflammatory activity and understand the molecular interactions between synthesized ligand molecules and target proteins.

The enzyme COX-1 (PDB: 1EQG) [39] and enzyme COX-2 (PDB: 1CX2) [40] were chosen as target proteins and Diclofenac was chosen as a well known anti-inflammatory reference drug. Cyclooxygenases (COX), also known as prostaglandin-endoperoxide synthases, are pivotal enzymes that are essential for the biosynthesis of prostaglandins, critical molecules involved in regulating inflammation, pain, and fever. The body houses two primary isoforms of these enzymes — cyclooxygenase-1 (COX-1) and cyclooxygenase-2 (COX-2). COX-1 is primarily responsible for the production of key signaling molecules such as prostaglandins, prostacyclin, and thromboxanes, contributing to processes related to pain sensitivity, blood clotting, and gastric mucosal protection [41]. Conversely, COX-2 is primarily involved in transmitting pain signals during inflammatory conditions and plays a significant role in prostaglandin synthesis within inflammatory cells and the central nervous system [42].

The docking results showed that for the studied structures, the binding affinity with the selected protein receptors was slightly higher than the binding affinity of these proteins with diclofenac, chosen as a reference drug (Table 1).

Table 1

Binding affinity (kcal/mol) of oxazolo[5,4-b]pyridine derivatives 12-14a-c and diclofenac in the active site of COX-1 (PDB: 1EQG) and COX-2 (PDB: 1CX2) proteins

Ligand Receptor	**Diclofenac**	**11a**	**11b**	**11c**	**12a**	**12b**	**12c**	**13a**	**13b**	**13c**	**14a**	**14b**	**14c**
1EQG	–8.4	–7.5	–7.9	–7.4	–7.3	–6.3	–5.6	–7.5	–7.9	–7.3	–9.1	–6.6	–6.4
1CX2	–8.1	–7.7	–9.4	–8.7	–8.2	–9.7	–9.2	–8.0	–9.6	–8.8	–9.1	–9.8	–9.0

As can be seen in Table 1, compounds **11–14b** exhibited the highest binding energy values with the 1CX2 receptor protein, so we further described its interaction in more detail (Table 2).

The interaction of compound **11b** with the enzyme cyclooxygenase-2 (COX-2) (PDB: 1CX2) has a higher binding affinity of –9.4 kcal/mol. This is explained by the formation of one carbon-hydrogen bond and three hydrogen bonds between the oxygen atom of the oxazole ring and the hydrogen atom of the carboxyl group oxygen of compound **11b** and the amino acid residues LEU352, HIS90, SER353, respectively. The oxazolopyridine and phenyl rings also form six π-Alkyl interactions with amino acids VAL523, LEU352, ALA527, and VAL349. Additionally, compound 2 forms van der Waals interactions with residual amino acids SER530, TRP387, TYR348, LEU359, TYR355, ARG120, ARG513, PHE518 (Fig. 2).

Table 2

Basic hydrogen bonds and acid interactions of oxazolo[5,4-b]pyridine derivatives 11-14и with the COX-2 (PDB: 1CX2) protein

Compound	Receptor	H-Hydrogen bonds	Residual Amino acid Interactions	
			Amide-Pi Stacked / Pi-Sulfur/ Pis interactions/ Pi-Pi Stacked/Pi-Anion/ Pi-Pi T-shaped/Pi-Alkyl/	Van-der Walls interactions
11b	1CX2	SER353, LEU352, HIS90	VAL523, VAL349, ALA527, LEU531, LEU352	SER530, TRP387, TYR348, LEU359, TYR355, ARG120, ARG513, PHE518
12b		TYR355, GLN192, HIS90, SER353	LEU352, VAL349, ALA527, VAL523, LEU531	LEU359, SER530, TRP387, TYR348, ARG513, PHE518, ALA516, ILE517, ARG120
13b		TYR355, HIS90, SER353	LEU352, VAL349, ALA527, VAL523, LEU531	LEU359, ARG120, SER530, TRP387, TYR348, ARG513, PHE518
14b		SER530	LEU352, VAL349, ALA527, VAL523, LEU531, HIS90, YR355, ARG120, TRP387, GLY526	ARG513, SER353, VAL116, LEU359, MET522, LEU384, TYR385, PHE518, TYR348

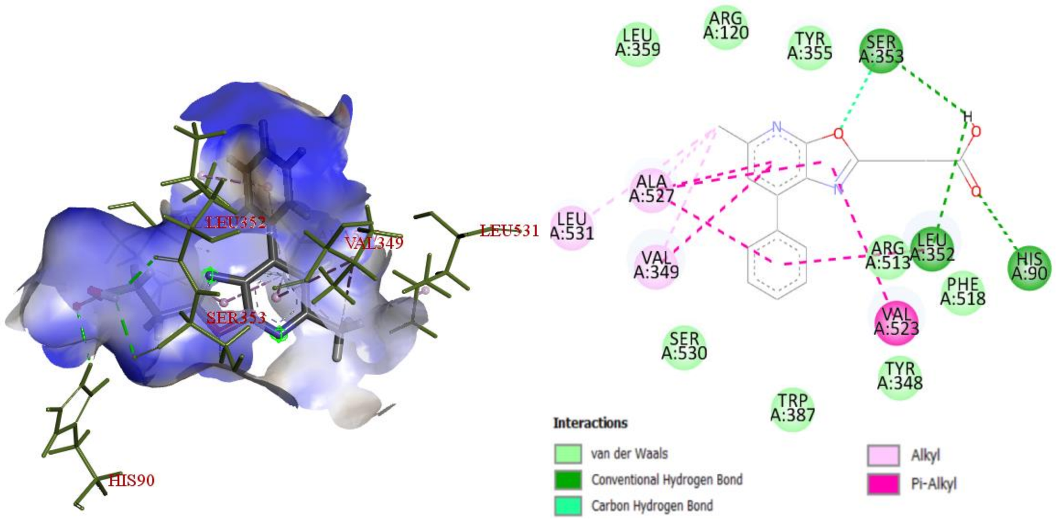

3D docking model;

(b) 2D docking model

Figure 2. Complex of **11b** with cyclooxygenase-2 (COX-2)

Compound **12b** has a binding affinity of –9.7 kcal/mol with cyclooxygenase-2 (COX-2) (PDB: 1CX2) due to the formation of six π-alkyl interactions of the oxazolopyridine and phenyl rings with the amino acids VAL349, LEU352, ALA527 and VAL523. Additionally, a carbon-hydrogen bond is formed between the amino acid residue SER 353 and the oxygen atom. Also, three hydrogen bonds are established between the nitrogen atom of the pyridine ring and the oxygen and hydrogen atoms of the carbonyl group with the amino acid residues GLN192, TYR355, HIS90, respectively. Compound **12b** forms van der Waals interactions with the residual amino acids LEU359, SER 530, TRP387, TYR348, ARG513, PHE518, ALA516, ILE517, ARG120 (Fig. 3).

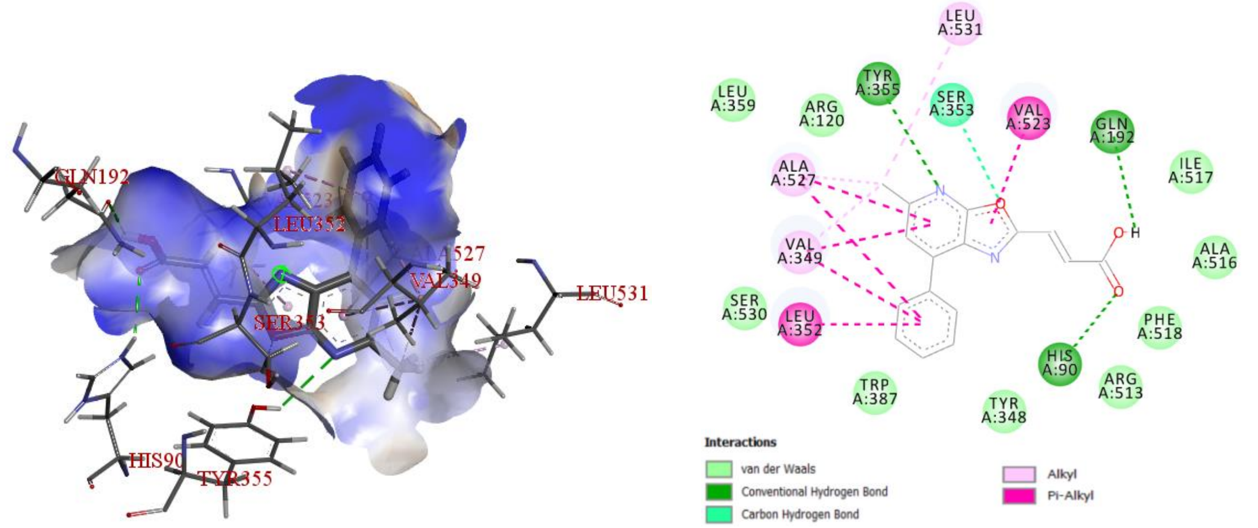

(*a*) 3D docking model; (*b*) 2D docking model

Figure 3. Complex of **12b** with cyclooxygenase-2 (COX-2)

It was found that compound **13b** has a docking score of –9.6 kcal/mol with cyclooxygenase-2 (COX-2) (PDB: 1CX2) due to the formation four π-Alkyl interactions observed between the phenyl and oxozolopyridine rings with amino acid residues LEU352, VAL349, ALA527, and VAL523, respectively. Additionally, there is one carbon-hydrogen bond interaction between the oxygen of the oxazole ring and the amino acid residue SER353. There are also two hydrogen bonds between the nitrogen atom of the pyridine ring and the amino acid TYR355, as well as between the oxygen atom of the carbonyl group and the amino acid residue HIS90. Compound **13b** also forms van der Waals interactions with residual amino acids LEU359, SER530, TRP387, TYR348, ARG513, PHE518, ALA516, ARG120 (Fig. 4).

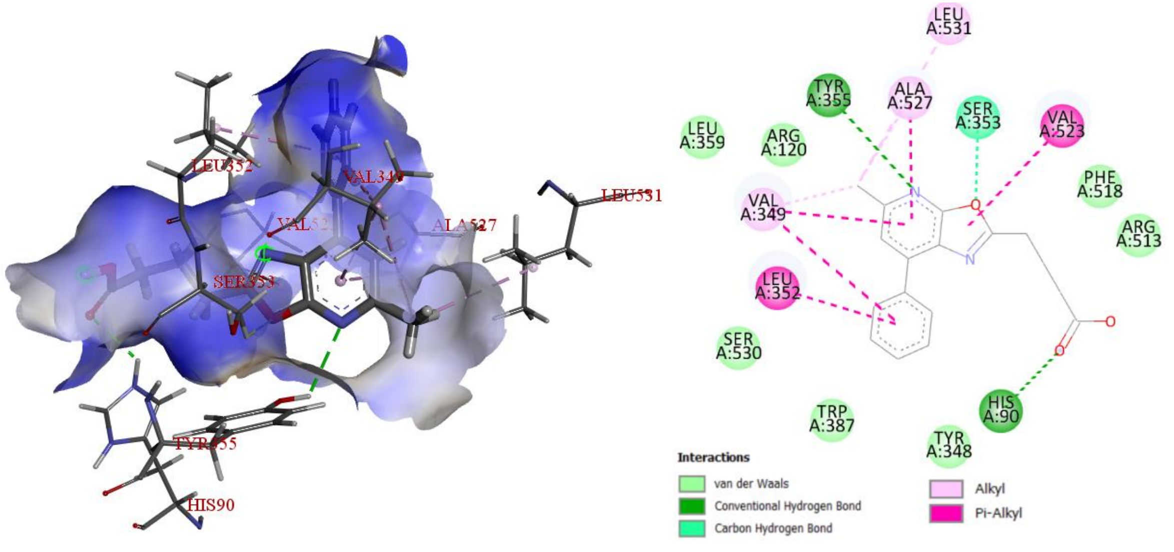

(*a*) 3D docking model; (*b*) 2D docking model

Figure 4. Complex of **13b** with cyclooxygenase-2 (COX-2)

In conclusion, compound **14b** has a binding affinity of -9.8 kcal/mol with cyclooxygenase-2 (COX-2) (PDB: 1CX2) due to the formation of a single carbon-hydrogen bond between the oxygen atom of the carbonyl group and the amino acid residue SER530. There are also eight π-alkyl interactions observed between the phenyl and oxozolopyridine rings with amino acid residues LEU351, VAL349, ALA527, LEU352, HIS90 and TYR355, respectively. Moreover, the benzoyl ring forms one π-π T-shaped and one amide-π stacked interaction with the amino acid residues TRP387 and GLY526, respectively. Compound **14b** also forms van der Waals interactions with the residual amino acids ARG513, SER 53, VOL 116, LEU359, MET522, LEU384, TYR385, PHE518, TYR348.

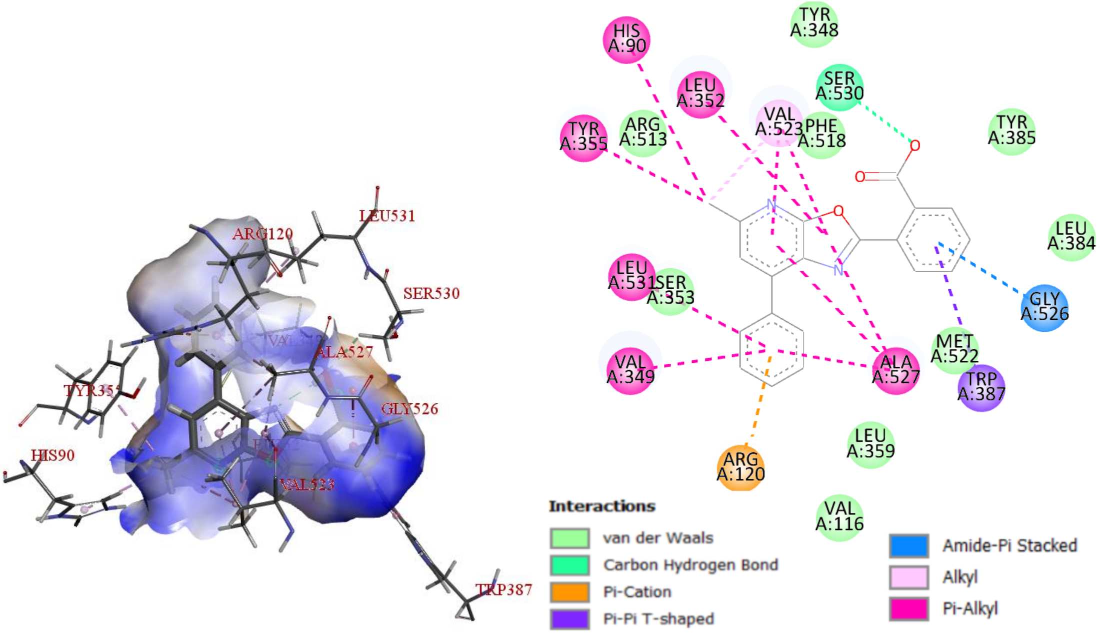

(*a*) 3D docking model; (*b*) 2D docking model

Figure 5. Complex of **14b** with cyclooxygenase-2 (COX-2)

It was found that the presence of a phenyl substituent at the 4th pyridone position in compounds **11–14b** increases their affinity to the selected receptors compared to other derivatives.

Thus, taking into account computer modeling, the newly synthesized oxazolo[5,4-b]pyridine derivatives based on 3-aminopyridin-2(1*H*)-ones are very promising for further study of their potential anti-inflammatory activity.

Conclusions

Consequently, our acylation reaction of 3-aminopyridones with dicarboxylic acid anhydrides showed that the monoamides formed at the first stage of the reaction undergo intramolecular cyclization to form oxazolo[5,4-b]pyridines **11–14a-c**. The presence of carboxylic acid linkers in structures **11–14a-c** not only increases water solubility of the compounds for further bioassays, but will also allow various modifications of the structure. In addition, the potential fluorescence of the condensed oxazolo[5,4-b]pyridine fragment [43] combined with the carboxylic acid linker will allow these derivatives to be used as possible biomarkers. The possible anti-inflammatory activity of the 12 newly obtained oxazolo[5,4-b]pyridine derivatives was evaluated using molecular docking with the AutoDock Vina program. Some compounds (**11–14b**) showed higher binding affinity to the target protein (1CX2) compared to well-known anti-inflammatory drug diclofenac. Molecular studies have revealed that the presence of a phenyl substituent at the 4th position of oxazolo[5,4-b]pyridine promotes a stronger interaction of compounds **11–14b** with the target protein. Therefore, the synthesized oxazolo[5,4-b]pyridines have high potential and prospects for further investigation their anti-inflammatory activity in vivo.

Funding

The study was supported by a grant from the Russian Science Foundation № 24-23-00472 "Development of methods for the preparation and practical application of new derivatives of bisoxazolo[5,4-b]pyridine with potential luminescent, complexing and catalytic activity", https://rscf.ru/en/project/24-23-00472/.

*Author Information**

**The authors' names are presented in the following order: First Name, Middle Name and Last Name*

Irina Valerievna Palamarchuk (*corresponding author*) — Assistant, School of Natural Sciences, University of Tyumen, 15a Perekopskaya St., 625003, Tyumen, Russia; e-mail: i.v.palamarchuk@utmn.ru; https://orcid.org/0000-0003-3376-6953

Ivan Vyacheslavovich Kulakov — Doctor of chemical sciences, Associated Professor, School of Natural Science, University of Tyumen, 15a Perekopskaya St., 625003, Tyumen, Russia; i.v.kulakov@utmn.ru; https://orcid.org/0000-0001-5772-2096

Author Contributions

The manuscript was written through contributions of all authors. All authors have given approval to the final version of the manuscript. CRediT: **Irina Valerievna Palamarchuk** investigation, formal analysis, data curation and writing — original draft preparation; **Ivan Vyacheslavovich Kulakov** conceptualization, methodology, validation, writing — review and editing and supervision.

Acknowledgments:

Spectrophotometric studies were carried out using the equipment of the Center for Collective Use “Rational Nature Management and Physicochemical Research” of University of Tyumen.

Conflicts of Interest

The authors declare no conflict of interest.

References

1 Bemis, J. E., Vu, C. B., Xie, R., Nunes, J. J., Ng, P. Y., Disch, J. S., Milne, J. C., Carney, D. P., Lynch, A. V., Jin, L., Smith, J. J., Lavu, S., Iffland, A., Jirousek, M. R. & Perni, R. B. (2009). Discovery of oxazolo[4,5-b]pyridines and related heterocyclic analogs as novel SIRT1 activators. *Bioorganic & Medicinal Chemistry Letters*, *19*(8), 2350–2353. https://doi.org/10.1016/j.bmcl.2008.11.106

2 Yeh, V. & Iyengar, R. (2008). Oxazoles. *Comprehensive Heterocyclic Chemistry III*, 4, 487–543. https://doi.org/10.1016/B978-008044992-0.00404-1

3 Yalçin I. & Şener E. (1993). QSARs of some novel antibacterial benzimidazoles, benzoxazoles, and oxazolopyridines against an enteric gram-negative rod; K. pneumoniae. *International journal of pharmaceutics*, *98*(1–3), 1–8. https://doi.org/10.1016/0378-5173(93)90034-D.

4 Park, H. R., Kim, J., Kim, T., Jo, S., Yeom, M., Moon, B., Choo, I. H., Lee, J., Lim, E. J., Park, K. D., Min, S. -J., Nam, G., Keum, G., Lee, C. J. & Choo, H. (2013). Oxazolopyridines and thiazolopyridines as monoamine oxidase B inhibitors for the treatment of Parkinson’s disease. *Bioorganic & medicinal chemistry, 21*(17), 5480–5487. https://doi.org/10.1016/j.bmc.2013.05.066

5 Viaud, M.-C., Jamoneau, P., Flouzat, Ch., Bizot-Espiard, J.-G., Pfeiffer, B., Renard, P., Caignard, D.-H., Adam, G., & Guillaumet, G. (1995). N-Substituted Oxazolo[5,4-b]pyridin-2(1H)-ones: A New Class of Non-Opiate Antinociceptive Agents. *J. Med. Chem*., *38*(8), 1278–1286. https://doi.org/10.1021/jm00008a006

6 Huang, Z., Zhang, Y., & Song, Y. WO Patent 2011085643.

7 Tekiner-Gulbas, B., Temiz-Arpaci, O., Yildiz, I., Aki-Sener, E., & Yalcin, I. (2006). 3D-QSAR study on heterocyclic topoisomerase II inhibitors using CoMSIA. *SAR QSAR Environ Res.*, *17*(2), 121–132. https://doi.org/10.1080/10659360600636105

8 Yildiz-Oren, I., Yalcin, I., Aki-Sener, E. & Ucarturk, N. Eur. J. Med. Chem. 2004, 39, 291. Yildiz-Oren, I., Yalcin, I., Aki-Sener, E., & Ucarturk, N. (2004). Synthesis and structure-activity relationships of new antimicrobial active multisubstituted benzazole derivatives. *Eur J Med Chem.*, *39*(3), 291–298. https://doi.org/10.1016/j.ejmech.2003.11.014

9 Yalçin, İ., Ören, İ., Şener, E., Akin, A., & Uçartürk, N. (1992). The synthesis and the structure-activity relationships of some substituted benzoxazoles, oxazolo (4,5-b) pyridines, benzothiazoles and benzimidazoles as antimicrobial agents. *European journal of medicinal chemistry*, *27*(4), 401–406. https://doi.org/10.1016/0223-5234(92)90154-S

10 Irlapati, N. R., Khedkar, N. R., Jape, R. B., Nandurdikar, R. Sh., Shaikh, Z. A. W., Sinha, N., Palle, V. P, & Kamboj, R. K. WO Patent 2014203217

11 Clark, R. L., Pessolano, A. A., Witzel, B., Lanza, T., & Shen, T. Y. (1978). 2-(Substituted phenyl)oxazolo[4,5-b]pyridines and 2-(Sybstituted phenyl)oxazolo[5,4-b]pyridines as Nonacidic Antiinflammatory Agents. *J. Med. Chem*., 1978, 21(11), 1158–1162. https://doi.org/10.1021/jm00209a014

12 Ferrins, L., Rahmani, R., Sykes, M. L., Jones, A. J., Avery, V. M., Teston, E., Almohaywi, B., Yin, J. X., Smith, J., Hyland, C., White, K. L., Ryan, E., Campbell, M., Charman, S. A., Kaiser, M., & Baell, J. B. (2013). 3-(Oxazolo[4,5-b]pyridin-2-yl)anilides

as a novel class of potent inhibitors for the kinetoplastid Trypanosoma brucei, the causative agent for human African trypanosomiasis. *European Journal of Medicinal Chemistry*, 2013, 66, 450–465. https://doi.org/10.1016/j.ejmech.2013.05.007

13 Tatipaka, H. B., Gillespie, J. R., Chatterjee, A. K., Norcross, N. R., Hulverson, M. A., Ranade, R. M., Nagendar, P., Creason, S. A., McQueen, J., Duster, N. A., Nagle, A., Supek, F., Molteni, V., Wenzler, T., Brun, R., Glynne, R., Buckner, F. S. & Gelb, M. H. (2014). Substituted 2-phenylimidazopyridines: a new class of drug leads for human African trypanosomiasis. *J. Med. Chem.*, *57*(3), 828–835. https://doi.org/10.1021/jm401178t

14 Xu, D., Xu, X., Liu, Z., Sun, L.-P., & You, Q. (2009). General and Efficient Synthesis of 2-Substituted Oxazolopyridines. *Synlett*, *7*, 1172–1174. https://doi.org/10.1055/s-0028-1088149

15 Doise, M., Dennin, F., Blondeau, D., & Sliwa, H. (1990). Synthesis of novel heterocycles: Oxazolo[4,5-b]pyridines and oxazolo[4,5-d]pyrimidines. *Tetrahedron Lett.*, *31*(8), 1155–1156. https://doi.org/10.1016/S0040-4039(00)88750-X

16 Doise, M., Blondeau, D., & Sliwa, H. (1992). Syntheses of Oxazolo [4,5-b]pyridines and [4,5-d]pyrimidines. *Synth. Commun.*, *22*(20), 2891–2901. https://doi.org/10.1080/00397919208021112

17 Myllymäki, M. J. & Koskinen, A. M. P. (2007). A rapid method for the preparation of 2-substituted oxazolo[4,5-b]pyridines using microwave-assisted direct condensation reactions. *Tetrahedron Lett.*, *48*(13), 2295–2298. https://doi.org/10.1016/j.tetlet.2007.01.161

18 Heuser, S., Keenan, M., & Weichert, A. G. (2005). New facile and mild synthesis of 2-substituted oxazolopyridines. *Tetrahedron Lett*., *46*(52), 9001–9005. https://doi.org/10.1016/j.tetlet.2005.10.109

19 Phoon, C. W., Ng, P. Y., Ting, A. E., Yeo, S. L., & Sima, M. M. (2001). *Bioorg. Med. Chem. Lett*., *11*(13), 1647–1650. https://doi.org/10.1016/S0960-894X(01)00263-3

20 Chu-Moyer, M. Y. & Berger, R. (1995). Preparation of the Four Regioisomeric 2-(Methylthio)oxazolopyridines: Useful Synthons for Elaboration to Amino substituted)oxazolopyridines. *J. Org. Chem*., *60*(17), 5721–5725. https://doi.org/10.1021/jo00122a073

21 Buckman; J. B. Nicholas; V. Serebryany, S. D. Seiwert. US Pat. Appl. 20110152246A1

22 Shatsauskas, A. L., Abramov, A. A., Saibulina, E. R., Palamarchuk, I. V., Kulakov, I. V., & Fisyuk, A. S. (2017). Synthesis of 3-amino-6-methyl-4-phenylpyridin-2(1*H*)-one and its derivatives. *Chem Heterocycl Comp.*, *53*, 186–191. https://doi.org/10.1007/s10593-017-2038-4

23 Palamarchuk, I. V. Matsukevich, M. V., Kulakov, I. V., Seilkhanov, T. M., & Fisyuk, A. S. (2019). Synthesis of N-substituted 2-aminomethyl-5-methyl-7-phenyloxazolo [5,4-b] pyridines. *Chemistry of Heterocyclic Compounds*, *55*(8), 788–791. https://doi.org/10.1007/s10593-019-02537-y

24 Shatsauskas, A. L., Zablotskii, Y. A., Chernenko, S. A., Zheleznova T. Yu., Shuvalov V. Yu., Kostyuchenko A. S., & Fisyuk A. S. (2021). Synthesis and photophysical properties of the products of the reaction of 5-methyl-7-phenyl[1,3]oxazolo[5,4-*b*]pyridin-2(1*H*)-one with amino acids. *Chem. Heterocycl. Comp.*, *57*, 1212–1219. https://doi.org/10.1007/s10593-021-03045-8

25 Kulakov, I. V., Palamarchuk, I. V., Shulgau, Z. T., Seilkhanov, T. M., Gatilov, Y. V., & Fisyuk, A. S. (2018). Synthesis, structure and biological activity 3-(arylmethyl) aminopyridine-2(1H)-ones and 1H-pyrido[2,3-b][1,4]oxazin-2(3H)-ones. *Journal of Molecular Structure*, 1166, 262–269. https://doi.org/10.1016/j.molstruc.2018.04.036

26 Palamarchuk, I. V.**,** Shulgau, Z. T., Kharitonova, M. A., & Kulakov, I. V. (2021). Synthesis and neurotropic activity of new 3-(arylmethyl)-aminopyridine-2(1H)-one. *Chemical papers*, *75*, 4729–4739. https://doi.org/10.1007/s11696-021-01696-7

27 Palamarchuk, I. V.**,** Shulgau, Z. T., Dautov, A. Y., Sergazy, S. D., & Kulakov, I. V. (2022). Design, synthesis, spectroscopic characterization, computational analysis, and in vitro α-amylase and α-glucosidase evaluation of 3-aminopyridin-2(1H)-one based novel monothiooxamides and 1,3,4-thiadiazoles. *Organic & Biomolecular Chemistry*, *20*, 8962–8976 https://doi.org/10.1039/D2OB01772E

28 Palamarchuk, I. V., Shulgau, Z. T., Sergazy, S. D., Zhulikeeva, A. M., Seilkhanov, T. M., & Kulakov, I. V. (2022). Synthesis, Molecular Docking, and Hemorheological Activity of New 4-(Thien-2-yl)-3-aminopyridine-2(1H)-one Derivatives. *Russ. J. Gen. Chem.*, *92*, 1692–1705. https://doi.org/10.1134/S1070363222090110

29 Sergazy, S., Shulgau, Z., Zhulikeyeva, A., Ramankulov, Y., Palamarchuk, I. V., & Kulakov, I. V. (2022). Cytoprotective Activity of Newly Synthesized 3-(Arylmethylamino)-6-Methyl-4-Phenylpyridin-2(1*H*)-Ones Derivatives. *Molecules*, *27*(17), 5362. https://doi.org/10.3390/molecules27175362

30 Kulakov, I. V., Matsukevich, M. V., Shulgau, Z. T., Sergazy, S., Seilkhanov, T. M., Puzari, A., & Fisyuk, A. S. (2015). Synthesis and antiradical activity of 4-aryl(hetaryl)-substituted 3-aminopyridin-2(1*H*)- ones. *Chem Heterocycl Comp.*, *51*, 991–996. https://doi.org/10.1007/s10593-016-1809-7

31 Palamarchuk I. V., Ogurtsova D. N., Seilkhanov T. M., & Kulakov I. V. (2019). Synthesis of N-derivatives of cytisine, anabasine, and salsoline alkaloids with pharmacophore 3-aminopyridine-2(1H)-one and 5-methyl-7-phenyloxazole[5,4-b]pyridine cycles. *Russian Journal of General Chemistry*, *89*(12), 2487–2491 https://doi.org/10.1134/S1070363219120259

32 Lengauer, T. & Rarey, M. (1996). Computational methods for bimolecular docking. *Curr. Opin. Struct. Biol.*, *6*, 402–406. https://doi.org/10.1016/S0959-440X(96)80061-3

33 Kitchen, D. B., Decornez, H., Furr, J. R., & Bajorath, J. (2004). Docking and scoring in virtual screening for drug discovery: methods and applications. *Nat. Rev. Drug. Discov*., *3*, 935–949. https://doi.org/10.1038/nrd1549

34 Trott, O. & Olson, A.J. (2010). AutoDock Vina: Improving the speed and accuracy of docking with a new scoring function, efficient optimization, and multithreading. *J. Comput. Chem.*, *31*, 455–461. https://doi.org/10.1002/jcc.21334

35 RCSB Protein Data Bank (RCSB PDB). Retrieved from https://www.rcsb.org/ (accessed on 25 Jan. 2024)

36 Morris, G. M., Huey, R., Lindstrom, W., Sanner, M. F., Belew, R. K., Goodsell, D. S., & Olson, A. J. (2009). Autodock4 and AutoDockTools4: Automated Docking with Selective Receptor Flexibility. *J. Comp. Chem.*, *16*, 2785–2791. https://doi.org/10.1002/jcc.21256

37 Discovery Studio 2015: Dassault Systemes BIOVIA, Discovery Studio Modelling Environment; Release 4.5; Dassault Systemes: San Diego, CA, USA, 2015.

38 Fraser, J. & Tittensor, E. (1957). Oxazolopyridines and oxazoloquinolines. Part II. Synthesis of 2′-hydroxyoxazolo(4′:5′-2:3)pyridine and related compounds. *J. Chem. Soc., 0*(0), 4625–4627. https://doi.org/10.1039/jr9570004625

39 Selinsky, B. S., Gupta, K., Sharkey, C. T., & Loll, P. J. (2001). Structural analysis of NSAID binding by prostaglandin H2 synthase: Time-dependent and time-independent inhibitors elicit identical enzyme conformations. *Biochemistry*, *40*(17), 5172-80. https://doi.org/10.1021/ bi010045s

40 Kurumbail, R. G., Stevens, A. M., Gierse, J. K., McDonald, J. J., Stegeman, R. A., Pak, J. Y., Gildehaus, D., Miyashiro, J. M., Penning, T. D., Seibert, K., Isakson, P. C., & Stallings, W. C. (1996). Structural basis for selective inhibition of cyclooxygenase-2 by anti-inflammatory agents. *Nature*, 384(6610), 644–648. https://doi.org/10.1038/384644a0

41 Watson, D. J., Harper, S. E., Zhao, P.-L., Quan, H., Bolognese, J. A., & Simon, T. J. (2000). Gastrointestinal tolerability of the selective cyclooxygenase-2 (COX-2) inhibitor rofecoxib compared with nonselective COX-1 and COX-2 inhibitors in osteoarthritis. *Archives of Internal Medicine*, *160*(19), 2998–3003. https://doi.org/10.1001/archinte.160.19.2998

42 Chhajed, S. S., Hiwanj, P. B., Bastikar, V. A., Upasani, C. D., Udavant, P. B., Dhake, A. S., & Mahajan, N. P. (2010). Structure based design and in-silico molecular docking analysis of some novel benzimidazoles. *International Journal of ChemTech Research*, *2*(2), 1135–1140.

43 Mac M., Baran W., Uchacz T., Baran B., Suder M., & Leśniewski S. (2007). Fluorescence properties of the derivatives of oxazolo[4,5-b]pyridyne, *Journal of Photochemistry and Photobiology A: Chemistry*, *192*, 188–196. https://doi.org/10.1016/j.jphotochem.2007.05.023.

How to Cite: Zhakina, A.Kh., Arnt, O.V., Vassilets, Ye.P., Alzhankyzy, A., & Zhakin, A.M. (2024) Synthesis, Characterization and Application of New Polymers Imprinted with Zinc (II) Ions. *Eurasian Journal of Chemistry, 29, 2(114), 45-53.* https://doi.org/10.31489/2959-0663/2-24-14

Article

Received: 21 February 2024 | Revised: 3 April 2024 |
Accepted: 12 April 2024 | Published online: 23 April 2024

UDC 544.42+519.242.7 https://doi.org/10.31489/2959-0663/2-24-14

Alma Kh. Zhakina*, Oxana V. Arnt, Yevgeniy P. Vassilets,
Arailym Alzhankyzy, Almat M. Zhakin

LLP "Institute of Organic Synthesis and Coal Chemistry of the Republic of Kazakhstan", Karaganda, Kazakhstan
*(*Corresponding author's e-mail: alzhakina@mail.ru)*

Synthesis, Characterization and Application of New Polymers Imprinted with Zinc (II) Ions

In this work, molecularly imprinted polymers with zinc imprints and their comparison polymers without imprints were synthesized. A comparative characterization of the physical parameters of the synthesized zinc-imprinted (ZnIP) and non-imprinted (NIP) polymers was carried out using the methods of elemental analysis, conductometry, scanning electron microscopy, and IR-Fourier spectroscopy. The ability of the resulting polymers to molecularly recognize zinc was evaluated. Based on experimental data on static adsorption, the adsorption capacity of ZnIP and NIP was determined using an atomic emission spectrometer. It was found that ZnIP is characterized by better physical parameters and a higher ability for molecular recognition of zinc compared to NIP. ZnIP with zinc imprints were found to have better sorption capacity for zinc than their reference polymers. The sorption of zinc by molecular imprinted ZnIP is mainly due to the complex formation and pores of the initial carbon product. The synthesized ZnIP have increased porosity. The presence of pores with a diameter <50 nm in ZnIP is associated with voids formed after acid hydrolysis, which is clearly visible in images recorded by scanning electron microscopy. Thus, the possibility of using ZnIP as a selective sorbent has been established.

Keywords: molecularly imprinted polymers, comparison polymer, sodium humate, polyvinyl alcohol, template, zinc, sorption, adsorbent.

Introduction

Currently, water pollution with heavy metals is constantly increasing and poses a great threat to the environment. Therefore, the analysis of environmental objects for the content of heavy metals and the development of appropriate detoxifiers are of great importance.

With the development of modern technologies, the interest of researchers in the problems of synthesis of molecularly imprinted polymers (MIP) in the field of molecular recognition is steadily growing. Due to the unique properties and the ability of MIP to molecular recognition, these polymers are finding new applications. To create new polymer materials with improved performance characteristics, it is possible to control the process of template formation during the formation of MIP and after its removal from the polymer matrix, the formation of a selective recognition cavity for the template of the molecule. Such polymers, which recognize target molecules with high selectivity, are relevant and are attracting increasing attention [1–10].

The use of molecularly imprinted polymers in the development of sorption materials is based on their ability to remove contaminants, including trace levels, in a highly selective manner, and the exceptional stability of polymer materials under harsh conditions makes it possible to simplify the process of water purification in general.

In recent years, researchers have made extensive use of the rapidly developing molecular imprinting technology to create new polymeric sorption materials [16–25]. The polymeric materials produced by molecular imprinting are widely and successfully used in industries such as chemical, pharmaceutical, biotechnological, and especially at the stages of purification of the final product [26–30].

As you know, zinc (Zn) is one of the most common heavy metals that is most often found in wastewater. Zinc compounds penetrate into natural water treatment from industrial wastewater. Dangerous forms of zinc in water are sulfates and chlorides, which belong to heavy metal salts. Both their excess and deficiency can cause damage to the systems of all living organisms [11–15]. Therefore, water purification from such a heavy metal as zinc is an important component of the water treatment system in production and industry.

Previously, molecular imprinted polymers have been synthesized and used for water purification from heavy metals [16, 20, 31, 32]. Continuing the research on the development of MIP, in this work zinc-imprinted polymers (ZnIP) and non-imprinted polymers (NIP) were synthesized based on the product of processing oxidized coal mining waste — humic acids (HA) and a functional monomer.

Humic acids are known to be a complex mixture of high-molecular and multifunctional compounds of aromatic, heterocyclic and alicyclic nature, replaced by alkyl chains of different lengths with limiting and unsaturated bonds. Humic acids are natural detoxifiers. The aromatic nuclei of humic acids contain a large number of carboxyl, hydroxyl, and quinoid groups, which allow them to participate in a variety of redox reactions. In this regard, it is of interest to create a MIP based on functionalized humic acids with zinc imprints using the molecular imprinting method for the selective isolation of zinc ions from an aqueous medium.

As an analogue of the structural fragments of sodium humate (HNa), we considered a functional monomer — polyvinyl alcohol (PVA), copolymerization with which should lead to enrichment of the imprinted polymer product with sites designed for molecular recognition of target zinc molecules.

The purpose of the study. On the basis of sodium humate, polyvinyl alcohol, to synthesize molecular imprinted polymers capable of molecular recognition of zinc and to conduct a comparative analysis of the textural properties of synthesized polymers.

Experimental

Materials

In this study the following materials were used: sodium humate (HNa), isolated from oxidized coal from the Shubarkol deposit (Karaganda, Kazakhstan); polyvinyl alcohol ($(C_2H_4O)_x$, $M = 1–15 \cdot 10^4$, produced by Sigma-Aldrich); template — zinc acetate ($(Zn(CH_3CO_2)_2 \cdot 2H_2O$, M=219.50 g/mol, produced by Sigma-Aldrich)); crosslinking monomer — formaldehyde (CH_2O, 37 % aqueous solution, produced by Sigma-Aldrich); initiator of free radical polymerization — benzoyl peroxide (BPO) ($C_{14}H_{10}O_4$, M=242.23 g/mol, produced by Sigma-Aldrich); solvent — distilled water.

Synthesis of Sodium humate (HNa)

Sodium humate was isolated from samples of oxidized coal from the Shubarkol deposit during alkaline impregnation caused by intercalation of sodium hydroxide into it. The alkaline impregnation method included the following stages: mixing dried coal with an aqueous alkali solution with a concentration providing a given NaOH/substrate mass ratio (1:10); heating (100 °C, 2 hours) with stirring and holding at room temperature; separation of the liquid phase from the residual coal. The residual coal was further treated with water, and the mixture was heated with stirring and the boiling point of a water bath for further 30 minutes. The first and second filtrates of sodium humate solutions were combined, poured into a crystallizer and dried at room temperature to a dry state. Dry sodium humate was weighed and the yield was determined. The yield of sodium humate is 76.00–82.00 % by weight of dry coal.

Synthesis of molecular imprinted polymers with Zn^{2+}

The synthesis of a molecular imprinted polymer with zinc was carried out according to a previously developed and modified method [20] as follows: a solution of $Zn(CH_3COO)_2$ was prepared, where the content of zinc ions introduced during tuning was 4.50 mg-eq. Then this solution was introduced into a solution of sodium humate. The mixture was kept for 3 hours with stirring until a stable prepolymerization complex was formed between the polymer molecules and the template. Next, a functional monomer (polyvinyl alcohol), a crosslinking agent (formaldehyde) and an initiator (benzoyl peroxide) were added to the prepolymerization complex. Benzoyl peroxide is an initiator of the oxidative process, which allows for the oxidative destruction of polyvinyl alcohol macromolecules with the formation of oligomers with an additional number of ketone, aldehyde and carboxyl groups. The oxidation process proceeds by a radical mechanism. Metals with variable valence contained in the mineral part of HNa act as catalysts for this process [33]. Next, the mixture was subjected to heat treatment at 70 °C for 180 minutes. At the end of the copolymerization process, the resulting product was centrifuged (Hermle Labortechnik GmbH, Wehingen, Germany) at a speed of 4000 rpm, washed with water to a neutral medium, dried, crushed and sieved. The template was removed from the polymer mesh by acid hydrolysis with 0.1 N HCl solution, heated to 50–60 °C and kept for 30 minutes. The resulting product was filtered and the precipitate was washed with water until the Cl^- ions disappeared. The comparison polymers (non-printed polymers) were synthesized using a similar technique without the participation of a template, all other participants in the polymerization reaction remained the same.

Investigation of the obtained results of zinc-imprinted and non-imprinted polymers

A complexometric analysis based on the titration of zinc ions with a solution of Trilon B in an acetate buffer with xylene orange as indicator, after binding of interfering elements with complexing agents, was used to determine the content of zinc ions in zinc-imprinted polymers (ZnIP). The content of zinc ions introduced during tuning was 4.50 mg-eq per gram of imprinted polymer.

The reaction in zinc-impregnated and non-imprinted (NIP) polymers was monitored by reverse titration, according to the content of oxygen-containing groups using the laboratory conductometer Anion-4100 (Infraspak-Analyte, Novosibirsk, Russia).

The number of carboxyl groups was determined by the acetate method. The measurements were carried out sequentially on three hitches, and the average value of the three experiments was taken as the final value.

The elemental analysis of ZnIP and NIP for the content of carbon, hydrogen, nitrogen and oxygen was carried out on an elemental analyzer (Elementar Unicube, Langenselbold, Germany).

The composition of the zinc-imprinted and non-imprinted polymers obtained was confirmed by IR spectroscopy data performed on the FSM-1201 IR Fourier spectrometer (Infraspec Company, St. Petersburg, Russia). The range of wave numbers was 4000-400 cm^{-1}, the error in the determination of the wave numbers did not exceed 2 cm^{-1}.

A MIRA 3 scanning electron microscope (Tescan Orsay Holding, Brno-Kohoutovice, Czech Republic) equipped with a system of detectors registering different signals was used to estimate the particle size and surface morphology of the obtained ZnIP and NIP. Images with topographic contrast were obtained using secondary electron detectors. The elemental composition on the ZnIP and NIP surfaces was determined by X-ray energy dispersive microanalysis.

The sorption properties of synthesized zinc-imprinted ZnIP and non-imprinted polymers (NIP) were studied using the method described in [16]. To do this, 1 g of composite samples were mixed with a solution of zinc salt. The mixture was stirred at 120 rpm in a thermostatically controlled rocking chair at 25 °C for 24 hours. The solutions were then centrifuged and filtered to determine the concentration of free zinc in them using an inductively coupled plasma atomic emission spectrometer ICAR6500 DUOLA (SPECTRO ARCOS EOP SPECTRO Analytical instruments GmbH, Germany).

Results and Discussion

Zinc-imprinted polymers (ZnIP) based on functionalized sodium humate capable of recognizing template molecules were obtained using the molecular imprinting method. Their composition and physicochemical properties have been studied. The scheme for the preparation of ZnIP is shown in Figure 1.

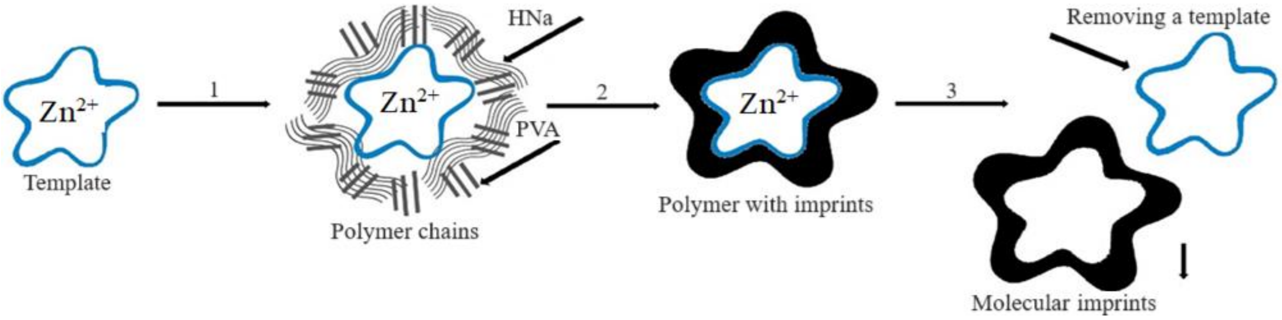

Figure 1. The scheme of obtaining a zinc-imprinted polymer

The results of the chemical studies of synthesized zinc-imprinted polymers are confirmed by data from elemental analysis, IR spectroscopy, complexometry, conductometry and electron microscope. The physicochemical characteristics of zinc-imprinted polymers (ZnIP) in comparison with non-imprinted polymers (NIP) are shown in Table.

As can be seen in Table, the oxygen content decreases by 4.54–6.41 % with the introduction of imprinted zinc polymers. This indicates the possibility of binding zinc ions by carboxyl and hydroxyl groups. A decrease in the content of oxygen-containing groups in zinc-imprinted polymers also makes it possible to assume their binding to zinc ions by the mechanism of complexation. Thus, in zinc-imprinted polymers, their content is 4.21–4.98 mg-eq/g, and in non-imprinted polymers — 4.82–5.75 mg-eq/g. The ZnIP yield is 78.42–80.69 %, and NIP yield is 77.26–79.84 %.

Table

Characteristics of imprinted polymers

№	Sample	Component Ratio (HNa:PVA)	C^g, %	H^g, %	O^g, %	Σ(COOH+OH) mg-eq/g	Yield, %
1	NIP_1	1:1	56.30±0.2	3.83±0.1	39.22±0.4	4.82±0.2	77.26
2	$ZnIP_1$		60.74±0.2	3.95±0.1	34.68±0.4	4.21±0.2	78.42
3	NIP_2	5:1	57.20±0.2	3.86±0.1	38.29±0.4	5.75±0.2	79.84
4	$ZnIP_2$		63.52±0.2	3.97±0.1	31.88±0.2	4.98±0.2	80.69

The IR spectra of non-imprinted and zinc-imprinted polymers are shown in Figure 2.

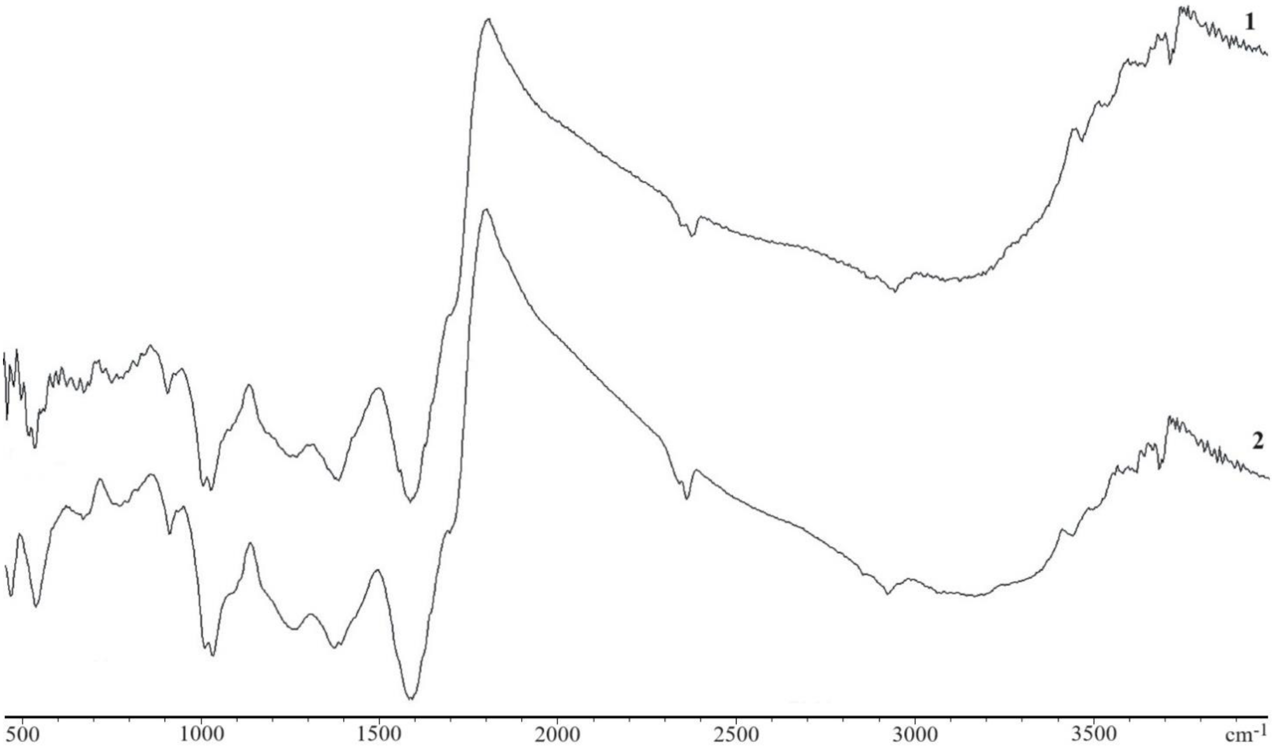

Figure 2. IR spectra: 1 –$ZnIP_1$, 2 — NIP_1

Analysis of the IR spectra of the zinc-imprinted polymers shows that the stretching peak characteristic of both the carboxylic groups at 1713 cm^{-1} and the hydroxyl groups at 3443 cm^{-1} suggest the possibility of zinc ions binding by the ion exchange and complexation mechanisms. There is a significant increase in absorption in the region of valence vibrations of methylene and methyl C–H at 2923 and 2857 cm^{-1}, as well as deformation of C–CH_3 groups at 1385 cm^{-1}. The observed facts can be explained by destructive processes leading to a reduction in the length of the aliphatic chain and an increase in the number of ring –CH_3 groups. The stretching peaks in the region of 1695–1713 cm^{-1} are attributed to the carboxyl and ketocarbonyl (C=O) groups, whereas peaks 1130–1190 cm^{-1} and 1150 cm^{-1} are associated with the stretching of C–O molecules of carbohydrates, alcohol and ether groups, respectively. An increase in the intensity of the band with a maximum at 915–933 cm^{-1} is associated with an increase in the content of substituted aromatic structures. The absence of absorption of the characteristic band of the COOH-group 1713 cm^{-1} and the appearance of new bands characteristic of the carboxylate grouping 1585 and 1385 cm^{-1} in zinc-imprinted polymers suggests that part of the zinc ions is bound by the carboxyl group to the chelate complex. The bond between Zn–O is in the range from 400 to 600 cm^{-1}. This means that peaks 467 and 485 cm^{-1} clearly represent Zn–O bonds. The evidence of the presence of coordination nodes with the participation of C–O on the surface and in the volume of composites is the absorption in the region of 600–800 cm^{-1}, which relate to the valence vibrations of carboxyls. The absence of absorption bands characterizing the valence oscillations of the Zn–O bond in the spectra of non-imprinted polymers indicates the decay of these bonds.

The textural characteristics of ZnIP and NIP with topographic contrast were obtained using a TESCAN MIRA 3 scanning electron microscope (Fig. 3-4). The elemental composition of the samples was determined by quartering in different areas of the sample surface using X-ray energy dispersive microanalysis X-Act (Oxford Instruments).

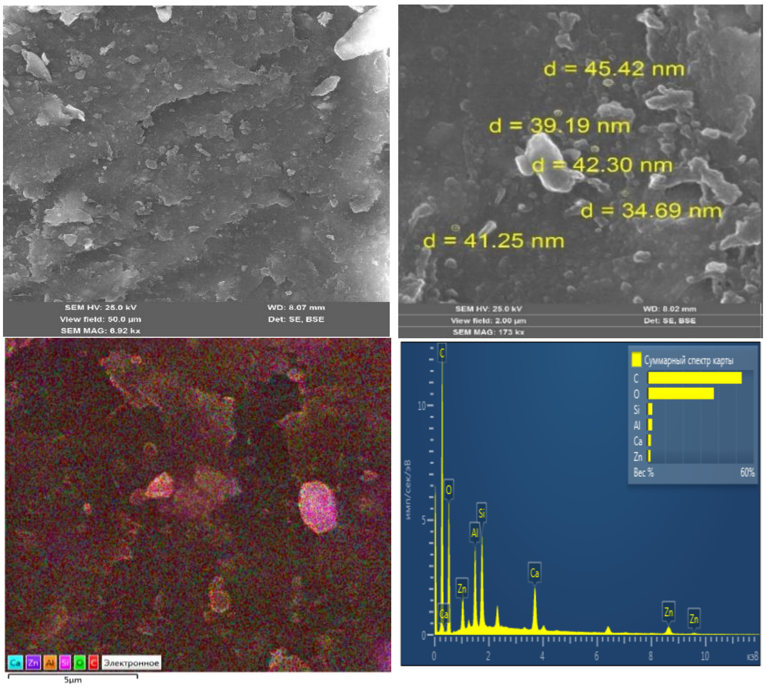

Figure 3. ZnIP$_1$ microstructure with elemental analysis

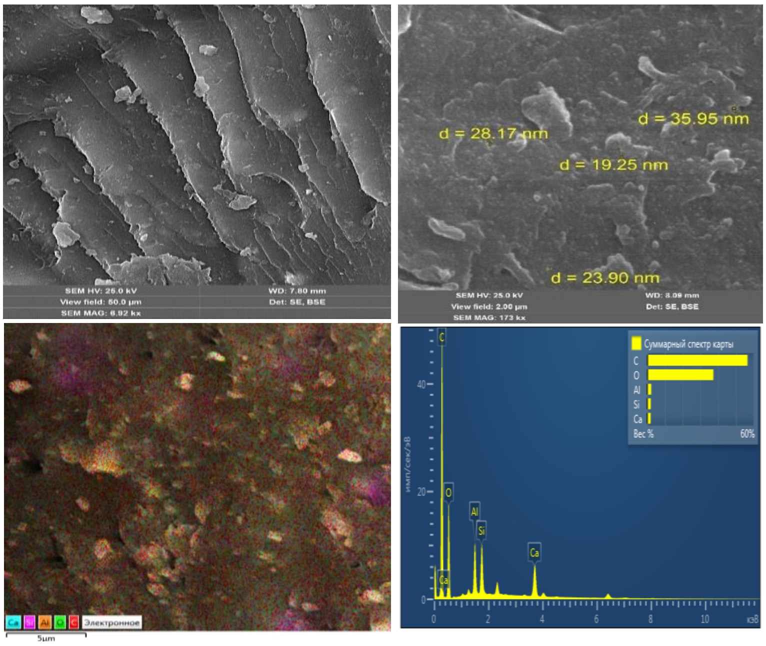

Figure 4. NIP$_1$ microstructure with elemental analysis

A comparative analysis of micrographs obtained of zinc-imprinted and non-imprinted polymers indicates a difference in their surface morphology and particle size. The ZnIP$_1$ electron micrographs (Fig. 3) show spherical and cubic formations and are characterized by increased porosity compared to NIP$_1$. It should be noted that removing the template from the polymer mesh uncorks additional pores, which is clearly visible in the images recorded by scanning electron microscopy (Fig. 3). The elemental composition and multilayer EDS-map confirm the composition of the products obtained, and the distribution of chemical elements on the microstructure confirms the presence of elements that make up both zinc-imprinted and non-imprinted polymers.

To study the binding capacity of the zinc-imprinted and non-imprinted obtained, experiments on static adsorption of zinc were carried out (Fig. 5).

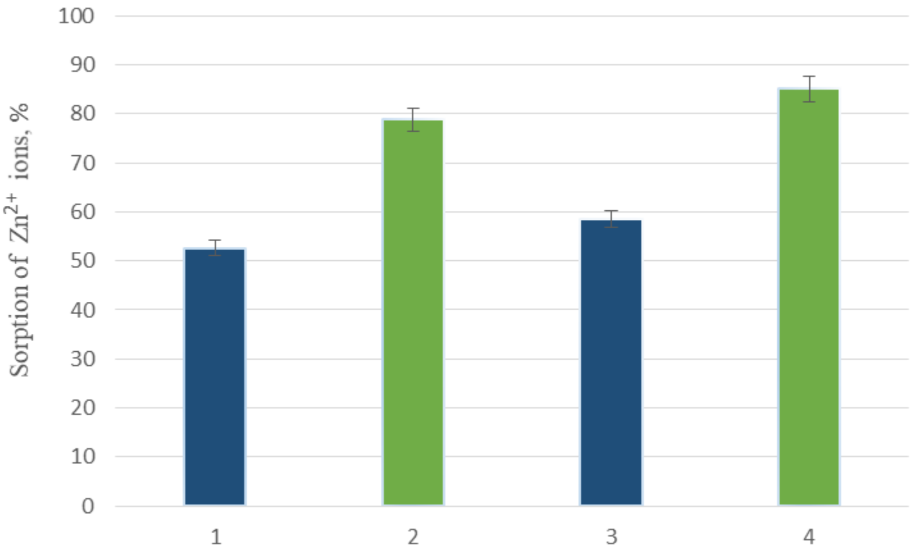

Figure 5. Results of sorption properties of synthesized polymers: 1 — NIP_2; 2 — $ZnIP_2$, 3 — NIP_1; 4 — $ZnIP_1$

A study of the adsorption properties of imprinted polymers pre-tuned to zinc ions showed a sharp increase in sorption capacity compared to non-imprinted polymers. The effect of improving sorption properties for Zn^{2+} is 78.90 % and 85.07 % for $ZnIP_2$ and $ZnIP_1$ samples, respectively. This confirms the assumption that there are pores in the system that corresponding to the ionic radius of the hydrolyzed metal and the effectiveness of the polymer selectively tuned to the sorbed ion.

Conclusions

Thus, two types of polymer sorbents were synthesized: zinc-imprinted polymers (ZnIP) and non-imprinted polymers (NIP). Synthesized zinc-imprinted and non-imprinted polymers were obtained with different ratios of sodium humate and polyvinyl alcohol. It was found that increasing the content of the functional polymer did not affect the yield of zinc-imprinted polymers. The decrease in oxygen-containing groups in the composition of the zinc-imprinted polymers indicates the possible binding of the template via the complexation mechanism. In this case, the sequential cross-linking of the prepolymerization complex with the functional monomer creates an imprinted sorption layer. An analysis of zinc-imprinted and non-imprinted polymers was carried out using modern physicochemical methods. The results of the evaluation the sorption properties of zinc-imprinted polymers and comparison polymers showed that imprinted polymers synthesized on the basis of sodium humate and polyvinyl alcohol at a ratio of 1:1 have the highest affinity for zinc. The obtained zinc-imprinted polymers using molecular imprinting technology can be recommended as sorption materials, the operating principle of which is based on the effect of molecular recognition and selective extraction.

Funding

This research is funded by the Science Committee of the Ministry of Science and Higher Education of the Republic of Kazakhstan (Grant No. AP19678338) “Fundamentals of creating molecularly imprinted polymers from coal waste”.

*Author Information**

**The authors' names are presented in the following order: First Name, Middle Name and Last Name*

Alma Khassenovna Zhakina (*corresponding author*) — Candidate of chemical sciences, Assoc. Professor, Head of the Laboratory of Polymer Chemistry of LLP "Institute of Organic Synthesis and Coal Chemistry of the Republic of Kazakhstan", Alikhanov str. 1, Karaganda, 100012, Kazakhstan; e-mail: alzhakina@mail.ru; https://orcid.org/0000-0001-5724-2279

Oxana Vasilievna Arnt — Master of technical sciences, Researcher of the Laboratory of Polymer Chemistry of LLP "Institute of Organic Synthesis and Coal Chemistry of the Republic of Kazakhstan", Alikhanov str. 1, Karaganda, 100012, Kazakhstan; e-mail: oxana230590@mail.ru; https://orcid.org/0000-0002-8996-4572

Yevgeniy Petrovich Vassilets — Master of pedagogical sciences, Researcher of the Laboratory of Polymer Chemistry of LLP "Institute of Organic Synthesis and Coal Chemistry of the Republic of Kazakhstan", Karaganda, Alikhanov str. 1, 100012, Kazakhstan; e-mail: vassilets88@mail.ru; https://orcid.org/0000-0003-2242-486X

Arailym Alzhankyzy — Master of chemical sciences, Junior Research of the Laboratory of Polymer Chemistry of LLP "Institute of Organic Synthesis and Coal Chemistry of the Republic of Kazakhstan", Alikhanov str. 1, Karaganda, 100012, Kazakhstan; e-mail: arailym_aljan@mail.ru; https://orcid.org/0000-0001-5790-8659

Almat Maulenuly Zhakin — Master of technical sciences, Junior Research of the Laboratory of Polymer Chemistry of LLP "Institute of Organic Synthesis and Coal Chemistry of the Republic of Kazakhstan", Alikhanov str. 1, Karaganda, 100012, Kazakhstan; e-mail: zhakin-almat@mail.ru; https://orcid.org/0000-0002-5940-7097

Author Contributions

The manuscript was written through contributions of all authors. All authors have given approval to the final version of the manuscript. CRediT: **Alma Khassenovna Zhakina** conceptualization, data curation, methodology, project administration, resources, software, writing — original draft, writing — review & editing; **Oxana Vasilievna Arnt** formal analysis, investigation, visualization; **Yevgeniy Petrovich Vassilets** formal analysis, investigation, visualization; **Arailym Alzhankyzy** formal analysis, investigation; **Almat Maulenuly Zhakin** formal analysis, investigation.

Conflicts of Interest

The authors declare no conflict of interest.

References

1 Jumadilov, T., Kondaurov, R., & Imangazy, A. (2022). Application of the Remote Interaction Effect and Molecular Imprinting in Sorption of Target Ions of Rare Earth Metals. *Polymers*, *14*(2), 321. https://doi.org/10.3390/polym14020321

2 Kadhem, A. J., Gentile, G. J., & Figalgo de Cortalezzi, M. M. (2021). Molecularly Imprinted Polymers (MIPs) in Sensors for Environmental and Biomedical Applications: A Review. *Molecules*, *26*(20), 6233–6267. https://doi.org/10.3390/molecules26206233

3 Sun, D., Song, Z., Zhang, Y., Wang, Y. Lv, M., Liu, H., Wang, L., Lu, W., Li, J., & Chen, L. (2021). Recent Advances in Molecular-Imprinting-Based SolidPhase Extraction of Antibiotics Residues Coupled With Chromatographic Analysis. *Front. Environ. Chem*, 2:703961. https://doi.org/10.3389/fenvc.2021.703961

4 Arabi, M., Ostovan, A., Li, J., Wang, X., Zhang, Z., Choo, J., & Chen, L. (2021). Molecular Imprinting: Green Perspectives and Strategies. *Adv. Mater*, 2100543. https://doi.org/10.1002/adma.202100543

5 Azizi, A., Shahhoseini, F. & Bottaro, C. S. (2020). Magnetic Molecularly Imprinted Polymers Prepared by Reversible Addition Fragmentation Chain Transfer Polymerization for Dispersive Solid Phase Extraction of Polycyclic Aromatic Hydrocarbons in Water. *J. Chromatogr. A.*, *1610*, 460534. https://doi.org/10.1016/j.chroma.2019.460534

6 Cavalera, S., Anfossi, L., Di Nardo, F., & Baggiani, C. (2024). Mycotoxins-Imprinted Polymers: A State-of-the Art Review. *Toxins*, *16*(47). https://doi.org/10.3390/toxins16010047

7 Saylan, Y., Kılıç, S. & Denizli, A. (2024). Biosensing Applications of Molecularly Imprinted-Polymer-Based Nanomaterials. *Processes*, *12*, 177. https://doi.org/10.3390/pr12010177

8 Zhang, L., Mo, H., Wang, C., Li, X., Jiang, S., Fan, W., & Zhang, Y. (2023). Synthesis and Properties of Cefixime Core-Shell Magnetic Nano-Molecularly Imprinted Materials. *Polymers, 15*, 4464. https://doi.org/10.3390/polym15224464

9 Fang, L., Miao, Y., Wei, D., Zang, Y., & Zhou, Y. (2021). Efficient removal of norfloxacin in water using magnetic molecularly imprinted polymer. *Chemosphere, 262*, 128032. https://doi.org/10.1016/j.chemosphere.2020.128032

10 Khalili, Z. & Nezhadali, A. (2024). A novel molecularly rabeprazole imprinted electrochemical sensor based on $Fe_3O_4@SiO_2$–MWNTs nanocomposite. *Microchemical Journal, 199,* 109926. https://doi.org/10.1016/j.microc.2024.109926

11 Hassan, M. U., Nawaz, M., Mahmood, A., Shah, A. A., Shah, A. N., Muhammad, F., Batool, M., Rasheed, A., Jaremko, M., Abdelsalam, N. R., Hasan, M. E., & Qari, S. H. (2022).The role of zinc to mitigate heavy metals toxicity in crops. *Frontiers in Environmental Science, 10.* https://doi.org/10.3389/fenvs.2022.990223

12 Alsafran, M., Saleem, M. H., & Rizwan, M. (2023). An overview of heavy metals toxicity in plants, tolerance mechanism, and alleviation through lysine-chelation with micro-nutrients — A novel approach. *Plant Growth Regul, 100,* 337–354 https://doi.org/10.1007/s10725-022-00940-8

13 Briffa, J., Sinagra, E., & Blundell, R. (2020). Heavy metal pollution in the environment and their toxicological effects on humans. *Heliyon, 6*(9), 1–26. https://doi.org/10.1016/j.heliyon.2020.e04691

14 Alengebawy, A., Abdelkhalek, S. T., Qureshi, S. R., & Man-Qun Wang (2021). Heavy Metals and Pesticides Toxicity in Agricultural Soil and Plants: Ecological Risks and Human Health Implications. *Toxics, 9*(3), 42. https://doi.org/10.3390/toxics9030042

15 Su, S., Huang, Y., Han, G., Guo, Z., & Liu, F. (2019). Study of the Adsorption of Humic Acid with Zn^{2+} by Molecular Dynamic Simulation and Adsorption Experiments. *Characterization of Minerals, Metals, and Materials,* 33–41. https://doi.org/10.1007/978-3-030-05749-7_4

16 Zhakina, A. Kh., Rakhimova, B. B., Vassilets, Ye. P., Arnt, O. V., & Muldakhmetov Z. (2024). Synthesis and Modification of a Natural Polymer with the Participation of Metal Nanoparticles, Study of Their Composition and Properties. *Polymers, 16*(2), 264. https://doi.org/10.3390/polym16020264

17 Kondaurov, R., Melnikov, Y., & Agibayeva L. (2023). Application of Molecular Imprinting for Creation of Highly Selective Sorbents for Extraction and Separation of Rare-Earth Elements. *Polymers, 15*, 846. https://doi.org/10.3390/polym15040846

18 Zhakina, A. Kh., Muldakhmetov, Z., Zhivotova, T. S., Rakhimova, B. B., Vassilets, Ye. P., Arnt, O. V., Alzhankyzy, A., & Zhakin, A. M. (2023). Synthesis of a Polymer Composite Based on a Modified Aminohumic Acid Tuned to a Sorbed Copper Ion. *Polymers, 15*(6), 1346. https://doi.org/10.3390/polym15061346

19 Zhakina, A. Kh., Arnt, O. V., Vassilets, Ye. P., Shur, V. Ya., & Volegov, A. S. (2020). Magnetoactive Compounds Based on Humic Acid and Magnetite as a Sorbent for Heavy Metals. *Russian Journal of Applied Chemistry, 93*(9), 1152–1159. https://doi.org/10.1134/S1070427220090086

20 Muldakhmetov, Z. M., Gazaliev, A. M., Zhakina, A. Kh., Vassilets, Ye. P., & Arnt, O. V. (2022). Synthesis of a composite based on humic acid tuned to sorbed copper ion. *Bulletin of the University of Karaganda. Chemistry, 4*(108), 182–189. https://doi.org/10.31489/2022Ch4/4-22-14.

21 Ferreira, V. R. A., Azenha, M. A., Pereira, C. M., & Silva, A. F. (2022). Molecularly Imprinted Methyl-Modified Hollow TiO_2 Microspheres. *Molecules, 27,* 8510. https://doi.org/10.3390/molecules27238510

22 Cavalera, S., Anfossi, L., Nardo, F., & Baggiani, C. (2024). MycotoxinsImprinted Polymers: A State-of-theArt Review. *Toxins, 16,* 47. https://doi.org/10.3390/toxins16010047

23 Seitz, W. R., Grenier, C. J., Csoros, J. R., Yang, R., & Ren, T. (2021). Molecular Recognition: Perspective and a New Approach. *Sensors,* 21, 2757. https://doi.org/10.3390/s21082757

24 Reville, E. K., Sylvester, E. H., Benware, S. J., Negic, S. S., & Berda, E. B. (2022). Customizable molecular recognition: advancements in design, synthesis, and application of molecularly imprinted polymers. *Polymer Chemistry, 13,* 3387–3411. http://dx.doi.org/10.1039/d1py01472b

25 Haller, P., Machado, I., Torres, J., Vila, A., & Veiga, N. (2021). Fe (III)-Complex-Imprinted Polymers for the Green Oxidative Degradation of the Methyl Orange Dye Pollutant. *Polymers, 13,* 3127. https://doi.org/10.3390/polym13183127

26 Agriopoulou, S., Stamatelopoulou, E., & Varzakas, T. (2020). Advances in Analysis and Detection of Major Mycotoxins in Foods. *Foods, 9*(4), 518. https://doi.org/10.3390/foods9040518

27 Yang, Y., Li, G., Wu, D., Liu, J., Li, X., Luo, P., Hu, N., Wang, H., & Wu, Y. (2020). Recent advances on toxicity and determination methods of mycotoxins in foodstuffs. *Trends in Food Science & Technology, 96,* 233–252. https://doi.org/10.1016/j.tifs.2019.12.021

28 Lamaoui, A., Mani, V., Durmus, C., Salama, K. N., & Amine A. (2024). Molecularly imprinted polymers: A closer look at the template removal and analyte binding. *Biosensors and Bioelectronics, 243,* 115774. https://doi.org/10.1016/j.bios.2023.115774

29 Ma, Q., Wei, Y., Zhao, N., Wang, S., Zhang, B., Liu, D., & Yuan, P. (2023). Construction of an allophane-based molecularly imprinted polymer for the efficient removal of antibiotic from aqueous solution. *Science of The Total Environment, 903,* 166464. https://doi.org/10.1016/j.scitotenv.2023.166464

30 Pérez-Cejuela, H. M., Herrero-Martínez, J. M., & Simó-Alfonso, E. F. (2020). Recent Advances in Affinity MOF-Based Sorbents with Sample Preparation Purposes. *Molecules, 25,* 4216. https://doi.org/10.3390/molecules25184216

31 Zhakina, A. Kh., Arnt, O. V., Vassilets, Ye. P., Zhivotova, T. S., Muldahmetov, Z. M., Gazaliev, A. M., & Semenova, S. A. (2020). Synthesis and Properties of a Composite Material Based on Coal Mining Waste. *News of the National Academy of Sciences of the Republic of Kazakhstan. Series of Chemistry and Technology, 2* (440), 6–13. https://doi.org/10.32014/2020.2518-1491.17

32 Zhakina, A. Kh. & Arnt, O. V. (2023). Molecular Imprinted Polymers From Coal Waste. *Current questions of modern science. Proceedings of the X International Scientific and Practical Conference* (pp. 12–14). Tallinn, Estonia.. https://conference-w.com/wp-content/uploads/2024/01/EST.T-2829122023.pdf

33 Zimin, Yu. S., Ageeva, A. F., Shamsetdinova, I. F., Borisov, I. M., & Monakov, Yu. B. (2006). Kinetics and mechanism of oxidation of polyvinyl alcohol under the influence of hydrogen peroxide. *Bashkir Chem. J.*, *13,* 1, 118–122

How to Cite: Kwiatkowski, A.L., Molchanov, V.S., Orekhov, A.S., Kuklin, A.I., & Philippova, O.E. (2024) Detecting Shape of Hybrid Polymer/Surfactant Micelles: Cryo-Transmission Electron Microscopy, Small-Angle Neutron Scattering and Dynamic Light Scattering Study. *Eurasian Journal of Chemistry, 29, 2(114), 54-60.* https://doi.org/10.31489/2959-0663/2-24-13

Article

Received: 22 January 2024 | Revised: 27 March 2024 |
Accepted: 9 April 2024 | Published online: 24 April 2024

UDC 544.42+519.242.7

https://doi.org/10.31489/2959-0663/2-24-13

Alexander L. Kwiatkowski[1*], Vyacheslav S. Molchanov[1], Anton S. Orekhov[2],
Alexander I. Kuklin[3], Olga E. Philippova[1]

[1]Physics Department, Lomonosov Moscow State University, Moscow, Russia;
[2]National Research Center, Kurchatov Institute, Moscow, Russia;
[3]Joint Institute for Nuclear Research, Dubna, Russia
*(*Corresponding author's e-mail: kvyatkovskij@physics.msu.ru)*

Detecting Shape of Hybrid Polymer/Surfactant Micelles: Cryo-Transmission Electron Microscopy, Small-Angle Neutron Scattering and Dynamic Light Scattering Study

In-depth study of shape of hybrid micelles in the micellar solutions of anionic surfactant potassium oleate, containing hydrophobic polymer poly(4-vinylpyridine) (P4VP) was conducted via cryo-transmission electron microscopy (cryo-TEM), small-angle neutron scattering (SANS) and dynamic-light scattering of visible light (DLS). Direct visualization of the solutions with cryo-TEM evidenced the coexistence of polymer-free spherical micelles and branched rodlike hybrid micelles with mean length of 200 nm and radius of 2 nm, governed by contour length of solubilized P4VP and length of hydrophobic "tail" of potassium oleate, respectively. The formation of branches in the hybrid micelles was explained by attaching the thermodynamically unfavorable end-caps of micelles to their polymer-loaded cylindrical fragments. By SANS it was shown that the cylindrical local shape and the radius of the micelles are independent of the concentration of embedded P4VP. Relaxation processes in the solutions were investigated with DLS. Three relaxation modes were observed for hybrid micelles, similar to polymer-free wormlike micelles. Fast and medium relaxation modes were attributed to diffusion of entangled micellar chains and their segments, respectively. The slow mode was related to electrostatic repulsion between similarly charged hybrid micelles.

Keywords: ionic surfactant, polymer-surfactant interactions, rodlike micelles, hybrid micelles, branching points, cryo-TEM, SANS, DLS.

Introduction

Self-organization of surfactants into the micelles of different shapes is of extensive attention of scientists during the last three decades [1–4]. Hydrophobic attraction of "tails" and electrostatic repulsion of charged hydrophilic "heads" of ionic surfactants define the shape of the resulting aggregate [2, 5]. Wormlike micelles (WLMs) are aggregates of cylindric form that consist of two hemispheric end-caps and central cylindrical part [3, 6–8]. Examples of practical applications of semi-dilute solutions of WLMs include their use as foaming agents [9], thickeners for fracturing fluids and cosmetic products [3, 7], drag-reducers [10–11] and drug delivery systems [12, 13].

Incorporation of a polymer into the WLMs of a surfactant results in the formation of hybrid micelles [14–20] that possess the unique properties of both components. For example, recently obtained hybrid micelles of anionic surfactant potassium oleate with embedded hydrophobic polymer poly(4-vinylpyridine) (P4VP) demonstrated both high response to hydrocarbon inherent to surfactant-based fracturing fluid and enhanced drag reducing efficiency inherent to polymer chains [21]. Thus, semi-dilute solution of the hybrid micelles could potentially be used not only as a fracturing fluid in oil production, but also as a drag-reducer for oil transportation.

In the previous papers [20–22], solutions of the hybrid micelles, saturated with P4VP, were investigated. Since the incorporated polymer influences the hydrophilic-hydrophobic balance of the micelles [20], the concentration of solubilized P4VP is the key parameter that governs their shape. The current paper is devoted to the detailed experimental study of the shape of the hybrid micelles, containing different amount of P4VP. Cryo-transmission electron microscopy (cryo-TEM) was used to directly image the micelles, while contrast matching technique in small-angle neutron scattering (SANS) was employed to investigate their local shape. Additionally, dynamic light scattering of visible light (DLS) provided information about relaxation processes in their aqueous solutions.

Experimental

Materials. Anionic surfactant potassium oleate (purity >98 %) from TCI Europe, inorganic salt KCl (purity > 99.5 %) from Fluka, ethanol (purity > 99 %) from Merck, KOH (purity > 99 %) from Acros Organics, and polymer P4VP (molar mass 60000 g/mol, contour length 140 nm) from Sigma-Aldrich were used as received. Water was purified using a Millipore Milli-Q system. For SANS experiments, mixture of water and deuterium oxide (purity 99.9 %, Sigma-Aldrich) was used as a solvent.

Sample preparation. Stock solutions of polymer-free WLMs were obtained by mixing 47 mM potassium oleate and 80 mM KCl with Milli-Q water and stirred with a magnetic stirrer for 24 hours. The pH of the solutions was kept at 11 with aqueous solution of 1 M KOH. Under these conditions the WLMs were formed in the samples [22].

Hybrid micelles were prepared by pouring the micellar stock solution on the thin polymer film. The film was prepared by full evaporation of ethanol from the drop of 5 wt.% P4VP solution in ethanol on the bottom of vial at room temperature. P4VP embedded into the micelles after stirring the stock solution of polymer-free micelles in the vial with polymer film using magnetic stirrer for 1 day. Content of P4VP in the final solutions was varied from 0.01 to 0.04 monomol/L (amount of monomer units per 1 L of solution).

Cryogenic transmission electron microscopy (cryo-TEM). Cryo-TEM experiments were performed using a Titan Krios (Thermo Fisher Scientific, Hillsboro, OR, USA) at acceleration voltage of 300 kV in bright-field TEM in a low-dose imaging mode. The microscope was equipped with a Falcon 2 direct electron detector (Thermo Fisher Scientific, Hillsboro, OR, USA). To receive the clear images of the aggregates, the stock solution of 47 mM potassium oleate and 0.02 monomol/L P4VP was diluted 4 times with aqueous solution containing 80 mM KCl. The samples were applied onto the Lacey carbon-coated side of the 300 mesh copper TEM grid with Vitrobot Mark 4 (Thermo Fisher Scientific, Hillsboro, OR, USA) [23]. After blotting the excess of the solution with filter paper the grid was plunged into liquid ethane. The images were processed with EPU 3.6 software.

Small-angle neutron scattering (SANS). SANS measurements were carried out using time-of-flight spectrometer YuMO of high-flux pulsed reactor IBR-2M (Joint Institute for Nuclear Research, Dubna, Russia). Details of the experiments and data treatment are described elsewhere [24]. The values of scattering length densities for potassium oleate, monomer unit of P4VP and deuterium oxide, calculated with SasView-5.0 program (http://www.sasview.org/), equaled to $\rho_{OK} = 0.15 \cdot 10^{-6}$ Å^{-2}, $\rho_{P4VP} = 2.00 \cdot 10^{-6}$ Å^{-2} and $\rho_{D2O} = 6.38 \cdot 10^{-6}$ Å^{-2}, respectively. To obtain scattering from potassium oleate molecules in the hybrid micelles, the contrast variation technique was applied. The mixture of deuterium oxide and water with volume ratio D_2O/H_2O=37/73 (v/v) was used as a solvent in the experiments to match the scattering from P4VP. The samples were put into the Hellma quartz cuvettes of 1 mm width. Temperature was kept at 20 °C. Data was obtained in the scattering vectors Q range from $6 \cdot 10^{-3}$ to $6 \cdot 10^{-1}$Å^{-1}.

Dynamic-light scattering of visible light (DLS). DLS data were collected with ALV/DLS/SLS-5022F (ALV GmbH, Langen, Germany). Scattering intensity was analyzed with ALV6010/EPP digital correlator. Variation of scattering angle was made by stepping-motor-driven goniometer system. Helium−neon laser (wavelength of 632.8 nm) was used as a light source. The temperature of the samples was kept at 20 °C by a thermostat Lauda Ecoline RE 306. The samples were filtered through 0.45 μm filter (Millipore Millex-FG) to prevent the intrusion of dust. Contin method was applied for data treatment [25].

Results and Discussion

The solutions of potassium oleate with embedded P4VP macromolecules were visualized by cryo-TEM (Fig. 1). In Figure 1 coexisting spherical and rodlike aggregates with mean length of 200 nm can be observed. The mean radii of cross section spherical and rodlike aggregates are circa equal to 2 nm and coincide with the length of the alkyl “tail” of potassium oleate [22]. Consequently, the observed spherical aggregates are, probably, polymer-free micelles of potassium oleate. The estimated mean length of the rodlike micelles (Fig. 1) is close to the contour length of P4VP. One can also easily detect many “Y-shaped” branching points in the rodlike micelles (Fig. 1). Note that zero-shear viscosity of the polymer-free micellar solution, containing similar amount of potassium oleate and KCl, as was demonstrated by steady shear rheological tests [22], was close to that of pure water. Consequently, spherical micelles or short rodlike micelles that do not contribute to the viscosity of the solution are present at these conditions. Detecting rather long rodlike micelles in the P4VP-containing solution is suggested to be the result of the solubilization of polymer chains by the micelles. Furthermore, branches in the micellar solutions at such low concentration of surfactant have never been observed before. As was shown by computer modelling, solubilization of P4VP induced the formation of additional branching points in the hybrid micelles by attaching the energetically unfavorable end-caps to the polymer-loaded cylindrical fragments [26, 27].

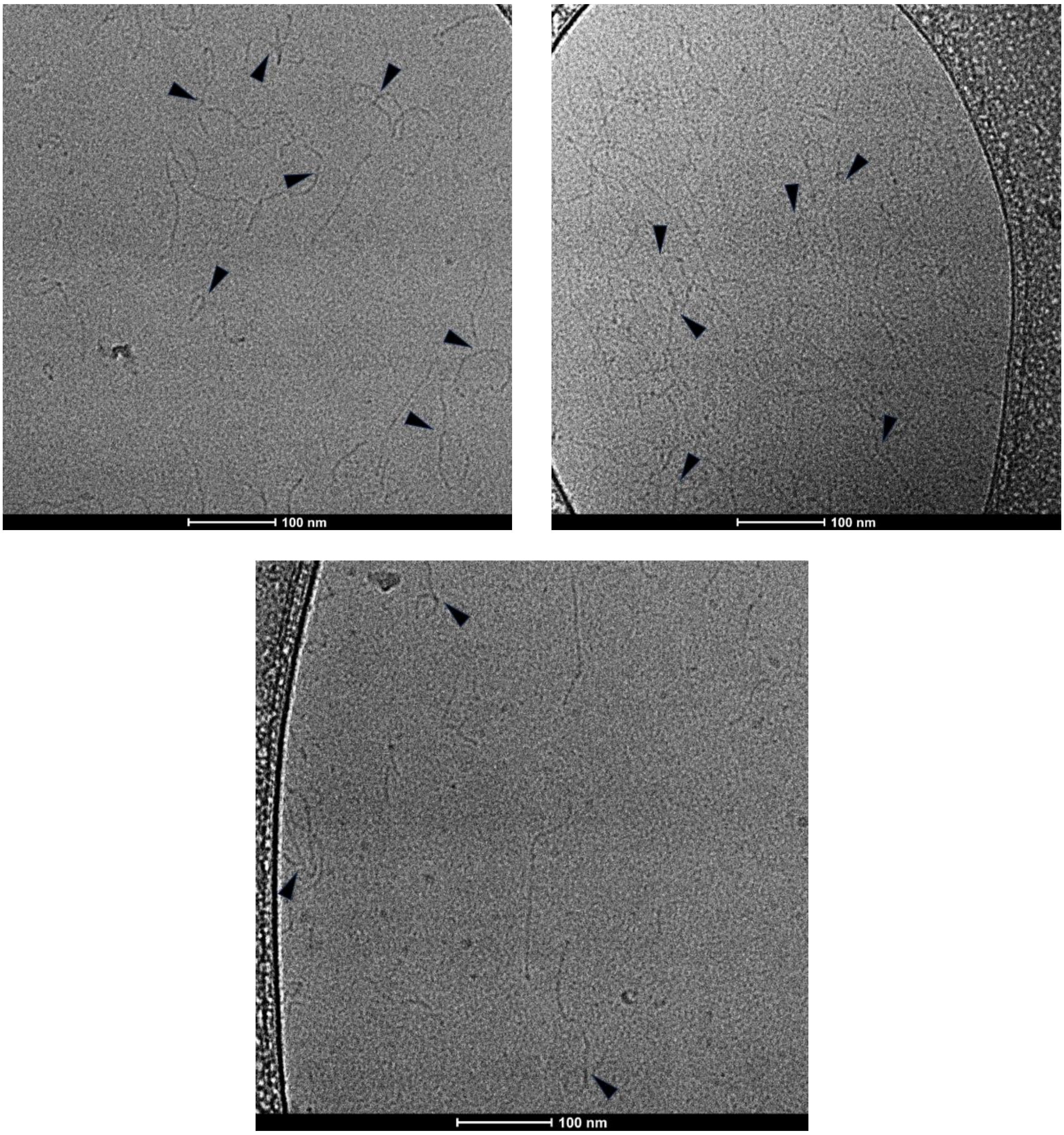

Figure 1. Spherical polymer-free micelles and prolate hybrid micelles in aqueous solution of 12.5 mM potassium oleate and 80 mM KCl, containing $2 \cdot 10^{-3}$ monomol/L P4VP, as imaged with cryo-TEM. The arrows point out the branching points in the hybrid micelles

The shape of hybrid micelles with different amount of embedded P4VP was revealed by SANS using contrast variation technique. In Figure 2a the neutron scattering intensity in the range of the small values of scattering vector Q behaves as: $I \sim Q^{-1}$. The scattering intensity $I(Q)$ from the rodlike particles can be expressed as [28]:

$$I(Q) = \Delta\rho^2 V_0 Q^{-1} \exp\left(-\frac{R^2Q^2}{2}\right), \tag{1}$$

where $\Delta\rho = \rho_{OK} - \rho_{solvent}$ is the scattering contrast, equal to the difference between the scattering density of potassium oleate and of the solvent, V_0 and R are the volume and radius of the rods. Consequently, in the case of rodlike scatterers, ln(IQ) vs Q^2 dependence should represent a straight line with the slope $a = -0.5 \cdot R^2$. Therefore, Q^{-1}-scaling in low-Q region of the scattering curves (Fig. 2a) indicates the local cylindric shape of the hybrid micelles at all studied concentrations of P4VP. The linear behavior of the corresponding ln(IQ) vs Q^2 dependencies confirms this observation (Fig. 2b). Mean radius of the hybrid micelles, estimated from the slopes of the dependencies, circa equals to 2 nm for all studied solutions and corresponds to one, evaluated from cryo-TEM image (Fig. 1).

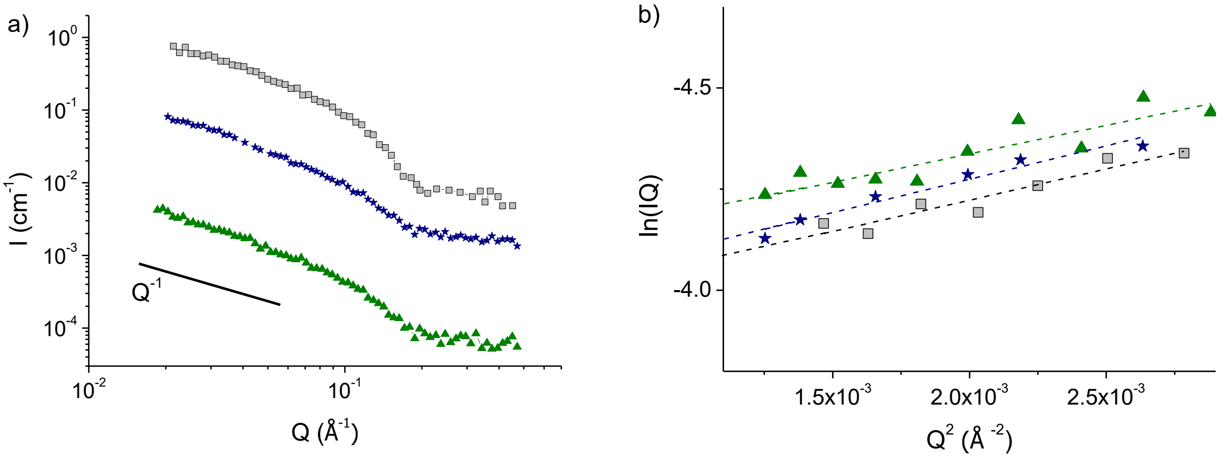

Figure 2. SANS curves in $I(Q)$ (a) and $ln(IQ)$ vs Q^2 (b) representations for micellar solutions of 47 mM potassium oleate with different concentrations of embedded P4VP: 0.01 monomol/L (squares); 0.02 monomol/L (stars); 0.03 monomol/L (triangles). Matching the scattering from P4VP is used (solvent: 80 mM KCl in D_2O/H_2O=37/73 (v/v), pH=11). The data for solutions with 0.01 monomol/L P4VP are actual values, data for solutions containing 0.02 monomol/L and 0.03 monomol/L are shifted by a factor of 10 and 100 for clarity. The solid line shows the slope of the $I \sim Q^{-1}$ dependence. The dashed lines are linear fits of the dependences

The relaxation processes in aqueous solutions of hybrid micelles were studied by DLS. The autocorrelation functions $g^{(1)}(q, t)$ of the scattered visible light by hybrid micelles with different amount of embedded P4VP decay multi-exponentially (Fig. 3a). Thus, in the corresponding decay time distributions $A(t)$ three relaxation modes with relaxation rates Γ_1, Γ_2 and Γ_3 can be observed (Fig. 3b). The obtained DLS data are very close to those of semi-dilute solutions of the entangled polymer chains and WLMs [29–31]. Therefore, in the case of hybrid WLMs the fast (I) and medium (II) relaxation modes (Fig. 2b), like in semi-dilute solutions of WLMs, could be attributed to translational diffusion of the chain segments and to the hindered motion of the entangled chains, respectively. Linear shape of the dependencies of the relaxation rates Γ_1 and Γ_2 on q^2 for fast and medium processes (Fig. 4a and b, respectively) confirm that they represent diffusive motion. By contrast, a non-linear dependence for slow (III) relaxation mode (Fig. 4c) suggests that this mode is the non-diffusive one. It is, probably, related to electrostatic repulsion of the similarly charged hybrid micelles of potassium oleate.

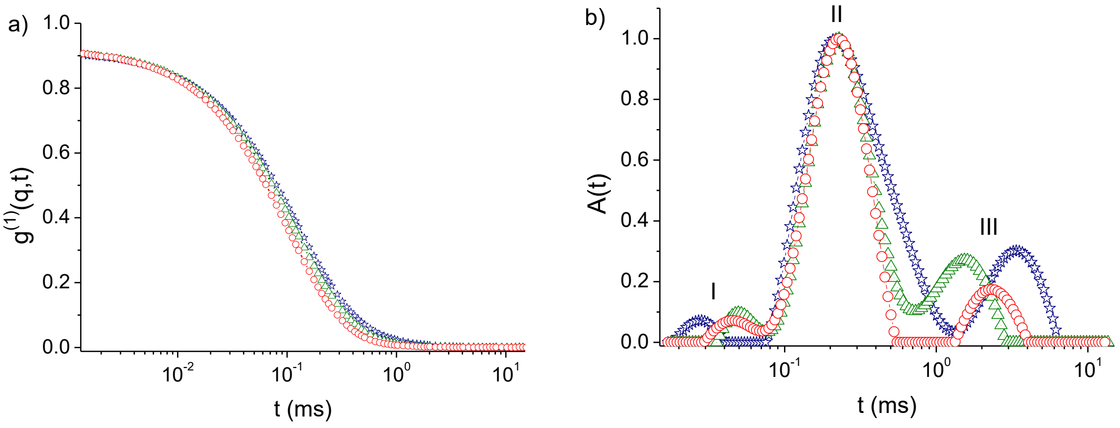

Figure 3. Field autocorrelation functions $g^{(1)}(q, t)$ (a) and decay time distributions $A(t)$ (b) at scattering angle θ=90° for micellar solutions of 47 mM potassium oleate with different concentrations of embedded P4VP: 0.02 monomol/L (stars); 0.03 monomol/L (triangles) and 0.04 monomol/L (circles). Solvent: 80 mM KCl in water at pH=11

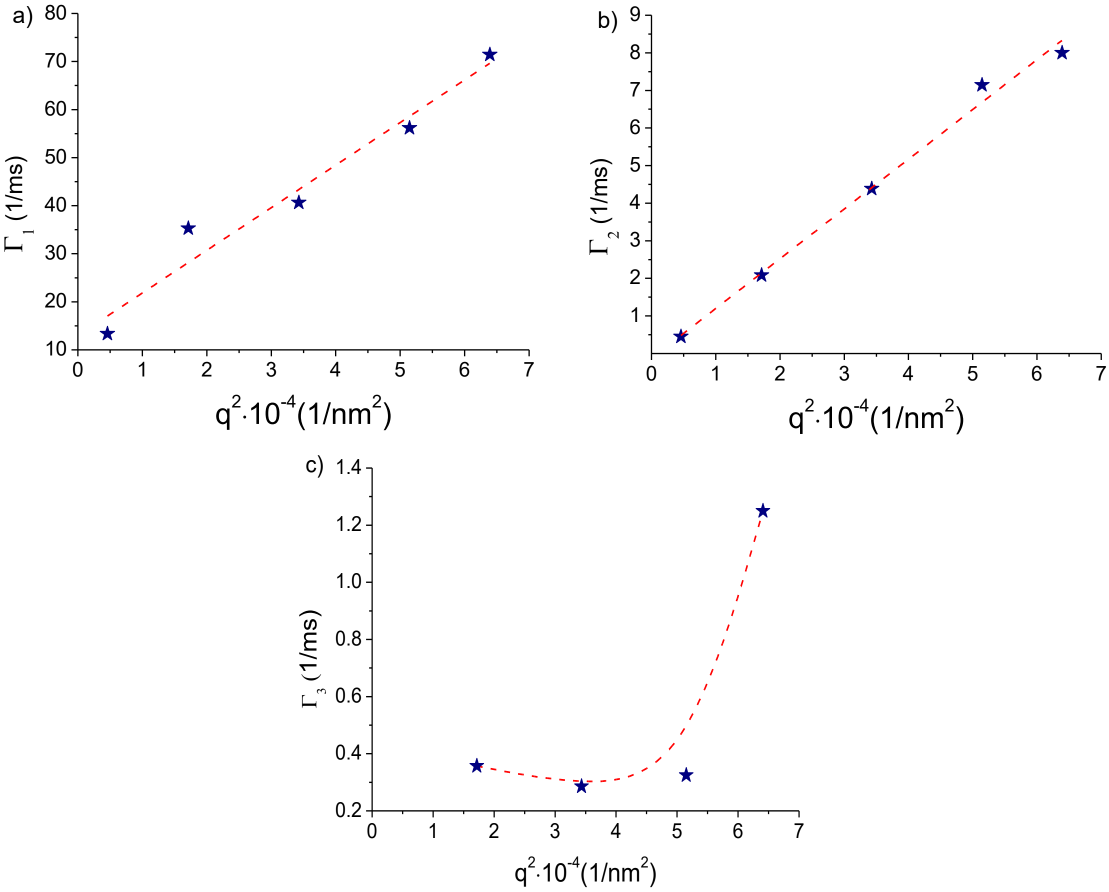

Figure 4. Γ vs q^2 dependences for first (a), second (b) and third (c) components of the field autocorrelation function $g^{(1)}(q, t)$ of the hybrid micelles in 47 mM solution of potassium oleate containing 0.02 monomol/L of P4VP. Solvent: 80 mM KCl in water at pH=11

Conclusions

Cryo-TEM, DLS and SANS were applied to shed light on the shape of hybrid micelles in the aqueous solutions of anionic surfactant potassium oleate with embedded hydrophobic polymer P4VP. Cryo-TEM evidenced the presence of branched rodlike micelles with mean length of 200 nm that is close to the averaged contour length of solubilized P4VP chains. Formation of branches in the hybrid micelles was caused by attaching of the thermodynamically unfavorable end-caps of micelles to the polymer-loaded central cylindrical parts. The local cylindrical shape of hybrid micelles, as was shown by SANS, was independent of the concentration of solubilized P4VP. Values of radii of the micelles, estimated from cryo-TEM-and SANS data were equal to the length of hydrophobic "tail" of potassium oleate. Relaxation processes in the hybrid micelles were shown by DLS to be quite similar to those in polymer-free WLMs of surfactant: two relaxation modes were attributed to diffusion of the entangled micellar chains and their segments; the third mode was related to the electrostatic repulsion between similarly charged micelles.

Funding

This research was financially supported by the Russian Science Foundation (project № 21-73-10197).

*Author Information**

**The authors' names are presented in the following order: First Name, Middle Name and Last Name*

Alexander Lvovich Kwiatkowski (*corresponding author*) — Candidate of physical and mathematical sciences, Leading Researcher, Lomonosov Moscow State University, Leninskie Gory, 1, 2, Moscow, 119991, Russia; e-mail: kvyatkovskij@physics.msu.ru; https://orcid.org/0000-0002-0514-384X

Vyacheslav Sergeevich Molchanov — Candidate of physical and mathematical sciences, Docent, Lomonosov Moscow State University, Leninskie Gory, 1, 2, Moscow, 119991, Russia; e-mail: molchanov@polly.phys.msu.ru; https://orcid.org/0000-0002-2846-0784

Anton Sergeevich Orekhov — Candidate of physical and mathematical sciences, Researcher, National Research Center, Kurchatov Institute, pl. Academica Kurchatova, 1, Moscow, 123182, Russia; e-mail: orekhov.anton@gmail.com; https://orcid.org/0000-0002-3006-2152

Alexander Ivanovich Kuklin — Candidate of physical and mathematical sciences, Professor, Joint Institute of Nuclear Research, ul. Joliot-Curie, 6, Dubna, 141980, Russia; e-mail: alexander.iw.kuklin@gmail.com; https://orcid.org/0000-0002-4530-2980

Olga Evgenievna Philippova — Doctor of physical and mathematical sciences, Professor, Lomonosov Moscow State University, Leninskie Gory, 1, 2, Moscow, 119991, Russia; e-mail: phil@polly.phys.msu.ru; https://orcid.org/0000-0002-1098-0255

Author Contributions

The manuscript was written through contributions of all authors. All authors have given approval to the final version of the manuscript. CRediT: **Alexander Lvovich Kwiatkowski** investigation, original draft preparation, review and editing; **Vyacheslav Sergeevich Molchanov** investigation, conceptualization; **Anton Sergeevich Orekhov** investigation; **Alexander Ivanovich Kuklin** investigation; **Olga Evgenievna Philippova** original draft preparation, review and editing.

Conflicts of Interest

The authors declare no conflict of interest.

References

1 Zana, R. (2005). Dynamics of Surfactant Self-Assemblies: Micelles, Microemulsions, Vesicles and Lyotropic Phases. Taylor and Francis Group. https://doi.org/10.1081/DIS-200067928

2 Israelachvili, J. N., Mitchell, D. J., & Ninham, B. W. (1976). Theory of Self-Assembly of Hydrocarbon Amphiphiles into Micelles and Bilayers. *Journal of the Chemical Society, Faraday Transactions, 72*, 1525–1568. https://doi.org/10.1039/f29767201525

3 Feng, Y., Chu, Z., & Dreiss, C. A. (2015). Smart Wormlike Micelles: Design, Characteristics and Applications. Springer-Verlag: Berlin, Heidelberg.

4 Vlachy, N., Renoncourt, A., Drechsler, M., Verbavatz, J. M., Touraud, D., & Kunz, W. (2008). Blastulae aggregates: New intermediate structures in the micelle-to-vesicle transition of catanionic systems. *Journal of Colloid and Interface Science, 320*(1), 360–363. https://doi.org/10.1016/j.jcis.2007.12.034

5 Israelachvili, J. N. (2011). Intermolecular and Surface Forces (3rd Ed). Academic Press.

6 Zana, R., & Kaler, E. W. (2007). Giant Micelles: Properties and Applications. CRC Press.

7 Chu, Z., Dreiss, C. A., & Feng, Y. (2013). Smart Wormlike Micelles. *Chemical Society Reviews, 42*(17), 7174–7203. https://doi.org/10.1039/c3cs35490c

8 Kwiatkowski, A. L., Molchanov, V. S., & Philippova, O. E. (2019). Polymer-like Wormlike Micelles of Ionic Surfactants: Structure and Rheological Properties. *Polymer Science — Series A, 61*(2), 215–225. https://doi.org/10.1134/S0965545X19020081

9 Falbe, J. (1987). Surfactants in Consumer Products: Theory, Technology and Application. In Surfactants in Consumer Products: Theory, Technology and Application. Springer-Verlag: Berlin, Heidelberg. https://doi.org/10.1007/978-3-642-71545-7

10 Ezrahi, S., Tuval, E., & Aserin, A. (2006). Properties, main applications and perspectives of worm micelles. *Advances in Colloid and Interface Science, 128–130*(2006), 77–102. https://doi.org/10.1016/j.cis.2006.11.017

11 Rodrigues, R. K., Folsta, M. G., Martins, A. L., & Sabadini, E. (2016). Tailoring of wormlike micelles as hydrodynamic drag reducers for gravel-pack in oil field operations. *Journal of Petroleum Science and Engineering, 146*, 142–148. https://doi.org/10.1016/j.petrol.2016.04.021

12 Le Garrec, D., Ranger, M., & Leroux, J. C. (2004). Micelles in anticancer drug delivery. *American Journal of Drug Delivery, 2*(1), 15–42. https://doi.org/10.2165/00137696-200402010-00002

13 Kim, J. H., Domach, M. M., & Tilton, R. D. (1999). Pyrene micropartitioning and solubilization by sodium dodecyl sulfate complexes with poly(ethylene glycol). *Journal of Physical Chemistry B, 103*(48), 10582–10590. https://doi.org/10.1021/jp991720z

14 Kuntz, D. M., & Walker, L. M. (2007). Solution Behavior of Rod-Like Polyelectrolyte-Surfactant Aggregates Polymerized from Wormlike Micelles. *Journal of Physical Chemistry B, 111*(23), 6417–6424. https://doi.org/10.1021/jp0688308

15 Massiera, G., Ramos, L., & Ligoure, C. (2002). Hairy Wormlike Micelles: Structure and Interactions. *Langmuir, 18*(15), 5687–5694. https://doi.org/10.1021/la025687a

16 Nakamura, K., & Shikata, T. (2007). Small Angle Neutron Scattering Study of Polyelectrolyte Conformation Incorporated Into Hybrid Threadlike Micelles Under Strong Shear Flows. *Journal of Physical Chemistry B, 111*(43), 12411–12417. https://doi.org/10.1021/jp072975c

17 Oikonomou, E., Bokias, G., Kallitsis, J. K., & Iliopoulos, I. (2011). Formation of Hybrid Wormlike Micelles upon Mixing Cetyl trimethylammonium Bromide with Poly(methyl Methacrylate-co-Sodium Styrene Sulfonate) Copolymers in Aqueous Solution. *Langmuir, 27*(8), 5054–5061. https://doi.org/10.1021/la200017j

18 Myhre, S., Amann, M., Willner, L., Knudsen, K. D., & Lund, R. (2020). How Detergents Dissolve Polymeric Micelles: Kinetic Pathways of Hybrid Micelle Formation in SDS and Block Copolymer Mixtures. *Langmuir, 36*(43), 12887–12899. https://doi.org/10.1021/acs.langmuir.0c02123

19 Khannanov, A., Rossova, A., Ulakhovich, N., Evtugyn, V., Valiullin, L., Nabatov, A., Kutyrev, G., & Kutyreva, M. (2022). Doxorubicin-Loaded Hybrid Micelles Based on Carboxyl-Terminated Hyperbranched Polyester Polyol. *ACS Applied Polymer Materials, 4*(4), 2553–2561. https://doi.org/10.1021/acsapm.1c01863

20 Kwiatkowski, A. L., Molchanov, V. S., Kuklin, A. I., Orekhov, A. S., Arkharova, N. A., & Philippova, O. E. (2022). Structural transformations of charged spherical surfactant micelles upon solubilization of water-insoluble polymer chains in salt-free aqueous solutions. *Journal of Molecular Liquids*, 347. https://doi.org/10.1016/j.molliq.2021.118326

21 Kwiatkowski, A. L., Molchanov, V. S., Chesnokov, Y. M., Ivankov, O. I., & Philippova, O. E. (2023). Hybrid Polymer–Surfactant Wormlike Micelles for Concurrent Use for Oil Recovery and Drag Reduction. *Polymers, 15*(23). https://doi.org/10.3390/polym15234615

22 Molchanov, V. S., Philippova, O. E., Khokhlov, A. R., Kovalev, Y. A., & Kuklin, A. I. (2007). Self-assembled networks highly responsive to hydrocarbons. *Langmuir, 23*(1), 105–111. https://doi.org/10.1021/la061612l

23 Iancu, C. V., Tivol, W. F., Schooler, J. B., Dias, D. P., Henderson, G. P., Murphy, G. E., Wright, E. R., Li, Z., Yu, Z., Briegel, A., Gan, L., He, Y., & Jensen, G. J. (2007). Electron cryotomography sample preparation using the vitrobot. *Nature Protocols, 1*(6), 2813–2819. https://doi.org/10.1038/nprot.2006.432

24 Kuklin, A. I., Soloviov, D. V., Rogachev, A. V., Utrobin, P. K., Kovalev, Y. S., Balasoiu, M., Ivankov, O. I., Sirotin, A. P., Murugova, T. N., Petukhova, T. B., Gorshkova, Y. E., Erhan, R. V., Kutuzov, S. A., Soloviev, A. G., & Gordeliy, V. I. (2011). New opportunities provided by modernized small-angle neutron scattering two-detector system instrument (YuMO). *Journal of Physics: Conference Series, 291*(1), 1–7. https://doi.org/10.1088/1742-6596/291/1/012013

25 Hassan, P. A., Rana, S., & Verma, G. (2015). Making sense of brownian motion: Colloid characterization by dynamic light scattering. *Langmuir, 31*(1), 3–12. https://doi.org/10.1021/la501789z

26 Kwiatkowski, A. L., Sharma, H., Molchanov, V. S., Orekhov, A. S., Vasiliev, A. L., Dormidontova, E. E., & Philippova, O. E. (2017). Wormlike surfactant micelles with embedded polymer chains. *Macromolecules, 50*(18), 7299–7308. https://doi.org/10.1021/acs.macromol.7b01500

27 Kwiatkowski, A. L., Molchanov, V. S., Kuklin, A. I., & Philippova, O. E. (2020). Opposite effect of salt on branched wormlike surfactant micelles with and without embedded polymer. *Journal of Molecular Liquids, 311*, 113301–113309. https://doi.org/10.1016/j.molliq.2020.113301

28 Svergun, D., & Feigin, L. (1987). Structure Analysis by SANS and SAXS. Plenum Press.

29 Calabrese, M. A., & Wagner, N. J. (2018). Detecting Branching in Wormlike Micelles via Dynamic Scattering Methods. *ACS Macro Letters, 7*(6), 614–618. https://doi.org/10.1021/acsmacrolett.8b00188

30 Li, J., Ngai, T., & Wu, C. (2010). The slow relaxation mode: From solutions to gel networks. *Polymer Journal, 42*(8), 609–625. https://doi.org/10.1038/pj.2010.59

31 Wu, C., & Ngai, T. (2004). Reexamination of slow relaxation of polymer chains in sol-gel transition. *Polymer, 45*(6), 1739–1742. https://doi.org/10.1016/j.polymer.2003.11.045

How to Cite: Sarsenbekova, A.Zh., Bolatbay, A.N., Havlicek, D., Issina, Zh.A., Sarsenbek, A.Zh., Kabdenova, N.A., & Kilybay, M.A. (2024) Effect of Heat Treatment on the Supramolecular Structure of Copolymers Based on Poly(propylene glycol fumarate phthalate) with Acrylic Acid. *Eurasian Journal of Chemistry, 29, 2(114), 61-73.* https://doi.org/10.31489/2959-0663/2-24-9

Article

Received: 22 January 2024 | Revised: 29 April 2024 |
Accepted: 14 May 2024 | Published online: 17 May 2024

UDC 66.092-977

https://doi.org/10.31489/2959-0663/2-24-9

Akmaral Zh. Sarsenbekova[1*], Abylaikhan N. Bolatbay[1], David Havlicek[2],
Zhannur A. Issina[1], Assiya Zh. Sarsenbek[1], Nurgul A. Kabdenova[1],
Muslim A. Kilybay[1]

[1]Karaganda Buketov University, Karaganda, Kazakhstan;
[2]Charles University, Prague, Czech Republic
*(*Corresponding author`s e-mail: chem_akmaral@mail.ru)*

Effect of Heat Treatment on the Supramolecular Structure of Copolymers Based on Poly(propylene glycol fumarate phthalate) with Acrylic Acid

Previous studies investigating the thermal decomposition of p-PGFPh:AA copolymers in an inert atmosphere have provided only a general understanding of the changes that occur during thermolysis. Comprehensive studies are required to gain a better understanding of these processes [1]. The most comprehensive information on the influence of various factors on both the kinetics and the supramolecular structure of the resulting products can be obtained by combining the method of thermal analysis with IR, mass spectrometry, and scanning electron microscopy. The compounds studied have two different compositions, namely p-PGFPh:AA 6.77:93.23 mol % and p-PGFPh:AA 86.67:13.33 mol %. These compounds were then subjected to a thermolysis process, which resulted in the emission of gases and a decrease in sample weight. The degradation process can be divided into three stages: 1) Depolymerization of the main chain; 2) Depolymerization of the side chain; 3) Final decomposition. These processes occur sequentially at different temperature ranges. According to TG- and DTG studies, complete decomposition of p-PGFPh:AA copolymers occurred at T_{term} = 340–350 °C. In this temperature range, a slight loss of sample mass (less than 10 wt %) was observed along with a slight gas evolution. The main gaseous products from the transformation of the studied samples were CO and CO_2. This was supported by IR-CO (2000–2200 cm^{-1}) and CO_2 (2310–2370 cm^{-1}) as well as mass spectrometric observations. The final products resulting from the thermolysis of p-PGFPh:AA copolymers were examined under an electron microscope. The results showed a similar morphological pattern of mesostructures with sizes ranging from 0.3–1.5 μm, which were observed depending on the porous structure of the initial polymer material. Based on the experimental data, it can be concluded that the p-PGFPh:AA copolymers (in proportions of 6.77:93.23 mol % and 86.67:13.33 mol %) have a relatively high degree of resistance to heating and do not undergo any changes in chemical composition, particle size and shape. In conclusion, the results clearly indicate that the selection of conditions for pyrolysis plays a crucial role in increasing the thermal stability of polymeric materials. This method allows for purposeful changes in the structure and properties of polymers.

Keywords: acrylic acid, poly(propylene glycol fumarate phthalate), polymer, micrographs, morphology, electron microscope, thermogravimetric analysis, supramolecular structure.

Introduction

In terms of production and consumption, the polymer materials industry has grown to enormous proportions, where extending the lifespan of such materials is equivalent to increasing their production from an economic standpoint [2]. It should be noted that it is important to stabilize polymer materials as raw material resources are being depleted each year. Predicting the service life of polymers is a crucial aspect of stabilization. Incorrect determination of the operating time of polymer materials can lead to unexpected premature failure of parts made of polymers and, as a consequence, to the failure of complex technical devices, which is unacceptable (technological factor). Reduced polymer service life leads to economic loss due to underutilization [3–5].

One way to improve the fire resistance of polymers is to add fire retardants as appropriate additives to ensure a safe environment [6–8].

A key concern is the degradation and stabilization of polymers. This involves both ecological and environmental protection issues. From an environmental point of view, it is becoming relevant to address problems related to recycling waste polymers and minimizing the amount of incinerated polymer waste [9–13].

A promising approach is to create polymers with a precisely defined lifespan. These polymers should be utilized while needed and decompose once they are no longer required.

The problem of stabilizing the properties of polymer products is diverse due to the variety of tasks involved. Solving this problem requires a good understanding of the scientific principles of stabilization, as well as knowledge of the mechanisms of polymer degradation and kinetic patterns [10–16].

A significant amount of research is currently being conducted into the ageing process of polymers, resulting in the development of effective measures for comprehensive protection against all types of degradation. The ageing of polymers is characterized by irreversible changes in the polymer chain, which ultimately lead to a loss of the performance characteristics of the polymer product. The aging of polymers is mainly determined by their structure, the stability of their bonds, and the type of side groups. At most, the macromolecular chains in our body tend to break down, resulting in the formation of many low molecular weight fractions. This process leads to a decrease in the average molecular weight and an expansion of molecular weight distribution [16-17].

The reactivity of the molecular chain causes polymer aging. The rate and direction of aging depend on the molecular and supramolecular structure. The supramolecular structure (morphology) is determined by the way the chains are arranged (packing) into spatially distinct elements in a solid (block) polymer, as well as the size, shape and relative arrangement of these elements. Indeed, the chemical properties of polymers are influenced by various factors such as the length and stereoisomerism of the chains, the way in which the macromolecules are stacked, and their crystallization [18–21].

The supramolecular structure of the polymer is not perfect. It contains correctly packed macromolecules in both crystalline and amorphous regions, but there are also many defects and disturbances of order. These features have significant consequences for the aging of solid polymers [22-23].

Firstly, structural and physical heterogeneity results in the non-uniform distribution of reagents and additives within the polymer system. Secondly, structural microheterogeneity leads to a broad distribution of regions exhibiting disparate frequencies of molecular motion within the polymer. This results in a wide range of kinetic constants and activation energies for elementary reactions. All this makes polymers more susceptible to aging [24–26].

Polymeric materials based on unsaturated polyester resins are widely used in various industries and in our daily lives due to their good mechanical properties, strength, biocompatibility, viscoelastic nature, and the ability to take any shape during processing. Extensive research has been carried out to develop methods for producing unsaturated polyester resins [27-28], including one of the main sources of raw materials — poly(propylene glycol fumarate phthalate), which is used to produce the proposed copolymer (which can be used as hydrogels in the processing of vegetable crops). It is worth noting that the production technology for this raw material has been fully developed [28-29].

The use of moisture sorbents in agriculture for growing crops has led to an increase in the use of hydrogels. However, the long-term use of artificial soil made from hydrogels can lead to their aging and degradation, which can result in reduced crop yields. At present, we do not fully understand the substances that cause the polymer gels added to natural soils and the structures that form the basis of artificial soils to degrade under the influence of various environmental factors. It is vital to identify these factors, including seasonal and daily fluctuations in temperature, in order to prevent the degradation process and maintain high crop yields. We are among the first in the world to emphasize the need to address these issues.

Solving these problems is impossible without studying the supramolecular structure (morphology) of polymer materials using electron microscopy as a function of annealing temperature (it is also important to note that heat treatment affects the morphology of the polymer!). The results obtained make it possible to reveal the mechanism of destruction of a real polymer and try to control it in the desired direction.

The objective of the research is to investigate the supramolecular structure formation mechanisms of copolymers of poly(propylene glycol fumarate phthalate) and acrylic acid, before and after being subjected to heat treatment.

Experimental

Copolymers based on poly(propylene glycol fumarate phthalate) [29] with acrylic acid (Sigma-Aldrich, Germany) at different initial ratios of 6.77:93.23 mol % and 86.67:13.33 mol % were selected as objects of study [27, 30].

Poly(propylene glycol fumarate phthalate) is a chemical compound produced by a polycondensation reaction of propylene glycol, phthalic anhydride, and fumaric acid. The reaction takes place at a temperature of

180 °C and is carried out using a standard procedure [30]. An aluminum chloride catalyst is used in a nitrogen stream to prevent unwanted gelatinization processes. The reaction time is 16 hours.

Copolymers were produced by mixing comonomers in dioxane at 60 °C in glass ampoules. The combination of comonomers ranged from 0.02–0.8 mol fractions with a total monomer concentration of 1 mol/l and [PB] = $1.0 \cdot 10^{-2}$ mol/l. The copolymers were extracted from the solution by precipitation with hexane followed by re-precipitation with a toluene solution. The samples were then dried under vacuum at 40–45 °C. The PB initiator was recrystallized from benzene several times and stored at –10 °C. The solvents, namely dioxane and ethanol were dried and purified according to known methods.

The study of the microstructure and quantitative analysis of the elemental composition of the surface layer of copolymers were carried out using a JEOL JSM-5910 electron microscope (Jeol Company, Japan). The samples were scanned at varying magnifications (×500, ×1500, ×3000, ×10000).

The copolymer's surface morphology was studied with the help of an NT-206 atomic force microscope (AFM) (manufactured by MTM in Minsk, Republic of Belarus) in a static scanning mode. A CSC 12/15 silicon cantilever was used for the same. The experimental data were analyzed and visualized using the SurfaceXplorer software (developed by Microtestmachines, an additional liability company) and nanoImages (Scientific Research Center for Preservation of the National Academy of Sciences of Belarus SSI).

The kinetics of the thermal destruction process was studied by thermal analysis with the registration of TGA-DSC-IR curves on a Netzsch Jupiter STA 449 F3 (Germany) combined with a QMS 403 Aeolos Quadro mass spectrometer (NETZSCH-Gerätebau GmbH, Germany) for better accuracy. The sample weighed 30 mg in the form of ground powder. TG curves of the samples were recorded in the range from 50 to 800 °C with heating rates of 5, 7.5, 10.0, 12.5 °C/min in a nitrogen atmosphere.

The experimental data obtained were processed using the licensed software "Origin Pro 8.1".

Results and Discussion

It is known that network polymers, i.e. PGFPh:AA copolymers, are particles with uncontrolled parameters of molecular weight and morphology [31]. In this work, the dimensional characteristics of the p-PGFPh:AA copolymer were assessed by electron microscopy and the morphological characteristics of p-PGFPh:AA polymer particles were studied.

Many polymeric materials have relatively high thermal stability; they decompose under the influence of high temperatures in a nitrogen atmosphere [32]. Thermal analysis was conducted on the p-PGFPh:AA copolymer (6.77:93.23 mol %) using thermal analysis to record TGA-DSC-IR curves on a Netzsch Jupiter STA 449 F3 instrument combined with a QMS 403 Aeolos Quadro mass spectrometer (Fig. 1). A detailed description of the degradation mechanism of p-PGFPh:AA copolymers of different initial ratios has been given in the referenced work [32].

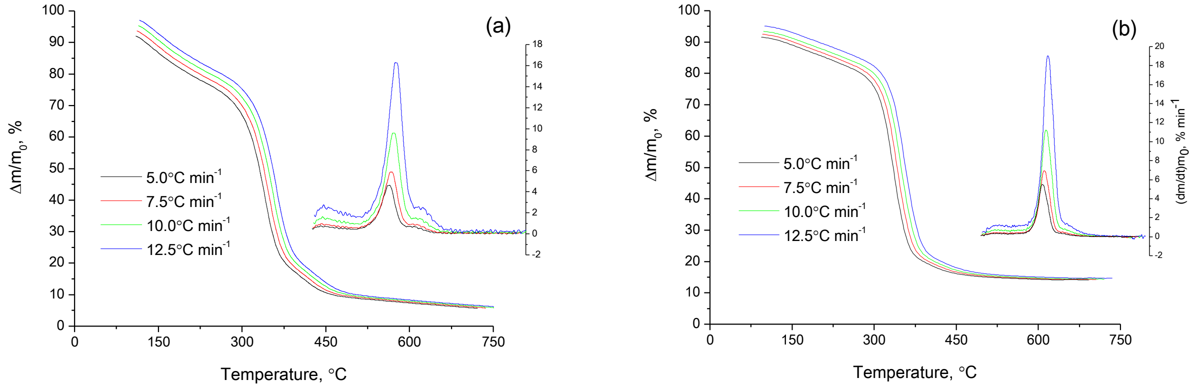

Figure 1. Thermograms of p-PGFPh:AA copolymers at the initial ratios M_1:M_2, mol %:
(*a*) — 6.77:93.23 mol %; (*b*) — 86.67:13.33 mol % in a nitrogen atmosphere

During the annealing process of p-PGFPh:AA copolymers, morphological changes occur along with changes in its chemical composition. The copolymer is a polymer chain of unsaturated polyester resin, which undergoes thermal decomposition in the absence of oxygen. This process can result in the destruction of the copolymer at the ester bond, and the release of carbon dioxide during thermal destruction. Analysis of gaseous products resulting from the thermal decomposition of p-PGFPh:AA copolymers (T_{max} = 340–350 °C) indicates the formation of toxic gases, including carbon monoxide (CO) and carbon dioxide (CO_2). Based on TG/DSC-MS analysis, it was found that increasing the proportion of acrylate units in the p-PGFPh:AA copolymer (6.77:93.23 mol %) resulted in a 50 % reduction in the formation of toxic gaseous products such as carbon monoxide (CO) and carbon dioxide (CO_2) (Fig. 2).

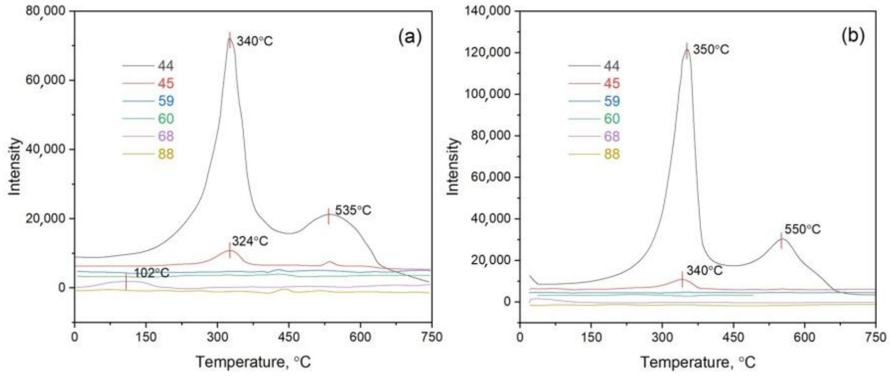

Figure 2. Chromatogram of the pyrolysis products of p-PGFPh:AA copolymers at the initial ratios M_1:M_2, mol %: (*a*) — 6.77:93.23 mol % and (*b*) — 86.67:13.33 mol %

In these mass spectra in Figure 2, the most intense peaks correspond to a molecular ion with a mass of 44 amu. The results of a search against the NIST mass spectrum database indicate that this peak corresponds to carbon dioxide (CO_2). The release of a small amount of CO_2 also occurs at ~538 °C for p-PGFPh:AA copolymers (6.77:93.23 mol %) and ~550 °C for p-PGFPh:AA copolymers (86.67:13.33). When comparing the thermograms of the samples, it can be concluded that p-PGFPh:AA copolymers are thermally stable [1]. During annealing, p-PGFPh:AA copolymers become black in color which can be attributed to the formation of carbon.

The reaction mechanism of the thermal degradation of the copolymer of poly(propylene glycol fumarate phthalate) with acrylic acid can be presented as follows [1]:

1. Initiation:

Decomposition of p-PGFPh under the influence of high temperatures and the formation of active radicals:

$$\text{p-PGFPh} \rightarrow \text{p-PG}\bullet + \bullet\text{FPh}$$

2. Reaction of p-PGFPh radicals with acrylic acid:

p-PG•/•FPh radicals can react with acrylic acid (AA) via an addition reaction to form an adduct:

$$\text{p-PG}\bullet + \text{AA} \rightarrow \text{p-PG-AA}\bullet$$

3. Continued breaking of chemical bonds:

The p-PG-AA• adduct can react further with other radicals or p-PGFPh molecules, breaking bonds and forming new radicals:

$$\text{p-PG-AA}\bullet + \text{p-PGFPh} \rightarrow \text{p-PG}\bullet + \text{p-PGFPh-AA}\bullet$$

4. Formation of destruction products:

The process of breaking down a p-PGFPh:AA copolymer can result in the formation of degradation products such as acrylic acid (AA) monomers, p-PGFPh monomers, and other fragmented compounds. These fragments can further degrade to smaller organic compounds such as acids, aldehydes, CO, CO_2, and other products. The thermal degradation of the copolymer leads to the cleavage of bonds within the macromolecule, resulting in the formation of reaction fragments and degradation products.

In some cases, certain volatile polymer products can be identified by a strong infrared absorption peak. This peak is usually associated with gas phase components of the pyrolysis products, which are mainly CO_2 (2310 cm^{-1}) and CO (2000 cm^{-1}). The results of IR spectrometric analysis confirm this conclusion (Fig. 3).

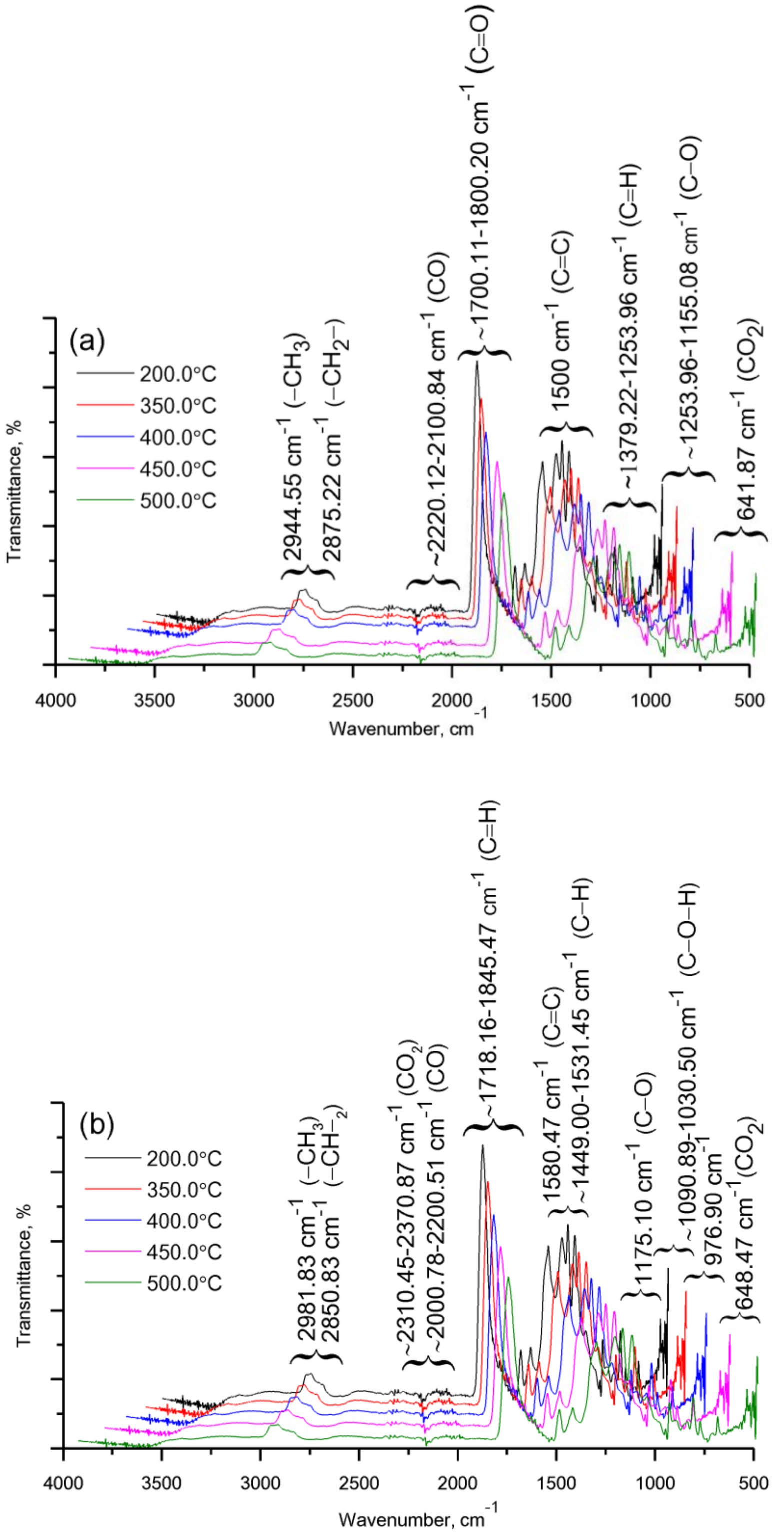

Figure 3. IR spectra of p-PGFPh:AA decomposition products at ratios M_1:M_2, mol %:
(*a*) — 6.77:93.23 and (*b*) — 86.67:13.33 recorded at temperatures between 200 and 500 °C

In order to determine the potential of p-PGFPh:AA copolymers as binder substances, it is important to understand how they change under high temperatures at different ratios (6.77:93.23 mol % and 86.67:13.33 mol %). To achieve this, it is necessary to study the evolution of the polymer morphology during heat treatment in a nitrogen atmosphere. Annealing can cause phase transformations, recrystallization, and changes in the morphology and characteristics of polymers. It is known that the mobility of polymer molecular chains increases with temperature. The morphology of polymers is influenced by chain mobility and recrystallization.

After being exposed to a temperature of 150 °C, the surface of p-PGFPh:AA copolymers (initially mixed in the ratio of 6.77:93.23 mol %) showed slight deformation with darkening as shown in Figure 4, *a*. When annealed at 200 °C, the surface appeared wavy with local formation of bumps and grooves. Charring of the material caused a significant darkening and turned it to a brown color as shown in Figure 4, *b*. The change in the surface topography of the copolymers becomes more pronounced as the temperature is increased to 350 °C: local formations appear in the form of mounds and pits, i.e. the surface becomes rough (Fig. 4, *c*). Annealing at 400 °C does not lead to any significant change in the morphology of the copolymer surface; it is only characterized by a greater darkening of the p-PGFPh:AA copolymer (Fig. 4, *d*). The copolymer annealed at 450 °C is characterized by a certain smoothing of the surface relief of the copolymers, but with an obvious blackening and a metallic sheen (Fig. 4, *f*). Membrane samples become hard and brittle. After annealing at 500 °C, the brittle copolymer begins to deteriorate and crumble, which indicates almost complete decomposition of the polymer (Fig. 4, *f*).

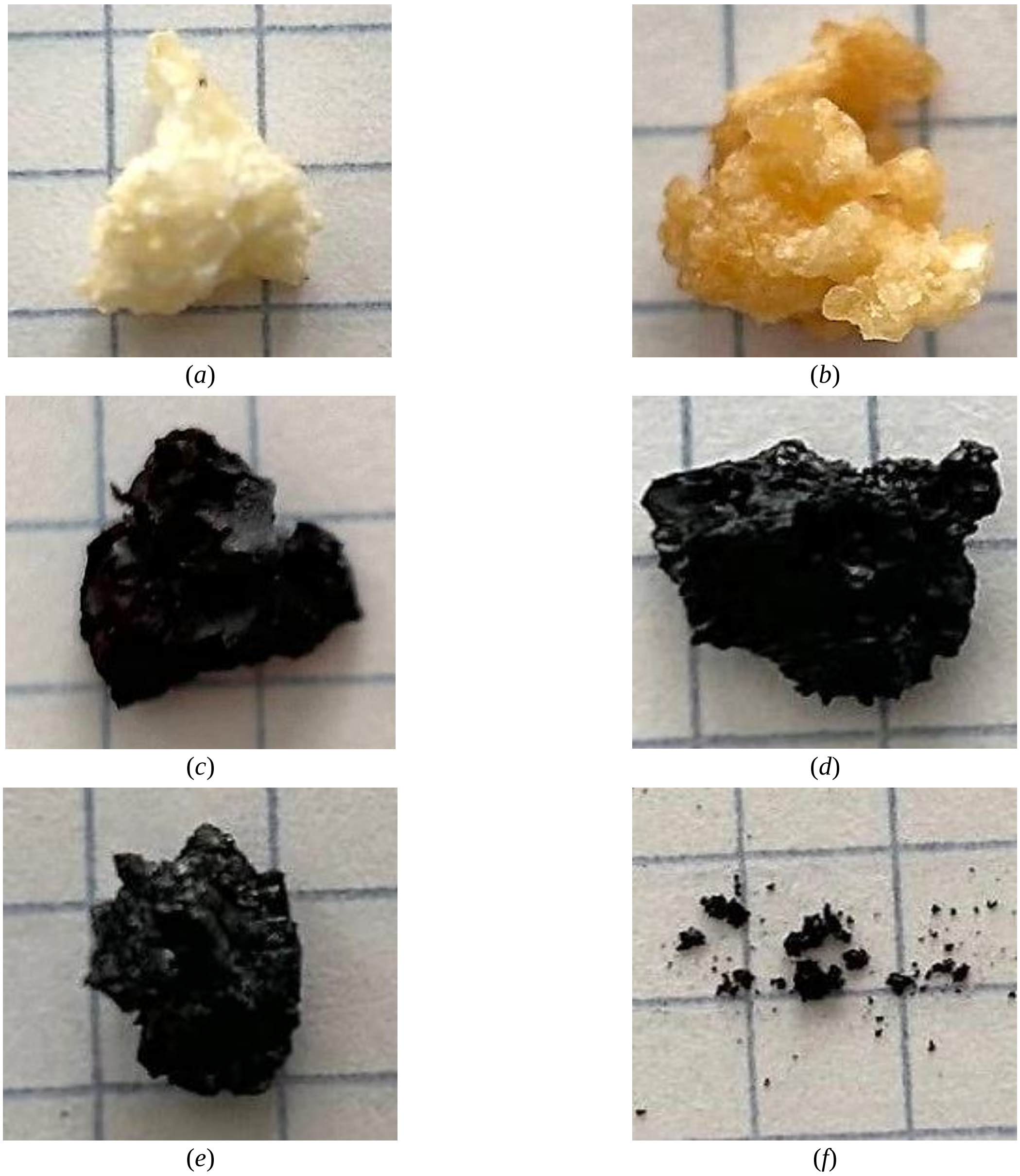
(*a*) (*b*)
(*c*) (*d*)
(*e*) (*f*)

a — 150 °C; *b* — 200 °C; *c* — 350 °C; *d* — 400 °C; *e* — 450 °C; *f* — 500 °C

Figure 4. Annealed copolymers p-PGFPh:AA at the initial ratios of 6.77:93.23 mol %

The change in film morphology was analyzed by scanning electron microscopy (Fig. 5). Micrographs of the synthesized poly(propylene glycol fumarate phthalate) with acrylic acid are shown in Figure 5 *a*, *b*. A study of the surface morphology of the resulting p-p-PGFPh:AA copolymer (at the initial ratio of 6.77:93.23 mol %) showed that the latter is a rather complex structural and morphological organization. Photographs of the sample show a characteristic openwork structure with a high proportion of smaller pores (Fig. 5, *a* and *b*).

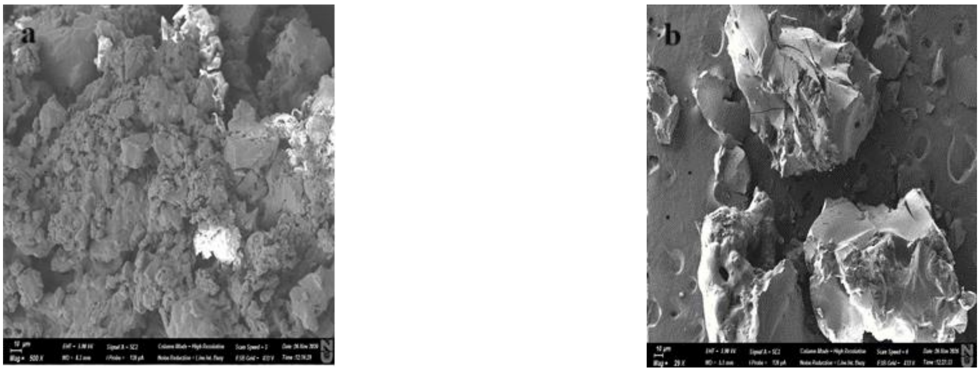

Figure 5. Scanned electron micrographs of the p-PGFPh:AA copolymer at the initial ratios of 6.77:93.23 mol % at magnification: ×3000

This is also evidenced by the data on the state of the surface prior to temperature modification obtained using an atomic force microscope (Fig. 6).

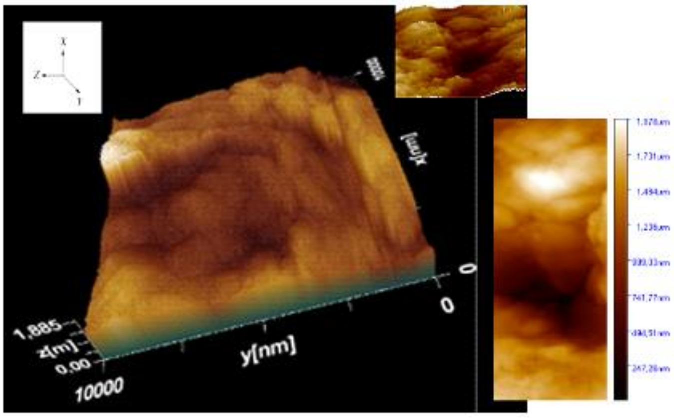

Figure 6. 3D visualization of the surface relief of the p-PGFPh:AA copolymer at the initial ratio of 6.77:93.23 mol % with backlit height

Analysis of the 3D image (Fig. 6) of the p-PGFPh:AA copolymer film (6.77:93.23 mol %) showed that the surface of this copolymer is not flat and has irregularities. A morphometric study of dimensional parameters requires consideration of the shape, radius of curvature, length, width, and height. The studied p-PGFPh:AA copolymer has a length of 105.39±9.86 nm, width of 110.49±11.69 nm, and height of 20.58±3.56 nm. The use of the root-mean-square roughness parameter (Rq is the deviation of the profile points from its center line) and subsequent analysis of the degree of development of the relief show that the surface of the copolymer under study is heterogeneous in texture (Rq values are about 8.69±0.5 nm (Fig. 6). Analysis of the above three-dimensional image of the surface of the p-PGFPh:AA copolymer (6.77:93.23 mol %) indicates that the analyzed surface of the sample is not flat and that there are irregularities of various sizes on its surface.

Annealing the copolymers at 290 °C leads to deformation of the polymers (Fig. 7). Figure 7 (*a*) shows that p-PGFPh:AA particles have different shapes and sizes, ranging from several tens to hundreds of microns.

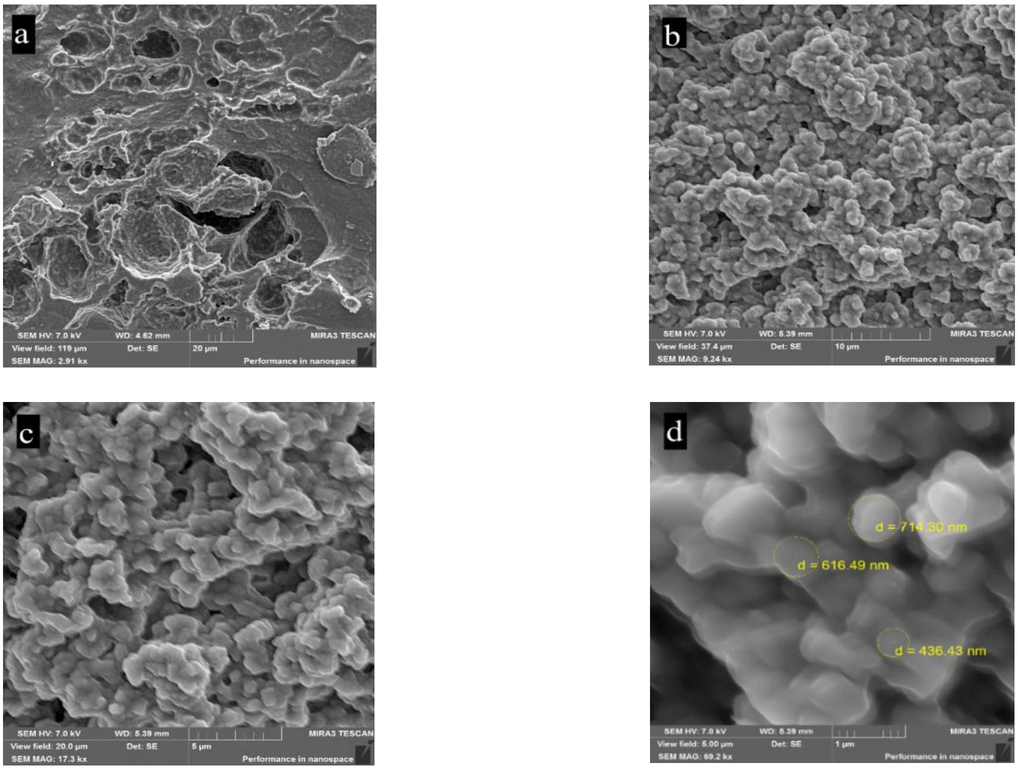

a — ×500; *b* — ×1500; *c* — ×3000; *d* — ×10000

Figure 7. Micrograph of the morphology of the p-PGFPh:AA copolymer at the initial ratio of 6.77:93.23 mol % after heat treatment at 290 °C with successive magnification

Figure 7(*a*) shows that the surface of the sample appears heterogeneous and has different textures with many microscopic bumps and pores (~20 nm). The convex part of the p-PGFPh:AA copolymer at the initial ratio of 6.77:93.23 mol % after heat treatment consists of sintered (shrunken) particles (Fig. 7, *a*). Upon further magnification (Fig. 7, *b*), it is clear that the sintered part consists of smaller compacted parts (Fig. 7, *c*), the surface of which is within the range of 400–700 nm on further magnification (Fig. 7, *d*). Analysis of the micrographs shows that the structural components are strikingly similar, differing only in size. The SEM images suggest the presence of microphases within the copolymer structure, which could be attributed to thermal treatment at 290 °C. The copolymer surface as illustrated in Figure 7 (*b*) and (*c*) appears to have an inconsistent, irregular structure, comprising a mixture of globules and pores of various shapes and sizes, with agglomerates of undefined shapes ranging from 10 to 65 μm. This may be due to changes in the crystal structure or chemical reactions within the copolymer.

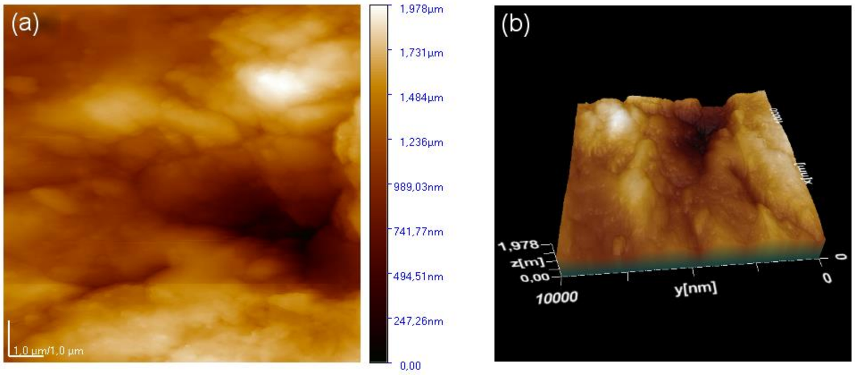

a — 2D; *b* — 3D

Figure 8. Images of the topography of the surface of the p-PGFPh:AA copolymer (6.77:93.23 mol %) after heat treatment at 290 °C

Figures 8 (*a*) and (*b*) show the p-PGFPh:AA copolymer with the characteristic topography (6.77:93.23 mol %) obtained using AFM: the surface is covered with spike-like protrusions, the width of which is 110.4±8.1 nm, the length is 25.1±2.7 nm, the average quadratic surface roughness Rq is 8.3±0.8 nm. The high flexibility (in comparison with the p-PGFPh:AA copolymer before firing) can be considered as one of the possible reasons for a slight increase in the surface roughness of this sample.

Next, micrographs of samples of the copolymer composition (6.77:93.23 mol %) were obtained after heat treatment at 440 °C (Fig. 9). The micrographs show the surface of a copolymer of poly(propylene glycol fumarate phthalate) with acrylic acid after heat treatment at 440 °C. The surface of the sample appears greatly altered compared to the untreated sample (Fig. 9). Many small convex and depressed formations can be observed. These structures have dimensions within ~1.5 μm (Fig. 9, *a*). The surface of the sample also appears to be relatively smooth, but with small features at the micro level. The presence of acrylic acid in the copolymer can influence its morphology and structure (Fig. 9, *b*).

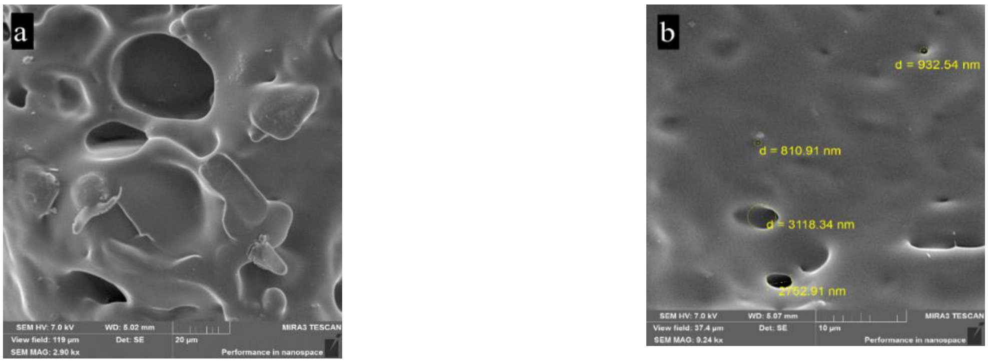

a — ×500; *b* — ×1500

Figure 9. Micrograph of the morphology of the p-PGFPh:AA copolymer at the initial ratio of 6.77:93.23 mol % after heat treatment at 440 °C with successive magnification

As shown above, the process of sintering and, accordingly, the structure formation of the p-PGFPh:AA copolymer during heat treatment is not a spontaneous process. Based on this, the effect of unsaturated polyester resin on the structure of the p-PGFPh:AA copolymer during heat treatment was investigated. Microscopic studies were carried out on the p-PGFPh:AA copolymer, where the content of poly(propylene glycol fumarate phthalate) in the copolymer was 86.67 mol %.

Figure 10 shows that significant changes in the morphology of the copolymer p-PGFPh:AA (86.67:13.33 mol %) were observed after heat treatment up to 240 °C. The copolymer film has an undefined architecture with a knobby surface, Figure 10 (*a*) and (*d*).

These changes may be related to melting processes, structural reorganization, or possible chemical reactions. Differences in the size and shape of structures may indicate heterogeneity in the sample after processing.

Next, micrographs of samples of the copolymer composition were obtained at the initial ratio of 86.67:13.33 mol % after heat treatment up to 440 °C (Fig. 11).

Numerous tiny convex structures with a diameter of approximately 1–5 micrometers are visible. These structures are uniformly distributed over the entire surface of the sample and may represent phase regions with distinct characteristics. The images (Fig. 11) do not show a specific orientation of pores and particles, which may indicate a random and disordered distribution of these elements on the surface. The micrograph indicates that heat treatment of the copolymer p-PGFPh:AA (copolymer at the initial ratio of 86.67:13.33 mol %) results in the formation of pores and small particles on its surface. These structural changes can have various causes, such as the release of gases, changes in the crystal structure or chemical reactions. Pores and particles influence the physical and chemical properties of the p-PGFPh:AA copolymer (86.67:13.33 mol %).

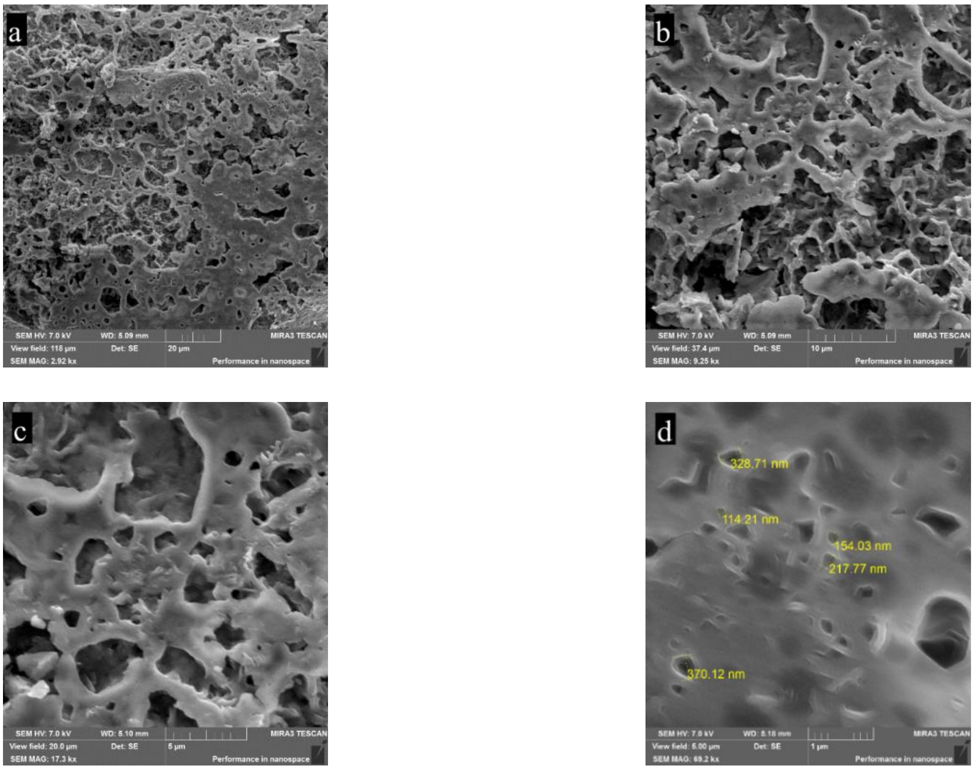

a — ×500; *b* — ×1500; *c* — ×3000; *d* — ×10000

Figure 10. Micrograph of the morphology of the p-PGFPh:AA copolymer at the initial ratio of 86.67:13.33 mol % after heat treatment up to 240 °C with successive magnification

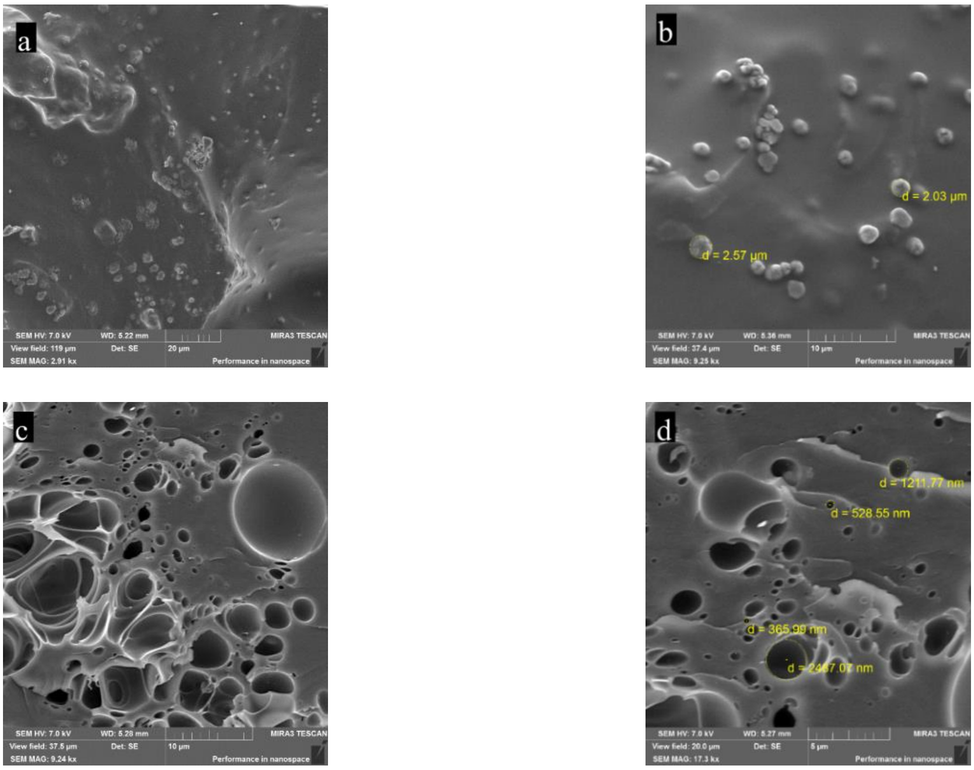

a — ×500; *b*, *c* — ×3000; *d* — ×10000

Figure 11. Micrograph of the morphology of the p-PGFPh:AA copolymer at the initial ratio of 86.67:13.33 mol % after heat treatment to 410 °C with successive magnification

From Figures 10 and 11 it can be seen that as the degree of unsaturation in the copolymer (p-PGFPh content in the copolymer) increases, the cured products become less hard and more viscous. This relationship is due to a reduction in the cross-linking density resulting in fewer chains to support the load.

Conclusions

The paper discusses the findings of microscopic studies carried out on copolymers of p-PGFPh:AA before and after heat treatment. In contrast, the structure of the p-PGFPh:AA copolymer (6.77:93.23 mol %) is isomorphic both before and after heat treatment to 290 °C. However, if the p-PGFPh:AA copolymer (6.77:93.23 mol %) has a “popcorn” structure, then it is completely preserved even after heat treatment up to 290 °C (Fig. 7, *b* and *c*). Consequently, the process of temperature exposure does not cause any change in the structure of the copolymer, and the morphology of polymers after heat treatment is determined only by the morphology of the original polymer. A scanning microscopy study of the cleavage surface of p-PGFPh:AA copolymers shows that the size of the smallest elements is ~20 nm (Fig. 7, *a*). Larger formations are also present in all electron microscopic images, but in some cases, at magnifications of 500 to 10,000 (e.g. Fig. 7, *b* and *c*), they can be seen to be composed of smaller spherical particles of ~10 nm in size. The p-PGFPh:AA copolymer (86.67:13.33 mol %) has a completely different morphology. The structure of the p-PGFPh:AA copolymer (86.67:13.33 mol %) turns out to be close to the structure of networks, the average size of spherical formations is 25–45 nm (Fig. 10, *b* and *c*). Despite significant differences in the morphology of p-PGFPh:AA copolymers at different component ratios, p-PGFPh:AA copolymers with monomer ratios of 6.77:93.23 mol % and 86.67:13.33 mol % have the same properties — porous structure. Consequently, these properties are not due to the nature of supramolecular formations, but to the properties of smaller structural units of the network at the molecular level. It was also shown that when heated in a nitrogen atmosphere to 800 °C, they formed the same amount of stable polymer residue, indicating the similarity of their thermal stability (Fig. 4).

The results obtained suggest that the degradation of p-PGFPh:AA copolymers is a complex process. It involves the breaking chemical bonds by heat as well as structuring reactions between macromolecules and their decomposition products. It is important to note that selecting conditions for pyrolysis plays a significant role in increasing the thermal stability of polymeric materials. This is because pyrolysis can be used to selectively modify the structure and properties of polymers.

Funding

This research was funded by the Science Committee of the Ministry of Science and Higher Education of the Republic of Kazakhstan (Grant No. AP15473241).

*Author Information**

**The authors' names are presented in the following order: First Name, Middle Name and Last Name*

Akmaral Zhakanovna Sarsenbekova (*corresponding author*) — PhD in Chemistry, Associate Professor, Karaganda Buketov University, Universitetskaya street, 28, 100024, Karaganda, Kazakhstan; e-mail: chem_akmaral@mail.ru; https://orcid.org/0000-0002-8951-3616

Abylaikhan Nurlanuly Bolatbay — Doctoral Student, Karaganda Buketov University, Universitetskaya street, 28, 100024, Karaganda, Kazakhstan; e-mail: abylai_bolatabai@mail.ru; https://orcid.org/0000-0001-5047-3066

David Havlicek — RNDr, Associate Professor, Faculty of Science, Department of Inorganic Chemistry, Charles University in Prague, Prague, Czech Republic; e-mail: havlicek@natur.cuni.cz; https://orcid.org/0000-0002-8854-6213

Zhannur Amirgalievna Issina — Master of technical sciences, Teaching Assistant, Karaganda Buketov University, Universitetskaya street, 28, 100024, Karaganda, Kazakhstan; e-mail: zhan_isa@mail.ru; https://orcid.org/0000-0001-8087-9585

Assiya Zhakanovna Sarsenbek — Master of natural sciences, Teaching Assistant, Karaganda Buketov University, Universitetskaya street, 28, 100024, Karaganda, Kazakhstan; e-mail: asiya93_93@mail.ru

Nurgul Almatovna Kabdenova — Master of technical sciences, Teaching Assistant, Karaganda Buketov University, Universitetskaya Street, 28, 100024, Karaganda, Kazakhstan; e-mail: nurgul_3005@mail.ru; https://orcid.org/0009-0007-3970-0257

Muslim Anuaruly Kilybay — Master of technical sciences, Teaching Assistant, Karaganda Buketov University, Universitetskaya street, 28, 100024, Karaganda, Kazakhstan; e-mail: muslim-kilybay@mail.ru; https://orcid.org/0000-0002-9339-3282

Author Contributions

The manuscript was written through contributions of all authors. All authors have given approval to the final version of the manuscript. CRediT: **Akmaral Zhakanovna Sarsenbekova, Abylaikhan Nurlanuly Bolatbay** & **David Havlicek** conceptualization, data curation, investigation, methodology, validation, visualization, writing-review & editing; **Zhannur Amirgalievna Issina** & data curation, formal analysis, visualization; **Assiya Zhakanovna Sarsenbek** data curation, formal analysis; **Nurgul Almatovna Kabdenova** & **Muslim Anuaruly Kilybay** conceptualization, data curation, formal analysis, funding acquisition, resources, supervision, validation, writing-original draft, writing-review & editing.

Conflicts of Interest

The authors declare no conflict of interest.

References

1 Sarsenbekova, A. Zh., Zhumanazarova, G. M., Tazhbayev, Y. M., Kudaibergen, G. K., Kabieva, S. K., Issina, Z. A., Kaldybayeva, A. K., Mukabylova, A. O., & Kilybay, M. A. (2023). Research the Thermal Decomposition Processes of Copolymers Based on Polypropyleneglycolfumaratephthalate with Acrylic Acid. *Polymers, 15*(7), 1725. https://doi.org/10.3390/polym15071725

2 Weitsman, Y., & Elahi, M. (2000). Effects of Fluids on the Deformation, Strength and Durability of Polymeric Composites – An Overview. *Mech. Time Depend. Mater.*, *4*(2), 107–126. https://doi.org/10.1023/A:1009838128526

3 Echtermeyer, A. T., Gagani, A., Krauklis, A., & Mazan, T. (2018). Multiscale Modelling of Environmental Degradation – First Steps. Durability of Composites in a Marine Environment 2, 135–149. Berlin/Heidelberg: Springer. https://doi.org/10.1007/978-3-319-65145-3_8

4 McGeorge, D., Echtermeyer, A., Leong, K., Melve, B., Robinson, M., & Fischer, K. (2009). Repair of floating offshore units using bonded fibre composite materials. *Compos. Part A Appl. Sci. Manuf., 40*(9), 1364–1380. https://doi.org/10.1016/j.compositesa.2009.01.015

5 Lee, H.-S., Rhee, S. Y., Yoon, J.-H., Yoo, J.-T., & Min, K. J. (2015). Establishment of Aerospace Composite Materials Data Center for Qualification. *Compos. Res., 28*(6), 402–407. https://doi.org/10.7234/composres.2015.28.6.402

6 Krauklis, A. E. (2019). Environmental Aging of Constituent Materials in Fiber-Reinforced Polymer Composites. *Thesis for the degree of PhD*. Norwegian University of Science and Technology, Trondheim, Norway.

7 Starkova, O., Gagani, A. I., Karl, C. W., Rocha, I. B. C. M., Burlakovs, J., & Krauklis, A. E. (2021). Modelling of Environmental Ageing of Polymers and Polymer Composites — Durability Prediction Methods. *Polymers, 14*(5), 907. https://doi.org/10.3390/polym14050907

8 Krauklis, A. E., Gagani, A. I., & Echtermeyer A. T. (2019). Long-Term Hydrolytic Degradation of the Sizing-Rich Composite Interphase. *Coatings, 9*(4), 263. https://doi.org/10.3390/coatings9040263

9 Chamas, A., Moon, H., Zheng, J., Qiu, Y., Tabassum, T., Jang, J. H. Abu-Omar, M. M., Scott, S. L., & Suh, S. (2020). Degradation Rates of Plastics in the Environment. *ACS Sustain. Chem. Eng.*, 8, 3494–3511. https://doi.org/10.1021/acssuschemeng.9b06635

10 Plota, A., & Masek, A. (2020). Lifetime Prediction Methods for Degradable Polymeric Materials — A Short Review. *Materials, 13*(20), 4507. https://doi.org/10.3390/ma13204507

11 Göpferich, A. (1996). Mechanisms of polymer degradation and erosion. *Biomaterials*, *17*(2), 103–114. https://doi.org/10.1016/0142-9612(96)85755-3

12 Wang, G.-X., Huang, D., Ji, J.-H., Völker, C., & Wurm, F. R. (2020). Seawater-Degradable Polymers — Fighting the Marine Plastic Pollution. *Adv. Sci.*, *8*, 2001121. https://doi.org/10.1002/advs.202001121

13 Lott, C., Eich A., Makarow, D., Unger, B., van Eekert, M., Schuman, E., Reinach, M. S., Lasut, M. T., & Weber, M. (2021). Half-Life of Biodegradable Plastics in the Marine Environment Depends on Material, Habitat, and Climate Zone. *Front. Mar. Sci.*, 8, 426. https://doi.org/10.3389/fmars.2021.662074

14 Ghosh, K., & Jones, B. H. (2021). Roadmap to Biodegradable Plastics—Current State and Research Needs. *ACS Sustain. Chem. Eng.*, 9, 6170–6187. https://doi.org/10.1021/acssuschemeng.1c00801

15 Dřímal, P., Hoffmann, J., & Družbík, M. (2007). Evaluating the aerobic biodegradability of plastics in soil environments through GC and IR analysis of gaseous phase. *Polym. Test.*, *26*(6), 729–741. https://doi.org/10.1016/j.polymertesting.2007.03.008

16 Kunioka, M., Ninomiya, F., & Funabashi, M. (2007). Novel evaluation method of biodegradabilities for oil-based polycaprolactone by naturally occurring radiocarbon-14 concentration using accelerator mass spectrometry based on ISO 14855-2 in controlled compost. *Polym. Degrad. Stab.*, 92, 1279–1288. https://doi.org/10.1016/j.polymdegradstab.2007.03.028

17 Di Bartolo, A., Infurna, G., & Dintcheva, N. (2021). A Review of Bioplastics and Their Adoption in the Circular Economy. *Polymers*, 13, 1229. https://doi.org/10.3390/polym13081229

18 Degli Innocenti, F., & Breton, T. (2020). Intrinsic Biodegradability of Plastics and Ecological Risk in the Case of Leakage. *ACS Sustain. Chem. Eng.* 8, 9239–9249. https://doi.org/10.1021/acssuschemeng.0c01230

19 Krauklis, A. E., Akulichev, A. G., Gagani, A., & Echtermeyer, A. T. (2019). Time—Temperature—Plasticization Superposition Principle: Predicting Creep of a Plasticized Epoxy. *Polymers*, 11, 1848. https://doi.org/10.3390/polym11111848

20 Wang, M., Xu, X., Ji, J., Yang, Y., Shen, J., & Ye, M. (2016). The hygrothermal aging process and mechanism of the novolac epoxy resin. *Compos. Part B Eng.*, 107, 1–8. https://doi.org/10.1016/j.compositesb.2016.09.067

21 Clancy, T., Frankland, S., Hinkley, J., & Gates, T. (2009). Molecular modeling for calculation of mechanical properties of epoxies with moisture ingress. *Polymer*, 50(12), 2736–2742. https://doi.org/10.1016/j.polymer.2009.04.021

22 Krauklis, A., Gagani, A. I., & Echtermeyer, A. T. (2018). Hygrothermal Aging of Amine Epoxy: Reversible Static and Fatigue Properties. *Open Eng.*, *8*, 447–454. https://doi.org/10.1515/eng-2018-0050

23 Starkova, O., Gaidukovs, S., Platnieks, O., Barkane, A., Garkusina, K., Palitis, E., & Grase, L. (2021). Water absorption and hydrothermal ageing of epoxy adhesives reinforced with amino-functionalized graphene oxide nanoparticles. *Polym. Degrad. Stab.*, 191, 109670. https://doi.org/10.1016/j.polymdegradstab.2021.109670

24 Celina, M. C., Dayile, A. R., & Quintana, A. (2013). A perspective on the inherent oxidation sensitivity of epoxy materials. *Polymer*, *54*(13), 3290–3296. https://doi.org/10.1016/j.polymer.2013.04.042

25 Down, J. L. (1986). The Yellowing of Epoxy Resin Adhesives: Report on High-Intensity Light Aging. *Studies in Conservation*, *31*(4), 159. https://doi.org/10.2307/1506247

26 Ernault, E., Richaud, E., & Fayolle, B. (2017). Thermal-oxidation of epoxy/amine followed by glass transition temperature changes. *Polym. Degrad. Stab.*, 138, 82–90. https://doi.org/10.1016/j.polymdegradstab.2017.02.013

27 Burkeev, M. Zh., Zhumanazarova G. K., & Zhakupbekova E. Zh. et al. (2020). Research of the influence of external factors on copolymersbased on unsaturated polyester resins. *Bulletin of the University of Karaganda — Chemistry*, *2*, 98, 51–57. https://doi.org/10.31489/2020Ch2/51-57

28 Burkeev, M. J., Tajbaev, E. M., Mustafin, E. S., Fomin, V. N., & Magzumova, A. K. (2008). *Sposob polucheniia nenasyschennoi poliefirnoi smoli iz maleinovoi kisloty i etilenglikolia [Method of Obtaining of Unsaturated Polyester Resin from Maleic Acid and Ethylene Glycol]*. Innovatsionnyi patent 31799/02, 26 Dekabr 2008 [in Russian].

29 Burkeev, M. J., Kovaleva, A. K., Tajbaev, E. M., Jakupbekova, E. J., & Jumagalieva, T. S. (2016). *Sposob polucheniia nenasyschennih poliefirnykh smol na osnove propilenglikolia ftalevogo angidrida i fumarovoi kisloti [The method of obtaining unsaturated polyester resins based on propylene glycol, phthalic anhydride and fumaric acid acids]*. Innovatsionnyi patent 31052/04, 15 Aprel 2016 [in Russian].

30 Burkeev, M. Z., Shibayeva, S. R., Khamitova, T. O., Plocek, J., Tazhbayev, Y. M., Davrenbekov, S. Z., Nurmaganbetova, M. T., Kazhmuratova, A. T., Zhumagalieva, T. S., & Kezdikbayeva, A. T. (2021). Synthesis and Catalytic Properties of New Polymeric Monometallic Composites Based on Copolymers of Polypropylene Glycol Maleate Phthalate with Acrylic Acid. *Polymers*, 13, 4369. https://doi.org/10.3390/polym13244369

31 Burkeev, M. Zh., Zhumanazarova, G. M., Tazhbayev, E. M., Kudaibergen, G. K., Aukadieva, S. B., & Zhakupbekova, E. Zh. (2020). Poly(propylenefumarate phthalate)and acrylic acid radical copolymerization constants and parameters. *Bulletin of the Karaganda University. “Chemistry” Series*, *97*(1), 68–74. https://doi.org/10.31489/2020ch1/68-74

32 Sarsenbekova, A. Zh., Kudaibergen, G.K., & Burkeev, M.Zh. (2019). Comparative analysis of the Thermal Decomposition Kinetics of Polyethylene Glycol Fumarate-Acrylic Acid Copolymers. *Russian journal of physical chemistry*, 7, 93, 1252-1257. https://doi.org/10.1134/s0036024419060281

How to Cite: Kwiatkowski, A.L., Kalinin P.V., & Philippova, O.E. (2024) Effect of Salt Content on Solubilization of Hydrophobic Polymer by Wormlike Micelles of Ionic Surfactant. *Eurasian Journal of Chemistry, 29, 2(114), 74-80.* https://doi.org/10.31489/2959-0663/2-24-15

Article

Received: 28 February 2024 | Revised: 6 April 2024 |
Accepted: 15 April 2024 | Published online: 24 April 2024

UDC 544.42+519.242.7

https://doi.org/10.31489/2959-0663/2-24-15

Alexander L. Kwiatkowski*, Pavel V. Kalinin, Olga E. Philippova

Physics Department, Lomonosov Moscow State University, Moscow, Russia
*(*Corresponding author's e-mail: kvyatkovskij@physics.msu.ru)*

Effect of Salt Content on Solubilization of Hydrophobic Polymer by Wormlike Micelles of Ionic Surfactant

The effect of concentration of inorganic salt KCl on solubilization of hydrophobic polymer poly(4-vinylpyridine) (P4VP) in aqueous solutions of ionic surfactant potassium oleate was experimentally investigated. As was shown by rheology, in the range of concentrations from 1 to 5 wt.% of salt the polymer-free solutions of surfactant mainly contain linear wormlike micelles (WLMs). The formation of branched WLMs was observed in the solutions containing 5–9 wt.% of KCl. In the presence of higher salt content the phase separation occurred, indicating the formation of a highly branched saturated network of WLMs. Enhanced screening of the charged groups of potassium oleate by oppositely charged ions of KCl caused elongation and branching of micelles that reflected in zero-shear viscosity of the solutions passing through the maximum. In the phase diagram, the saturation concentration with P4VP of both linear and branched WLMs decreased with increasing salt content. In the case of linear WLMs, this could be explained by the constant number of embedded polymer chains per 1 WLM, while simultaneously decreasing number of WLMs in the system. As for the branched WLMs, it was caused by shortening of the linear parts of micelles due to the formation of branching points. For this reason, almost no P4VP was dissolved in the solution containing the highly branched saturated network.

Keywords: ionic surfactant, polymer solubilization, wormlike micelles, hybrid micelles, branched micelles, saturated network, rheology, phase diagram.

Introduction

Ionic surfactants are able to self-assemble into very long micelles with local cylindrical morphology. They are called wormlike micelles (WLMs) [1–4]. These micelles typically have a diameter of a few nanometers and a contour length of up to several micrometers producing micellar aggregates that resemble worms. These worms, when entangled in a transient network, impart significant macroscopic viscoelastic properties to solutions. Their viscoelastic properties are easy to manipulate because the non-covalently bonded network of WLMs is highly sensitive to external conditions, such as the concentration of low molecular weight salt [5–10] or hydrophobic additives [1–3, 11–13]. Ions of salt screen the electrostatic repulsion of similarly charged surfactant head groups and induce the elongation of micelles and their branching [5–10], as they make hemispherical end caps of WLMs highly unfavorable. In contrast, hydrocarbons induce shortening of micelles and finally their transformation into microemulsion droplets, because they concentrate in the micellar core [14-15].

These properties of WLMs are of extended practical significance. In particular, they allow WLMs to be used as oil-sensitive thickeners for fracturing fluids in oil recovery [16–18]. In contrast to polymer-based fracturing fluids, the surfactant-based fluids have the advantage of not requiring the addition of breakers to reduce the viscoelasticity at the back flow of oil [19], because they spontaneously transform into microemulsion droplets upon contact with hydrocarbons. At the same time, for further transportation of oil through the pipeline the polymer chains possess an advantage — they provide higher drag reducing efficiency. The advantages of both surfactant- and polymer-based fluids for hydraulic fracturing and oil transportation can be combined while using hybrid WLMs of surfactant with embedded polymer chains. Such a system has recently been proposed [20]. It consisted of WLMs of potassium oleate armored with poly(4-vinylpyridine) (P4VP) polymeric chains [20].

However, all the experiments were carried out at a single salt concentration, whereas in practical applications different salt concentrations may be encountered. The salinity of the solution significantly affects the shape of hybrid micelles and the location of the polymer within them [21]. This, in turn, impacts the maximum amount of polymer that can be solubilized inside the micelles and becomes one of the key parameters that govern hydraulic fracturing and drag reduction when using hybrid micelles.

The present paper is aimed at the experimental investigation of the effect of salt on the phase behavior of the hybrid micelles of anionic surfactant potassium oleate with embedded hydrophobic polymer P4VP and the determination of the maximum amount of polymer that can be solubilized by the micelles at different concentrations of inorganic salt KCl.

Experimental

Materials. Surfactant potassium oleate (TCI Europe, purity >98 %), salt KCl (Sigma-Aldrich, purity > 99.5 %) and polymer P4VP (Sigma-Aldrich, Mw=160000 g/mol, contour length 380 nm) were used for preparation of hybrid surfactant/polymer micelles. Polydispersity of P4VP, as evaluated by dynamic light scattering, was equal to 0.06 (see Supplementary Materials for details). P4VP was dissolved in ethanol (Merck, purity > 99 %). Other solutions were prepared with de-ionized water purified using Millipore Milli-Q system. The pH of aqueous solutions was maintained at 11 with KOH (Acros Organics, purity > 99 %).

Sample preparation. A series of polymer-free micellar solutions with constant concentration of surfactant equal to 47 mM and salt concentration ranging from 1 to 11 wt% were prepared by mixing potassium oleate and KCl with water using a magnetic stirring bar for 1 day. At high salt concentration (9, 10 and 11 wt%) the solutions became phase separated (Fig. 1).

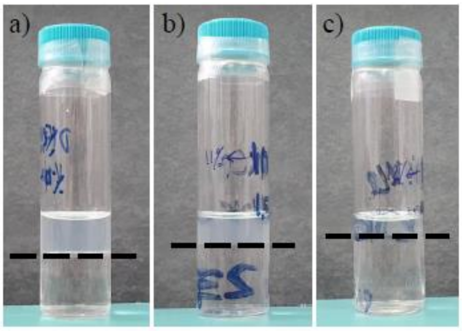

Figure 1. Phase separated polymer-free aqueous solutions of 47 mM potassium oleate containing different concentrations of KCl: 9 (a), 10 (b) and 11 wt% (c) at pH 11. The horizontal dashed lines indicate the interfaces

As P4VP is insoluble in water, the following method, previously described elsewhere [21], was used to prepare hybrid potassium oleate/P4VP micelles. First, a stock solution of hybrid potassium oleate/P4VP micelles was obtained in the absence of salt. For this purpose, an aqueous solution of potassium oleate was poured onto the thin film of polymer P4VP in the vial and stirred for 24 hours. The polymer film was preliminary formed by evaporation of ethanol from the P4VP solution during 24 hours at room temperature. The concentration of P4VP in the stock solutions was varied from 0 to 0.4 wt%. Then an appropriate amount of potassium oleate with water was added to the same vial to prepare solutions of hybrid micelles at different salt concentrations.

Rheology. The steady shear and shear oscillatory rheology was measured on a stress-controlled Anton Paar Physica MCR 301 rheometer. Aluminum cone-plate (50 mm, 1°) and Couette (i.d. 24.661 mm, o.d 26.667 mm) geometries were used as measuring cells for viscous and fluid samples, respectively. Peltier elements were used to maintain a constant temperature of 20 °C. Steady shear tests were conducted at shear rates ranging from $3\cdot10^{-3}$ to 300 1/s. The oscillatory shear tests were carried out in the frequency range from $2\cdot10^{-2}$ to 200 rad/s within the viscoelastic linear regime as previously determined by strain measurements.

Determination of the saturation concentration of hybrid micelles at high salt content. In the solutions of hybrid micelles with a high amount of embedded P4VP, at all studied concentrations of salt, the phase separation occurred leading to the precipitation of polymer. At low concentrations of KCl, the saturation concentration of hybrid micelles was visually detected by the appearance of turbidity. When a high amount of KCl was added (7, 8 and 9 wt%), for more accurate determination of the saturation concentration, the solid precipitate was carefully separated from the homogeneous liquid phase and dried in an oven until a constant mass was obtained. After weighing the dried precipitate, the dependencies of thus determined mass of the precipitate on the initial concentration of added P4VP at 7, 8 and 9 wt% of KCl were obtained. They represent straight lines (Fig. 2). The x-coordinates of their intersections with the horizontal axis correspond to the saturation concentrations of hybrid potassium oleate/P4VP micelles in the presence of different concentrations of KCl.

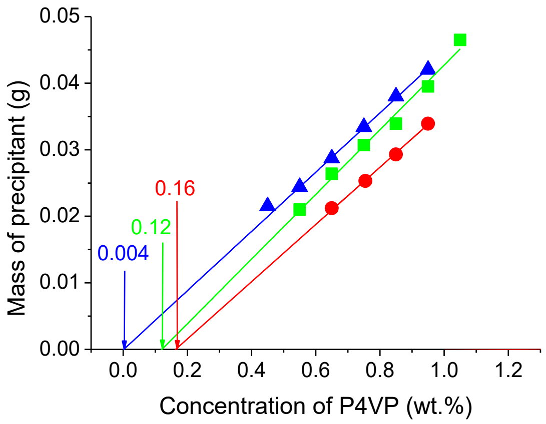

Figure 2. The dependencies of the mass of the precipitate on the initial concentration of added P4VP in 47 mM aqueous solutions of potassium oleate containing different concentrations of KCl: 7 wt% (circles), 8 wt% (squares), and 9.0 wt% (triangles) at pH 11. The arrows indicate the position of the intersection of the dependencies with the horizontal axis

Results and Discussion

Effect of salt on polymer-free micelles. The steady shear and oscillatory rheological data of the polymer-free solutions of potassium oleate at different concentrations of KCl are shown in Figures 3a and b, respectively. In Figure 3a at low shear rates the plateau of the viscosity is observed (i.e. zero-shear viscosity η_0). In the literature [1, 22–24], the plateau-value η_0 is attributed to the viscosity of the solution undamaged by shear (Figure 3a). The subsequent decrease in viscosity, called shear-thinning [9, 24–26], is the result of the alignment of the chains along the direction of the shear flow (Fig. 3a).

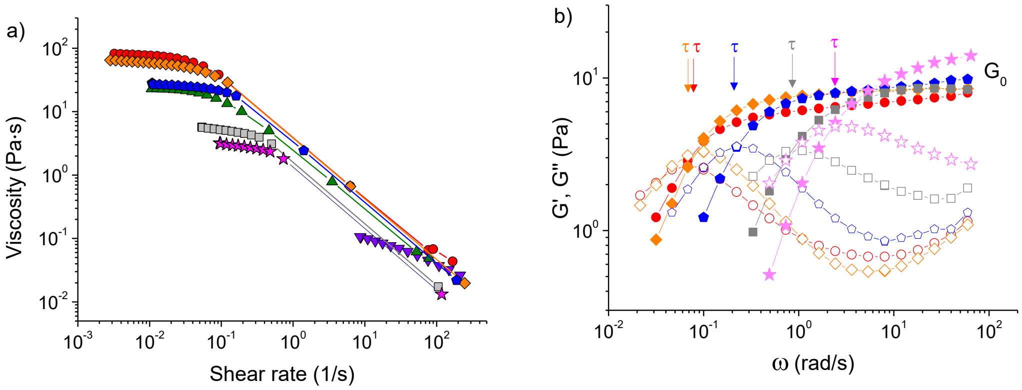

Figure 3. Apparent viscosity versus shear rate (a) and storage G' (filled symbols) and loss G'' (open symbols) moduli versus frequency of the applied stress ω (b) for 47 mM potassium oleate solutions, containing different concentrations of KCl: 4.0 wt% (circles), 6.0 wt% (diamonds), 7.0 wt% (pentagons), 8.5 wt%. (squares) and 9.0 wt% (stars) at pH 11. The arrows indicate the position of the intersection of the $G'(\omega)$ and $G''(\omega)$ dependencies

The value of η_0 passes through the maximum with increasing concentration of KCl (Fig. 4). As the K^+ ions of salt screen the repulsion of the negatively charged headgroups of potassium oleate on the surface of micelles, the increase of the amount of KCl in the solutions induces the transition of spherical micelles into the wormlike ones and their further elongation. This results in an increase of the η_0 value by 3 orders of magnitude (Fig. 4). At concentrations of KCl higher than 6 wt.%, the zero-shear viscosity decreases due to the formation of branches in the micelles [10, 26-27]. The relaxation mechanism of branched WLMs, which represents sliding of the branching points along the micelle, requires less energy, than process of reptation in semidilute solutions of linear micelles [10, 28–30]. The phase separation in the samples with high salt content (Fig. 1), is probably related to the formation of a saturated network of WLMs, which contains many branching points and almost no end-caps [26, 31-32].

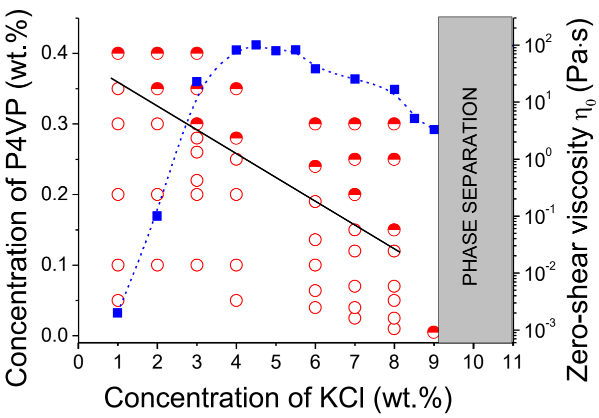

Figure 4. Zero-shear viscosity η_0 of polymer-free solutions (blue) and phase diagram of potassium oleate/P4VP hybrid micelles (red) versus concentration of KCl. Open circles indicate homogeneous and filled circles indicate phase separated samples. Solid line indicates the onset of phase separation in potassium oleate/P4VP hybrid micelles. The grey square limits the region of phase separation in 47 mM potassium oleate solutions without polymer at pH 11

The dependencies of storage G' and loss G'' moduli on the frequency ω of shear stress applied to the micellar solutions with different salt content are depicted in Figure 3b. At high frequencies, $G' > G''$, and the solutions demonstrate an elastic response to the applied stress. According to literature [2, 27, 33], the plateau value of storage modulus G_0 is proportional to the amount of elastically active entanglements between the micelles in the physical network. At low frequencies, $G' < G''$, and the samples behave as viscous liquids. The studied samples demonstrate Maxwellian behavior with single relaxation time [10, 23-24, 34]. The abscissa intercept ω_c of $G'(\omega)$ and $G''(\omega)$ defines the relaxation time of the samples τ, as $\tau = \omega_c^{-1}$ (Fig. 3b).

In Figure 3b a small increase of the plateau modulus G_0 at high salt concentration is observed. This may be due to the intermicellar linkages produced by branching of WLMs occurring upon screening of the repulsion of similarly charged headgroups of surfactant with oppositely charged ions of salt. Simultaneously, the relaxation time τ is decreasing with increasing amount of branching points, since more rapid relaxation occurs (Fig. 3b) as a result of sliding of branches along the worms. Similar results have been obtained previously for other systems containing WLMs of ionic surfactants [1, 9-10, 26, 35-36].

Solubilization of P4VP by WLMs at different salt content. In order to investigate the solubilization of P4VP by micelles of potassium oleate at different concentrations of KCl, the following phase diagram was constructed (Fig. 4). At all the concentrations, a solid precipitate was formed when a large amount of polymer was added to the system. In the solution with 6 % KCl, elemental analysis previously demonstrated that the precipitate was the pure polymer (without surfactant) [37]. The supernatant represented the solution of hybrid micelles saturated with P4VP. Therefore, in this study, the formation of a precipitate indicates that the micelles have reached their saturation with a polymer.

From Figure 4 it can be seen that the concentration of saturation of micelles with polymer decreases with increasing salt content. In the range of 1–5 wt.% of KCl mainly linear WLMs are present in the polymer-free solutions. The viscosity of the solutions increases due to elongation of micelles (Fig. 4). At constant concentration of surfactant, the elongation of micelles is accompanied by a decrease of the total number of micelles in the system. According to the literature [37], 1-2 macromolecules of P4VP are embedded into linear WLMs of potassium oleate. Solubilization of a larger number of macromolecules is energetically unfavorable, since leads to the drop of entropy. As a result, the total amount of P4VP chains in saturated hybrid micelles decreases.

Another possible reason for the decrease in the saturation concentration of linear WLMs could be the increase of the packing density of surfactant molecules in their central part. Higher screening of potassium oleate anions by counterions of KCl will provide their closer approach to each other and reduction of the volume at the boundary between the hydrophobic core and hydrophilic corona of the micelles, where P4VP is localized [37-38].

The rheological data (Fig. 3a) demonstrated the drop of viscosity of the solutions without polymer in the range 5–9 wt.% of KCl (Fig. 4) due to the enhanced amount of branched WLMs. The formation of branching points in the micelles appears simultaneously with shortening of their central cylindric parts [39-40], where P4VP chains are embedded in the hybrid micelles [37]. Consequently, the presence of branched micelles can lead to a decrease in the concentration of saturation with polymer (Fig. 4). It is unlikely that the polymer will be solubilized at the branching points due to their high mobility. This accounts for the near-absence of solubility of PVP in systems with more than 9 wt% of KCl (Fig. 4).

Thus, the increasing ionic strength of solutions similarly affects the solubilization of P4VP, both, by linear and branched WLMs of potassium oleate (Fig. 4).

Conclusions

According to rheological data, in aqueous solutions of 47 mM potassium oleate with 1–5 wt% of KCl mostly linear WLMs are present. The zero-shear viscosity η_0 of the solutions increases with increasing length of WLMs due to screening of the electrostatic repulsion of surfactant headgroups. Branched WLMs are formed at KCl concentration between 5 and 9 wt%. The faster relaxation mechanism of branched WLMs results in the decrease in η_0 and relaxation time τ as evidenced by rheology. The concentration of P4VP in the saturated hybrid micelles decreases in the whole range of KCl concentration studied. For linear WLMs, it is the result of a constant number of polymer chains being embedded per 1 WLM at the time when the total number of WLMs decreases in the system. As to the branched WLMs, the drop of saturation concentration is caused by low probability of P4VP solubilization by mobile branching points, where the boundary between the hydrophobic core and hydrophilic corona of the micelles, where P4VP is localized, is reduced, and the reduction of linear parts of the micelles. For this reason, almost no P4VP was dissolved in the solution with 9 wt.% of KCl, which contained the highly branched saturated network of WLMs.

Supplementary Materials

Supplementary Materials is available free at https://ejc.buketov.edu.kz/index.php/ejc/article/view/92/81

Funding

This research was financially supported by the Russian Science Foundation (project № 21-73-10197).

*Author Information**

**The authors' names are presented in the following order: First Name, Middle Name and Last Name*

Alexander Lvovich Kwiatkowski (*corresponding author*) — Candidate of physical and mathematical sciences, Leading Researcher, Lomonosov Moscow State University, Leninskie Gory, 1, 2, Moscow, 119991, Russia; e-mail: kvyatkovskij@physics.msu.ru; https://orcid.org/0000-0002-0514-384X

Pavel Vasilyevich Kalinin — Bachelor in physics, Lomonosov Moscow State University, Leninskie Gory, 1, 2, Moscow, 119991, Russia; e-mail: kalinin@polly.phys.msu.ru

Olga Evgenievna Philippova — Doctor of physical and mathematical sciences, Professor, Lomonosov Moscow State University, Leninskie Gory, 1, 2, Moscow, 119991, Russia; e-mail: phil@polly.phys.msu.ru; https://orcid.org/0000-0002-1098-0255

Author Contributions

The manuscript was written through contributions of all authors. All authors have given approval to the final version of the manuscript. CRediT: **Alexander Lvovich Kwiatkowski** investigation, original draft preparation, review and editing; **Pavel Vasilyevich Kalinin** investigation; **Olga Evgenievna Philippova** original draft preparation, review and editing.

Conflicts of Interest:

The authors declare no conflict of interest.

References

1 Feng, Y., Chu, Z., & Dreiss, C. A. (2015). *Smart Wormlike Micelles: Design, Characteristics and Applications*. Springer-Verlag: Berlin, Heidelberg.

2 Dreiss, C. A., & Feng, Y. (2017). *Wormlike Micelles: Advances in Systems, Characterisation and Applications*. The Royal Society of Chemistry.

3 Zana, R., & Kaler, E. W. (2007). *Giant Micelles: Properties and Applications*. CRC Press.

4 Zana, R. (2003). Polymer/surfactant systems. In K. Esumi & M. Ueno (Eds.). *Structure-performance relationships in surfactants* (pp. 547–599).

5 Hassan, P. A., Raghavan, S. R., & Kaler, E. W. (2002). Microstructural Changes in SDS Micelles Induced by Hydrotropic Salt. *Langmuir, 18*(7), 2543–2548. https://doi.org/10.1021/la011435i

6 Candau, S. J., Khatory, A., Lequeux, F., & Kern, F. (1993). Rheological Behaviour of Wormlike Micelles: Effect of Salt Content. *Journal de Physique IV Colloque*, *3*, 197–209. https://doi.org/10.1051/jp4:1993117

7 Khatory, A., Lequeux, F., Kern, F., & Candau, S. J. (1993). Linear and Nonlinear Viscoelasticity of Semidilute Solutions of Wormlike Micelles at High Salt Content. *Langmuir*, *9*(2), 1456–1464. https://doi.org/10.1021/la00030a005

8 Oelschlaeger, C., Suwita, P., & Willenbacher, N. (2010). Effect of Counterion Binding Efficiency on Structure and Dynamics of Wormlike Micelles. *Langmuir*, *26*(10), 7045–7053. https://doi.org/10.1021/la9043705

9 Kwiatkowski, A. L., Molchanov, V. S., Orekhov, A. S., Vasiliev, A. L., & Philippova, O. E. (2016). Impact of Salt Co- and Counterions on Rheological Properties and Structure of Wormlike Micellar Solutions. *The Journal of Physical Chemistry B*, *120*(49), 12547–12556. https://doi.org/10.1021/acs.jpcb.6b09817

10 Kwiatkowski, A. L., Molchanov, V. S., & Philippova, O. E. (2019). Polymer-like Wormlike Micelles of Ionic Surfactants: Structure and Rheological Properties. *Polymer Science — Series A*, *61*(2), 215–225. https://doi.org/10.1134/S0965545X19020081

11 Siriwatwechakul, W., LaFleur, T., Prud'homme, R. K., & Sullivan, P. (2004). Effects of Organic Solvents on the Scission Energy of Rodlike Micelles. *Langmuir*, *20*(21), 8970–8974. https://doi.org/10.1021/la035853u

12 Francisco, K. R., Marcelo, A., Sabadini, E., Karlsson, G., & Dreiss, C. A. (2010). Effect of Monomeric and Polymeric Co-Solutes on Cetyltrimethylammonium Bromide Wormlike Micelles : Rheology, Cryo-TEM and Small-Angle Neutron Scattering. *Journal of Colloid And Interface Science*, *345*(2), 351–359. https://doi.org/10.1016/j.jcis.2010.01.086

13 Afifi, H., Karlsson, G., Heenan, R. K., & Dreiss, C. A. (2011). Solubilization of Oils or Addition of Monoglycerides Drives the Formation of Wormlike Micelles with an Elliptical Cross-Section in Cholesterol-Based Surfactants: A Study by Rheology, SANS, and Cryo-TEM. *Langmuir*, *27*(12), 7480–7492. https://doi.org/10.1021/la201026s

14 Shibaev, A. V., Ospennikov, A. S., Kuznetsova, E. K., Kuklin, A. I., Aliev, T. M., Novikov, V. V., & Philippova, O. E. (2022). Universal Character of Breaking of Wormlike Surfactant Micelles by Additives of Different Hydrophobicity. *Nanomaterials*, *12*(24). https://doi.org/10.3390/nano12244445

15 Shibaev, A. V., Tamm, M. V., Molchanov, V. S., Rogachev, A. V., Kuklin, A. I., Dormidontova, E. E., & Philippova, O. E. (2014). How a Viscoelastic Solution of Wormlike Micelles Transforms into a Microemulsion upon Absorption of Hydrocarbon: New Insight. *Langmuir*, *30*(13), 3705–3714. https://doi.org/10.1021/la500484e

16 Yang, J. (2002). Viscoelastic Wormlike Micelles and Their Applications. *Current Opinion in Colloid and Interface Science*, *7*(5–6), 276–281. https://doi.org/10.1016/S1359-0294(02)00071-7

17 Tong, S., Gu, M., Singh, R., & Mohanty, K. K. (2019). Proppant transport in foam fracturing fluid during hydraulic fracturing. *Journal of Petroleum Science and Engineering*, *182*, 106279. https://doi.org/10.1016/j.petrol.2019.106279

18 Davoodi, S., Al-Shargabi, M., Wood, D. A., & Rukavishnikov, V. S. (2023). A comprehensive review of beneficial applications of viscoelastic surfactants in wellbore hydraulic fracturing fluids. *Fuel*, *338*, 127228. https://doi.org/10.1016/j.fuel.2022.127228

19 Barati, R., & Liang, J. T. (2014). A review of fracturing fluid systems used for hydraulic fracturing of oil and gas wells. *Journal of Applied Polymer Science*, *131*(16), 1–11. https://doi.org/10.1002/app.40735

20 Kwiatkowski, A. L., Molchanov, V. S., Chesnokov, Y. M., Ivankov, O. I., & Philippova, O. E. (2023). Hybrid Polymer–Surfactant Wormlike Micelles for Concurrent Use for Oil Recovery and Drag Reduction. *Polymers*, *15*(23). https://doi.org/10.3390/polym15234615

21 Kwiatkowski, A. L., Molchanov, V. S., Kuklin, A. I., Chesnokov, Y. M., & Philippova, O. E. (2022). Salt-Induced Transformations of Hybrid Micelles Formed by Anionic Surfactant and Poly(4-vinylpyridine). *Polymers*, *14*, 5086. https://doi.org/10.3390/polym14235086

22 Croce, V., Cosgrove, T., Dreiss, C. A., King, S., Maitland, G., & Hughes, T. (2005). Giant Micellar Worms under Shear: A Rheological Study Using SANS. *Langmuir*, *21*(15), 6762–6768. https://doi.org/10.1021/la0479410

23 Schramm, G. G. S. (1994). *A Practical Approach to Rheology and Rheometry*. Gebrueder Haake.

24 Malkin, A. Y., & Isayev, A. I. (2012). *Rheology Concepts, Methods, and Applications*. Elsevier. https://doi.org/https://doi.org/10.1016/B978-1-895198-49-2.50001-3

25 Förster, S., Konrad, M., & Lindner, P. (2005). Shear thinning and orientational ordering of Wormlike Micelles. *Physical Review Letters*, *94*(1), 14–17. https://doi.org/10.1103/PhysRevLett.94.017803

26 Rogers, S. A., Calabrese, M. A., & Wagner, N. J. (2014). Rheology of Branched Wormlike Micelles. *Current Opinion in Colloid and Interface Science*, *19*(6), 530–535. https://doi.org/10.1016/j.cocis.2014.10.006

27 Dreiss, C. A. (2007). Wormlike Micelles: Where Do We Stand? Recent Developments, Linear Rheology and Scattering Techniques. *Soft Matter*, *3*(8), 956–970. https://doi.org/10.1039/b705775j

28 Lequeux, F. (1992). Reptation of Connected Wormlike Micelles. *Europhysics Letters*, *19*(8), 675–681. https://doi.org/10.1209/0295-5075/19/8/003

29 Lequeux, F. (1996). Structure and rheology of wormlike micelles. *Current Opinion in Colloid & Interface Science*, *1*(3), 341–344. https://doi.org/10.1016/S1359-0294(96)80130-0

30 Croce, V., Cosgrove, T., Maitland, G., & Hughes, T. (2003). Rheology, Cryogenic Transmission Electron Spectroscopy, and Small-Angle Neutron Scattering of Highly Viscoelastic Wormlike Micellar Solutions. *Langmuir*, *19*(10), 8536–8541. https://doi.org/10.1021/la0345800

31 Georgiev, M. T., Aleksova, L. A., Kralchevsky, P. A., & Danov, K. D. (2020). Phase separation of saturated micellar network and its potential applications for nanoemulsification. *Colloids and Surfaces A: Physicochemical and Engineering Aspects*, *607*(June), 125487. https://doi.org/10.1016/j.colsurfa.2020.125487

32 Bernheim-Groswasser, A., Zana, R., & Talmon, Y. (2000). Sphere-to-Cylinder Transition in Aqueous Micellar Solution of a Dimeric (Gemini) Surfactant. *Journal of Physical Chemistry B*, *104*(17), 4005–4009. https://doi.org/10.1021/jp994301a

33 De Gennes, P. G. G. (1979). *Scaling Concepts in Polymer Physics*. University Press.

34 Calabrese, M. A., Rogers, S. A., Murphy, R. P., & Wagner, N. J. (2015). The Rheology and Microstructure of Branched Micelles under Shear. *Journal of Rheology*, *59*(5), 1299–1328. https://doi.org/10.1122/1.4929486

35 Riley, J. K., Richards, J. J., Wagner, N. J., & Butler, P. D. (2018). Branching and Alignment in Reverse Worm-like micelles Studied with Simultaneous Dielectric Spectroscopy and RheoSANS. *Soft Matter*, *14*(26), 5344–5355. https://doi.org/10.1039/C8SM00770E

36 Parker, A., & Fieber, W. (2013). Viscoelasticity of Anionic Wormlike Micelles: Effects of Ionic Strength and Small Hydrophobic Molecules. *Soft Matter*, *9*(4), 1203–1213. https://doi.org/10.1039/C2SM27078A

37 Kwiatkowski, A. L., Sharma, H., Molchanov, V. S., Orekhov, A. S., Vasiliev, A. L., Dormidontova, E. E., & Philippova, O. E. (2017). Wormlike surfactant micelles with embedded polymer chains. *Macromolecules*, *50*(18), 7299–7308. https://doi.org/10.1021/acs.macromol.7b01500

38 Kwiatkowski, A. L., Molchanov, V. S., Sharma, H., Kuklin, A. I., Dormidontova, E. E., & Philippova, O. E. (2018). Growth of wormlike micelles of surfactant induced by embedded polymer: role of polymer chain length. *Soft Matter*, *14*, 4792–4804. https://doi.org/10.1039/C8SM00776D

39 Calabrese, M. A., & Wagner, N. J. (2018). Detecting Branching in Wormlike Micelles via Dynamic Scattering Methods. *ACS Macro Letters*, *7*(6), 614–618. https://doi.org/10.1021/acsmacrolett.8b00188

40 Victorov, A. I. (2019). Self-Assembly into Branches and Networks. In R. Nagarajan (Ed.), *Self-Assembly. From Surfactants to Nanoparticles* (pp. 41–75). John Wiley and Sons.

How to Cite: Shakayeva, A.Kh., Yeszhanov, A.B., Zhumazhanova, A.T., Korolkov, I.V., Zdorovets, M.V. (2024) Fabrication of Hydrophobic PET Track-Etched Membranes using 2,2,3,3,4,4,4-Heptafluorobutyl Methacrylate for Water Desalination by Membrane Distillation. *Eurasian Journal of Chemistry, 29, 2(114), 81-88.* https://doi.org/10.31489/2959-0663/2-24-5

CHEMICAL TECHNOLOGY

Article

Received: 25 January 2024 | Revised: 2 May 2024 |
Accepted: 10 May 2024 | Published online: 17 May 2024

UDC 62-278, 66.067

https://doi.org/10.31489/2959-0663/2-24-5

Aigerim Kh. Shakayeva[1*], Arman B. Yeszhanov[1], Ainash T. Zhumazhanova[1],
Ilya V. Korolkov[1], Maxim V. Zdorovets[1]

Institute of Nuclear Physics of the Republic of Kazakhstan, Almaty, Kazakhstan
*(*Corresponding author's e-mail: shakayevaa19@gmail.com)*

Fabrication of Hydrophobic PET Track-Etched Membranes using 2,2,3,3,4,4,4-Heptafluorobutyl Methacrylate for Water Desalination by Membrane Distillation

The world is currently facing a drinking water problem. Human activity, climate change and pollution of existing water bodies are exacerbating the problem. The scientists around the world are currently trying to purify water using effective and inexpensive methods. One such method is membrane distillation. Membrane distillation is a versatile thermally driven membrane separation process. This method of water purification has the potential to remove salts and other non-volatile components. The work is concerned with the desalination of salt solutions by membrane distillation using ion-track membranes based on polyethylene terephthalate (PET). PET ion-track membranes (PET TMs) were modified by photoinitiated graft polymerization of 2,2,3,3,4,4,4-heptafluorobutyl methacrylate (HFBMA) to make them hydrophobic. Optimal polymerization conditions (monomer concentration, reaction time) were determined, which led to an increase of water CA from 51 to 105°. The obtained membranes were used to purify the solution from NaCl. The effect of salt concentration as well as membrane properties on performance and degree of purification was studied. The results show that large pore size PET TMs modified with HFBMA has the potential to desalinate water in an efficient manner.

Keywords: Ion-track membranes, membrane distillation, UV-initiated grafting, poly(ethylene terephthalate), water desalination, fluorine-containing compounds.

Introduction

Water plays a vital role in sustaining life on Earth. Although most of the planet is made up of water, but water scarcity is a major concern for the world's population [1]. Fresh water, which is essential for the survival of plants and mammals, including humans, accounts for only 3 % of the hydrosphere. The rest is salt water, which is not suitable for human consumption [2]. Population growth, rapid industrial development, urbanization and climate change are all increasing the demand for water and exacerbating the problem of pollution of available water bodies. All of these factors contribute significantly to the global water deficit. The search for effective and affordable methods of desalination is urgent [3].

A significant part of the Earth is made up of salt water. There is an urgent need to desalinate this water by removing salts and minerals [4]. There are currently several methods of water treatment reverse osmosis, nanofiltration, thermal distillation and membrane distillation (MD) and more [5, 6]. Among all these methods, membrane distillation has several advantages, including operation at low temperatures and hydrostatic pressures, high water recovery, high salt rejection (especially those with a salinity between 70 and 300 g salt per kg solution), less sensitivity to membrane fouling, and the potential for pollutant removal and usage of renewable energy resources. MD has realized several types [7] and successfully applied in many fields, such as purification of sea water, industrial and mining effluents from heavy metals, dyes, radioactive waste, acid solutions [8–12].

As mentioned above, the main characteristics of MD membranes are porosity and hydrophobicity. As materials with high suitability for MD applications, polymeric, inorganic and ceramic membranes have attracted much attention [13]. Polymeric membranes can be easily modified. They have low thermal conductivity, typically in the range of 0.1–0.5 $Wm^{-1}\cdot K^{-1}$. In general, MD membranes can be produced by track etching, sintering, phase inversion, electrospinning, etc. In addition, several types of membranes are produced by a combination of the abovementioned methods. MD requires membranes with specific characteristics such as high LEP, optimal thermal conductivity, stability, non-fouling properties, superior permeability as well as high purification degree [14].

Ion-track membranes (TMs) have these characteristics. TMs have ~~a~~ unique properties and structure that includes microscopic channels through which vapour transport occurs [15, 16]. These membranes provide high separation efficiency, which is particularly important in desalination processes [17]. Various ion-track membranes (TMs), including PVDF, PE, PDMS, PP, PTFE and PET have been used for membrane distillation [18].

In our previous studies [9, 19], PET TMs were modified with styrene and fluorosilane to small pore size by photoinitiated graft polymerization. MD has successfully used these membranes for both water desalination and the decontamination of low-level liquid radioactive waste. This article presents the preparation of large pore size hydrophobic PET TMs by grafting 2,2,3,3,4,4,4-heptafluorobutyl methacrylate (HFBMA) and their use for water desalination. The unique properties of fluorine containing compounds explain the choice of this monomer. They have low surface energy, their chemical backbone formed by stable carbon-fluorine bonds (~485 kJ mol^{-1}), and the particular electronic structure of fluorine, is characterized by high electronegativity, low polarizability and a small van del Waals radius (1.32 Å). As a result, there are weak dispersion interactions on the surface of fluorocarbons, and the wettability and surface tension of fluoropolymers are very low [20].

Experimental

Reagents

2,2,3,3,4,4,4-heptafluorobutyl methacrylate (HFBMA) (97 %), N,N-dimethylformamide (99,9 %) (DMF), benzophenone (BP) (97 %), NaCl, ethanol (98 %), 2-propanol (99,8 %). All monomers were passed through a chromatographic column to remove the inhibitor. All NaCl solutions were prepared in deionized water (18.2 MΩ).

PET TMs Preparation and Graft Polymerization of HFBMA

The PET TMs were obtained by irradiating Hostaphan® brand PET films (Mitsubishi polyester film, Germany) with a thickness of 12 μm using Kr ions at an energy of 1.75 MeV/nucleon and an ion fluence of 1×10^6 ions/cm². This was conducted using the DC-60 ion accelerator (Astana Branch of the Institute of Nuclear Physics of the Republic of Kazakhstan). Irradiated PET film was etched in 2.2 M NaOH solution at 85 °C at 6–20 min. After chemical etching, the samples were washed in acetic acid and deionized water. Membranes were obtained with pore density of 1×10^6 pores/cm^2 and different pore sizes depending of etching time.

The samples were then immersed in the initiator (5 % BP in DMF) for 24 h, washed in ethanol and dried in air. The amount of BP adsorbed on the surface of PET TeMs was determined by UV-vis-spectroscopy at 253 nm [21]. According to the calibration curve, the concentration of BP was 580 μmol/g. This value was kept constant. After PET TMs were placed in a solution of HFBMA in 2-propanol. HFBMA concentrations ranged from 1–10 %. The reaction mixture was flushed with Ar to remove the dissolved oxygen. Graft polymerization was carried out using OSRAM Ultra Vitalux E27 (UVA: 315–400 nm, 13.6 W; UVB: 280–315 nm, 3.0 W) for 30–60 min. After reaction the samples were washed in 2-propanol and water and dried.

Methods of Characterization of the PET TeMs

Chemical changes before and after modification were measured by Fourier Transform Infrared (FTIR) spectrometer (InfraLUM FT-08) with ATR accessory (GradiATR, PIKE). Spectra were recorded in the range of 400–4000 cm^{-1}, with 20 scans and a resolution of 2 cm^{-1} at room temperature.

The morphology and elemental composition of the membrane surface was analyzed using a Hitachi TM 3030 with a Bruker XFlash MIN SVE EDX instrument at 15 kV acceleration voltage. The EDX spectrum is selected in 120 seconds. The sample is coated with a layer of gold prior to analysis. The results are presented as an average based on three data points.

CA was assessed by the static drop method and measured at five locations on the sample at room temperature.

Direct Contact Membrane Distillation

Direct Contact Membrane Distillation (DCMD) has been applied for water desalination. Figure 1 shows a scheme of the DCMD.

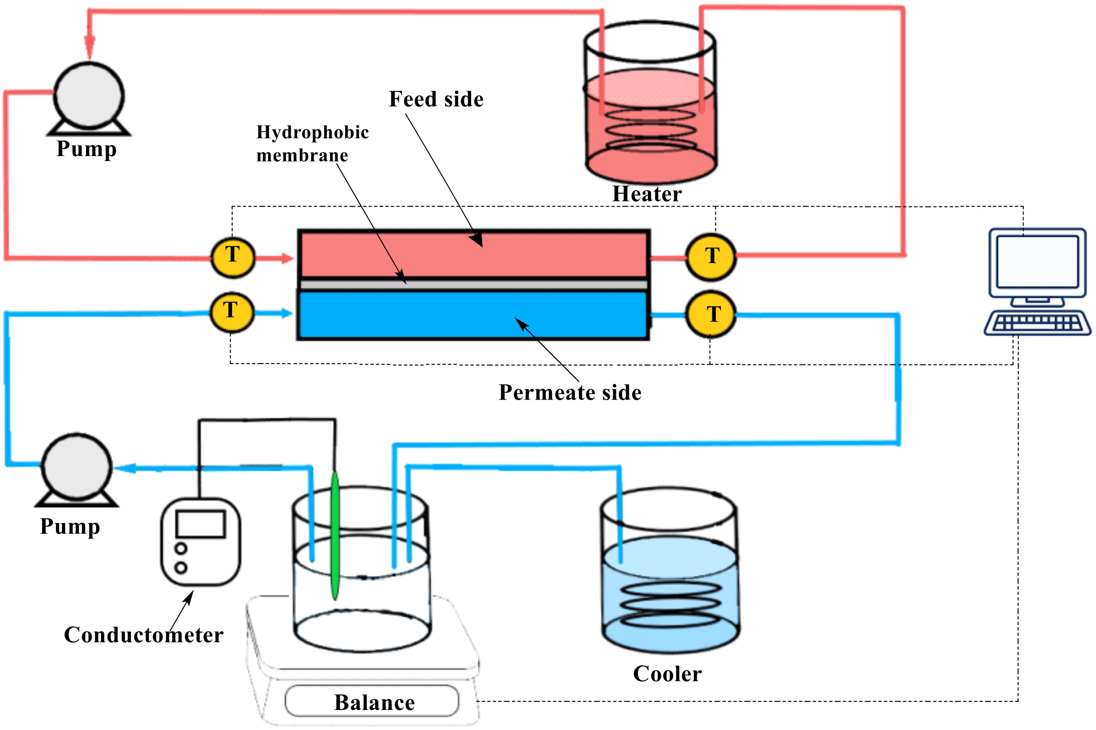

Figure 1. DCMD scheme

Type–T thermocouples were used to control the temperature at the inlets and outlets of the membrane cell, temperature differential was maintained at 70 °C. Peristaltic pumps were used to control permeate (13.5 ± 0.3 L/h) and feed flow (27.3 ± 0.3 L/h). Every 30 seconds, the collected liquid was weighed (± 0.01 g). The degree of purification was controlled by conductimetry measurements. The performance and degree of purification were computed based on the equations set out in [9].

Results and Discussion

The modification of PET TMs surfaces were functionalized according to the scheme presented in Figure 2. During the process of chemical etching, the hydrolysis of ester groups in the PET film led to the breakdown of its backbone. As a result, carboxylic and hydroxyl groups at the chain ends, providing reactive sites for monomer attachment during polymerization.

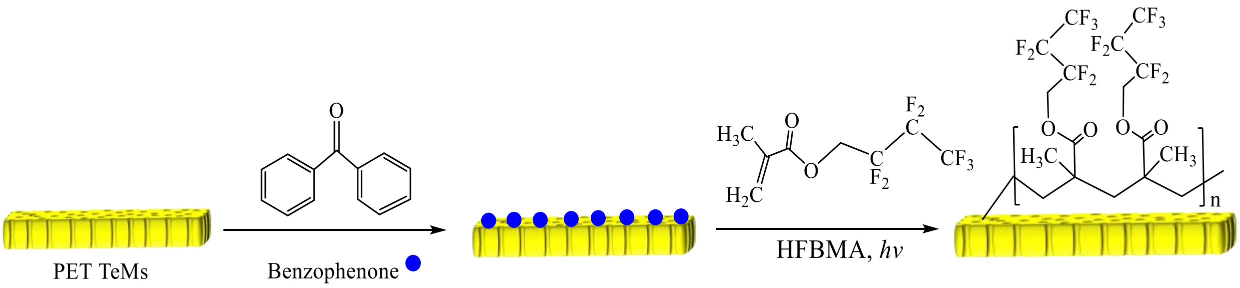

Figure 2. Graft polymerization of HFBMA

The polymerization process was influenced by monomer concentration, polymerization time and distance from the UV-source. The effect of the distance from the UV-lamp on the polymerization process was studied. When the distance exceeded 7 cm, polymerization did not occur, as no characteristic peaks were observed in the FTIR-spectra. As the distance decreased, the solvent was rapidly volatilized. Consequently, 7 cm was identified as the optimal distance.

Qualitative analysis of the obtained PET TMs samples was conducted using FTIR spectroscopy. Figure 3 depicts the FTIR spectroscopy results of the PET TMs before and after grafting. Before graft polymerization, the FTIR spectra exhibit the fluctuations, which are consistent with the data in work [19]. After modification with monomer concentration of 7 and 10 % in the FTIR spectra show the presence of peaks at 910 cm^{-1} belonging to the $C\text{-}F_2$ group and 1190 cm^{-1} belonging to the C-F group [22, 23].

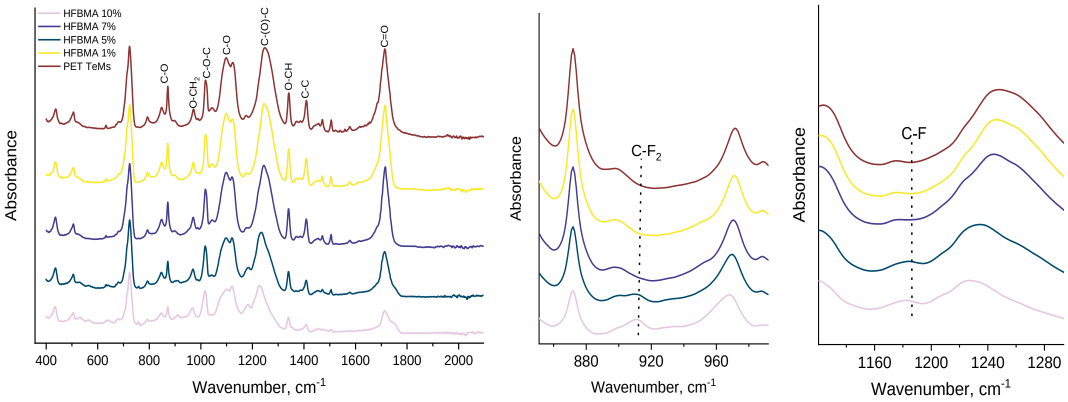

Figure 3. FTIR spectra of initial and modified PET TMs at different monomer concentration

The water repellent effects of the PET TMs were evaluated by measuring CA for each grafted sample (Fig. 4). The chemical composition and surface roughness have a significant effect on the CA.

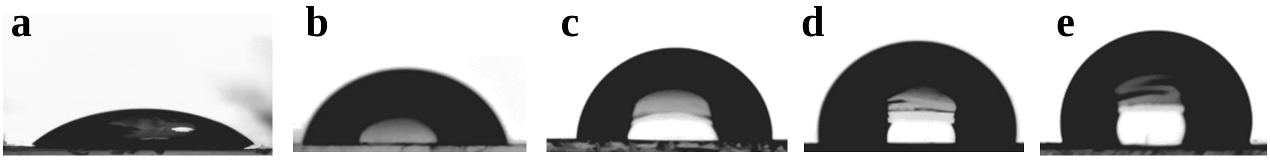

51°±3 73°±3 84°±5 85°±3 105°±2

Figure 4. CA for initial PET TMs (*a*) and grafted PET TMs for 60 min
at different concentrations (1 % (*b*), 5 % (*c*), 7 % (*d*) and 10 % (*e*))

As shown in Figure 4, the membrane surface becomes hydrophobic with increasing monomer concentration. The CA for the sample at a HFBMA concentration of 10 % averaged 105º±2º, and the water droplet did not spread for a long time. As the monomer concentration decreased, the water droplet spread faster and seeped through the membrane. The presence of HFBMA on the surface leads to increased surface roughness of PET TeMs, which we can observe using SEM (Fig. 5).

SEM images show that the PET TMs surface is uniform at 1 % and 7 % monomer concentration. The pores are open and not clogged with monomer, pore diameter decreases by 10–40 nm. At a HFBMA concentration of 10 %, a thick polymer layer forms, and the pores of the TM are not clogged with polymer. The pore diameter decreases by ~100 nm. The surface exhibits an uneven distribution of the polymer layer, characterized by polymer "islands" in certain regions that display high resistance to solvents. These islands increase roughness and form a hydrophobic layer.

Having obtained these results, the effect of grafting time on the photoinitiated graft polymerization process was studied. 10 % monomer was chosen as the optimum monomer concentration. Following the modification, the emergence of peaks at 910 cm^{-1} ($C\text{-}F_2$ ring) and 1190 cm^{-1} (C-F ring) was detected on the FTIR spectra in various reaction time. With increasing polymerization time and monomer concentration, formation of homopolymer was observed, which filled the pores of the TMs.

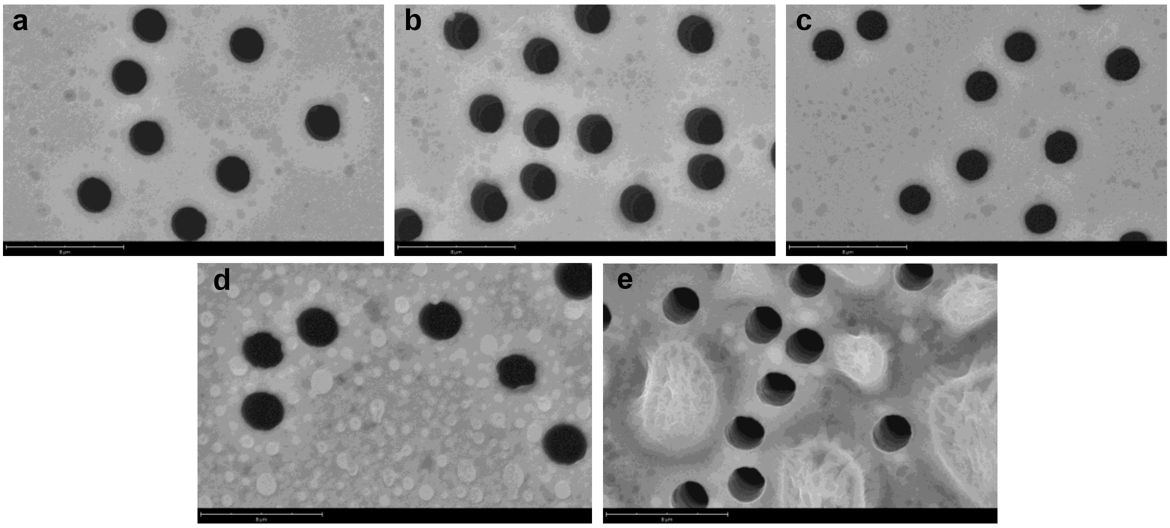

a — initial PET TMs; *b* — 1 % HFBMA; *c* — 7 % HFBMA; *d* — 10 % HFBMA (side 1); *e* — 10% HFBMA (side 2)

Figure 5. SEM microphotographs of PET TMs

As the grafting time increases, the CA changes from 59º±2º at 30 minutes to 105º±2º at 60 minutes. Figure 6 depicts the CA images of both unmodified and modified PET TMs over the time span from 30 to 60 min. The TMs surface becomes hydrophobic and a drop of water at a reaction time of 60 min does not spread for a long time. Conversely, at shorter polymerization times, the surface remains water-insoluble, and the drop spreads rapidly and penetrates through the membrane's pores.

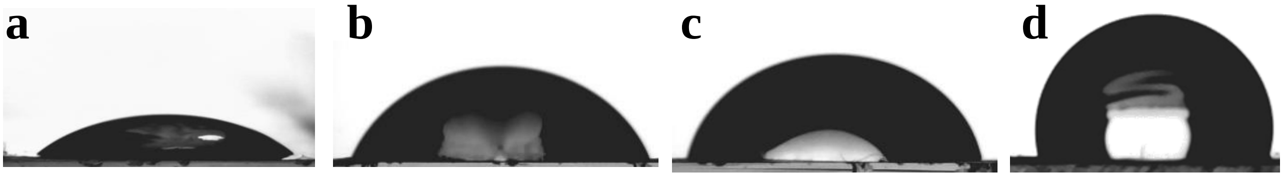

51°±3 59°±2 76°±3 105°±3

a — initial PET TeMs; *b* — 30 min; *c* — 45 min; *d* — 60 min

Figure 6. Effect of polymerization time on CA

The elemental composition was studied using EDX. According to the EDX analysis, the concentration of fluorine increases with both the reaction time and the monomer concentration. The maximum fluorine concentration is recorded in the sample where the monomer concentration is 10 %, and the polymerization time is 60 minutes.

The burst strength was evaluated at a pressure that would damage a circular sample of 1 cm^2 surface. Burst strength for initial PET TMs was more than >0.449 MPa. For modified membranes with pore size of 640 nm, burst strength is 0.425 MPa, for 960 nm = 0.438 MPa and for 1290 nm more than >0.449 MPa (Table).

Table

Elemental analysis, CA and pore size were obtained for PET TMs under different grafting parameters

№ sample	Grafting time, min	HFBMA concentration, %	CA, °±3°	Pore diameter (from SEM analysis), nm	Concentration of F, %
1	0	–	51	2473±121	–
2	30	10	59	2471±94	0.89±0.46
3	45	10	76	2425±64	1.018±0.25
4	60	10	105	2399±91	13.00±1.85
5	60	7	85	2419±95	0.44±0.15
6	60	1	73	2463±149	0.3±0.1

Thus, according to the results of the experiment, the optimal conditions for graft polymerization of HFBMA are the distance from the UV-lamp 7 cm, HFBMA concentration 10 % and reaction time 60 min. The formation of a polymer layer on the surface of PET TMs was demonstrated by EDX, FTIR spectroscopy, SEM images and CA.

Obtained hydrophobic PET TMs at optimal grafted parameters were used for water desalination process by membrane distillation. Membranes with different pore sizes (640, 960, 1290 and 2400 nm) were taken for the process. In order to simulate practical conditions, salt concentrations were gradually increased from 7.5 to 30 g/L. After each experiment, the membranes were washed in warm water for 12 hours to remove salt residues. However, these membranes did not remove salt from the water because of LEP value is not high enough. The results of water desalination using modified membranes are shown in Figure 7.

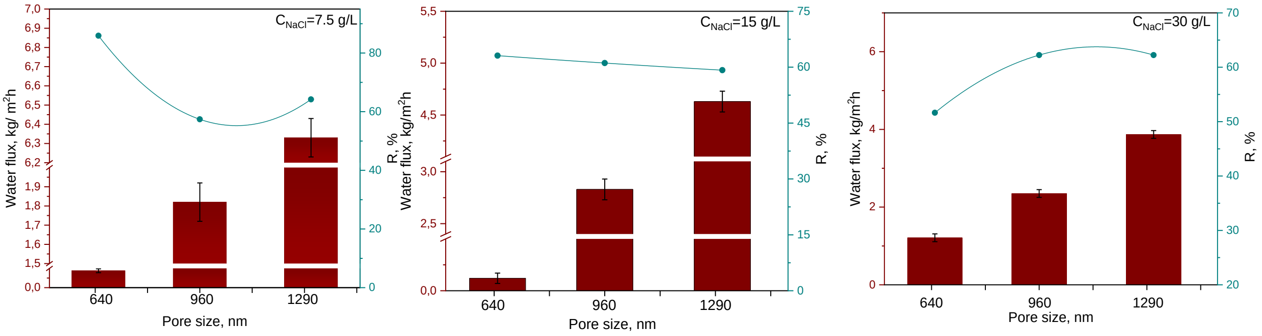

Figure 7. Effects of pore diameter on MD performance at different NaCl concentrations

The data illustrated in the graphs indicate the effect of varying NaCl concentration on water flux and degree of salt rejection. A decrease in water flux is evident with an increase in pore diameter from 600 to 1200 nm. Furthermore, a reduction in water flow is observed with the rise in NaCl concentration from 7.5 to 30 g/L. Increasing the size of pores in the membrane enhances the available space for water passage, leading to a higher rate of water flow through the membrane. This is achieved by reducing hydraulic resistance and augmenting the membrane's surface area for water passage. In addition, in highly concentrated solutions there is a decrease in water activity and a change in viscosity which affect the water flux [24, 25]. The pore diameter has a strong effect on the salt rejection, as can be seen in Figure 8. TMs with pore sizes of 640, 960 and 1290 nm have a salt rejection of 85.9 %, 63.5 % and 59.2 % respectively. This phenomenon is due to the non-uniformity of the grafted layer and thus insufficient hydrophobicity of the membrane. As a result, salts that were originally intended to be retained by the membrane begin to penetrate through it, reducing the salt rejection [9].

Conclusions

In this study, a water-repellent membrane was developed by polymerization of HFBMA onto porous PET TMs for desalination via DCMD. The optimal parameters for the photoinitiated graft polymerization of HFBMA were determined as a UV lamp distance of 7 cm, a monomer concentration of 10 %, and a polymerization time of 60 min. The PET TMs obtained were analyzed using FTIR spectroscopy, SEM and CA measurements. The polymer layer deposited increased surface roughness, resulting in hydrophobic properties with a water contact angle of 105°±3°. This hydrophobic coating conferred physicochemical stability and anti-wetting properties to the fabricated PET TMs, making them suitable for membrane distillation. PET TMs with larger pore diameters exhibited a lower degree of salt rejection but demonstrated high water flux due to an increased likelihood of liquid permeation. The most significant correlation between water flux and salt rejection was observed for PET TMs with a pore diameter of 650 nm.

Funding

The research titled “Development of methods for hydrophobization of PET track-etched membranes for water purification by membrane distillation” (grant No AP14869096) was funded by the Ministry of Science and Higher Education of the Republic of Kazakhstan.

*Author Information**

**The authors' names are presented in the following order: First Name, Middle Name and Last Name*

Aigerim Khairatovna Shakayeva (*corresponding author*) — Master of Chemical Sciences, Engineer, Astana Branch, Institute of Nuclear Physics of the Republic of Kazakhstan, Abylay Khana 2/1, 010000, Astana, Kazakhstan; e-mail: shakayevaa19@gmail.com; https://orcid.org/0000-0001-5731-1115

Arman Bakhytzhanovich Yeszhanov — Master of Chemical Sciences, Junior Scientific Researcher, Astana Branch, Institute of Nuclear Physics of the Republic of Kazakhstan, Abylay Khana 2/1, 010000, Astana, Kazakhstan; e-mail: a.yeszhanov@inp.kz; https://orcid.org/0000-0002-1328-8678

Ainash Turlybekovna Zhumazhanova — PhD, Engineer, Astana Branch, Institute of Nuclear Physics of the Republic of Kazakhstan, Abylay Khana 2/1, 010000, Astana, Kazakhstan; e-mail: ainash.zhumazhanova@gmail.com; https://orcid.org/0000-0002-5483-9552

Ilya Vladimirovich Korolkov — PhD, Associated Professor, Senior Researcher, Astana branch, Institute of Nuclear Physics of the Republic of Kazakhstan, Abylay Khana 2/1, 010000, Astana, Kazakhstan; e-mail: i.korolkov@inp.kz; https://orcid.org/0000-0002-0766-2803

Maxim Vladimirovich Zdorovets — Candidate of Physical and Mathematical Science, Professor. Director, Astana Branch, Institute of Nuclear Physics of the Republic of Kazakhstan, Abylay Khana 2/1, 010000, Astana, Kazakhstan; e-mail: mzdorovets@inp.kz; https://orcid.org/0000-0003-2992-1375

Author Contributions

All authors contributed to the preparation of the manuscript. All authors approved the final version of the manuscript. CRediT: **Aigerim Khairatovna Shakayeva** investigation, writing original draft, data curation, visualization; **Arman Bakhytzhanovich Yeszhanov** data curation, formal analysis, investigation; **Ainash Turlybekovna. Zhumazhanova** investigation, data curation; **Ilya Vladimirovich Korolkov** — supervision, writing — review & editing, project administration; **Maxim Vladimirovich Zdorovets** — funding acquisition, data curation.

Conflicts of Interest

The authors declare that they had no known competing financial interests or personal relationships that might appear to influence the work reported in this article.

References

1 Shiklomanov, I.A. (2000). Appraisal and Assessment of World Water Resources. *Water International*, 25, 1, 11–32. https://doi.org/10.1080/02508060008686794

2 Elimelech, M., & Phillip, W.A. (2011). The future of seawater desalination: Energy, technology, and the environment. *Science*, 333, 6043, 712–717. DOI: 10.1126/science.1200488

3 Bohn, P.W., Elimelech, M., Georgiadis, J.G., Mariñas, B. J., & Mayes, A. M. (2009). Science and technology for water purification in the coming decades. *Nanoscience and Technology: A Collection of Reviews from Nature Journals*, 337–346. https://doi.org/10.1142/9789814287005_0035

4 Zhou, Y., & Tol, R.S.J. (2005). Evaluating the costs of desalination and water transport. *Water Resources Research*, 41, 3, 1–10. https://doi.org/10.1029/2004WR003749

5 Abdelrasoul, A. (Ed.). (2020). Advances in Membrane Technologies. IntechOpen. doi: 10.5772/intechopen.82587

6 Zakharov, A., Tukesheva, A., Bin Haque, S.F., Ferraris, J., Zakhidov, A., Tazhibayeva, T., Bazarbayeva, T., & Pavlenko, V. (2023). Review of the current state of technology for capacitive deionization of aqueous salt solutions. *Bulletin of the Karaganda University "Physics Series," 111*(3), 16–33. https://doi.org/10.31489/2023ph3/16-33

7 Al-Obaidani S. Curcio, E., Macedonio, F., Di Profio, G., & Al-Hinai, H. (2008). Potential of membrane distillation in seawater desalination: Thermal efficiency, sensitivity study and cost estimation. *Journal of Membrane Science*, 323, 1, 85–98. https://doi.org/10.1016/j.memsci.2008.06.006

8 Jiang, M., Fang, Zh., Liu, Zh., Huang, X., Wei, H., &Yu, C. (2023). Application of membrane distillation for purification of radioactive liquid. *Cleaner Engineering and Technology*, 12, 100589. https://doi.org/10.1016/j.clet.2022.100589

9 Korolkov, I.V., Yeszhanov, A.B., Zdorovets, M.V., Gorin, Y.G., Güven, O., Dosmagambetova, S.S., Khlebnikov, N.A., Serkov, K.V., Krasnopyorova, M.V., Milts, O.S., & Zheltov, D.A. (2019). Modification of PET ion track membranes for membrane

distillation of low-level liquid radioactive wastes and salt solutions. *Separation and Purification Technology*, 227, 115694. https://doi.org/10.1016/j.seppur.2019.115694

10 Sivakumar, M., Ramezanianpour, M., & O'Halloran, G. (2013). Mine Water Treatment Using a Vacuum Membrane Distillation System. *APCBEE Procedia*, 5, 157–162. https://doi.org/10.1016/j.apcbee.2013.05.028

11 Bhuyan, C., Konwar, A., Bora, P., Rajguru, P., & Hazarika, S. (2023). Cellulose nanofiber-poly(ethylene terephthalate) nanocomposite membrane from waste materials for treatment of petroleum industry wastewater. *Journal of Hazardous Materials*, 442, 129955. https://doi.org/10.1016/j.jhazmat.2022.129955

12 Alves, V.D., & Coelhoso, I.M. (2006). Orange juice concentration by osmotic evaporation and membrane distillation: A comparative study. *Journal of Food Engineering*, 74, 1, 125–133. https://doi.org/10.1016/j.jfoodeng.2005.02.019

13 Ravi, J., Othman, M., Matsuura, T., Ro'il Bilad, M., El-badawy, T.H., Aziz, F., Ismail, A.F., Rahman, M.A., & Jaafar, J. (2020). Polymeric membranes for desalination using membrane distillation: A review. *Desalination*, 490, 114530. https://doi.org/10.1016/j.desal.2020.114530

14 Chamani, H., Woloszyn, J., Matsuura, T., Rana, D., & Lan, Ch.Q. (2021). Pore wetting in membrane distillation: A comprehensive review. *Progress in Materials Science*, 122, 100843. https://doi.org/10.1016/j.pmatsci.2021.100843

15 Mashentseva, A.A., Barsbay, M., Aimanova, N.A. & Zdorovets, M.V. (2021). Application of Silver-Loaded Composite Track-Etched Membranes for Photocatalytic Decomposition of Methylene Blue under Visible Light. *Membranes*, 11, 60. https://doi.org/10.3390/membranes11010060

16 Kozlovskiy, A., Borgekov, D., Kenzhina, I., Zdorovets, M., Korolkov, I., Kaniukov, E., Kutuzau, M., & Shumskaya, A. (2019). PET ion-track membranes: Formation features and basic applications. *Springer Proceedings in Physics*, 221, 76, 461–479. https://doi.org/10.1007/978-3-030-17759-1_31

17 Yeszhanov, A.B., Korolkov, I.V., Shakayeva, A.Kh., Lissovskaya, L. I., & Zdorovets, M.V. (2023). Preparation of Poly(Ethylene Terephthalate) Track-Etched Membranes for the Separation of Water-Oil Emulsions. *Eurasian Journal of Chemistry*, 110, 2, 131–138. https://doi.org/10.31489/2959-0663/2-23-5

18 Yeszhanov, A.B., Korolkov, I.V., Dosmagambetova, S.S., Zdorovets, M.V., & Güven, O. (2021). Recent Progress in the Membrane Distillation and Impact of Track-Etched Membranes. *Polymers*, 13, 15, 2520. https://doi.org/10.3390/polym13152520

19 Korolkov, I.V. Gorin, Y.G., Yeszhanov, A.B., Kozlovskiy, A.L., & Zdorovets, M.V. (2018). Preparation of PET track-etched membranes for membrane distillation by photo-induced graft polymerization. *Materials Chemistry and Physics*, 205, 55–63. https://doi.org/10.1016/j.matchemphys.2017.11.006

20 Bongiovanni, R., Nettis, E., & Vitale, A. (2020). Fluoropolymers for oil/water membrane separation. *Opportunities for Fluoropolymers*, P. 209–246. https://doi.org/10.1016/B978-0-12-821966-9.00008-0

21 Korolkov, I.V., Mashentseva, A.A., Güven, O., & Taltenov, A.A. (2015). UV-induced graft polymerization of acrylic acid in the sub-micronchannels of oxidized PET track-etched membrane. *Nuclear Instruments and Methods in Physics Research, Section B: Beam Interactions with Materials and Atoms*, 365, 419-423. http://dx.doi.org/10.1016/j.nimb.2015.07.057

22 Luo, Z. Hong, He, & Yun T. (2008). Synthesis and characterization of poly(dimethylsiloxane)-block-poly(2,2,3,3,4,4,4-heptafluorobutyl methacrylate) diblock copolymers with low surface energy prepared by atom transfer radical polymerization. *Reactive and Functional Polymers*, 68, 5, 931–942. https://doi.org/10.1016/j.reactfunctpolym.2008.01.004

23 Zhang Z. Hu, Yu., Liu, Zh., & Guo, T. (2012). Synthesis and evaluation of a moisture-promoted healing copolymer. *Polymer*, 53, 14, 2979–2990. DOI:10.1016/j.polymer.2012.04.048

24 Abdel-Karim, A., Leaper, S., Skuse, C., Zaragoza, G., Gryta, M., & Gorgojo, P. (2021). Membrane cleaning and pretreatments in membrane distillation — a review. *Chemical Engineering Journal*, 422, 129696. https://doi.org/10.1016/j.cej.2021.129696

25 Qtaishat, M.R., & Matsuura, T. (2015). Modelling of pore wetting in membrane distillation compared with pervaporation. *Pervoparation, Vapour Permeation and Membrane Distillation: Principles and Aplications*, 385, 413. https://doi.org/10.1016/B978-1-78242-246-4.00013-1

How to Cite: Muravlev, D.A., Doroganov, A.P., Philippova, O.E., & Shibaev, A.V. (2024) Natural Polyelectrolyte Hydrogels With Two Types of Cross-Links with Different Energy. *Eurasian Journal of Chemistry, 29, 2(114), 89-95.* https://doi.org/10.31489/2959-0663/2-24-12

Article

Received: 27 February 2024 | Revised: 22 April 2024 |
Accepted: 24 April 2024 | Published online: 7 May 2024

UDC 544.42+519.242.7

https://doi.org/10.31489/2959-0663/2-24-12

Dmitry A. Muravlev[1], Anton P. Doroganov[1], Olga E. Philippova[1], Andrey V. Shibaev[1, 2]*

[1]*Department of Physics, Lomonosov Moscow State University, Moscow, Russia;*
[2]*Chemistry Faculty, Karaganda Buketov University, Karaganda, Kazakhstan*
*(*Corresponding author's e-mail: shibaev@polly.phys.msu.ru)*

Natural Polyelectrolyte Hydrogels with Two Types of Cross-Links with Different Energy

For the first time, gels of a polymer cross-linked by two types of ionic cross-links of different energies, namely trivalent chromium (III) ions and divalent iron (II) ions, were prepared. The negatively charged polysaccharide xanthan, a polyelectrolyte of natural origin, was used as a polymer. A study of xanthan gels cross-linked with each cross-linker separately was carried out to identify the optimal concentrations of each cross-linker for the production of a double cross-linked gel. The mechanical properties of hydrogels under oscillatory shear deformations were then studied. It was demonstrated that the simultaneous use of two cross-linkers resulted in a synergistic increase in the elastic modulus (plateau storage modulus) compared to gels cross-linked with each cross-linker separately. For a gel with two types of cross-links, the elastic modulus was 16 Pa. In contrast, for gels cross-linked with either chromium (III) cations or iron (II) cations, the elastic modulus was approximately 0.6 and 0.5 Pa, respectively. The strong effect can be attributed to the different nature of cross-linking between xanthan macromolecules and chromium (III) and iron (II) cations, as well as the different strength of the cross-links formed. The optimal range of pH values was determined in which a synergistic increase in the elastic modulus of gels with two types of cross-links was observed compared to the corresponding gels cross-linked with each cross-linker separately. Consequently, the concurrent utilization of two cross-linking agents that generate cross-links with disparate energy levels represents an efficacious strategy to improve the tensile strength of polymer hydrogels.

Keywords: polymer gel, polysaccharide, xanthan, polymer network, polyelectrolyte, cross-linking, viscoelasticity, rheological properties.

Introduction

In recent years, the creation and study of hydrogels with high mechanical strength has attracted considerable interest [1–11]. An urgent problem is the search for new ways to increase the mechanical properties of hydrogels so that they can withstand high mechanical loads. One such method is the simultaneous use of several different cross-linkers with different properties. A recently proposed approach in the literature involves the creation of gels with two distinct types of cross-linking: strong covalent and weak non-covalent ("physical") [12–15]. This approach extends the principle underlying the creation of the so-called "double" networks [16] to single polymer networks: when deformed, strong covalent cross-links maintain gel elasticity, while weak ones break, acting as "sacrificial" bonds, and provide energy dissipation in a sufficiently large volume, which prevents the spread of the break and gel destruction.

A number of networks cross-linked by chemical covalent and "physical" cross-links have been proposed to date. Ionic cross-links are often used as "physical" cross-links [17]. However, there are practically no examples of gels cross-linked simultaneously by two types of ionic cross-links with different energies. This approach appears to offer considerable potential, as the type of ions employed can be varied to alter the ionic cross-linking energy over a broad spectrum.

Thus, the purpose of this work is to prepare polymer gels cross-linked simultaneously with two types of ionic cross-linkers of different energies and to study their mechanical properties in comparison with the corresponding gels cross-linked with each cross-linker separately. The polysaccharide xanthan, which has negatively charged carboxylate groups, was selected as a polymer, and chromium Cr^{3+} and iron Fe^{2+}cations, which have different charge values and, accordingly, different binding energies with the polymer, were used as cross-linkers.

Experimental

Materials

The xanthan gum Ziboxan F200 was procured from the company Deosen Biochemical Limited. The chemical structure of this polysaccharide is shown in Figure 1. Its molar mass amounts to 1,000,000 g/mol (and the degree of polymerization is approximately 1,100), as determined by viscometry in a previous study [18]. Previously reported ^{1}H NMR data [18] indicates that the degrees of substitution by acetyl and pyruvate groups, expressed in the number of these groups per monomer link, are equal to 0.56 and 0.41, respectively.

Chromium (III) chloride hexahydrate (purity 98 %), iron (II) sulfate heptahydrate (purity 99 %), sodium azide (purity 99.5 %) provided by Sigma Aldrich were used as received. All solutions were prepared with distilled deionized water from the Milli-Q system (Millipore). The pH values of the samples were adjusted with sodium hydroxide (purity 98 %) from Acros and hydrochloric acid (purity 99 %) from Uralkhiminvest.

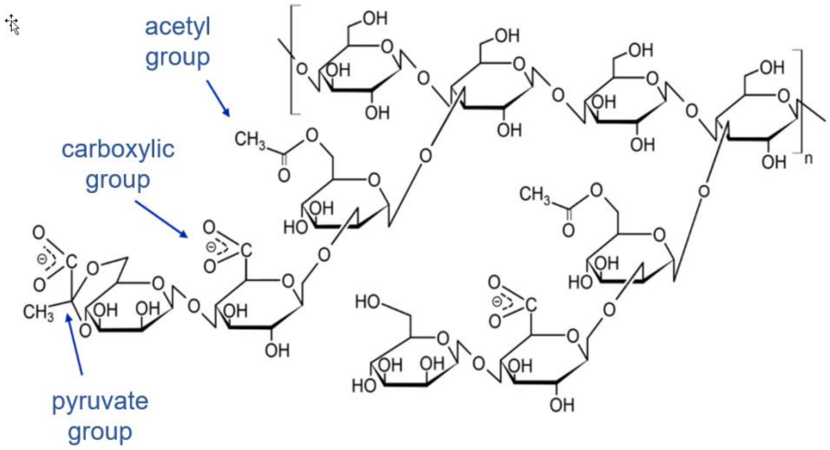

Figure 1. Chemical structure of the polysaccharide xanthan

Preparation of Samples

Firstly, a 2 wt% aqueous solution of xanthan was prepared by dissolving a calculated amount of the polymer in distilled deionized water in the presence of 3 mM sodium azide, a bacteriostatic agent, at agitation with a magnetic stirrer during 24 h. Secondly, 1 wt% aqueous solutions of cross-linkers (chromium chloride and iron chloride) were prepared by stirring for 5–10 min. Subsequently, the samples were left for 48 hours to allow hydrolysis of Cr^{3+} and Fe^{2+} ions to proceed, as previously described [19].

Gels with one or two types of cross-links were prepared by simultaneous mixing of aqueous solutions of xanthan, each of the cross-linking agents and acid or alkali (1M KOH or 1M HCl) in required proportions. Then the system was stirred intensively for 2-3 min and left for 7 days for cross-linking. The preliminary experiments indicated that the time needed for cross-linking was the time required for the xanthan solution to gel, i.e. to change from a viscoelastic fluid to a viscoelastic solid, as described in [20].

Rheometry

The mechanical properties of the hydrogels were studied under shear deformation using an Anton Paar Physica SmartPave 102 rotational rheometer, as described in detail elsewhere [21]. For these experiments, cylindrical gel samples (8 mm in height, 25 mm in diameter) were prepared. The measurements were carried out using a plane-plane measuring cell with a diameter of 25 mm at a temperature of 20.00 ± 0.05 °C. A hood with Peltier elements controlling the temperature was used to prevent solvent evaporation during the experiments.

The measurements were carried out in the harmonic oscillation mode, wherein the frequency dependencies of the storage modulus (G') and loss modulus (G") were recorded at varying frequency ω from 0.04 to 50 s^{-1}. All experiments were performed in the linear viscoelastic regime at strain amplitudes (γ) between 1 and 5 %, during which the storage and loss moduli are independent of the amplitude.

Results and Discussion

In the present work, we prepared and studied hydrogels of xanthan polysaccharide cross-linked simultaneously by two types of ions, namely chromium (Cr^{3+}) and iron (Fe^{2+}). Xanthan monomer links contain negatively charged pyruvate and carboxylate groups, and cross-linking by metal ions occurs mainly by pyruvate groups, although less accessible carboxylate groups can also participate in the cross-linking [22].

Firstly, to determine the optimal conditions for the formation of gels with two types of cross-links, we studied the systems cross-linked by each cross-linker separately with varying concentrations of the cross-linkers. Figure 2 illustrates the dependences of the storage modulus at high frequencies (which, in the case of gels, is analogous to the elastic modulus) on the concentration of each of the cross-linkers. It can be observed that the curve exhibits a similar characteristic appearance for both cross-linkers. At low cross-linker concentrations, the G' values are low (approximately 0.1 Pa), and no gel formation occurs. Subsequently, when the cross-linker concentration is increased, the storage modulus begins to increase, which corresponds to the onset of gel formation. G' reaches a plateau at high cross-linker concentrations. This is explained by the formation of cross-links by all available functional groups, which results in the inability to form new cross-links with further increases in the cross-linker concentration.

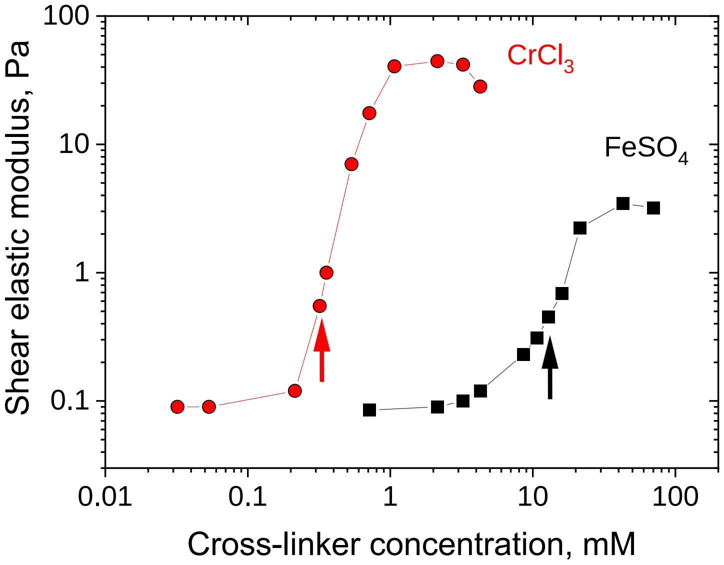

Figure 2. Dependences of the storage modulus G' at high frequencies (modulus of elasticity) on the cross-linker concentration ($CrCl_3$ — circles, $FeSO_4$ — squares) for aqueous solutions containing 0.1 wt. % xanthan. Temperature is 20 °C.

It is notable that the curve for Fe^{2+} ions is shifted with respect to the curve for Cr^{3+} ions in the region of significantly elevated cross-linker concentrations. This phenomenon appears to be associated with a diminished cross-linking efficacy of xanthan by divalent ions relative to trivalent ions [23]. Thus, different concentrations of each of the ions are required to obtain gels with two types of cross-linking. The concentrations indicated by the arrows in Figure 1 (0.32 mM $CrCl_3$ and 13 mM $FeSO_4$), which are close to the onset of the gel formation, were used.

There were obtained transparent, single-phase, and homogeneous xanthan hydrogels cross-linked by both types of cross-linkers simultaneously as well as by each cross-linker separately. Figure 2 shows frequency dependences of the storage modulus and loss modulus for these hydrogels. It can be observed that the addition of a single cross-linker, either $CrCl_3$ or $FeSO_4$, results in the formation of gels. This is evidenced by the fact that the G' values are consistently greater than the G" values across the entire frequency range. However, the gels are relatively weak, with a modulus of elasticity (storage modulus of accumulation at the plateau G_0) of less than 1 Pa. When two cross-linkers are used simultaneously, a gel is also formed, and a synergistic increase in the elastic modulus is observed: for a gel with two types of cross-links G_0 is 16 Pa, while for Cr^{3+} and Fe^{2+} cross-linkers it is only about 0.6 and 0.5 Pa, respectively. Using the theory for rubber-like elasticity of cross-linked random coil polymers [24] and taking into account the dangling end [24] one can estimate the average molar mass between network junctions, M_c, from the plateau modulus G_0 using the following equation [20]:

$$M_c = \left(KcRT / G_0\right)\left(1 + KcRT / G_0 M_w\right),$$

where K is the empirical factor ranging from 3–10, c is the polymer concentration in g/l, R is the molar gas constant, T is the temperature and M_w is the molar mass of polymer. With an intermediate K value (K=5), this yields an average molar mass between junctions equal to 200,000 g/mol and 300,000 g/mol for the networks cross-linked by Cr^{3+} and Fe^{2+} ions separately. This is by several orders of magnitude higher than the molar mass of the repeat unit of xanthan. It indicates that only a small fraction of the ions contributes to the cross-linking process, which is consistent with the previously reported results for ionic cross-linking of xanthan [20]. When two types of ions are used simultaneously, the average molar mass between junctions increases significantly (M_c~ 10,000 g/mol). It is probable that this synergistic behavior can be explained by the different nature of cross-linking by chromium and iron ions, and by the fact that when xanthan is cross-linked by only one ion, it is near the onset of gelation (because M_c is only a few times less than the polymer molecular weight). At these conditions, one could expect that some polymer chains and many cross-linkers do not participate in the network formation. The use of two ions results in enhanced gelation, incorporation of more polymer chains into the network, and the appearance of more cross-linking points. This leads to an increase in the elastic modulus. Consequently, the simultaneous use of two cross-linkers allows for a synergistic increase in the elastic modulus of gels compared to systems cross-linked with only one cross-linker.

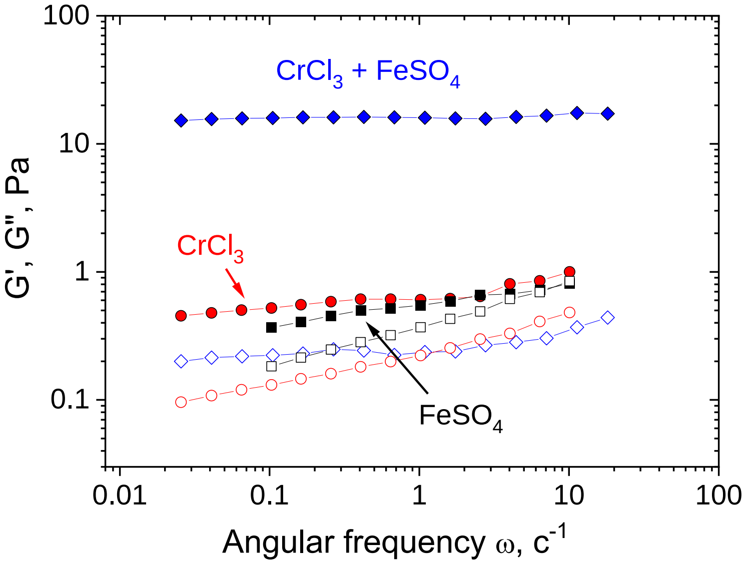

Figure 3. Frequency dependences of the storage modulus (G', shaded symbols)
and loss modulus (G", empty symbols) for aqueous solutions containing 0.1 wt.% xanthan
and 0.32 mM $CrCl_3$ (circles), 13 mM $FeSO_4$ (squares), and both crosslinkers simultaneously (diamonds).
Temperature is 20 °C, pH 5.6

One of the determining factors for the formation of ionic cross-links between xanthan molecules is the pH value. Since the optimum conditions for the formation of cross-links by Cr^{3+} and Fe^{2+} ions appear to be different, the effect of pH on gels cross-linked by both cross-linkers simultaneously and by each of the cross-linkers separately was investigated. Figure 4 shows the pH dependences of the elastic modulus for such gels. It can be observed that the curves for gels cross-linked by two or one cross-linker exhibit a similar characteristic appearance. At low pH (< 2.1) the G' values are rather low, and the gels are not formed. This is attributed to the protonation of the carboxyl groups of xanthan in this pH range, which impedes the interaction of ions with them [25]. At intermediate pH values (from 2.1 to 7.8), gel formation and a sharp increase in the elastic modulus for all three types of gels occur, which is due to the cross-linking of deprotonated carboxyl groups of xanthan by ions. The range in which the gels have the highest modulus of elasticity is narrower for Fe^{2+} ions than for Cr^{3+} ions. Throughout the pH range from ~2.1 to 7.8, a synergistic increase in the elastic modulus is observed as compared to gels with a single cross-linker. Finally, at pH values greater than 7.8, the elastic modulus drops and gels are not formed because both types of Cr^{3+} and Fe^{2+} ions change into water insoluble hydroxides unable to cross-link the carboxylate groups of xanthan.

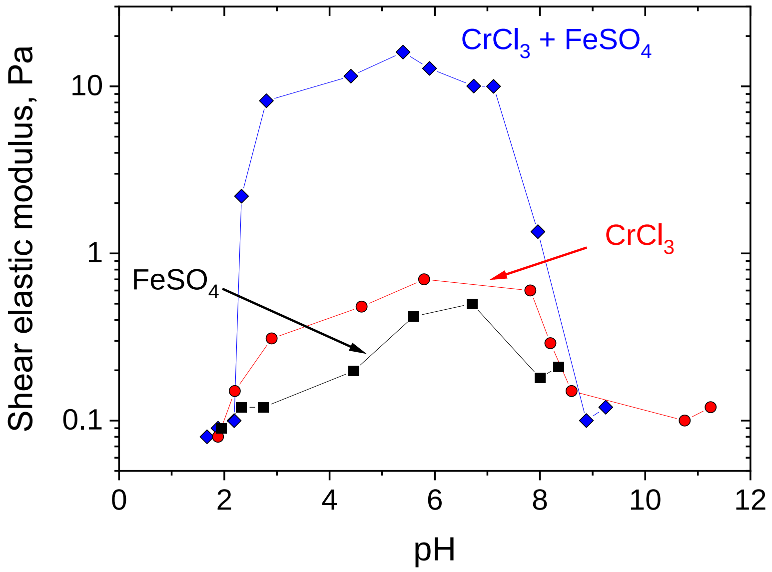

Figure 4. Dependences of the storage modulus G' at high frequencies (modulus of elasticity) on pH for aqueous solutions containing 0.1 wt.% xanthan and 0.32 mM $CrCl_3$ (circles), 13 mM $FeSO_4$ (squares), and both cross-linkers simultaneously (diamonds). Temperature is 20 °C

Conclusions

For the first time, we obtained xanthan hydrogels cross-linked simultaneously by two types of ions, Cr^{3+} and Fe^{2+}. We also determined the optimum range of cross-linker concentrations and pH, in which a synergistic increase in the elasticity modulus of gels by more than 30 times as compared to gels cross-linked by each of the ions separately was observed.

Funding

This work was supported by the Russian Science Foundation (Project No. 21-73-10197 “Stimuli-responsive hydrogels with controlled anisotropy based on double polymer networks” https://rscf.ru/en/project/21-73-10197/).

*Author Information**

**The authors' names are presented in the following order: First Name, Middle Name and Last Name*

Dmitry Aleksandrovich Muravlev — Junior Research Assistant, Faculty of Physics, Lomonosov Moscow State University, Leninskiye Gory 1, bld. 2, 119991, Moscow, Russia; e-mail: mit89-angel@yandex.ru; https://orcid.org/0000-0001-5243-9574

Anton Pavlovich Doroganov — Student, Faculty of Physics, Lomonosov Moscow State University, Leninskiye Gory 1, bld. 2, 119991, Moscow, Russia; e-mail: doroganov.a@mail.ru

Olga Evgen’evna Philippova — Doctor of physico-mathematical sciences, Professor, Department of Physics, Lomonosov Moscow State University, 119991, Moscow, Russia; e-mail: phil@polly.phys.msu.ru; https://orcid.org/0000-0002-1098-0255

Andrey Vladimirovich Shibaev (*corresponding author*) — Candidate of physico-mathematical sciences, Associate Professor, Department of Physics, Lomonosov Moscow State University, 119991, Moscow, Russia; Chemistry Faculty, Karaganda Buketov University, Universitetskaya street, 28, 100024, Karaganda, Kazakhstan; e-mail: shibaev@polly.phys.msu.ru; https://orcid.org/0000-0002-3019-5764

Author Contributions

The manuscript was written through contributions of all authors. All authors have given approval to the final version of the manuscript. CRediT: **Dmitry Aleksandrovich Muravlev** sample preparation, results processing; **Anton Pavlovich Doroganov** sample preparation, rheological measurements; **Olga Evgen’evna**

Philippova conceptualization, supervision, writing of the manuscript; **Andrey Vladimirovich Shibaev** data treatment, supervision, writing of the manuscript.

Acknowledgements

Rheological measurements were performed by using Anton Paar SmartPave 102 rotational rheometer, which was purchased with support from M.V. Lomonosov Moscow State University Program of Development.

Conflicts of Interest:

The authors declare no conflict of interest.

References

1 Chen, Q., Chen, H., Zhua, L., & Zheng, J. (2015). Fundamentals of double network hydrogels. *J. Mater. Chem., B, 3*, 3654–3676. https://doi.org/10.1039/C5TB00123D

2 Hua, M., Wu, S., Ma, Y., Zhao, Y., Chen, Z., Frenkel, I., Strzalka, J., Zhou, H., Zhu, X., & He, X. (2021). Strong tough hydrogels via the synergy of freeze-casting and salting out. *Nature, 590 (7847)*, 594–599. https://doi.org/10.1038/s41586-021-03212-z

3 Huang, X., Li, J., Luo, J., Gao, Q., Mao, A., & Li, J. (2021). Research progress on double-network hydrogels. *Materials Today Communications*, *29*, 102757. https://doi.org/10.1016/j.mtcomm.2021.102757

4 Zhao, X., Chen, X., Yuk, H., Lin, S., Liu, X., & Parada, G. (2021). Soft materials by design: unconventional polymer networks give extreme properties. *Chem. Rev.*, *121* (8), 4309–4372. https://doi.org/10.1021/acs.chemrev.0c01088

5 Shibaev, A.V., Osiptsov A. A., & Philippova, O. E. (2022). Novel trends in the development of surfactant-based hydraulic fracturing fluids: A review. *Gels, 2021,* 7(4), 258. https://doi.org/10.3390/gels7040258

6 Park, N. & Kim, J. (2022). Anisotropic hydrogels with a multiscale hierarchical structure exhibiting high strength and toughness for mimicking tendons. *ACS Appl Mater Interfaces*, *14*(3), 4479–4489. https://doi.org/10.1021/acsami.1c18989

7 Wang, Y., Jiao, A., Qiu, C., Liu, Q., Yang, Y., Bian, S., Zeng, F., & Jin, Z. (2022). A combined enzymatic and ionic cross-linking strategy for pea protein/sodium alginate double-network hydrogel with excellent mechanical properties and freeze-thaw stability. *Food Hydrocolloids*, *131*, 107737, https://doi.org/10.1016/j.foodhyd.2022.107737

8 Xue, B., Bashir, Z., Guo, Y., Yu, W., Sun, W., Li, Y., Zhang, Y., Qin, M., Wang, W., & Cao, Y. (2023). Strong, tough, rapid-recovery, and fatigue-resistant hydrogels made of picot peptide fibres. *Nature Commun*, *14*, 2583. https://doi.org/10.1038/s41467-023-38280-4

9 Yin, Y., Gu, Q., Liu, X., Liu, F., & McClements, D. J. (2023). Double-network hydrogels: design, fabrication, and application in foods and biomedicines. *Adv. Colloid Interface Sci., 320*, 102999. https://doi.org/10.1016/j.cis.2023.102999

10 Wang, M., Sun, S., Dong, G., Long, F., & Butcher, J. T. (2023). Soft, strong, tough, and durable protein-based fiber hydrogels. *Proc. Natl. Acad. Sci. U.S.A.*, *120* (8), e2213030120. https://doi.org/10.1073/pnas.2213030120

11 Kuang, X., Arıcan, M. O., Zhou, T., Zhao, X., & Zhang, Y. S. (2023). Functional tough hydrogels: design, processing, and biomedical applications. *Acc. Mater. Res.*, *4* (2), 101–114. https://doi.org/10.1021/accountsmr.2c00026

12 Narita, T., Mayumi, K., Ducouret, G., & Hebraud, P. (2013). Viscoelastic properties of poly(vinyl alcohol) hydrogels having permanent and transient cross-links studied by microrheology, classical rheometry, and dynamic light scattering. *Macromolecules*, *46* (10), 4174–4183. https://doi.org/10.1021/ma400600f

13 Mayumi, K., Guo, J., Narita, T., Hui, C. Y., & Creton, C. (2016). Fracture of dual crosslink gels with permanent and transient crosslinks. *Extrem. Mech. Lett.*, *6*, 52–59. https://doi.org/10.1016/j.eml.2015.12.002

14 Cheng, Q., Ding, S., Zheng, Y., Wu, M., Peng, Y., Diaz-Dussan, D., Shi, Z., Liu, Y., Zeng, H., Cui, Z., & Narain, R. (2021). Dual cross-linked hydrogels with injectable, self-healing, and antibacterial properties based on the chemical and physical cross-linking. *Biomacromolecules, 22*(4), 1685–1694. https://doi.org/10.1021/acs.biomac.1c00111

15 Jiayi Ai, Kai Li, Jianbin Li, Fei Yu, & Jie Ma (2021). Super flexible, fatigue resistant, self-healing PVA/xylan/borax hydrogel with dual-crosslinked network. *Int. J. Biol. Macromol.*, *172*, 66–73. https://doi.org/10.1016/j.ijbiomac.2021.01.038

16 Gong, J. P., Katsuyama, Y., Kurokawa, T., & Osada, Y. (2003). Double-network hydrogels with extremely high mechanical strength. *Adv. Mater.*, *15*, 1155–1158. https://doi.org/10.1002/adma.200304907

17 Nolte, H., John, S., Smidsrød, O., & Stokke, B. T. (1992). Gelation of xanthan with trivalent metal ions. *Carbohydr. Polym.*, *18*, 243–251. https://doi.org/10.1016/0144-8617(92)90089-9

18 Philippova, O. E., Shibaev, A. V., Muravlev., D. A., & Mityuk, D. Yu. (2016). Structure and rheology of solutions and gels of stiff polyelectrolyte at high salt concentration. *Macromolecules, 49* (16), 6031–6040. https://doi.org/10.1021/acs.macromol.6b01392

19 Shibaev, A. V., Doroganov, A. P., Larin, D. E., Smirnova, M. E., Cherkaev, G. V., Kabaeva, N. M., Kitaeva, D. Kh., Buyanovskaya, A. G., & Philippova, O. E. (2021). Hydrogels of polysaccharide carboxymethyl hydroxypropyl guar crosslinked by multivalent metal ions. *Polym. Sci.*, *Ser. A 63*, 24–33. https://doi.org/10.1134/S0965545X21010089

20 Lund, T., Smidsrød, O., Stokke, B. T., & Elgsaeter, A. (1988). Controlled gelation of xanthan by trivalent chronic ions. *Carbohydrate Polymers*, *8*(4), 245–256. https://doi.org/10.1016/0144-8617(88)90064-1

21 Shibaev, A. V., Ospennikov, A. S., Kuznetsova, E. K., Kuklin, A. I., Aliev, T. M., Novikov, V. V., & Philippova, O. E. (2022). Universal character of breaking of wormlike surfactant micelles by additives of different hydrophobicity. *Nanomaterials, 12*, 4445. https://doi.org/10.3390/nano12244445

22 Bergmann, D., Furth, G., & Mayer, C. (2008). Binding of bivalent cations by xanthan in aqueous solution. *Int. J. Biol. Macromol.*, *43*, 245−251. https://doi.org/10.1016/j.ijbiomac.2008.06.001

23 Ma, L. & Barbosa-Canovas, G.V. (1997). Viscoelastic properties of xanthan gels interacting with cations. *J. Food Sci.*, *62*, 1124–1128. https://doi.org/10.1111/j.1365-2621.1997.tb12227.x

24 Treloar, L. R. G. (1975). *The physics of rubber elasticity*. Clarendon Press, Oxford.

25 Shibaev, A. V., Muravlev, D. A., Muravleva, A. K., Matveev, V. V., Chalykh, A. E., & Philippova, O. E. (2020). pH-dependent gelation of a stiff anionic polysaccharide in the presence of metal ions. *Polymers*, *12*(4), 868. https://doi.org/10.3390/polym12040868

How to Cite: Megbenu, H.K., Azhikhanova, Zh., Ingkar, G., Rakhimgaliyev, N., Mels, A., Kenzheshov, A., Askarov, A., Shaimardan, M. & Nuraje, N. (2024) Catalytic Dehydration of Biomass-Derived Feedstocks to Obtain 5-Hydroxymethylfurfural and Furfural. *Eurasian Journal of Chemistry, 29, 2(114), 96-105.* https://doi.org/10.31489/2959-0663/2-24-1

Article

Received: 14 November 2023 | Revised: 2 April 2024 |
Accepted: 7 April 2024 | Published online: 23 April 2024

UDC 661.7

https://doi.org/10.31489/2959-0663/2-24-1

Harry K. Megbenu[1], Zhanat Azhikhanova[2], Gulnaz Ingkar[1],
Nurzhan Rakhimgaliyev[1], Aizada Mels[1], Almaz Kenzheshov[1], Almas Askarov[1],
Minavar Shaimardan[2], & Nurxat Nuraje[1]*

[1]*Nazarbayev University, Astana, Kazakhstan;*
[2]*National Laboratory Astana, Nazarbayev University, Astana, Kazakhstan*
*(*Corresponding author's e-mail: nurxat.nuraje@nu.edu.kz)*

Catalytic Dehydration of Biomass-Derived Feedstocks to Obtain 5-Hydroxymethylfurfural and Furfural

Biomass-produced furanics, furfural and 5-hydroxymethylfurfural (5-HMF), are considered as vital platform chemicals used in the production of active pharmaceutical ingredients (APIs), commodity goods, and fuels. The primary challenge associated with their production pertains to the high cost involved in scaling up to industrial levels. Consequently, it is essential to explore more cost-effective options that yield efficient end products. In this study, the use of Lewis and Brønsted acids such as HCl and $AlCl_3$ enhances the isomerization of glucose through catalytic dehydration into 5-HMF. It was observed that employing moderate reaction conditions increased the yield of 5-HMF to 44.94 % and 50.60 % respectively, with changes in HCl concentration and $AlCl_3$ mass loading. The suitable conditions to achieve the highest yield of 5-HMF were 100 μL of HCl, 0.75 g of $AlCl_3$, reaction temperature 150 °C, and reaction time 4 h. In the second experiment, corncob was converted into furfural in the presence of 20 % H_2SO_4, in combination with NaCl as a promoter. The optimal conditions under which a yield of 44.77 % was achieved were as follows: 50 mL of 20 % H_2SO_4, reaction temperature 140 °C, 0.5 g of NaCl, 5 g of corncob, and reaction time 160 min. Furthermore, a proposed reaction mechanism was outlined to elucidate the pathway for the production of the aforementioned platform chemicals.

Keywords: Furfural, Hydroxymethylfurfural, 5-HMF, catalysts, dehydration, biomass, glucose, corncob, extraction.

Introduction

The ongoing decline of fossil fuel reserves resulting from the persistent utilization of petroleum and coal feedstocks, coupled with the pressing climate emergency, has spurred the scientific community to prioritize the exploration of bio-based alternatives [1]. In response, biorefinery concept has emerged to investigate and yield economically viable products for fossil fuel compounds, thereby contributing to a reduction in greenhouse gas emissions [2]. In recent research, significant interest has resulted in the development of bio active platform chemicals. Various platform chemicals, such as succinic acid, levulinic acid, 5-hydroxymethylfurfural (5-HMF), and furfural could be synthesized from biomass resources as reported by [3, 4]. Furfural and 5-HMF holds unique position among bio-active chemicals due to their physical and chemical properties, comprising aldehyde, furan ring components, and alcohol. According to the U.S. Department of Energy (US DOE), furfural and 5-HMF are designated as two of the "top 10" platform chemicals for specialty and bulk chemicals [5]. These platform compounds are typically synthesized by acid-catalyzed dehydration of C6 and C5 sugars, which are obtained from the hydrolysis of cellulose and hemicellulose. For the past few years, researchers main focus is to study the optimization conditions for furfural and 5-HMF production from biomass [6–8], investigating the separation and extraction methods to increase the selectivity and yield [9, 10].

5-HMF production from biomass shows promising properties among the platform chemicals as reported by the US DOE and can be easily transformed into active pharmaceutical ingredients (APIs) as well as other valuable chemicals [11]. Biomass-produced agrobased resources such as lignocellulose, are vital resource for the synthesis of 5-HMF and are highly abundant in the environment. It usually follows a three-step reaction under acidic conditions involving hydrolysis of cellulose to glucose to form fructose through isomerization followed by dehydration to 5-HMF [12]. Different approaches are employed by researchers for the conversion of starch-rich agricultural waste into 5-HMF [13]. 5-HMF conversion from biomass-derived residues is mostly investigated via optimization of reaction parameters such as catalyst loading, temperature, pressure, and reaction time. Yosuke M. et al. applied liquid-liquid extraction for the synthesis of 5-HMF from monosaccharides using methyl isobutyl ketone (MIBK) solvent. An 85 % yield of 5-HMF was achieved by addition of Lewis acid which promotes isomerization of glucose into five membered ring structure [14]. A combination of Lewis and Bronsted acid catalysts was employed by Huixiang and his team in the synthesis of 5-HMF from carbohydrates using a low boiling point (BP) solvent [15]. From their work, about 70 % of 5-HMF was achieved when isopropyl alcohol (IPA) solvent was used.

Furfural, on the other hand, possesses outstanding applications in the production of active pharmaceutical ingredients, polymeric materials, food additives, cosmetics, pesticides, insecticides, disinfectants, etc. [16, 17]. Their synthesis involves acid-catalyzed dehydration of hemicellulose or furan-containing compounds as crucial C5 sugar components. A wide range of agro-based biomass sources can be used for the synthesis of furfural. For instance, Adebayo and his colleagues synthesized furfural and furfuryl alcohol from corncob, elephant grass, sunflower, and baobab pulp in a Lewis acid medium [18]. Likewise, furfural synthesis was achieved from agro-based biomass resources such as rice husk, sugarcane bagasse, cotton seeds, and oat hulls via heterogeneous acid catalysts [19]. One major challenge faced by researchers focuses on improving the yield and purity of furfural by optimizing the reaction conditions such as temperature, catalyst loading, solvent used, and reaction time.

This research explores the variation of Brønsted acid (HCl) and Lewis's acid ($AlCl_3$) as catalysts in the conversion of glucose into 5-HMF under moderately optimized conditions using a high pressure batch reactor. Additionally, the synthesis of another platform chemical viz furfural was studied using corncob as the primary feedstock in the conversion process. In the furfural synthesis, NaCl was employed as a promoter to augment the hydrolysis and dehydration of corncob into furfural. To elucidate the reaction pathway to produce these platform chemicals, a plausible reaction mechanism is proposed in this work.

Experimental

Materials

Corncob was purchased from the local market (delivered from farmland Jetysu region of Kazakhstan); all other chemical reagents used in this experiment were obtained from Sigma-Aldrich: D-(+)-Glucose monohydrate, ≥ 99 %; 5-hydromehtylfurfural (5-HMF), ≥ 99 %; Furfural, 99 %; Ethylene Glycol, 99.8 %; Isopropyl alcohol (IPA), 99.5 %; Methanol (HPLC grade), ≥ 99.8 %, Dichloromethane (DCM), ≥ 99.9 %; Aluminium chloride anhydrous ($AlCl_3$), Sodium chloride (NaCl), 99.8 %; Hydrochloric acid (HCl), ≥37 %; and Sulfuric acid (H_2SO_4).

5-HMF Synthesis

To a 150 mL high pressure batch reactor (Buchi-1297840), 2 g of glucose, $AlCl_3$ (0.25–1.5 g), HCl (50–200 μL), 45 mL of IPA, and 5 mL of deionized (DI) water were added and gently stirred to obtain a homogenous solution mixture. The homogeneous mixture was heated in a high pressure reactor at 10 bar at a temperature of 150 °C for 4h at a stirring rate of 350 rpm. After the reaction was stopped, the mixture was quickly collected and filtered under vacuum and the analyte was extracted with ethyl acetate and solvent removed under reduced pressure. An approximate mass of light brown solution was obtained, which was separated into organic and aqueous phases. Samples taken from two phases were filtered through a 0.22 μm syringe filter and diluted with methanol for HPLC analysis. The concentrate was preserved in clean Pyrex glass vials for further analysis. The 5-HMF yield was calculated as follows:

$$\text{5-HMF yield (\%)} = \frac{N_{\text{5-HMF}}}{N_{\text{glucose}}} \times 100\ \%,$$

where $N_{\text{5-HMF}}$ denotes the moles of 5-HMF produced and N_{glucose} represents the moles of glucose used. To confirm the effectiveness of the chosen method, all experiments were carried out in triplicate.

Furfural Synthesis

5 g of corncob, 0.5 g of NaCl, and 50 mL of 20 % H_2SO_4 was prepared under the fume hood. The mixture was transferred into a high pressure batch reactor (Buchi-129784, Germany) at 10 bar, where the reaction was carried out separately at different temperatures of 100, 120, 140, 160, and 180 °C for 160 min. The distillate was filtered and extraction carried out by liquid-liquid approach using dichloromethane (DCM) sol-

vent after which the furfural was separated under reduced pressure using rotavap (Buchi R-210). Furfural yield was calculated as follows:

$$\text{Furfural yield (\%)} = \frac{N_{\text{Furfural}}}{N_{\text{hemicellulose}}} \times 100\ \%\ ,$$

where N_{Furfural} is the mole of furfural product after reaction and extraction and $N_{\text{hemicellulose}}$ is the mole of hemicellulose (pentose) content in corncob.

The hemicellulose content used was based on literature values obtained by several researchers from the National Institute of Technology, India. According to their findings, the hemicellulose content obtained from lignocellulosic dry corncob is between 26–36 % [20]. The average of the reported amount (31 %) was used in calculating the theoretical mass of the hemicellulose content in our corncob. Furfural content was calculated based on the concentrations obtained by UHPLC where samples were measured according to the calibration (with R^2 0.9962) prepared for furfural analysis. All experiments were carried out in triplicates to confirm the effectiveness of the chosen methods.

Scheme of the 5-HMF and furfural production from glucose and corncob respectively is presented in Figure 1.

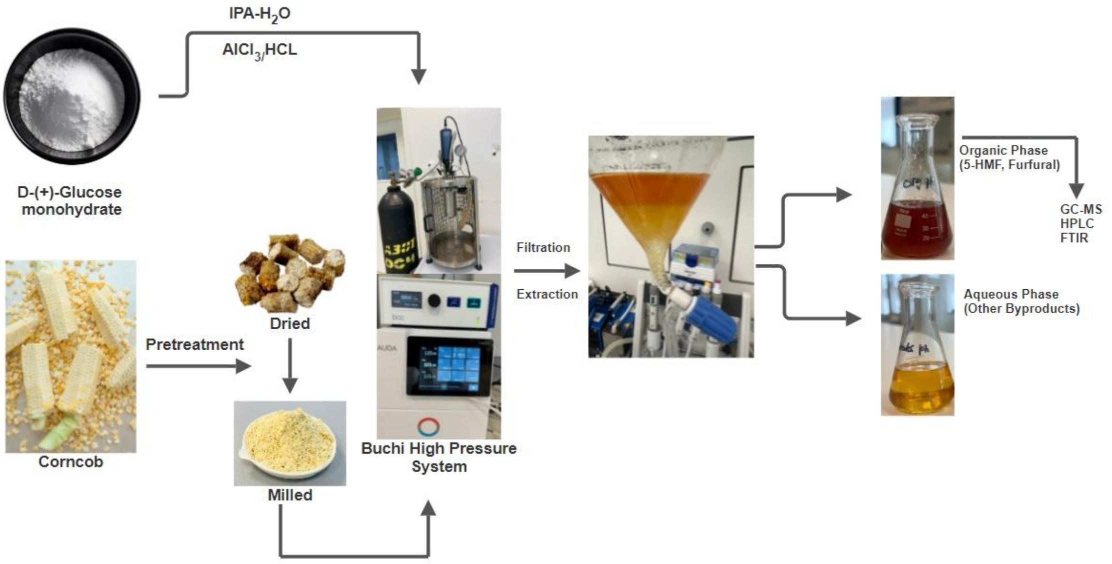

Figure 1. Process flowsheet of 5-HMF and furfural production from glucose and corncob respectively

Characterization

Characterization analyses were performed qualitatively and quantitatively for pure standards and synthesized products. Prior characterization of the pure furfural standard, purification was carried out by a simple distillation process as the furfural changed color to dark brown due to improper preservation. Furfural and 5-HMF were characterized by FTIR, UHPLC, and GCMS to understand the physical and chemical features. The functional groups were detected using FTIR spectrometer (Thermo Scientific Nicolet iS10, USA) to study the chemical composition of furfural and 5-HMF. All spectra were recorded in the range 4000–500 cm^{-1} with a scanning speed of 1 $cm^{-1}s^{-1}$ and a 4 cm^{-1} resolution. 5-HMF concentration obtained from glucose conversion was analyzed by UHPLC (Ultimate 3000, Thermo Fisher Scientific, USA) and equipped with a UV detector (C18 column, 150 mm length, particle size 1.9-micron, diameter 2.1 mm). The eluent used was a mixture of water: methanol (80:20, v/v) at a flow rate of 0.2 mL/min. The column temperature was 30 °C and the sample injection volume was 1 μL. The analysis was repeated two times and the 5-HMF was measured at 284 nm wavelength and quantified using an external standard calibration curve with series of dilutions ranging from 0.5 mg/L to 30 mg/L. The quantitative analysis of furfural used the same parameters as for the analysis of 5-HMF. The only difference is the change in wavelength from 284 nm to 275 nm for furfural analysis. A TSQ 8000 Evo Triple Quadrupole GC-MS/MS (Thermo Fisher Scientific) instrument with ion source temperature of 200 °C, the operating system at 70 eV, capillary temperature of 200 °C, with injection split (20:1 ratio, 1 μL) at 270 °C injector temperature was used to perform qualitative analysis of the synthesized products. 5 % phenyl residues: 95 % methyl polysiloxane capillary column (Trace GOLD TG-5MS-GC Column 30 m × 0.25 μm × 0.25 mm, Thermo) was used. The oven temperature was programmed as follows: initially at 60 °C for 5 min, increased to 260 °C at a flow rate of 15 °C/min and maintained at 260 °C for 20 min, and finally increased to 270 °C rate 2 °C/min, maintained at 270 °C for 5 min. Helium (He) was used as the carrier gas at a flow rate of 1 mL/min. The full scan of the EI ionization mode was carried out in the range of m/z 45–600. Data collection, compound identification, and peak processing were performed with Xcalibur (Thermo Scientific).

Results and Discussion

The purchased furfural standard was purified and characterized by FTIR, GCMS, and HPLC to study their physicochemical properties. FTIR was as well measured for the as-prepared sample products and compared with pure standards and feedstocks. The results obtained by FTIR showed prominent peaks in which different functional groups were identified by comparison with literature data. In Figure 2, the chemical composition of glucose, corncob, synthesized 5-HMF and furfural as well as pure 5-HMF and furfural standards are presented.

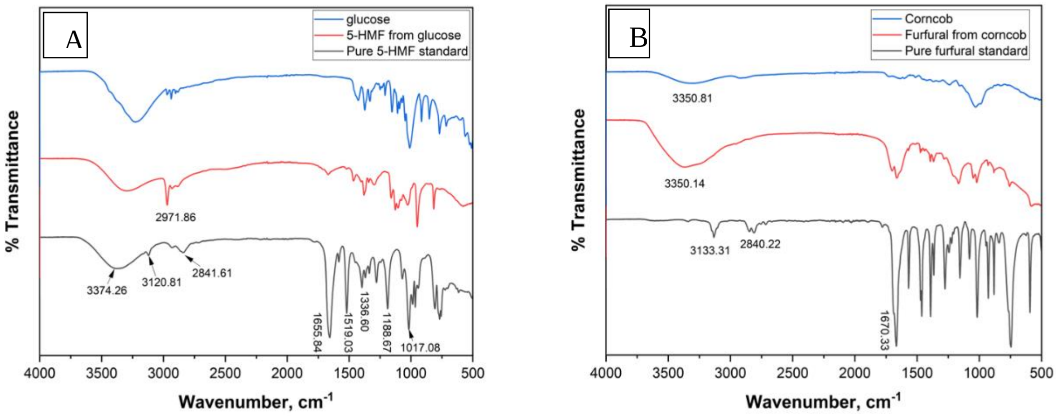

Figure 2. FTIR spectra of 5-HMF (A) and furfural (B)

The IR spectra of glucose, 5-HMF, and pure 5-HMF standard in Figure 2(A) show the chemical composition consistent with molecular structures and expected functional groups, confirming the identity of these compounds. Though peaks were observed in the same spectral region from all samples, in overall, the pure 5-HMF standard shows peaks with higher intensities compared with that of raw glucose and 5-HMF obtained from glucose. A broad absorption band at 3374.26 cm^{-1} was observed in all three materials at the same position which could be attributed to the stretching vibrations of 5-HMF hydroxyl groups [21]. The absorption bands in the region 3120.81–2841.61 cm^{-1} from pure 5-HMF standard through synthesized 5-HMF were attributed to the presence of methylene group (-CH_2-). Further, the pure 5-HMF standard possesses a sharp band at 1655.84 cm^{-1}, which was assigned to the stretching vibration of C=O (carbonyl group). However, this prominent was not so recognizable in the raw glucose and 5-HMF samples produced from glucose. The presence of C-O stretching vibration was justified by absorption peaks at 1017 cm^{-1} and 1188 cm^{-1} in all samples as already reported [22].

Figure 2(B) shows the IR spectra of pure furfural standard, furfural produced from corncob and raw corncob. In the pure furfural spectrum, moderate intensity bands at 2810 and 2840.22 cm^{-1} represent C-H stretch for the aldehyde group while at 3133.31 cm^{-1}, the presence of aliphatic C-H stretch was recorded, at the same time these peaks were not observed in corncob and furfural synthesized from corncob. At a wavelength of 1670.33 cm^{-1}, the presence of the conjugated carbonyl group showed an intense peak confirming the presence of the carbonyl functional group in the furfural compound. This is also observed in the same region from furfural-derived corncob. This occurs in the conjugated unsaturated aldehyde region but not the ketone group. The spectral range between 881 to 745.69 cm^{-1} could be attributed to the C-H bending vibration while at 1460.98 cm^{-1}, the –C=C functional group was recorded [23]. The spectral region between 881–876 cm^{-1} and 773–770 cm^{-1} is indicative of the –CH out-of-plane bending vibrations associated with aromatic rings and their derivatives where these peaks are recorded in pure furfural and that of furfural derived from corncob [24]. In summary, more intense peaks are observed in pure furfural standard and synthesized furfural compared with raw corncob spectra.

GC-MS/MS qualitative analysis was performed to confirm glucose and corncob transformation into 5-HMF and furfural respectively. From the result, the purity and molecular composition of 5-HMF and furfural was confirmed by qualitative analysis using a TSQ 8000 triple quadruple GC-MS/MS analytical instrument. The chromatogram exhibited distinctive retention time at 3.62 min and 4.16 min for 5-HMF and furfural respectively showing the mass-to-charge ratio (m/z) and relative abundance of all fragments generated during the bombardment by electron impact ionization process as shown in Figure 3.

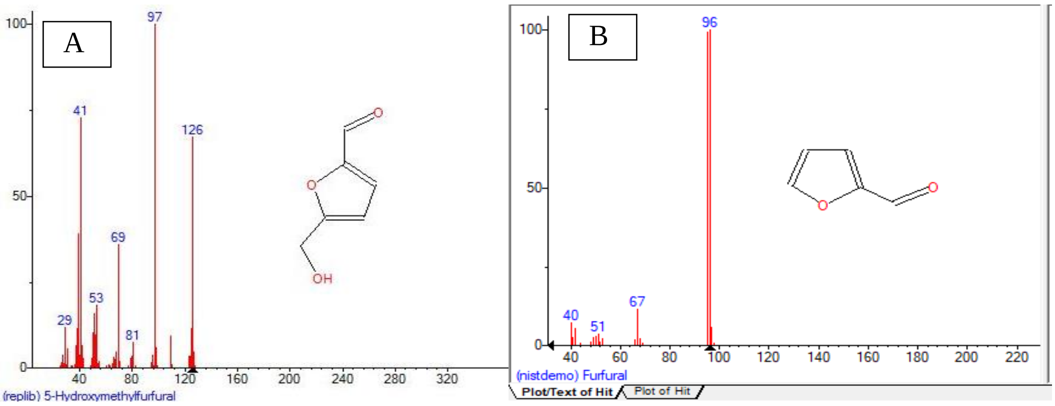

Figure 3. GC-MS/MS qualitative test for 5-HMF (A) and furfural (B) from glucose and corncob respectively

The spectrum of the 5-HMF derivative with m/z 126 corresponds to the molecular mass of the parent ion (M). A methyl group loss fragment (–CH_3) at m/z 97 denotes the base peak, while oxidative products (e.g., HCOOH) and fragments resulting from furan ring opening forming dehydrated products are also observed after bombardment (Fig. 3(A)). In addition, fragments resulting from substituents or side chains may also be evident. For furfural fragments, as shown in Figure 3(B), the m/z value at 96 corresponds to the molecular mass of furfural as well as the base peak since it shows the highest intensity amongst all other fragments. Importantly, a fragment with m/z 67 corresponds to a furanic cation which plays a vital role in furfural synthesis. The fragments obtained from as prepared 5-HMF, and furfural are in agreement with those already reported in the literature.

A quantitative and qualitative analysis was carried out with UHPLC ultimate 3000 (Thermo Scientific) with UV-vis detector at 284 and 275 nm wavelength for 5-HMF and furfural respectively (Fig. 4). Prior to analysis, a calibration curve was prepared using pure 5-HMF and furfural standard. The correlation coefficients 0.9999 and 0.9998 for 5-HMF and furfural respectively proved the efficiency of the curve.

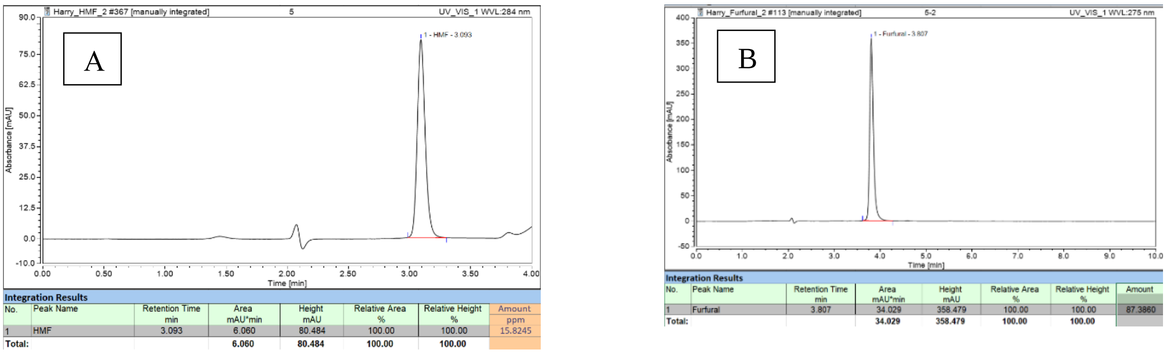

Integration Results

No.	Peak Name	Retention Time min	Area mAU*min	Height mAU	Relative Area %	Relative Height %	Amount ppm
1	HMF	3.093	6.060	80.484	100.00	100.00	15.8245
Total:			**6.060**	**80.484**	**100.00**	**100.00**	

Integration Results

No.	Peak Name	Retention Time min	Area mAU*min	Height mAU	Relative Area %	Relative Height %	Amount
1	Furfural	3.807	34.029	358.479	100.00	100.00	87.3860
Total:			**34.029**	**358.479**	**100.00**	**100.00**	

Figure 4. UHPLC analysis for 5-HMF (*A*) and furfural (*B*) synthesized from glucose and corncob respectively

An intense peak in Figure 4(A) was determined at a retention time of 3.093 min for 5-HMF with the highest concentration of 257.87 mg/L amongst all synthesized samples. Furfural confirmation test was also conducted on UHPLC where a furfural peak was observed at 3.807 min as shown in Figure 4(B).

Effect of HCl Volume and $AlCl_3$ Loading Towards 5-HMF Production from Glucose

The synthesis of 5-HMF from glucose conversion exhibits potential pathways, inclusive of both direct dehydration and intermediated routes, possibly involving compounds like fructose as reported by [25]. Lewis acids, such as $AlCl_3$, VCl_3, and $SnCl_4$ are found to be useful in the glucose isomerization to fructose compared with Brønsted acids. Furthermore, fructose then undergoes dehydration in the presence of Brønsted acid (HCl) leading to the formation of 5-HMF. Figure 5(A) shows the effect of HCl volume for 5-HMF conversion from glucose. The study aimed to investigate the impact of variations in HCl volume and $AlCl_3$ catalyst loading on 5-HMF yield. Different HCl volumes, ranging from 50 to 250 µL, were tested in a 50 mL IPA:H_2O ratio to facilitate the conversion of glucose into 5-HMF. The experimental procedure involved heating the reaction mixture in a high pressure batch reactor to 150 °C and maintaining a steady temperature for a residence time of 4 h.

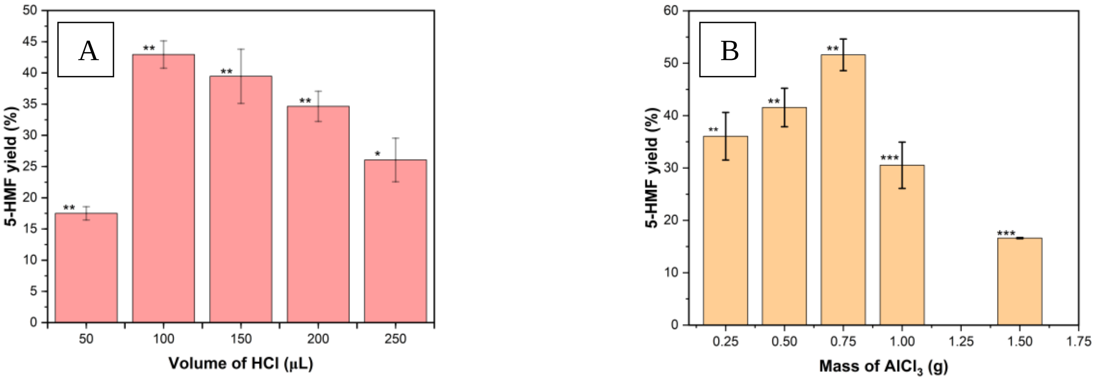

Figure 5. HCl concentration (A) and $AlCl_3$ mass loading (B) variation for 5-HMF production from glucose (Asterisks denotes level of significance based on one sample t-test assuming statistical significance at * = :$P < 0.05$ ** = :$P<0.005$ *** = :$P <0.0005$)

The 5-HMF yield exhibited an increase from 17.51 % to 42.94 % when HCl volumes of 50 and 100 µL were respectively used (Fig. 5(A)). However, as the HCl volume was further increased to 150–250 µL, the 5-HMF yield gradually decreased within the range of 39.46 % to 26.06 %. Based on the findings, the optimal conditions were determined to be a 100 µL HCl volume and 1 g of $AlCl_3$. Between 100–200 µL HCl volume shows a good trend in transforming glucose to 5-HMF. However, the yield is relatively low when too low or too high concentration of HCl was tested as shown in Figure 5(A). This trend is similar to the work that was already reported by [26-27]. As widely accepted, the formation of 5-HMF requires relatively moderate conditions. Increasing the acidity of the medium might facilitate the dehydration reaction but highly acidic medium may not be favorable as seen in the trend of product yield. In addition, choosing a higher temperature for highly acidic medium might convert the 5-HMF to levulilic acid as an intermediate [28]. The results obtained from statistical data prove that the difference the triplicates of each experiment conducted towards 5-HMF synthesis was highly significant ($p < 0.05$). To summarize, a moderate HCl concentration is required for a good yield of 5-HMF while low or higher concentration may suppress the glucose conversion to 5-HMF.

Empirical research was conducted by varying the mass of $AlCl_3$ to monitor the yield of 5-HMF, aiming to determine the optimal quantity of $AlCl_3$ conducive to the conversion of glucose into 5-HMF, as depicted in Figure 5(B). To study the effect of $AlCl_3$ mass loading, different masses varied from 0.25–1.5 g of $AlCl_3$ dosage were used. The maximum yield of 51.60 % was reached when 0.75 g of $AlCl_3$ was used in the presence of 100 µL HCl for a reaction time of 4 h at 10 bar pressure. Increasing the mass of $AlCl_3$ from 0.25 to 0.75 g shows a good correlation by increasing the yield of 5-HMF yield while further increment of $AlCl_3$ mass results in low yield. Increasing trends were found in the work of [29], however, they did not include further increment of $AlCl_3$ dosage in their research. One possible reason for the yield decline after increasing the mass of $AlCl_3$ could be related to the agglomeration of the catalyst due the higher amount in solution or possibility of converting the glucose into other byproducts such as humins.

Effect of Temperature on Corncob Dehydration into Furfural Using H_2SO_4/NaCl Medium

In the furfural synthesis from corncob via a Brønsted acid catalysed dehydration reaction method in the presence of NaCl, effect of temperature variation on corncob conversion into furfural was the main parameter studied. To achieve furfural, Cl^- ions in the presence of 20 % H_2SO_4 enhance the transformation of corncob hemicellulose layers during dehydration process to produce furfural. H_2SO_4 serves as a catalyst while addition of NaCl as a promoter. From the results, furfural synthesis from corncob using a high pressure batch system significantly impacts the yield when temperature was varied (Fig. 6).

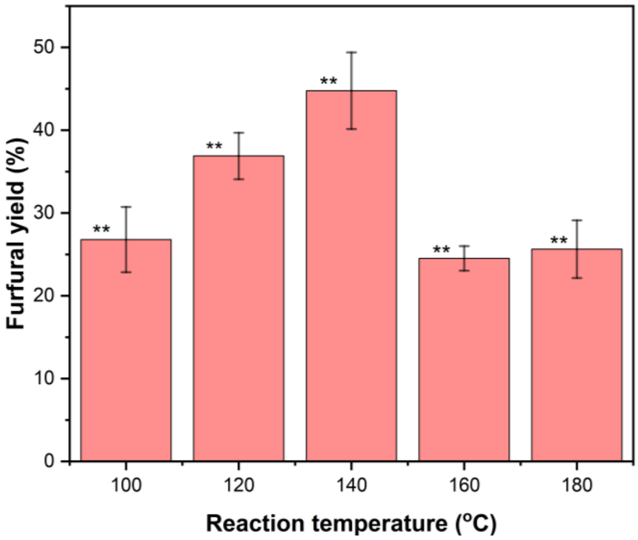

Figure 6. Effect of temperature on corncob dehydration into furfural using H_2SO_4/NaCl medium
(Asterisks denotes level of significance based on one sample t-test assuming
statistical significance at at * = :P < 0.05 ** = :P<0.005 *** = :P <0.0005)

As can be seen in Figure 6, NaCl dramatically promoted the conversion of corncob into furfural in the presence of H_2SO_4 catalyst at a reaction temperatures ranging from 100 °C to 180 °C at 10 bar pressure in 160 min reaction time. The highest furfural yield of 44.77 % was obtained for 140 °C reaction temperature while the lowest yield (24.52 %) at 160 °C reaction temperature. From the outcome and the chemistry involved in the synthesis, it could be attributed to the fact that corncob dehydration of hemicellulose (pentose) according to this reaction is highly favoured at moderate temperatures. The reaction likely proceeds efficiently at a reaction temperature of 140 °C leading to higher furfural yield. In contrast, the choice of higher reaction temperature may be too aggressive for this reaction resulting in the low yield. This could also occur due to undesired side reactions or the rehydration of furfural into other by-products such as humins and levulinic acid. The results obtained from statistical data proves that the difference the triplicates of each experiment conducted towards furfural synthesis was highly significant ($p < 0.005$). The results obtained highlight the importance of temperature optimisation in achieving a higher yield.

Reaction Mechanism

The reaction routes for glucose conversion into 5-HMF are shown in Figure 7(A). Glucose conversion in the presence of Brønsted and Lewis acids proceeded through a coupled route, involving the use of $AlCl_3$ for isomerization of glucose to fructose and the fructose dehydration in the presence of halogen to produce 5-HMF. 5-HMF degradation may occur, leading to the formation of byproducts such as formic acid, levulic acid, or humins [30]. In Figure 7(B), the furfural reaction pathway is divided into two major steps: in the first step, hydrolysis of corncob into a pentosan derivative, xylose may occur, which is further converted into furfural in the second step via a dehydration process [31].

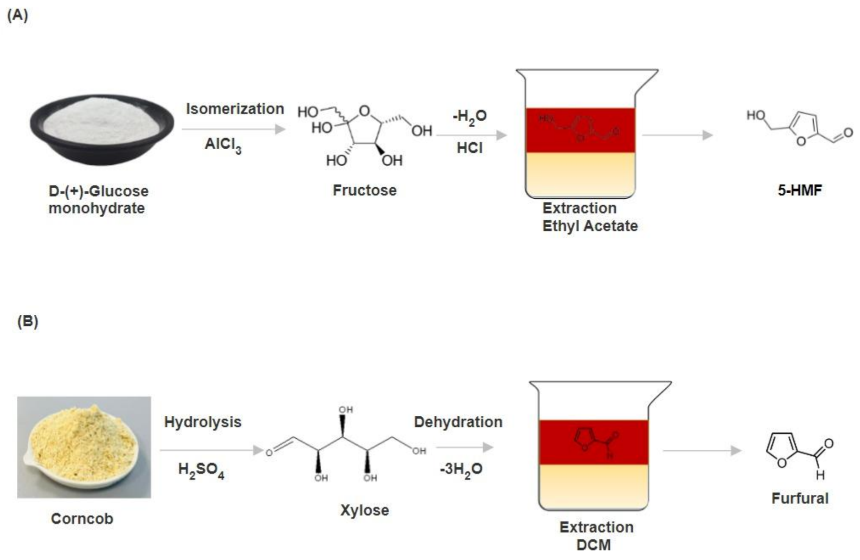

Figure 7. Possible reaction mechanism for 5-HMF and furfural production from glucose and corncob respectively

The use of H_2SO_4 acts as a catalyst in both steps, resulting in the production of furfural from corncob. The use of NaCl helps to increase furfural yield, serves as a promoter, as well as aids in the stabilization of oxonium or carbocation intermediates for the H_2SO_4 catalyst.

Conclusions

This study highlights the impact of Brønsted and Lewis acids in the catalytic conversion of biomass-derived glucose and corncob into 5-Hydroxymethylfurfural (5-HMF) and furfural, respectively. The results obtained clearly demonstrate that selecting optimal conditions, including concentration, reaction temperature, reaction time, catalyst, and solvent system, is crucial for achieving high yield when transforming various biomass feedstocks into their respective products. HCl and $AlCl_3$ have been demonstrated to exhibit effective conversion mechanisms when used in conjunction with IPA, H_2O, and 20 % H_2SO_4 to produce 5-HMF and furfural. The addition of NaCl as a promoter significantly enhances the conversion of corncob into furfural when H_2SO_4 is employed as a catalyst. Impressive yields of 42.94 % for 5-HMF (HCl concentration variation), 51.6 % for 5-HMF ($AlCl_3$ mass loading variation) and 44.77 % for furfural were achieved. This research work also proposed a plausible mechanism for glucose and corncob conversion into the aforementioned platform chemicals.

Funding

This research is funded by the Science Committee of the Ministry of Education and Science of the Republic of Kazakhstan (Grant No. AP14871259) and the Collaborative Research Grant of Nazarbayev University (Project ref. no. 20122022CRP1609).

*Author Information**

**The authors' names are presented in the following order: First Name, Middle Name and Last Name*

Harry Kwaku Megbenu — PhD student, Department of Chemical and Materials Engineering, School of Engineering and Digital Sciences, Nazarbayev University, Qabanbay Batyr Ave 53, Astana, 010000, Kazakhstan; e-mail: harry.megbenu@nu.edu.kz; https://orcid.org/0000-0001-9144-5950

Zhanat Azhikhanova — Junior researcher, National Laboratory Astana, Nazarbayev University, Qabanbay Batyr Ave 53, Astana, 010000, Kazakhstan; e-mail: zhanat. azhikhanova@nu.edu.kz

Gulnaz Ingkar — Bachelor student, Nazarbayev University, Qabanbay Batyr Ave 53, 010000, Astana, Kazakhstan; e-mail: gulnaz.ingkar@nu.edu.kz

Nurzhan Rakhimgaliyev — Bachelor student, Nazarbayev University, Qabanbay Batyr Ave 53, Astana, 010000, Kazakhstan; e-mail: nurzhan.rakhimgaliyev@nu.edu.kz

Aizada Mels — Bachelor student, Nazarbayev University, Qabanbay Batyr Ave 53, Astana, 010000, Kazakhstan; e-mail: aizada.mels@nu.edu.kz

Almaz Kenzheshov — Bachelor student, Nazarbayev University, Qabanbay Batyr Ave 53, Astana, 010000, Kazakhstan; e-mail: almaz.kenzheshov@nu.edu.kz

Almas Askarov — Bachelor student, Nazarbayev University, Qabanbay Batyr Ave 53, Astana, 010000, Kazakhstan; e-mail: almas.askarov@nu.edu.kz

Minavar Shaimardan — PhD, Researcher, National Laboratory Astana, Nazarbayev University, Qabanbay Batyr Ave 53, Astana, 010000, Kazakhstan; e-mail: minavar.shaimardan@nu.edu.kz; https://orcid.org/0000-0001-7571-820X

Nurxat Nuraje (*corresponding author*) — PhD, Associate Professor, Department of Chemical and Materials Engineering, School of Engineering and Digital Sciences. Head of laboratory "Renewable Energy" National Laboratory Astana, Nazarbayev University, Qabanbay Batyr Ave 53, Astana, 010000, Kazakhstan; e-mail: nurxat.nuraje@nu.edu.kz; https://orcid.org/0000-0002-4335-8905

Author Contributions

The manuscript was written through contributions of all authors. All authors have given approval to the final version of the manuscript. CRediT: **Harry Kwaku Megbenu** conceptualization, data curation, investigation, methodology, validation, visualization, writing original draft & editing; **Zhanat Azhikhanova** data curation, methodology, & formal analysis; **Gulnaz Ingkar** data curation, methodology & formal analysis; **Nurzhan Rakhimgaliyev** data curation, methodology & formal analysis; **Mels Aizada** data curation, methodology & formal analysis; **Almaz Kenzheshov** data curation, methodology & formal analysis; **Almas Askarov** data curation, methodology & formal analysis; **Minavar Shaimardan** conceptualization, data curation, formal analysis, resources, supervision, & validation; **Nurxat Nuraje** conceptualization, data curation, formal analysis, funding acquisition, resources, supervision, validation, & editing.

Acknowledgments

Authors thank Nazarbayev University and National Laboratory Astana for providing access to lab facilities.

Conflict of interest

The authors declare no conflict of interest.

References

1 Zhou, C., Zhao, J., Yagoub, A. E. G. A., Ma, H., Yu, X., Hu, J., Bao, X., & Liu, S. (2017). Conversion of glucose into 5-hydroxymethylfurfural in different solvents and catalysts: Reaction kinetics and mechanism. *Egyptian Journal of Petroleum*, *26*(2), 477–487. https://doi.org/10.1016/j.ejpe.2016.07.005

2 Wanninayake, P., Rathnayake, M., Thushara, D., & Gunawardena, S. (2022). Conversion of rice straw into 5-hydroxymethylfurfural: review and comparative process evaluation. In *Biomass Conversion and Biorefinery* (Vol. 12, Issue 3, pp. 1013–1047). Springer Science and Business Media Deutschland GmbH. https://doi.org/10.1007/s13399-021-01351-x

3 Isikgor, F. H., & Becer, C. R. (2015). Lignocellulosic biomass: a sustainable platform for the production of bio-based chemicals and polymers. *Polymer Chemistry*, *6*(25), 4497–4559. https://doi.org/10.1039/c5py00263j

4 Pulicharla, R., Lonappan, L., Brar, S. K., & Verma, M. (2016). Production of Renewable C5 Platform Chemicals and Potential Applications. In *Platform Chemical Biorefinery: Future Green Chemistry* (pp. 201–216). Elsevier. https://doi.org/10.1016/B978-0-12-802980-0.00011-0

5 Bozell, J. J., & Petersen, G. R. (2010). Technology development for the production of biobased products from biorefinery carbohydrates — the US Department of Energy's "top 10" revisited. *Green Chemistry*, *12*(4), 539–555. https://doi.org/10.1039/b922014c

6 Adebayo, A. J., Ogunjobi, J. K., Oluwasina, O. O., & Lajide, L. (2023a). Comparative Production and Optimisation of Furfural and Furfuryl Alcohol from Agricultural Wastes. *Chemistry Africa*. https://doi.org/10.1007/s42250-023-00594-7

7 He, O., Zhang, Y., Wang, P., Liu, L., Wang, Q., Yang, N., Li, W., Champagne, P., & Yu, H. (2021). Experimental and kinetic study on the production of furfural and HMF from glucose. *Catalysts*, *11*(1), 1–13. https://doi.org/10.3390/catal11010011

8 Ji, L., Tang, Z., Yang, D., Ma, C., & He, Y. C. (2021). Improved one-pot synthesis of furfural from corn stalk with heterogeneous catalysis using corn stalk as biobased carrier in deep eutectic solvent–water system. *Bioresource Technology*, *340*. https://doi.org/10.1016/j.biortech.2021.125691

9 Dietz, C. H. J. T., Kroon, M. C., Di Stefano, M., Van Sint Annaland, M., & Gallucci, F. (2018). Selective separation of furfural and hydroxymethylfurfural from an aqueous solution using a supported hydrophobic deep eutectic solvent liquid membrane. *Faraday Discussions*, *206*, 77–92. https://doi.org/10.1039/c7fd00152e

10 Wang, Z., Bhattacharyya, S., & Vlachos, D. G. (2021). Extraction of Furfural and Furfural/5-Hydroxymethylfurfural from Mixed Lignocellulosic Biomass-Derived Feedstocks. *ACS Sustainable Chemistry and Engineering*, *9*(22), 7489–7498. https://doi.org/10.1021/acssuschemeng.1c00982

11 Souzanchi, S., Nazari, L., Rao, K. T. V., Yuan, Z., Tan, Z., & Xu, C. (Charles). (2023). 5-HMF production from industrial grade sugar syrups derived from corn and wood using niobium phosphate catalyst in a biphasic continuous-flow tubular reactor. *Catalysis Today*, *407*, 274–280. https://doi.org/10.1016/j.cattod.2021.07.032

12 Cao, L., Yu, I. K. M., Chen, S. S., Tsang, D. C. W., Wang, L., Xiong, X., Zhang, S., Ok, Y. S., Kwon, E. E., Song, H., & Poon, C. S. (2018). Production of 5-hydroxymethylfurfural from starch-rich food waste catalyzed by sulfonated biochar. *Bioresource Technology*, *252*, 76–82. https://doi.org/10.1016/j.biortech.2017.12.098

13 Roy Goswami, S., Mukherjee, A., Dumont, M. J., & Raghavan, V. (2016). One-Pot Conversion of Corn Starch into 5-Hydroxymethylfurfural in Water-[Bmim]Cl/MIBK Biphasic Media. *Energy and Fuels*, *30*(10), 8349–8356. https://doi.org/10.1021/acs.energyfuels.6b01699

14 Muranaka, Y., Matsubara, K., Maki, T., Asano, S., Nakagawa, H., & Mae, K. (2020). 5-Hydroxymethylfurfural Synthesis from Monosaccharides by a Biphasic Reaction-Extraction System Using a Microreactor and Extractor. *ACS Omega*, *5*(16), 9384–9390. https://doi.org/10.1021/acsomega.0c00399

15 Li, H., Xia, Z., Yan, P., & Zhang, Z. C. (2022). Production of crude 5-hydroxymethylfurfural from glucose by dual catalysts with functional promoters in low-boiling hybrid solvent. *Catalysis Today*, *402*, 10–16. https://doi.org/10.1016/j.cattod.2022.01.017

16 Gao, G., Remón, J., Jiang, Z., Yao, L., & Hu, C. (2022). Selective hydrogenation of furfural to furfuryl alcohol in water under mild conditions over a hydrotalcite-derived Pt-based catalyst. *Applied Catalysis B: Environmental*, *309*. https://doi.org/10.1016/j.apcatb.2022.121260

17 Slak, J., Pomeroy, B., Kostyniuk, A., Grilc, M., & Likozar, B. (2022). A review of bio-refining process intensification in catalytic conversion reactions, separations and purifications of hydroxymethylfurfural (HMF) and furfural. *Chemical Engineering Journal*, *429*. https://doi.org/10.1016/j.cej.2021.132325

18 Adebayo, A. J., Ogunjobi, J. K., Oluwasina, O. O., & Lajide, L. (2023b). Comparative Production and Optimisation of Furfural and Furfuryl Alcohol from Agricultural Wastes. *Chemistry Africa*. https://doi.org/10.1007/s42250-023-00594-7

19 Zhang, L., Xi, G., Yu, K., Yu, H., & Wang, X. (2017). Furfural production from biomass–derived carbohydrates and lignocellulosic residues via heterogeneous acid catalysts. *Industrial Crops and Products*, *98*, 68–75. https://doi.org/10.1016/j.indcrop.2017.01.014

20 Qu, Y., Gandam, P. K., Latha Chinta, M., Gandham, A. P., Prem, N., Pabbathi, P., Konakanchi, S., Bhavanam, A., Atchuta, S. R., Raju Baadhe, R., & Kant Bhatia, R. (2022). *A New Insight into the Composition and Physical Characteristics of Corncob-Substantiating Its Potential for Tailored Biorefinery Objectives*. https://doi.org/10.3390/fermentation

21 Dai, J., Fu, X., Zhu, L., Tang, J., Guo, X., & Hu, C. (2016). One-Pot Deoxygenation of Fructose to Furfuryl Alcohol by Sequential Dehydration and Decarbonylation. *ChemCatChem*, *8*(7), 1379–1385. https://doi.org/10.1002/cctc.201501292

22 Surendra, B. S., & Veerabhadraswamy, M. (2017). Microwave assisted synthesis of polymer via bioplatform chemical intermediate derived from Jatropha deoiled seed cake. *Journal of Science: Advanced Materials and Devices*, *2*(3), 340–346. https://doi.org/10.1016/j.jsamd.2017.07.004

23 Mohamad, N., Abd-Talib, N., & Kelly Yong, T. L. (2020a). Furfural production from oil palm frond (OPF) under subcritical ethanol conditions. *Materials Today: Proceedings*, *31*, 116–121. https://doi.org/10.1016/j.matpr.2020.01.256

24 Mohamad, N., Abd-Talib, N., & Kelly Yong, T. L. (2020b). Furfural production from oil palm frond (OPF) under subcritical ethanol conditions. *Materials Today: Proceedings*, *31*, 116–121. https://doi.org/10.1016/j.matpr.2020.01.256

25 Li, M., Li, W., Lu, Y., Jameel, H., Chang, H. M., & Ma, L. (2017). High conversion of glucose to 5-hydroxymethylfurfural using hydrochloric acid as a catalyst and sodium chloride as a promoter in a water/γ-valerolactone system. *RSC Advances*, *7*(24), 14330–14336. https://doi.org/10.1039/c7ra00701a

26 Dallas Swift, T., Nguyen, H., Anderko, A., Nikolakis, V., & Vlachos, D. G. (2015). Tandem Lewis/Brønsted homogeneous acid catalysis: conversion of glucose to 5-hydoxymethylfurfural in an aqueous chromium(III) chloride and hydrochloric acid solution. *Green Chemistry*, *17*(10), 4725–4735. https://doi.org/10.1039/c5gc01257k

27 Guo, W., Heeres, H. J., & Yue, J. (2020). Continuous synthesis of 5-hydroxymethylfurfural from glucose using a combination of AlCl3 and HCl as catalyst in a biphasic slug flow capillary microreactor. *Chemical Engineering Journal*, *381*. https://doi.org/10.1016/j.cej.2019.122754

28 Herbst, A., & Janiak, C. (2016). Selective glucose conversion to 5-hydroxymethylfurfural (5-HMF) instead of levulinic acid with MIL-101Cr MOF-derivatives. *New Journal of Chemistry*, *40*(9), 7958–7967. https://doi.org/10.1039/c6nj01399f

29 De, S., Dutta, S., & Saha, B. (2011). Microwave assisted conversion of carbohydrates and biopolymers to 5-hydroxymethylfurfural with aluminium chloride catalyst in water. *Green Chemistry*, *13*(10), 2859–2868. https://doi.org/10.1039/c1gc15550d

30 Kumar, A., Chauhan, A. S., Shaifali, & Das, P. (2021). Lignocellulosic biomass and carbohydrates as feed-stock for scalable production of 5-hydroxymethylfurfural. *Cellulose*, *28*(7), 3967–3980. https://doi.org/10.1007/s10570-021-03764-3

31 Yazdizadeh, M., Nasr, M. R. J., & Safekordi, A. K. (2018). A new methodology for the production of furfural as a renewable energy source from bagasse in acidic aqueous media. *Energy Sources, Part A: Recovery, Utilization and Environmental Effects*, *40*(2), 125–133. https://doi.org/10.1080/15567036.2016.1248801